Hi-Q Rotor
Low Wind Speed Technology

Final Report

January 11, 2010

From Wind Tunnel Testing to Field Testing

EERE: INVENTIONS & INNOVATION PROGRAM

Department of Energy
Agreement Number: DE-FG36-06GO16046
Project Period: 09/29/2006 to 09/28/2009

Hi-Q Products, Inc.
506 N. Garfield Avenue, Suite 100-A
Alhambra, CA 91801
Phone: 626-308-4400

Principal Investigator: Todd E. Mills
Todd@hiqproducts.com

Hi-Q Rotor Patent Pending

Table of Contents

List of Figures

List of Tables

List of Symbols and Acronyms

Symbol	Description	Unit
A	Wind Turbine Rotor Swept Area	m^2
A.C.	Aerodynamic Center	---
ASB	Aft Swept Blade	---
B	Barometric Pressure	Pa
BR	Blockage Ratio	---
$b_{tail\ fin}$	Span of the Vertical Tail Fin	m
$c_{\ rotor}$	Section Chord	ft
C_D	Drag Coefficient	~
C_L	Lift Coefficient	~
C_Q	Torque Coefficient	~
CFD	Computational Fluid Dynamics	---
C.G.	Center of Gravity	---
C_p	Aerodynamic Power Coefficient	---
$C_{p,i}$	Power Coefficient in bin i	---
$C_{T\ rotor\ Hi\text{-}Q}$	Hi-Q Design #61 Rotor Thrust Coefficient	---
$c_{tail\ fin}$	Chord of the Vertical Tail Fin	m
$c_{tail\ rudder}$	Chord of the Vertical Tail Fin Rudder	m
$C_{y\ tail\ fin}$	Aerodynamic Side Force Coefficient of the Vertical Tail Fin	---
D	Diameter	ft
D_{rotor}	Rotor Diameter	m
D_s	Support Diameter	ft
DX	Section Depth	ft
DY	Section Height	ft
E	Young's Modulus	ksi
F	Force	lb
FE	Finite Element	---
FSB	Forward Swept Blade	---

$F_{y\ tail\ fin}$	Aerodynamic Side Force of the Vertical Tail Fin	N
H	Height of the Wind Tunnel Test Section	ft
HAWT	Horizontal Axis Wind Turbine	---
Hi-Q	Hi-Q Design #61 Rotor	---
IEC	International Electrotechnical Commission	---
I_{xx}	Rotor Moment of Inertia about X-axis (axis of rotation)	slug-ft^2
L.E.	Leading Edge	---
l_s	Support Length	ft
$l_{\ unfolded}$	Rotor Length Unfolded	ft
$M_{tail\ hinge}$	Moments Acting About the Tail Hinge	N-m
$M_{tail\ hinge\ friction}$	The Static Friction in the Tail Hinge	N-m
$M_{tower\ hinge}$	Moments Acting About the Tower Hinge	N-m
N (or N_{rotor})	Numbers of Rotor Blades	---
n	Rotor Revolution per Second	rps
N_i	Number of 10 minute Data Sets in bin i	---
P	Rotor Power	W
$P_{10\ min}$	Measured Power Average over 10 minutes	W
P_i	Normalized and Averaged Power Output for each bin	W
$P_{n,i,j}$	Normalized Power Output of data set j in bin i	W
P_n	Normalized Power Output	W
P_w	Vapor Pressure	Pa
Q	Rotor Torque	ft-lbf
R	Rotor Blade Radius	ft
R_0	Gas Constant of Dry Air	Jkg^{-1}k^{-1}
RPM	Rotor Revolution Speed	rpm
r_t	Transition Radius	degree
R_W	Gas Constant of Water Vapor	Jkg^{-1}k^{-1}
S_{blade}	Rotor Blade Area	m^2
S_{rotor}	Rotor Swept Area	m^2

$S_{tail\ fin}$	Tail Fin Surface Area	m^2
T	Absolute Temperature	K
$T_{rotor\ blade}$	Thrust Force of the Rotor Blade	N
TSR	Tip Speed Ratio	---
t	Blade Thickness	in
t_h	Hub Thickness	ft
V_i	Normalized and Averaged Wind Speed for each bin	m/s
$V_{n,i,j}$	Normalized Wind Speed of data set j in bin i	m/s
V_{wind}	Wind Velocity	m/s
W	Width of the Wind Tunnel Test Section	ft
W_{tail}	Weight of the Tail	N
$W_{tail\ boom}$	Weight of the Tail Boom	N
$W_{tail\ fin}$	Weight of the Tail Fin	N
$w_{\ rotor}$	Rotor Blade Width	ft
$X_{LE\ tail\ fin}$	(Longitudinal) Distance from Origin to Tail Fin L.E. Location	m
$X_{rotor\ blade}$	(Longitudinal) Distance from Origin to Rotor Blade	m
$X_{tail\ CG}$	(Longitudinal) Distance from Origin to Tail C.G. Location	m
$X_{tail\ fin\ side\ force}$	(Longitudinal) Distance from Origin to Tail Fin A.C. Location	m

Symbol	**Description**	**Unit**
$X_{tail\ hinge}$	(Longitudinal) Distance from Origin to Tail Hinge	m
$X_{tower\ hinge}$	(Longitudinal) Distance from Origin to Tower Hinge	m
$Y_{rotor\ blade}$	(Lateral) Distance from Origin to Rotor Blade	m
$Y_{tower\ hinge}$	(Lateral) Distance from Origin to Tower Hinge	m
ϕ	Relative Humidity	---
$\Lambda_{c/4}$	Quarter chord sweep	deg
λ	Tip Speed Ratio	---
θ	Angles between the Tail Boom and the Horizontal Plane	deg
ρ	Air Density	kg/m^3

ρ_0	Reference Air Density	kg/m^3
$\rho_{10\ min}$	Measured Air Density Average over 10 minutes	kg/m^3
σ_{rotor}	Rotor Solidity Ratio	---
σ	Stress (Yield)	psi
σ_{rotor}	Rotor Solidity Ratio	---
τ_{12}	Stress (Shear)	psi
ω	Rotational Speed	rad/s
ψ	Angles between the Tail Boom and the Vertical Plane	deg

Subscripts	**Description**
1	Principal
10 min	10 minute Average
aft	Aft Blade
f	Flexure
fwd	Forward Blade
i	Bin
j	Set
L	Landing
LE	Leading edge
LOF	Lift-off
max	Maximum
min	Minimum
n	Normalized
p	Power
paired	Both Forward and Aft Blade present
rotor	Rotor Blade
t	tension
test-section	Wind Tunnel Test Section
v	Vertical tail
wind mill	Wind Turbine

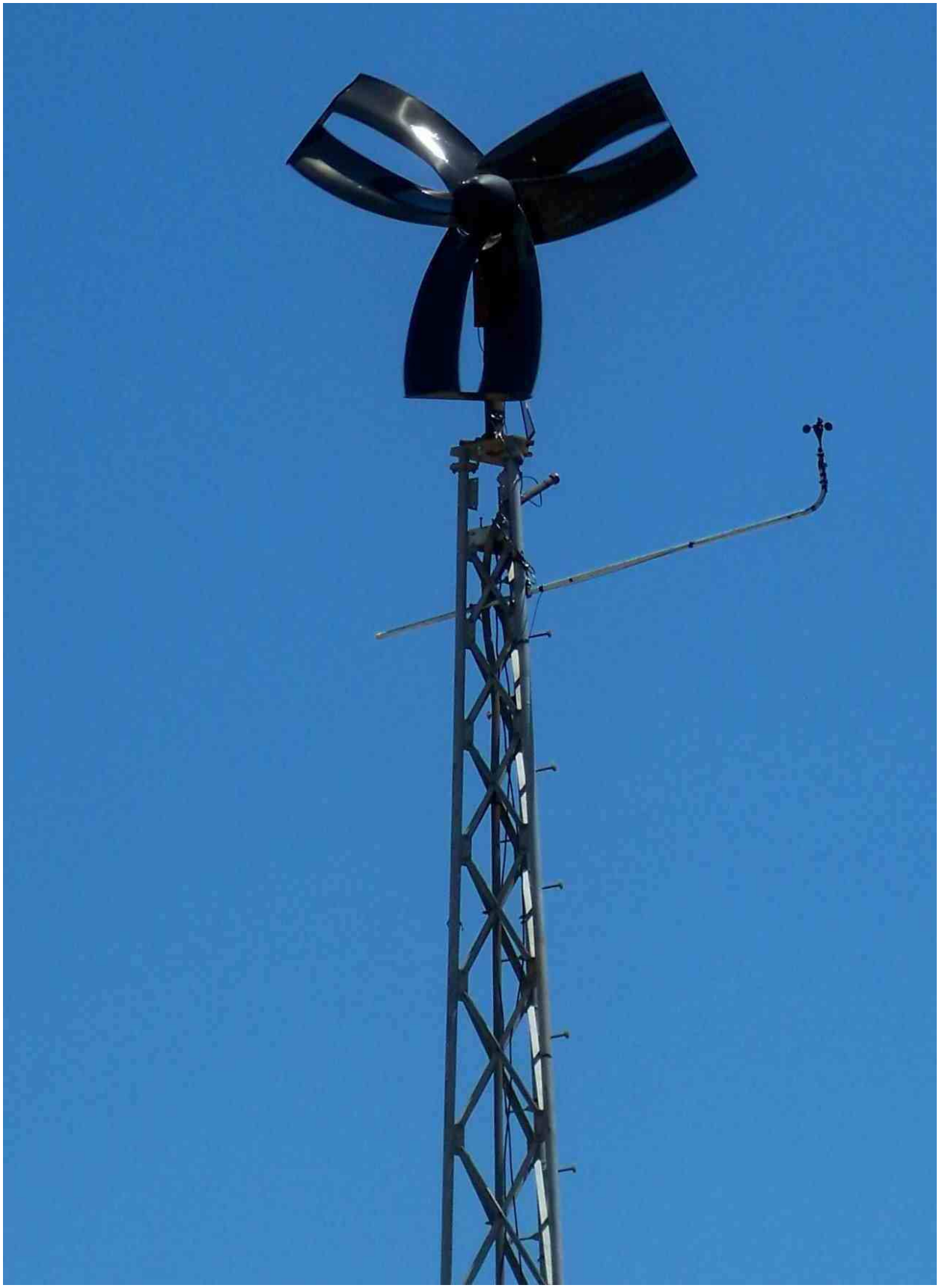

1. Executive Summary

The original investigation (Technology Readiness Level 1-3) of the Hi-Q Rotor, undertaken with help from a PIER Grant provided by the State of California, was completed August 2006. In September of 2006, we began optimizing the Rotor design for a full-scale rotor and field test investigation with the Department of Energy. (Technology Readiness Level 4-7)

From Wind Tunnel Testing to Field Testing. The project objective for this stage of investigation, under DOE Award DE-FG36-06GO16046, was to optimize the performance of the Hi-Q Rotor which was found to be efficient and advantageous over state-of-the-art turbines for collecting wind energy in low wind conditions. The Hi-Q Rotor is a new kind of rotor targeted for harvesting wind in Class 2, 3, and 4 sites, and has application in areas that are closer to cities, or "load centers." An advantage of the Hi-Q Rotor is that the rotor has non-conventional blade tips and uniquely "organizes wind flow," producing less turbulence (vortices), and is quieter than standard wind turbine blades which is critical to the low-wind populated urban sites.

The goal for the project was to improve the current design by building a series of *theoretical and numeric models* (iterations), and composite prototypes to determine a best of class device. From this investigation, an optimized design, the Hi-Q Rotor #61, was determined and an 8-foot diameter, full-scale rotor was built and mounted using a Bergey LX-1 generator and furling system which were adapted to support the rotor. The Hi-Q Rotor was then tested side-by-side against the state-of-the-art Bergey XL-1 at the Alternative Energy Institute's Wind Test Center at West Texas State University for six weeks, and real time measurements of power generated were collected and compared.

Conclusions

Based on the data collected, the results of our first full-scale prototype wind turbine proved that higher energy can be captured at lower wind speeds with the new Hi-Q Rotor. The Hi-Q Wind Turbine is more productive than the Bergey from 6 m/s to 8 m/s, making it ideal in Class 3, 4, and 5 wind sites.

Early wind tunnel testing showed that the cut-in-speed of the Hi-Q rotor is much lower than a conventional tested HAWT (Horizontal Axis Wind Turbine) enabling the Hi-Q Wind Turbine to begin collecting energy before a conventional HAWT has started spinning. Also, torque at low wind speeds for the Hi-Q Wind Turbine is higher than the tested conventional HAWT and enabled the wind turbine to generate power at lower wind speeds.

Looking at the data collected for the two turbines, it is observed that the Bergey XL.1 is more productive at 9 m/s and up, making it a better choice for Class 6 and 7 wind sites. HOWEVER, the sudden decrease in power output of the new Hi-Q Rotor at wind speeds of 8 m/s and above is attributed to the furling of the tail boom. By improving the furling system, customizing it for low wind speed, it is likely that there will be an increase in the normalized average power of the Hi-Q Wind Turbine at wind speeds above 8 m/s. Even though the maximum output of the Hi-Q Rotor is less than the Bergey, the Hi-Q Rotor is almost 15% more productive at 6-7 m/s. Even with a poorly functioning generator, significant improvements over the standard Bergey XL.1 were observed at these low wind speeds,

The final results in this first full scale prototype confirm our contention that the Hi-Q Rotor design is ideal for harvesting wind in low wind sites, Class 2, 3, 4, and 5, and has application in the critical and heretofore untapped areas that are closer to cities, "load centers," and may even be used directly in urban areas. The additional advantage of the Hi-Q Rotor's non-conventional blade tips, which eliminates most air turbulence, is noise reduction which makes it doubly ideal for populated urban areas.

Recommendations

Hi-Q Products recommends one final stage of development to take the Hi-Q Rotor through Technology Readiness Levels 8-9. During this stage of development, the rotor will be redesigned to further increase efficiency, match the rotor to a more suitable generator, and lower the cost of

manufacturing by redesigning the structure to allow for production in larger quantities at lower cost.

Before taking the rotor to market and commercialization, it is necessary to further optimize the performance before by finding a better generator, one more suitable for lower wind speeds and rpms should be used in all future testing. Also, the autofurling system for the Hi-Q Rotor needs adjustment and the Bergey XL.1 settings should not be used. It is recommended to further experiment with the proper hinge locations and fin sizes to obtain the optimal settings for the autofurling system. DARcorporation, Hi-Q Products' design and research team, recommends further optimizing the blade shapes in conjunction with cheaper manufacturing processes to make construction of the blades more cost effective.

The redesigned rotor will be tested first in the wind tunnel to increase efficiency. It is expected that more slender blades with a different endplate/endcap can be designed to improve rotor efficiency. Slender blades will lower the cost of materials too. Several generators will be spec d out, preferably in the 3-5KW range which is a more suitable power range for powering houses. The generators will be calibrated and the generator with peak performance in the 200-300 rpm range will be chosen. The blade design will be adjusted in such a way that it will operate at this optimum rpm range. Matching the aerodynamic design of the blades to the generator peak efficiency will result in an optimal operating low wind speed turbine.

The design will be perfected using the DAR developed Blade Element Method (BEM) software and CFD tools. Several scale models of the designs will be tested in the wind tunnel to select to best design. Once the best design is chosen, full scale design will proceed. Loads will be determined using CFD analysis. The rotor will be designed in carbon fiber composites. Where possible the aluminum parts and steel shafts of the full size rotor will be replaced with composites. The generator attachment and rotor hub will be designed from scratch. A new autofurling system will be specifically designed for this rotor instead of reusing an existing design. The design will be manufactured by DARcorporation and installed at West Texas A&M University for a period of three months. During testing the power curves will be established for the full scale rotor and generator combination. This phase of development will include the

commercial market validation of the technology and prepares the foundation for production preparation.

Impact of the Technology

The potential impact of this fully developed technology will be the expansion and proliferation of energy renewal into the heretofore untapped Class 2, 3, 4, and 5 Wind Sites, or the large underutilized sites where the wind speed is broken by physical features such as mountains, buildings, and trees. Market estimates by 2011, if low wind speed technology can be developed are well above: 13 million homes, 675,000 commercial buildings, 250,000 public facilities. Estimated commercial exploitation of the Hi-Q Rotor show potential increase in U.S. energy gained through the clean, renewable wind energy found in low and very low wind speed sites. This new energy source would greatly impact greenhouse emissions as well as the public sector's growing energy demands.

2. Phase I Technical Progress Report

2.1 Nomenclature

This section presents the primary variables used in designing the rotor CAD model. The coordinate system of the model is shown in Figure 2.1 and Figure 2.2, with the X-axis being the axis of rotation. The rotor is to have a fixed diameter of 1.5 ft. Asides from it, the rotor model is parametrically controlled by the rotor side profile, shown in Figure 2.3.

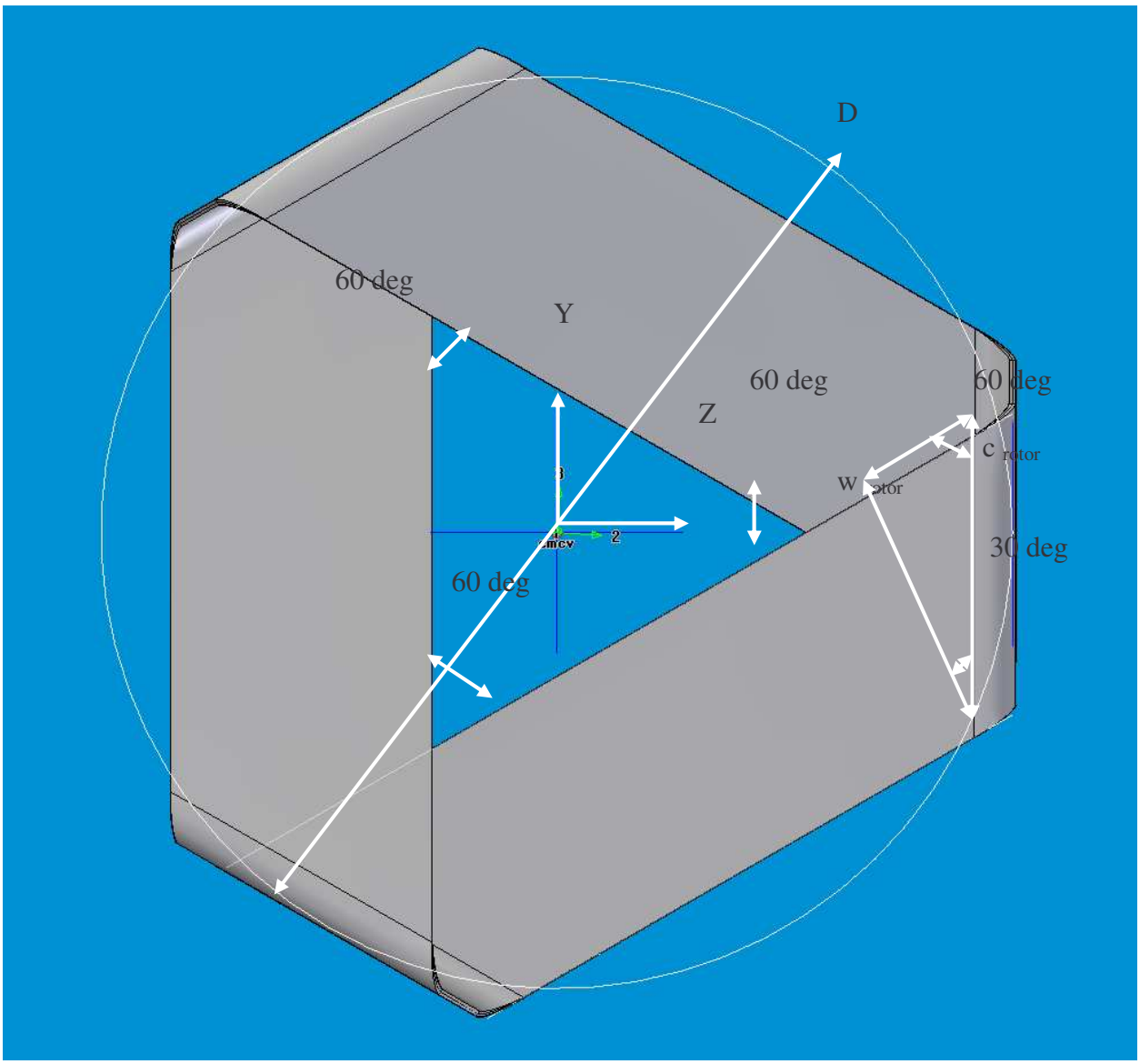

Figure 2.1 Coordinate System of the Rotor (Front View)

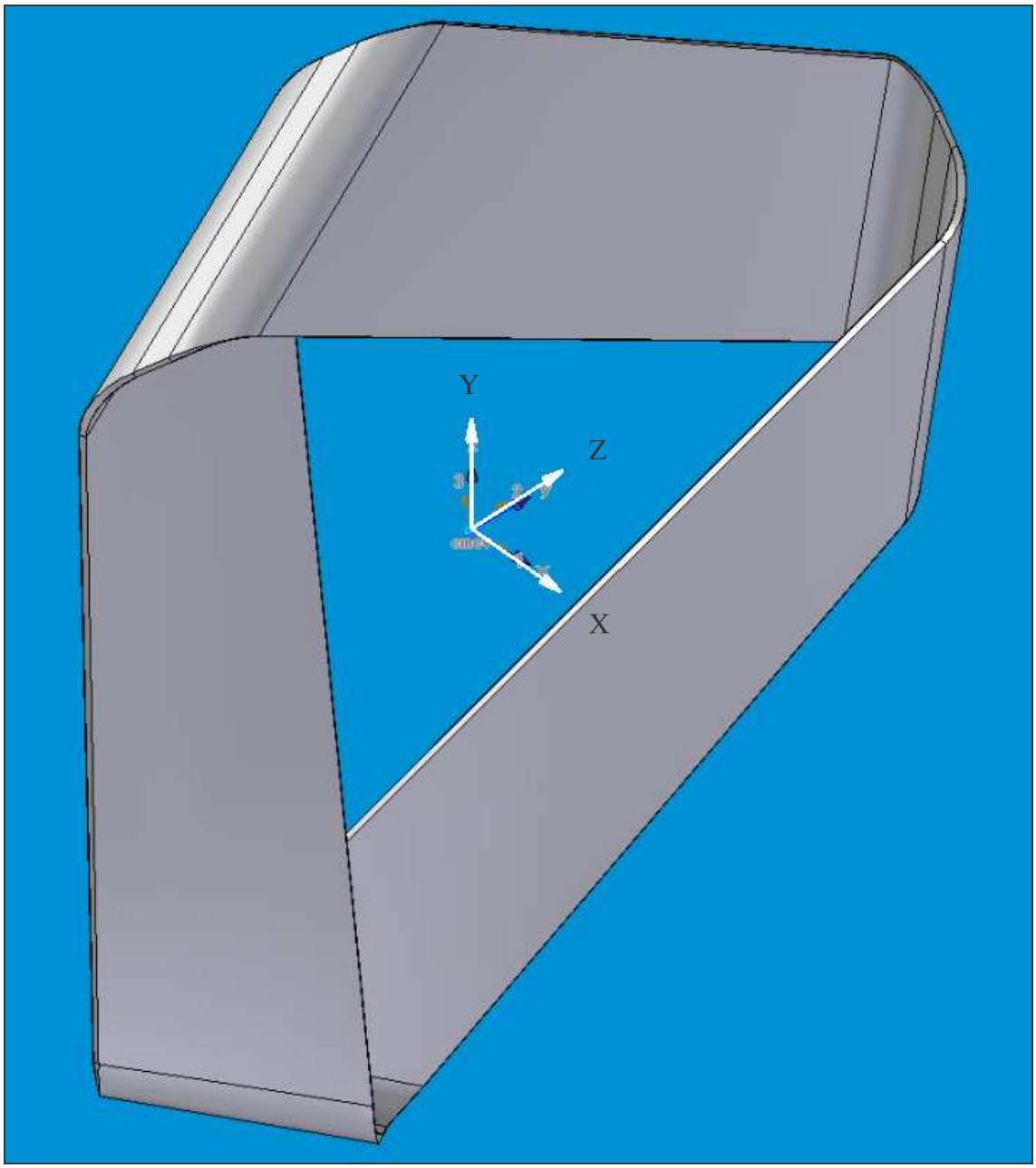

Figure 2.2 Coordinate System of the Rotor (Isometric View)

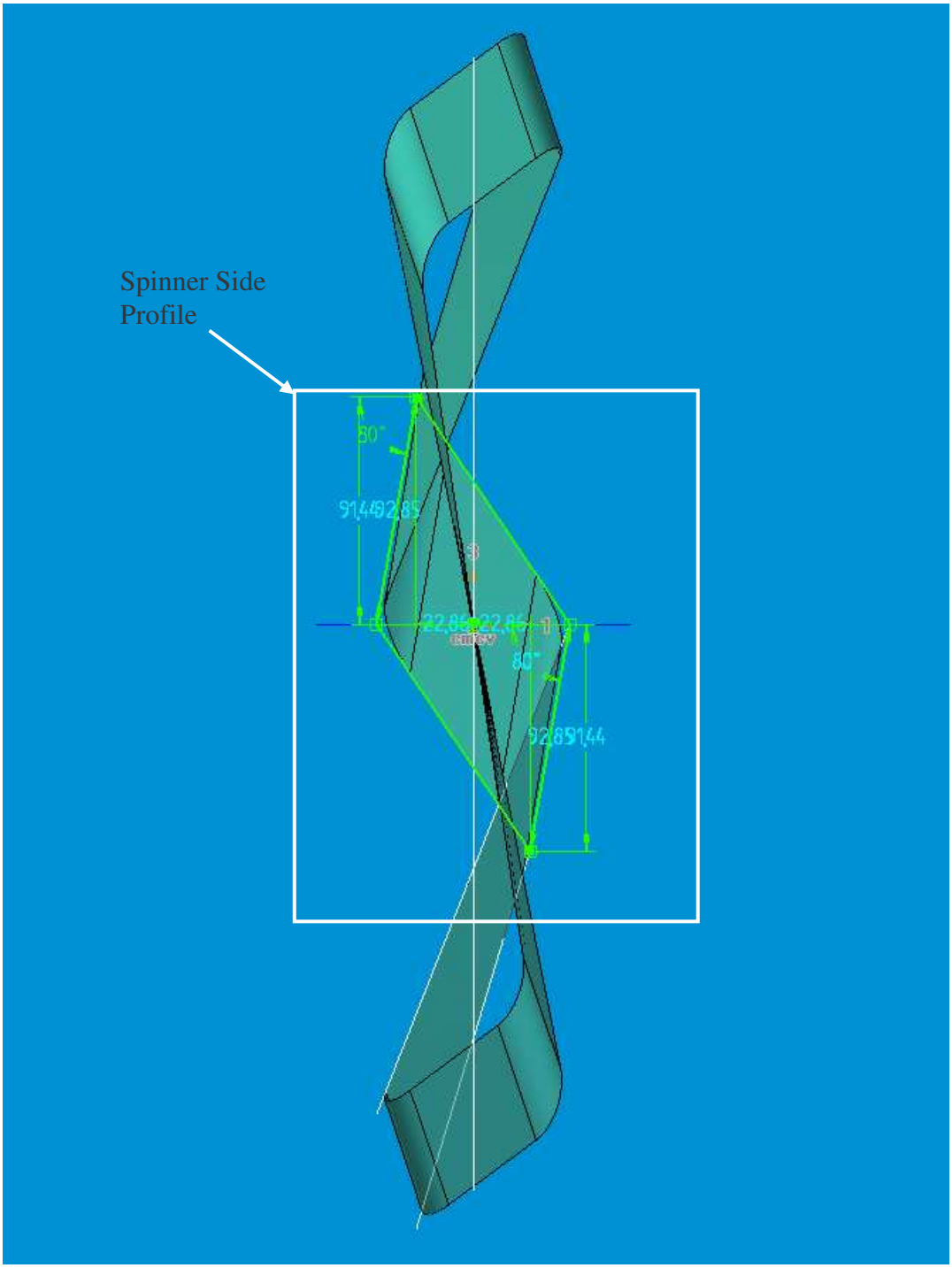

Figure 2.3 Full Rotor Side View

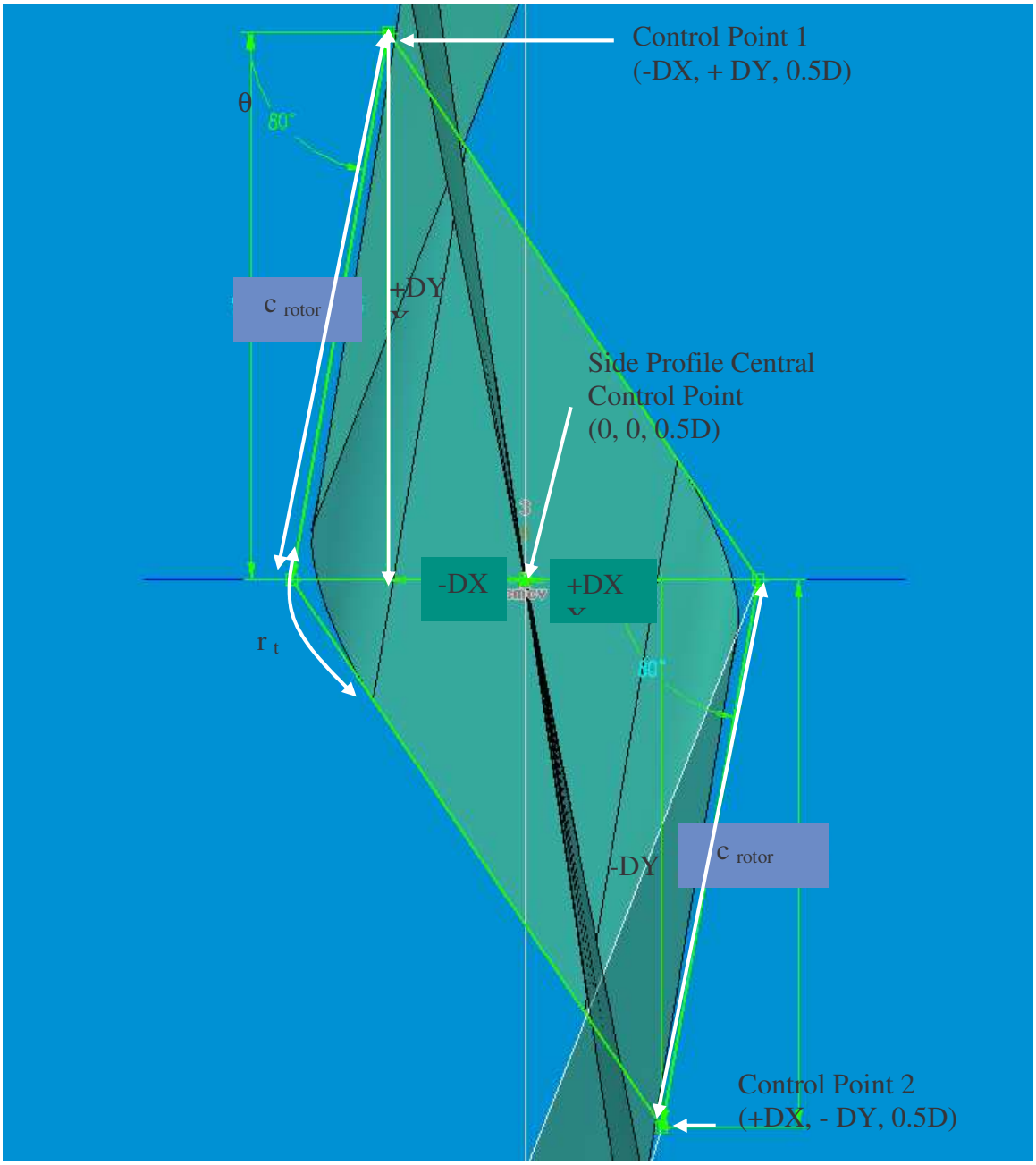

Figure 2.4 Detailed Rotor Side Profile (Side View)

It is observed in Figure 2.4 that the two control points are positioned relative to the side profile central control point (0, 0, 0.5D). The Coordinates of the two control points are (-DX, +DY, 0.5D) & (+DX, -DY, 0.5D).

Based on Figure 2.1, it is observed that the width of the rotor blade (w_{blade}), is a function of the rotor section chord (c_{rotor}).

$$w_{rotor} = \cos(30^o)\, c_{rotor}$$

where: c_{rotor} is a function of the section height (DY) and section angle (θ).

Based on Figure 2.4, the rotor section chord (c_{rotor}) is defined as:

$$c_{rotor} = \frac{DY}{\sin(\theta)}$$

Subsequently: w_{blade} can be expressed as:

$$w_{rotor} = \frac{DY}{\sin(\theta)} \cos(30^o)$$

If the entire rotor blade, with a certain blade thickness, t and blade width, w_{rotor} is to be unfolded to form a straight sheet, then its total length is defined as the rotor unfolded length, $l_{unfolded}$. With a fixed rotor diameter of 1.5 ft, $l_{unfolded}$ is a function of DX, DY, θ, and r_t.

For example:

DX = 0

DY = 20% of Rotor diameter = 0.300 ft

θ = 82.5 degree

r_t = 0.03621 ft

t = 0.005 ft (0.060 in)

$$\therefore w_{rotor}/D = \frac{DY/D}{\sin(\theta)} \cos(30^o) = \frac{0.20}{\sin(82.5^o)} \cos(30^o) = 0.1747$$

$$\Rightarrow w_{rotor}/D = 0.175$$

$$\Rightarrow w_{rotor} = 0.262 \text{ ft}$$

From the CAD model, it is found that:

$l_{unfolded}/D = 2.851$

$\Rightarrow l_{unfolded} = 4.277$ ft

The methodology of analyzing the aerodynamic performance of any rotor design is as follows:

For any particular rotor design at a given wind speed, a series of CFD analyses on different rotational speeds (or rotor RPM) is carried out. The power generation capability (power coefficient, C_p), of the rotor design, as a function of the rotor tip speed ratio, λ, is plotted. The rotor tip speed ratio is defined as follows:

$$\lambda = \frac{1/2\, D\Omega}{V}$$

The rotor power coefficient is defined as:

$$C_p = \frac{P}{\rho n^3 D^5}$$

where: $n = \frac{RPM}{60}$

$$P = 2\pi Q$$

A typical performance estimate based on blade element momentum technique (BEM) on a horizontal axis wind turbine (HAWT) rotor is documented in Reference 1.

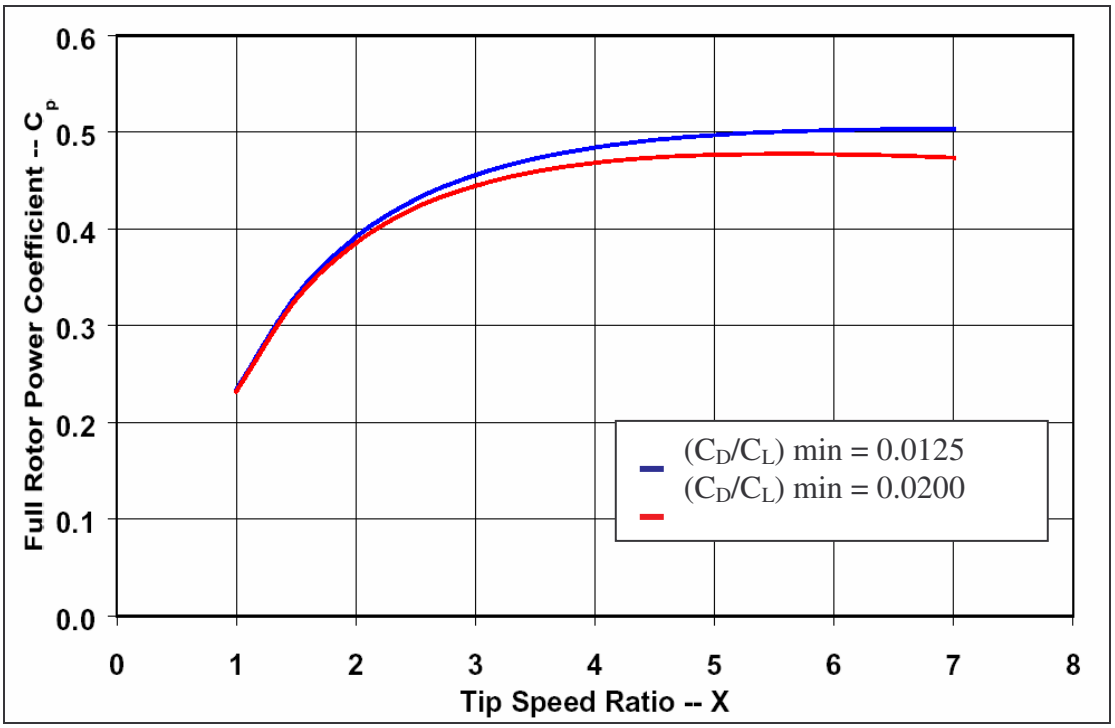

Figure 2.5 Estimated Maximum Rotor Performance (extracted from Reference ***Error! Reference source not found.****)*

According to Reference **Error! Reference source not found.**, the red curve in **Error! Reference source not found.** represents a realistic estimate of a conventional HAWT rotor power generation capability.

The main objective of the project is to computationally analyze different rotor designs power generation capability and compare the results with the above theoretical estimates

The family of rotors has the following designation:

HIQ mc x_{mc}ac $(t/c)_{max}$ $x_{(t/c)\ max}$ R_{LE}/C ϕ_{TE} DX/D DY/D C/D r_t/D θ

mc: Maximum camber of the rotor airfoil in percent of chord

x_{mc}: Location of maximum camber in percent of the chord from the leading edge

$(t/c)_{max}$: Maximum thickness in percent of chord

$x_{(t/c)\ max}$ Location of maximum thickness in percent chord from the leading edge

R_{LE}/C: Leading edge radius in percent chord

ϕ_{TE}: Trailing edge angle in degrees

DX/D: Position of rotor side profile control point in X-axis with respect to the side profile central control point in percent of rotor diameter

DY/D: Position of rotor side profile control point in Y-axis with respect to the side profile central control point in percent of rotor diameter

C/D: Chord in percent of rotor diameter

r_t/D: Tip transition radius in percent diameter

θ: Rotor section angle in degrees

2.2 CAD Models

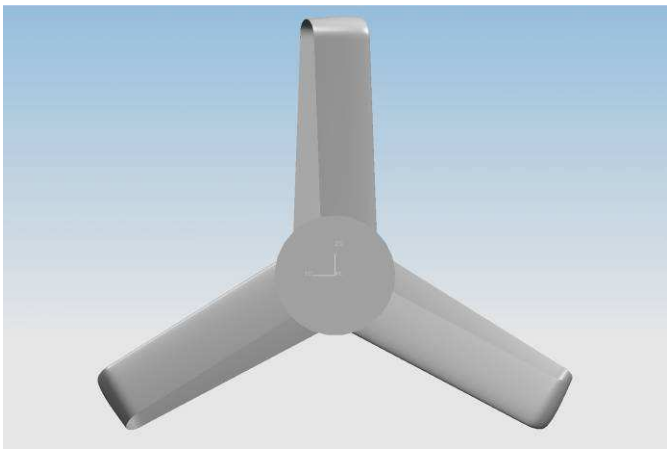

Figure 2.6 Front View of 3-Blade Design Tip Separation 1.5 in, Tip Stagger 0.5 in

Figure 2.7 Side View of 3-Blade Design Tip Separation 1.5 in, Tip Stagger 0.5 in

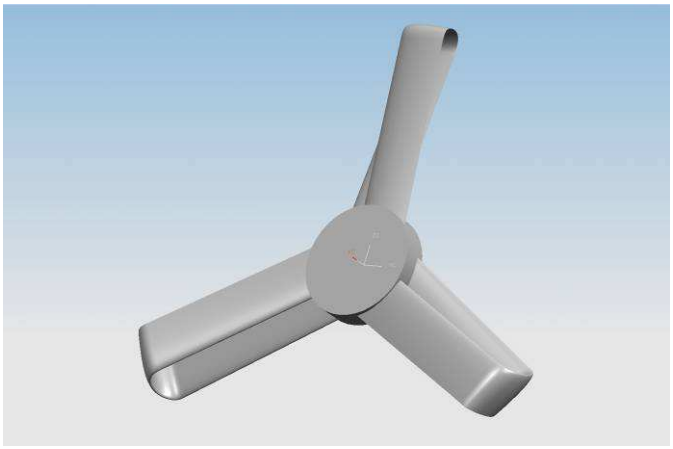

Figure 2.8 Tilted View of 3-Blade Design Tip Separation 1.5 in, Tip Stagger 0.5 in

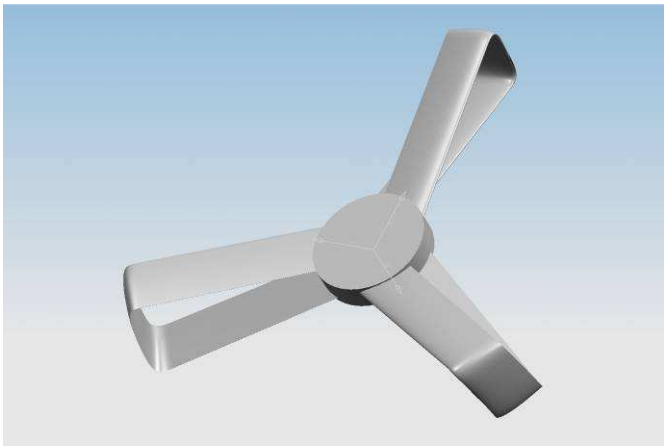

Figure 2.9 Tilted View of 3-Blade Design with Tip Separation Set to 1.5 in and Tip Stagger 0.5 in

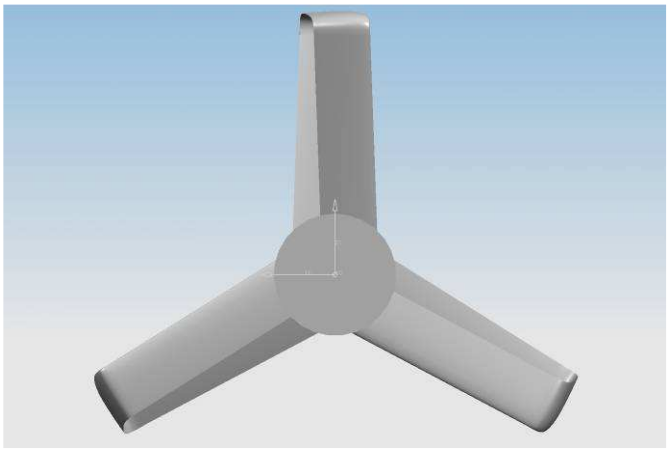

Figure 2.10 Front View of 3-Blade Design with Tip Separation Set to 3.0 in and Tip Stagger 0.5 in

Figure 2.11 Side View of 3-Blade Design with Tip Separation 3.0 in and Tip Stagger 0.5 in

Figure 2.12 Tilted View of 3-Blade Design with Tip Separation Set to 1.5 in and Tip Stagger 1.0 in

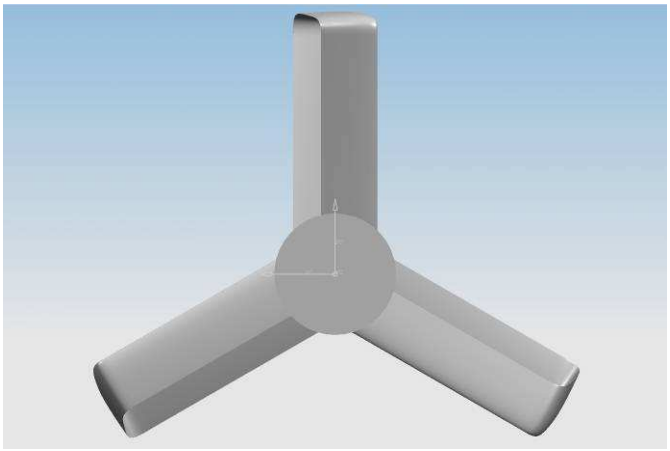

Figure 2.13 Front View of 3-Blade Design with Tip Separation Set to 1.5 in and Tip Stagger 1.0 in

Figure 2.14 Side View of 3-Blade Design with Tip Separation Set to 1.5 in and Tip Stagger 1.0 in

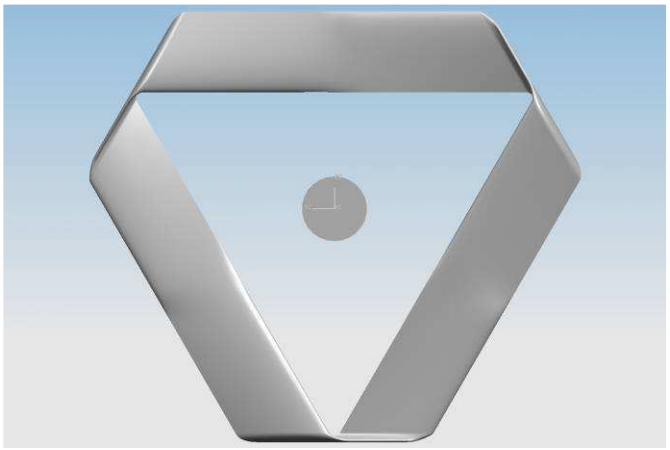

Figure 2.15 Front View Original Design with X offset set to 0.25 in

Figure 2.16 Side View of Original Design with X offset set to 0.25 in

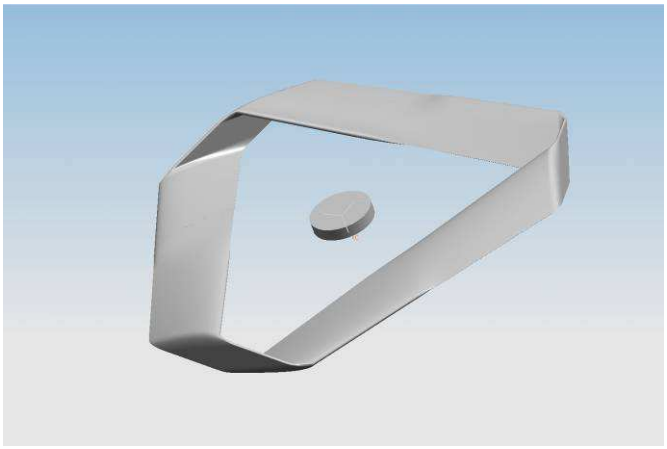

Figure 2.17 Tilted View of Original Design with X offset set to 0.25 in

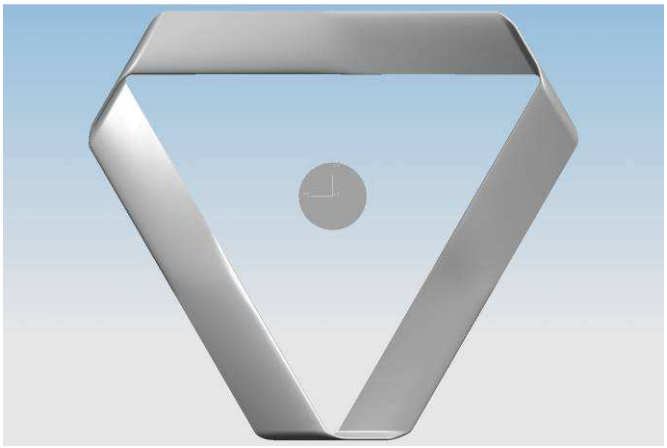

*Figure 2.18 Front View of Original Design with Y offset set to 0.15*Diameter, Theta (angle of tip) 75 degrees*

*Figure 2.19 Side View of Original Design with Y offset set to 0.15*Diameter, Theta (angle of tip) 75 degrees*

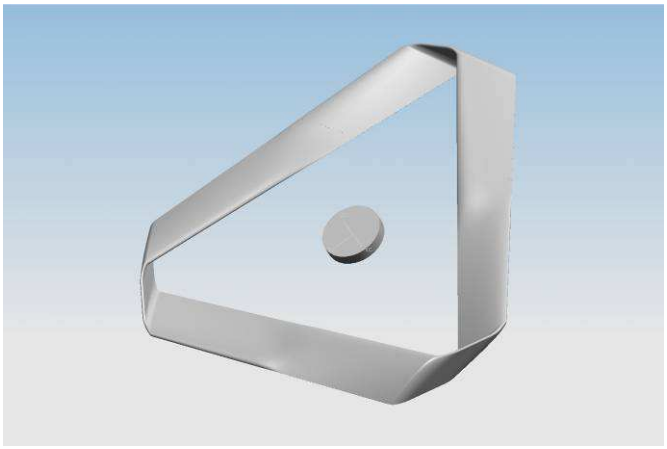

*Figure 2.20 Tilted View of Original Design with Y offset set to 0.15*Diameter, Theta (angle of tip) 75 degrees*

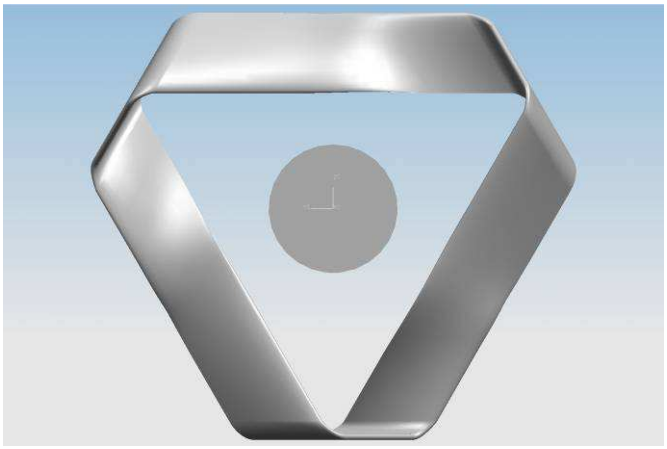

Figure 2.21 Front View of Original Design with High DX, Low Theta, and Middle Sections Not Corrected to New Theta

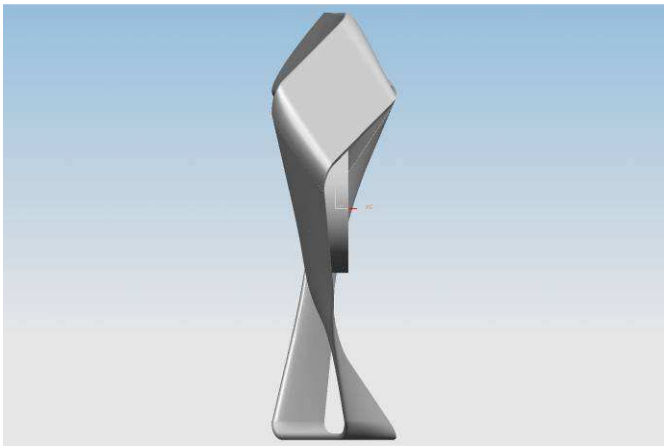

Figure 2.22 Side View of Original Design with High DX, Low Theta, and Middle Sections Not Corrected to New Theta

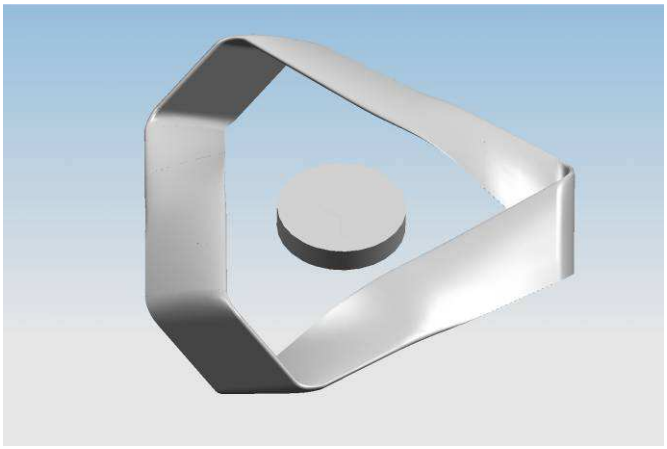

Figure 2.23 Tilted View of Original Design with High DX, Low Theta, and Twist Not Corrected to New Theta

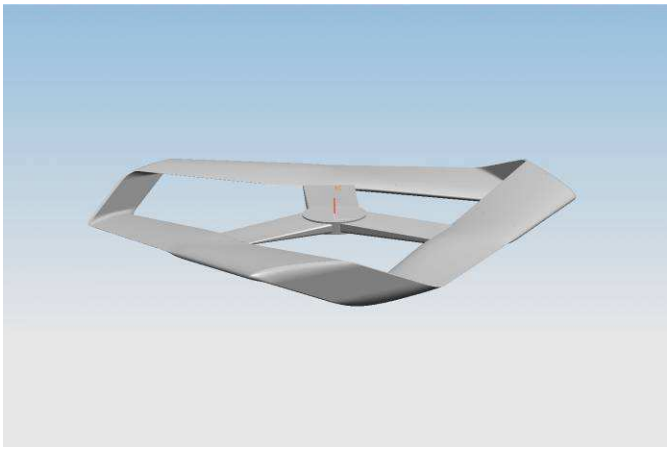

Figure 2.24 Tilted View of Original Design with DX = 0 and DY = 3.6

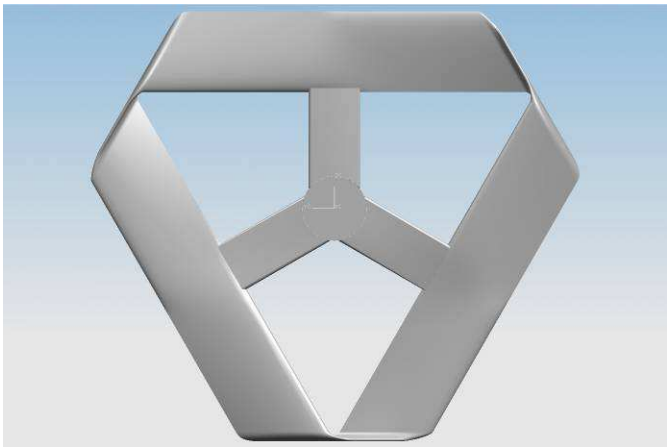

Figure 2.25 Front View of Original Design with DX = 0 and DY = 3.6

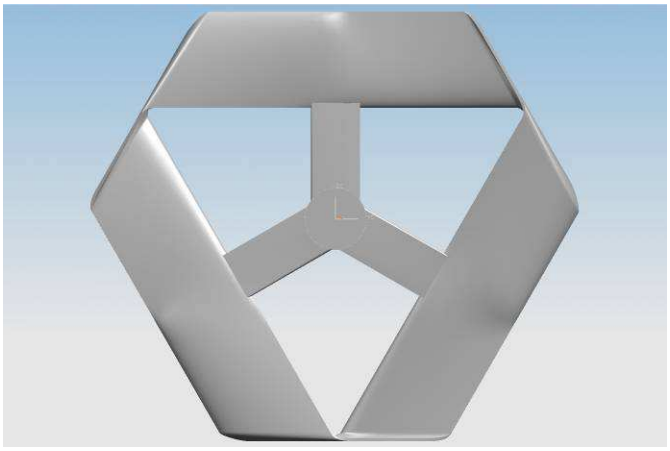

Figure 2.26 Tilted View of Original Design with DX = 0 and DY = 4.5

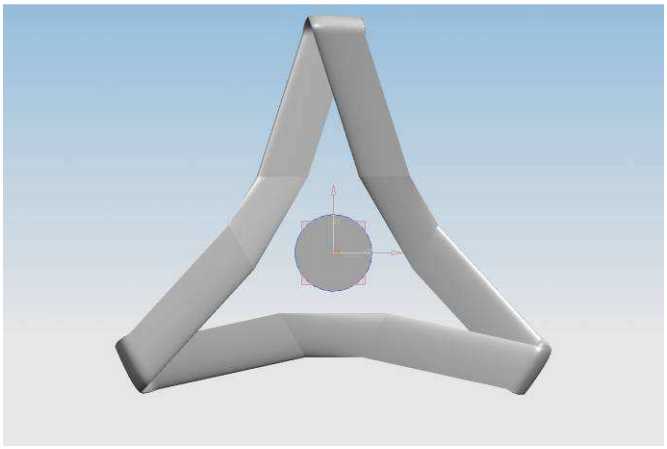

Figure 2.27 Bent Triangular Design

2.3 Initial CFD Analysis

Using Blue Ridge Numerics CFDesign and the models created in Unigraphics NX, a new method has been developed to speed up CFD analysis. Analysis that used to take 100 hours are now cut down to about 4 hours. The following figures show pressure distributions over the surface of the rotor. These pressure distributions are used to analyze which part of the rotor makes the rotor spin and thus generate power.

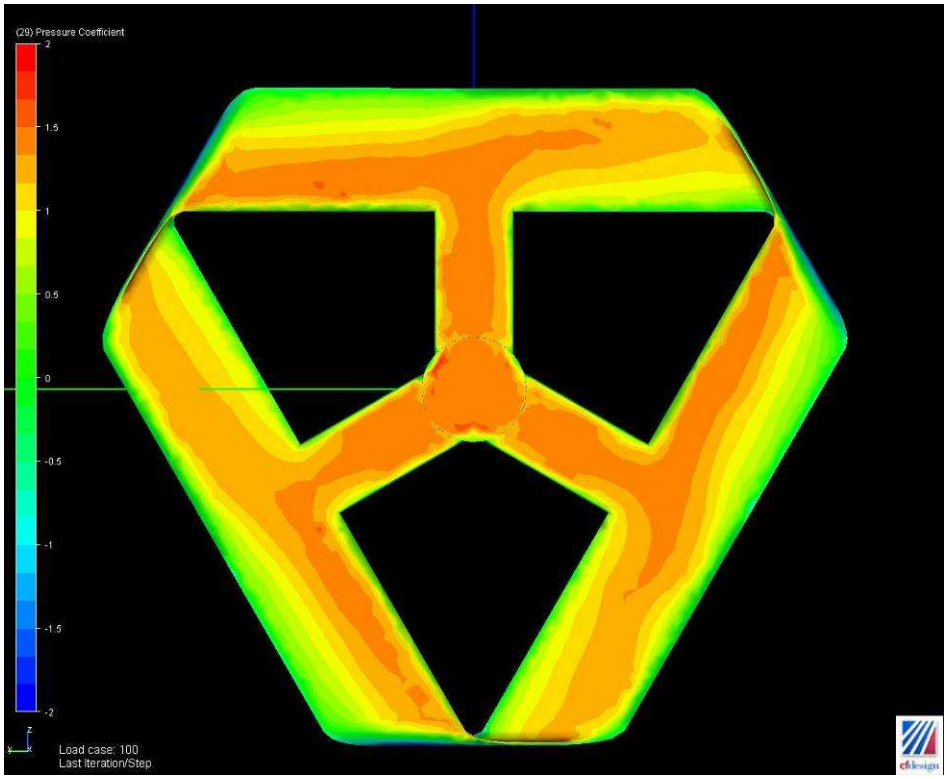

Figure 2.28 Pressure Contours: Front View

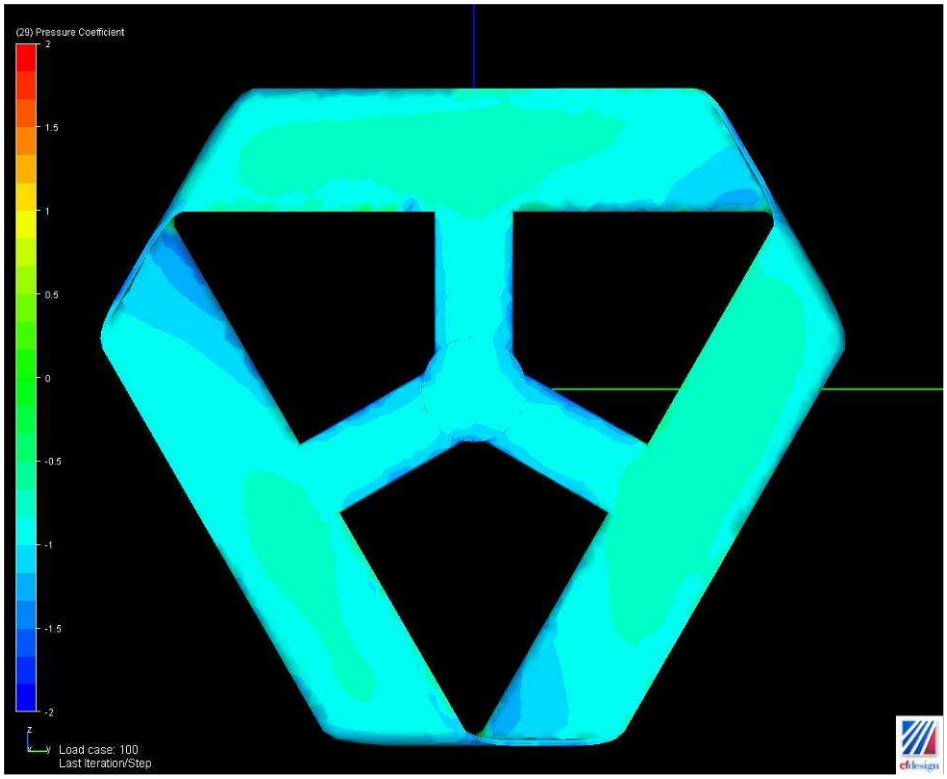

Figure 2.29 Pressure Contours: Rear View

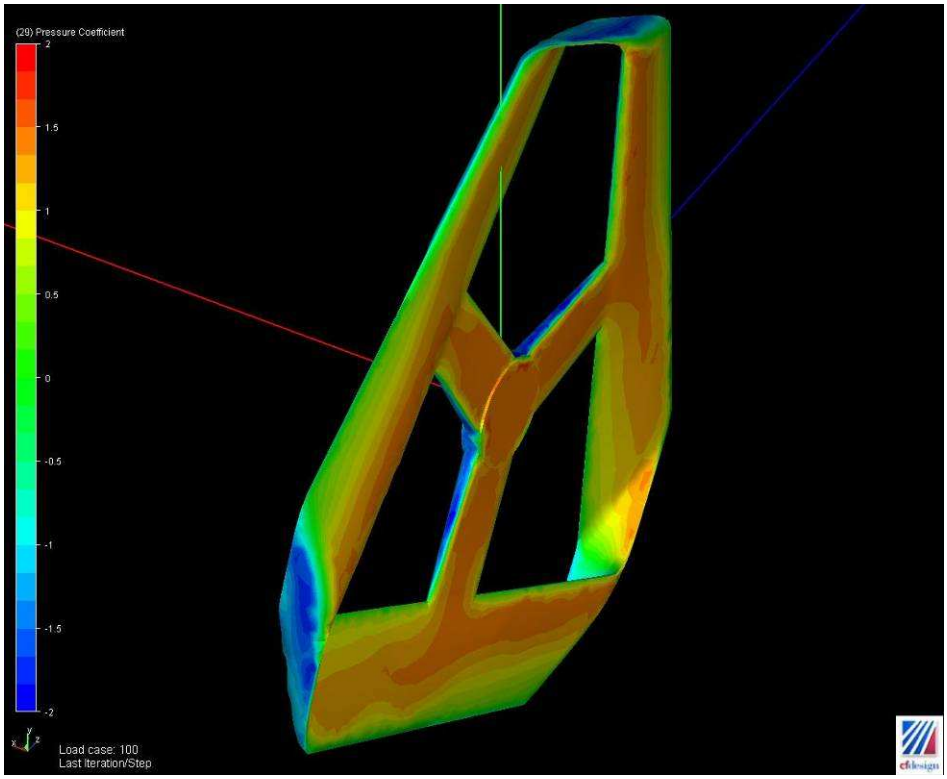

Figure 2.30 Pressure Contours: Isometric View

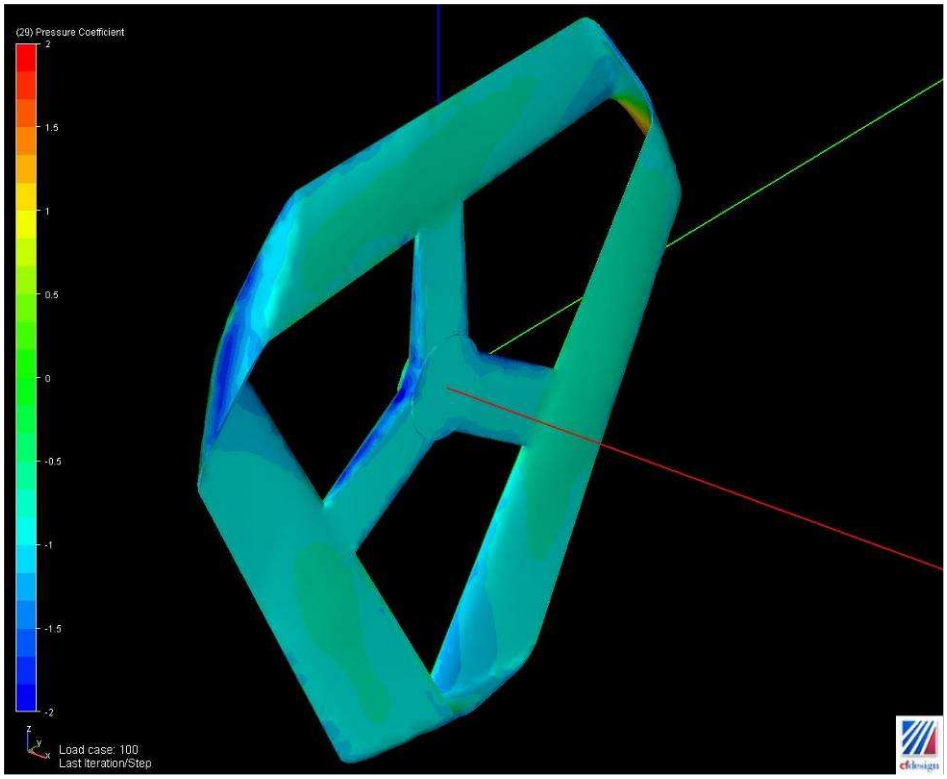

Figure 2.31 Pressure Contours: Isometric View (2)

2.4 Blade Element Theory

This section presents the equations used for the Hi-Q rotor design using blade element momentum technique. The equations are currently programmed in a MathCAD filke and are being transferred to a program written in Borland (CodeGear) Delphi so that batch jobs can be run.

The coordinate system and variables are defined in Figure 2.32.

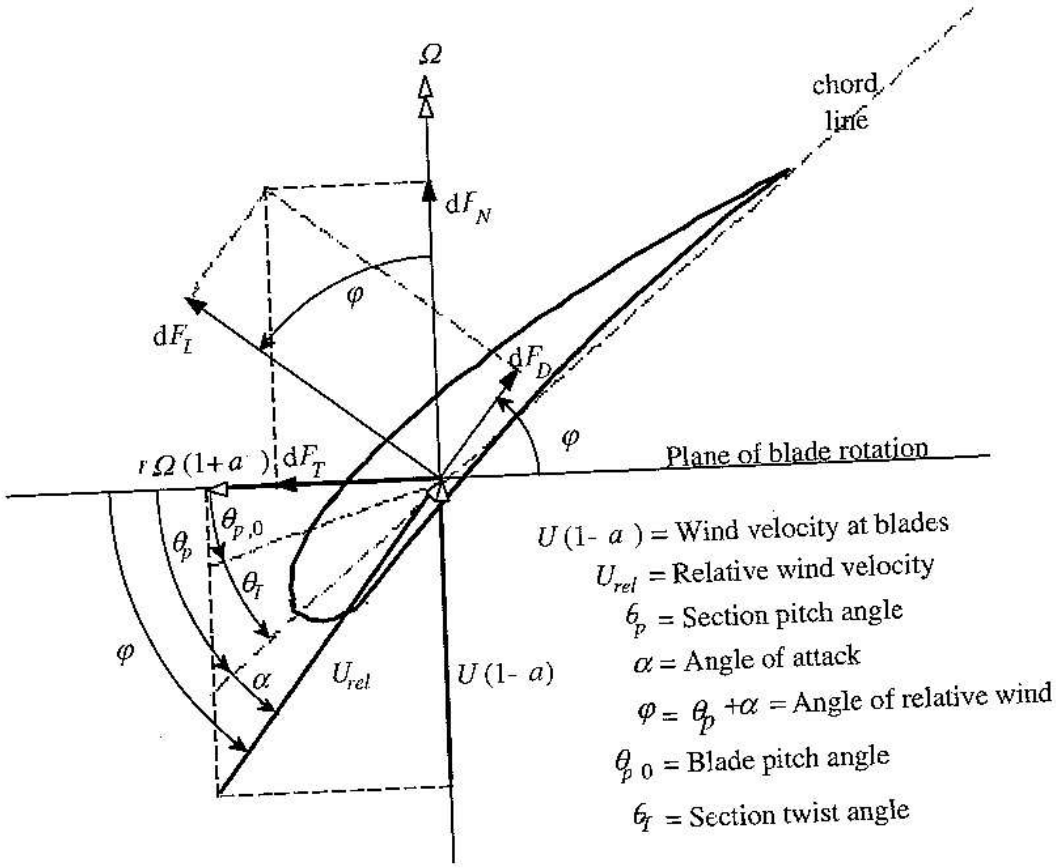

Figure 2.32 Blade Section Aerodynamics

The first step in designing the Hi-Q rotor is the airfoil selection. For this the airfoil lift curve slope c_{l_α}, the airfoil zero angle of attack lift coefficient c_{l_0}, and the drag trendline c_d are to be defined.

The rotor sectional lift and drag coefficients at a blade radial location is defined as follows:

$$c_l = c_{l_0} + c_{l_\alpha}\alpha$$

Where, c_{l_α} & c_{l_0} are adjusted for Mach number effect (Prandtl-Glauert correction).

$$c_{l_\alpha} = \frac{c_{l_{\alpha @\, M=0}}}{\sqrt{1-M^2}} \qquad \& \qquad c_{l_0} = \frac{c_{l_{0 @\, M=0}}}{\sqrt{1-M^2}}$$

$$c_d = f(\alpha) = c_d(\alpha)$$

Where c_d (as a function of angle of attack) is adjusted for Mach and Reynolds number effect

The relative speed of wind at the rotor is defined as follows:

$$U_{rel} = \frac{U(1-a)}{\sin\phi}$$

Where,

$$\phi = \theta_p + \alpha$$

And

$$\theta_p = \theta_T + \theta_{p,0}$$

θ_p = Section pitch angle

θ_T = Section twist angle

$\theta_{p,0}$ = Blade pitch angle at the tip

Note that the rotor blade spanwise pitch distribution, $\theta = f(\mathrm{r})$, is a user defined input parameter.

The airfoil sectional dimensional lift and drag per unit span (radius) are expressed as:

$$dF_L = \frac{1}{2} c_l \rho U_{rel}^2 c$$

$$dF_D = \frac{1}{2} c_d \rho U_{rel}^2 c$$

Note that the rotor blade airfoil chord, $c = f(r)$, is a user defined input parameter.

Resolving the sectional aerodynamic forces normal and parallel to the disk plane gives

$$dF_N = dF_L \cos\phi + dF_D \sin\phi$$

$$dF_T = dF_L \sin\phi - dF_D \cos\phi$$

For a rotor with B number of blades, the total normal force (or thrust) is given by

$$dF_N = \frac{1}{2} \rho U_{rel}^2 B \left(c_l \cos\phi + c_d \sin\phi \right) c dr$$

And the elemental differential torque due to the tangential force operating at a distance, r, from the center is given by

$$dQ = Br\, dF_T$$

or

$$dQ = \frac{1}{2} \rho U_{rel}^2 B \left(c_l \sin\phi - c_d \cos\phi \right) c r dr$$

Equations (5-8) and (5-10) can be simplified further as follows

$$dF_N = \sigma' \pi \rho \frac{U^2 (1-a)^2}{\sin^2 \phi} \left(c_l \cos\phi + c_d \sin\phi \right) r dr$$

$$dQ = \sigma' \pi \rho \frac{U^2 (1-a)^2}{\sin^2 \phi} (c_l \sin\phi - c_d \cos\phi) r^2 dr$$

Where,

$\sigma' = \frac{Bc}{2\pi r}$, is defined as the local solidity.

The elemental thrust and power coefficients are as follows:

$$dC_T = \frac{\sigma' (1-a^2)}{\sin^2 \phi} (c_l \cos\phi + c_d \sin\phi) dr$$

$$dC_P = \Omega dC_Q$$

The overall rotor thrust and power can be described as:

$$C_T = \int_0^1 dC_T \, dr$$

$$C_P = \int_{\lambda_h}^{\lambda} dC_p \, d\lambda_r = \frac{8}{\lambda^2} \int_{\lambda_h}^{\lambda} \lambda_r^3 a' (1-a) \left(1 - \frac{c_d}{c_l} \cot\phi\right) d\lambda_r$$

Where,

λ_h is the local tip speed ratio at the hub

$\lambda_r = \frac{\Omega r}{U}$

$a' = -\frac{1}{2} + \frac{1}{2} \sqrt{\left[1 + \frac{4}{\lambda_r^2} a(1-a)\right]}$

The numerical integration is performed using the Simpson's rule, which states that:

$$\int_a^b f(x)dx \approx \frac{h}{3}\Big[f(x_0) + 4f(x_1) + 2f(x_2) + 4f(x_3) + \ldots + 4f(x_{n-1}) + f(x_n)\Big].$$

Where: h = (b-a)/n

3. Phase I Summary of Aerodynamic Performance of 60 Hi-Q Rotor Designs

To help with the design and the analysis of the aerodynamic performance of the Hi-Q wind turbine rotor, an analytical code using the blade-element-momentum (BEM) technique has been developed.

Based on the initial concept studies, several important parameters influencing the aerodynamic performance of the Hi-Q rotor have been identified. They include:

- Airfoil selection
- Reynolds number (or rotor blade airfoil section chord, c_{eff})
- Rotor blade airfoil section pitch distribution (θ)
- Rotor blade airfoil section planform area ($S_{eff} = c_{eff} * b_{eff}$)

The definition of the airfoil section chord and the airfoil sectional planform area is illustrated in Figure 3.1.

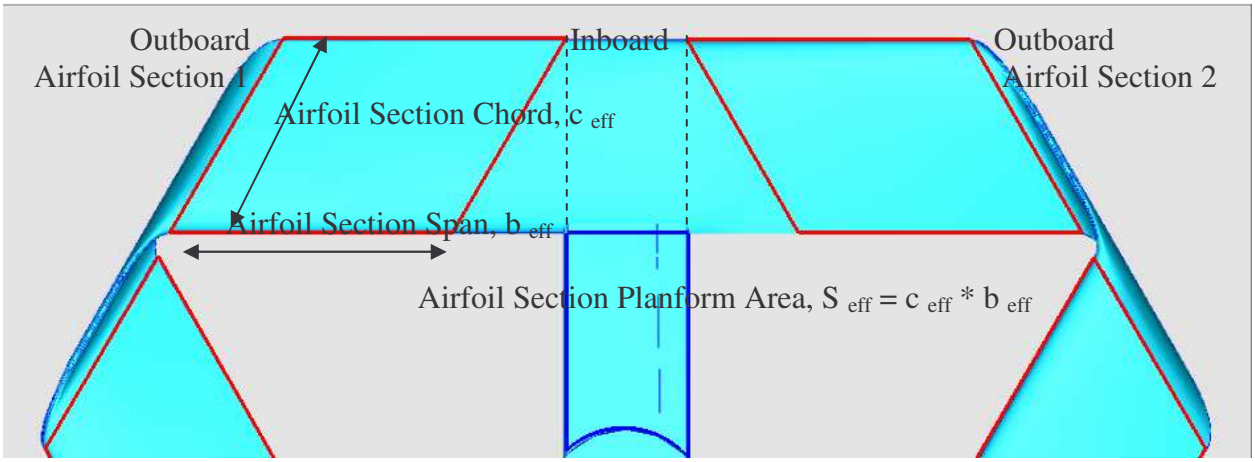

Figure 3.1 The Airfoil Sections on Hi-Q Rotor Planform

In the present design stage, 5 different airfoils, 2 different airfoil section chords, 3 different airfoil section planform area, and 2 different airfoil section pitch distributions, are selected, resulting in a matrix with 60 designs. A summary of the geometric characteristics of the 60 Hi-Q rotor designs is listed in

Table 3.1.

Table 3.1 Geometric Characteristics of the 60 Hi-Q Rotor Designs

Design #	Airfoil	c_{eff} [ft]	b_{eff} [ft]	$\theta_{AS1} = \theta_{AS2}$	$\theta_{AS1} \neq \theta_{AS2}$
1	NACA0012	0.257	0.399	Y	
2	NACA0012	0.257	0.399		Y
3	NACA0012	0.257	0.349	Y	
4	NACA0012	0.257	0.349		Y
5	NACA0012	0.257	0.299	Y	
6	NACA0012	0.257	0.299		Y
7	NACA0012	0.385	0.335	Y	
8	NACA0012	0.385	0.335		Y
9	NACA0012	0.385	0.285	Y	
10	NACA0012	0.385	0.285		Y
11	NACA0012	0.385	0.235	Y	
12	NACA0012	0.385	0.235		Y
13	NACA0016	0.257	0.399	Y	
14	NACA0016	0.257	0.399		Y
15	NACA0016	0.257	0.349	Y	
16	NACA0016	0.257	0.349		Y
17	NACA0016	0.257	0.299	Y	
18	NACA0016	0.257	0.299		Y
19	NACA0016	0.385	0.335	Y	
20	NACA0016	0.385	0.335		Y
21	NACA0016	0.385	0.285	Y	
22	NACA0016	0.385	0.285		Y
23	NACA0016	0.385	0.235	Y	
24	NACA0016	0.385	0.235		Y
25	S822	0.257	0.399	Y	
26	S822	0.257	0.399		Y
27	S822	0.257	0.349	Y	
28	S822	0.257	0.349		Y
29	S822	0.257	0.299	Y	
30	S822	0.257	0.299		Y

Table 3.1 (Contd.) Geometric Characteristics of the 60 Hi-Q Rotor Designs

Design #	Airfoil	c_{eff} [ft]	b_{eff} [ft]	$\theta_{AS1} = \theta_{AS2}$	$\theta_{AS1} \neq \theta_{AS2}$
31	S822	0.385	0.335	Y	
32	S822	0.385	0.335		Y
33	S822	0.385	0.285	Y	
34	S822	0.385	0.285		Y
35	S822	0.385	0.235	Y	
36	S822	0.385	0.235		Y
37	S823	0.257	0.399	Y	
38	S823	0.257	0.399		Y
39	S823	0.257	0.349	Y	
40	S823	0.257	0.349		Y
41	S823	0.257	0.299	Y	
42	S823	0.257	0.299		Y
43	S823	0.385	0.335	Y	
44	S823	0.385	0.335		Y
45	S823	0.385	0.285	Y	
46	S823	0.385	0.285		Y
47	S823	0.385	0.235	Y	
48	S823	0.385	0.235		Y
49	S825	0.257	0.399	Y	
50	S825	0.257	0.399		Y
51	S825	0.257	0.349	Y	
52	S825	0.257	0.349		Y
53	S825	0.257	0.299	Y	
54	S825	0.257	0.299		Y
55	S825	0.385	0.335	Y	
56	S825	0.385	0.335		Y
57	S825	0.385	0.285	Y	
58	S825	0.385	0.285		Y
59	S825	0.385	0.235	Y	
60	S825	0.385	0.235		Y

Note: The reader is reminded that $\theta_{AS1} = \theta_{AS2}$ refers to rotor designs with the pitch distribution of the airfoil section 1 being optimized to produce the highest sectional power coefficient, while the pitch distribution of the airfoil section 2 is made equal to those of the airfoil section 1. On

the other hand, $\theta_{AS1} \neq \theta_{AS2}$ refers to rotor designs with the pitch distribution of the airfoil section 1 and 2 each being optimized separately to produce the highest sectional power coefficient

3.1 Effect of Airfoil Selection

Keeping other parameters the same, i.e. c_{eff} = 0.385 ft, as well as b_{eff} = 0.349 ft and $\theta_{AS1} \neq \theta_{AS2}$, the effect of airfoil selection on the aerodynamic performance of the Hi-Q rotor is investigated. The basic characteristics of the 5 selected airfoils are summarized in Table 3.2, while the profiles of the 5 selected airfoils are illustrated in Figure 3.2 through Figure 3.6.

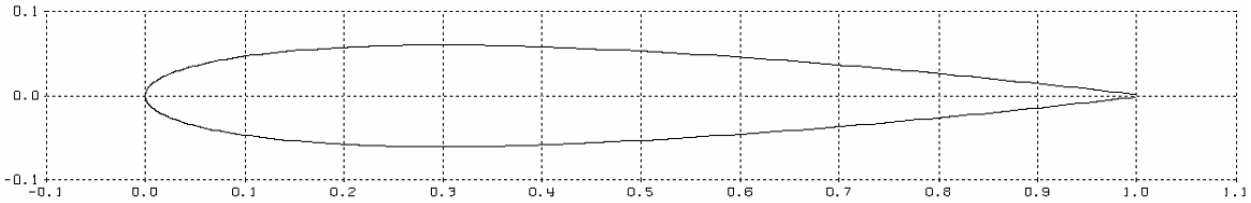

Figure 3.2 The NACA 0012 Airfoil Profile

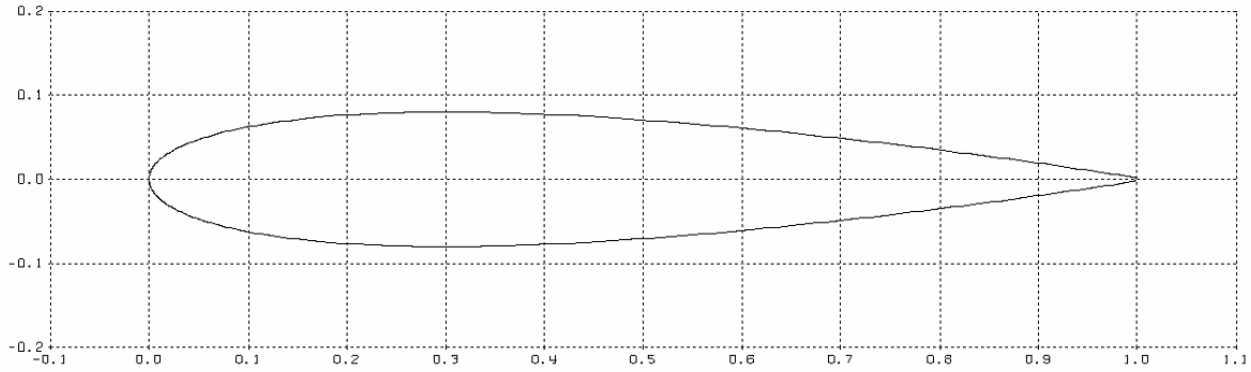

Figure 3.3 The NACA 0016 Airfoil Profile

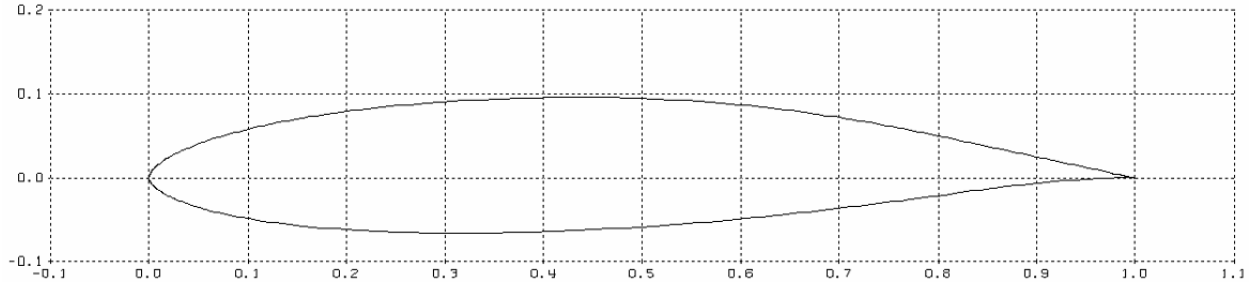

Figure 3.4 The S822 Airfoil Profile

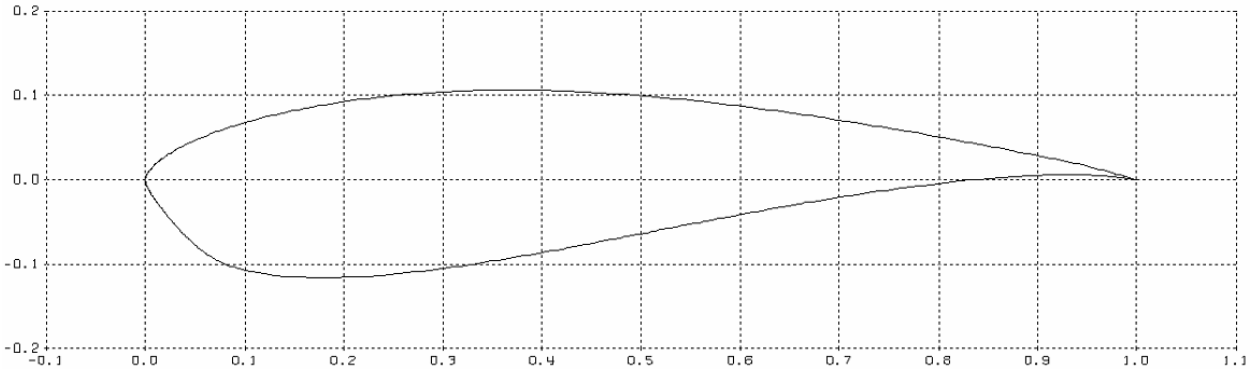

Figure 3.5 The S823 Airfoil Profile

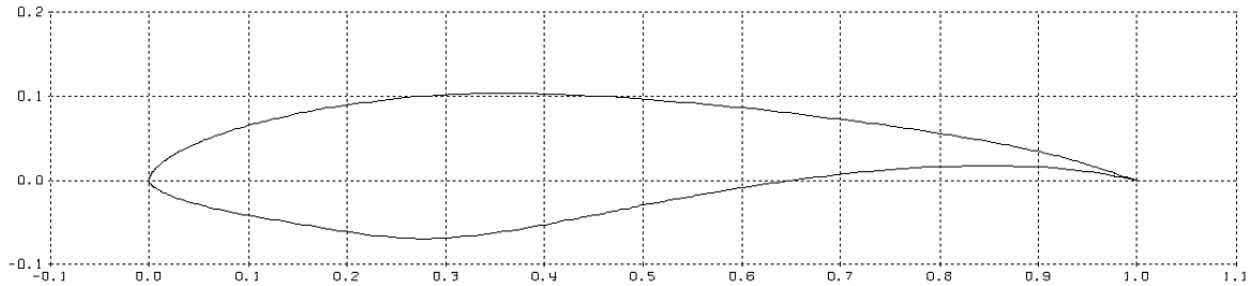

Figure 3.6 The S825 Airfoil Profile

Table 3.2 Basic Characteristics of the 5 Selected Airfoils

	Thickness Ratio, t/c [%]	Camber [~]	Leading Edge Radius, r_{LE} [~]
NACA 0012	12.00	0	0.01572
NACA 0016	16.00	0	0.02807
S822	16.01	0.0189	0.00721
S823	21.15	0.0247	0.01090
S825	17.04	0.0401	0.00736

The aerodynamic performance of the 5 rotor designs, expressed in terms of power coefficient vs. rotor tip speed ratio, Cp vs. λ, is shown in Figure 3.7.

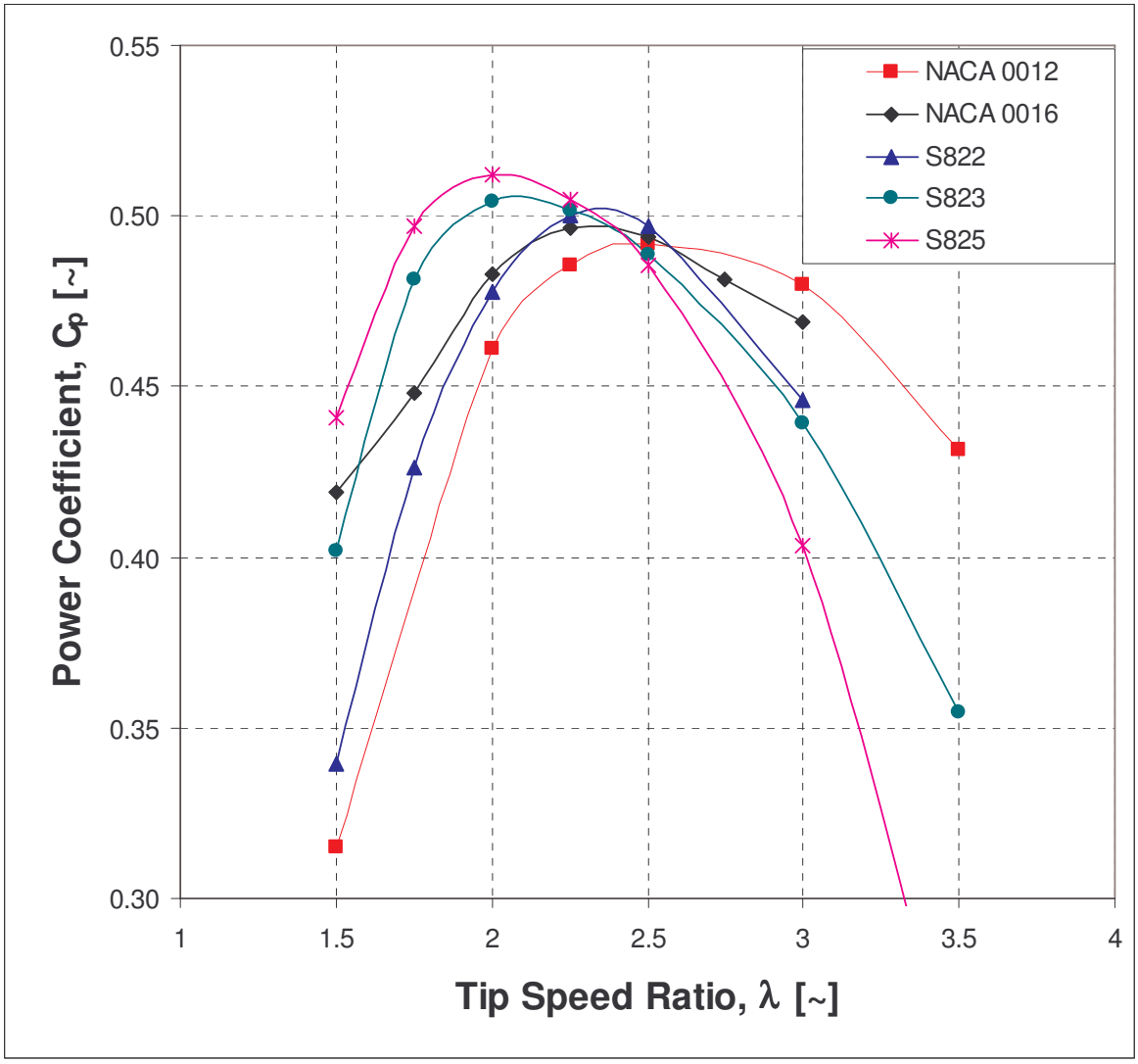

Figure 3.7 Effect of Airfoil Selection on the Aerodynamic Performance of the Hi-Q Rotor (c_{eff} = 0.385 ft, b_{eff} = 0.349 ft and $\theta_{AS1} \neq \theta_{AS2}$)

As observed in Figure 3.7, with everything else being kept the same, the Hi-Q rotor with the S825 airfoil, has a maximum attainable power coefficient of 0.5122, compared to the rotor with the NACA 0012 airfoil of 0.4920. In other words, the difference in maximum attainable power coefficient among the 5 rotors (of different airfoil selection), is 4.1%.

3.2 Effect of Airfoil Section Planform Area (or b_{eff})

Keeping other parameters the same, i.e. c_{eff} = 0.385 ft and $\theta_{AS1} \neq \theta_{AS2}$, the effect of airfoil section span, or b_{eff}, on the aerodynamic performance of the Hi-Q rotor is investigated. The

results of the present study, expressed in terms of a change in maximum attainable power vs. b $_{eff}$, are shown in Figure 3.8.

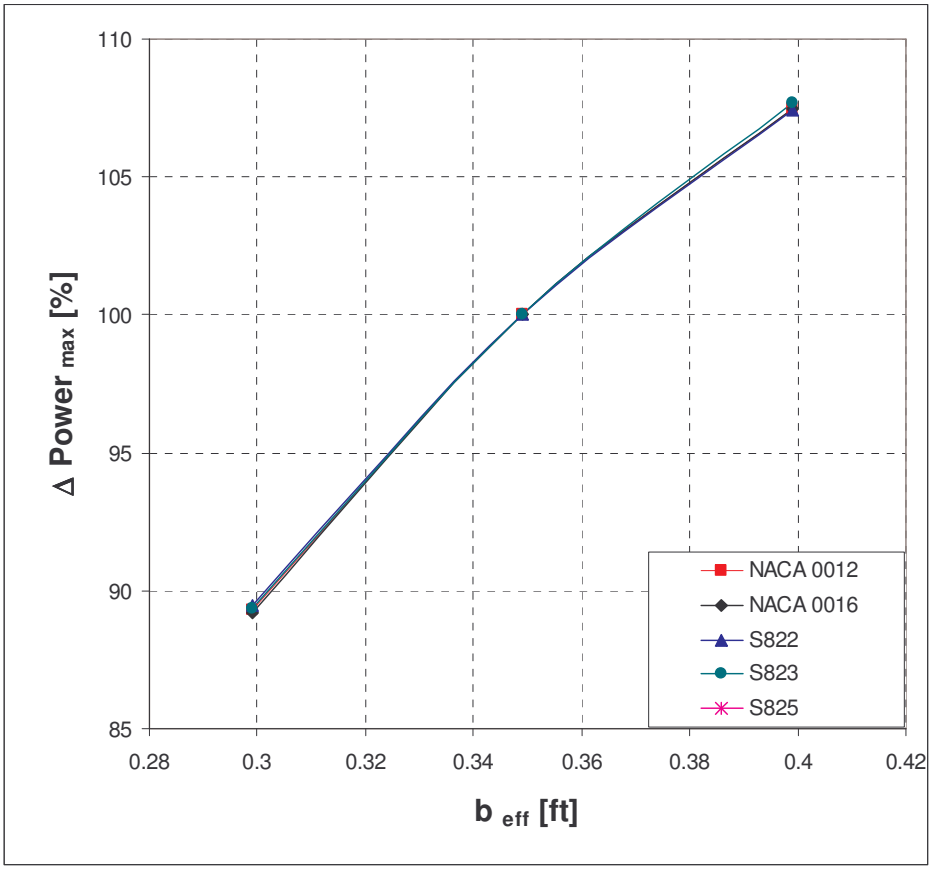

Figure 3.8 Effect of Airfoil Section Span, b $_{eff}$, on the Maximum Attainable Power of the Hi-Q Rotor (c $_{eff}$ = 0.385 ft and $\theta_{AS1} \neq \theta_{AS2}$)

From Figure 3.8, it is observed that an increase in the airfoil section span (or airfoil section planform area if the airfoil section chord is kept constant) increases the maximum attainable power of the rotor, and for all practical purposes it can be concluded that the increment in rotor power is independent of airfoil selection.

3.3 Effect of Airfoil Section Chord (or Reynolds Number)

Keeping $\theta_{AS1} \neq \theta_{AS2}$, the effect of airfoil section chord, or c $_{eff}$, on the aerodynamic performance of the Hi-Q rotor is investigated. The results of the present study, expressed in terms of a change in maximum attainable power coefficient vs. c $_{eff}$, are shown in Figure 3.9, as well as in terms of a change in maximum attainable power vs. c $_{eff}$ in Figure 3.10, respectively.

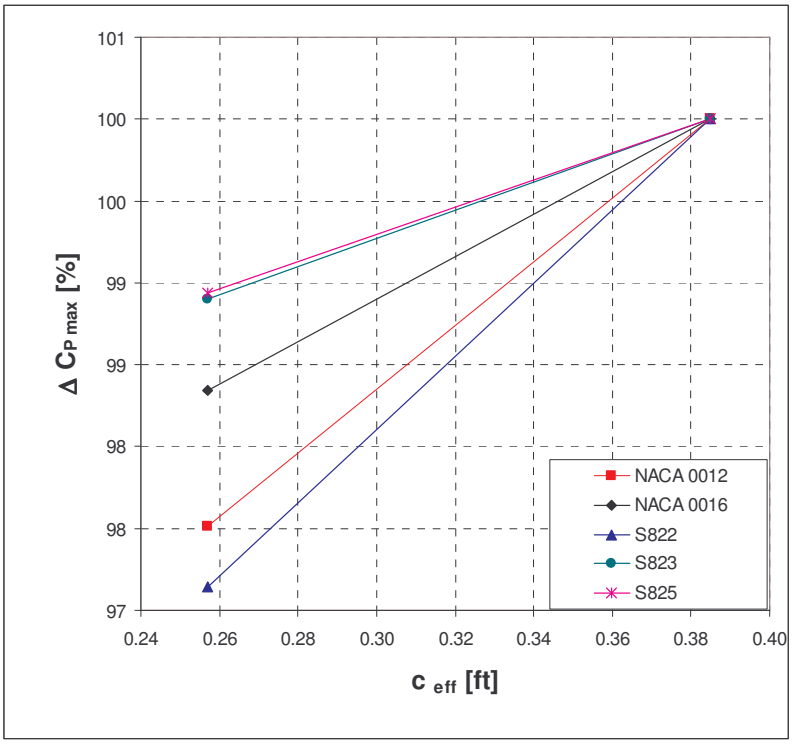

Figure 3.9 Effect of Airfoil Section Chord, c_{eff}, on the Maximum Attainable Power Coefficient of the Hi-Q Rotor ($\theta_{AS1} \neq \theta_{AS2}$)

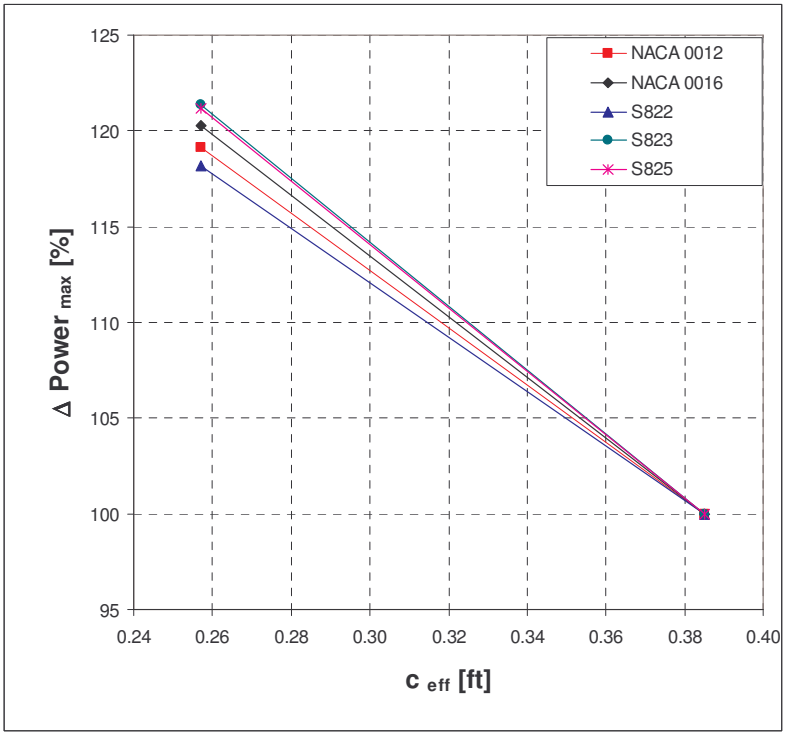

Figure 3.10 Effect of Airfoil Section Chord, c_{eff}, on Maximum Attainable Power of Hi-Q Rotor ($\theta_{AS1} \neq \theta_{AS2}$)

It is observed in Figure 3.9 that a reduction in airfoil section chord results in a reduction in maximum attainable rotor power coefficient by 1% – 3%. However, observing Figure 3.10, it is found that there is an increase in the maximum attainable power by about 18 – 21%, depending on the airfoil selection. The reader is reminded to pay special attention to this finding.

It is logical that a reduction in chord, which is accompanied by a reduction in Reynolds number, increases the airfoil sectional drag coefficient, thus a reduction in the rotor power coefficient as observed in Figure 3.9. However, due to the unique configuration of the Hi-Q rotor, a reduction in the maximum attainable power coefficient does not necessarily indicate a reduction in the maximum attainable rotor power. After reviewing the geometry of the Hi-Q rotor, it is found that due to the unique geometric characteristics of the Hi-Q rotor, compared to a conventional N-bladed horizontal axis wind turbine rotor, HAWT, the standard equation that translates the rotor non-dimensional power coefficient into dimensional rotor power needs to be modified.

For a conventional HAWT, the equation that relates the rotor power coefficient to rotor power is as follows:

$$C_p = \frac{P}{\frac{1}{2}\rho U^3 A_{rotor}}$$

$$\Rightarrow C_p = \frac{P}{\frac{1}{2}\rho U^3 \left[\pi \left(R_{rotor}\right)^2\right]}$$

Since both of the airfoil sections on the Hi-Q rotor do not begin from the center of the rotor, the above equation needs to be modified in such a way that the unique geometric characteristics of Hi-Q rotor can be properly reflected.

The proper equation should be as follows:

$$C_p = \frac{P}{\frac{1}{2}\rho U^3 \pi \left[\left(R_{rotor\_outboard\_station}\right)^2 - \left(R_{rotor\_inboard\_station}\right)^2\right]}$$

For airfoil section 1:

$R_{rotor\_outboard\_station} = R_{rotor}$

$R_{rotor\_inboard\_station} < R_{rotor}$

For airfoil section 2:

$R_{rotor\_outboard\_station} > R_{rotor}$

Note: Refer to Figure 3.1 on the definition of the location of the inboard or the outboard station.

It is found that as the airfoil section chord is reduced from 0.385 ft to 0.257 ft, the term, $\left[\left(R_{rotor\_outboard\_station}\right)^2 - \left(R_{rotor\_inboard\_station}\right)^2\right]$ increases, and the rate of increase of the term, outgrows the reduction in the maximum attainable rotor power coefficient.

When comparing the aerodynamic performance of two Hi-Q rotors of different c_{eff} and b_{eff}, the dimensional maximum attainable power, P_{max}, should be used, over the dimensionless maximum attainable power coefficient, $C_{p\,max}$.

3.4 Effect of Airfoil Section Pitch Distribution

Keeping other parameters the same, i.e. c_{eff} = 0.385 ft and b_{eff} = 0.349 ft, the effect of airfoil section pitch distribution on the aerodynamic performance of the Hi-Q rotor is investigated. The results of the present study are summarized in Table 3.3.

Table 3.3 Effect of Rotor Airfoil Section Pitch Distribution on the Maximum Attainable Power of the Hi-Q Rotor (c_{eff} = 0.385 ft and b_{eff} = 0.349 ft)

Airfoil	$\theta_1 = \theta_2$	$\theta_1 =/ \theta_2$
	D P_{max} [%]	
NACA 0012	100	105
NACA 0016	100	105
S822	100	105
S823	100	105
S825	100	107

From Table 3.3, it is found that having an optimized pitch distribution, one for each airfoil section, certainly helps increasing the aerodynamic performance of the rotor.

Out of the 60 Hi-Q rotor designs, the five rotors with the highest maximum attainable power are selected. There are as follows

Table 3.4 Five Hi-Q Rotor Designs with the Highest Maximum Attainable Power

Design #	Airfoil	c_{eff} [ft]	b_{eff} [ft]	$\theta_{AS1} \neq \theta_{AS2}$	$P_{max\ attainable}$ [W]
50	S825	0.257	0.399	Y	5.304
38	S823	0.257	0.399	Y	5.225
26	S822	0.257	0.399	Y	5.118
14	NACA0016	0.257	0.399	Y	5.103
2	NACA0012	0.257	0.399	Y	5.024

Note: For all 60 rotor designs, the wind speed is assumed to be 6.17 m/s (or 12 kts), and the rotor diameter is assumed to be 16 inches.

The aerodynamic performance of the 5 rotor designs is shown in Figure 3.11.

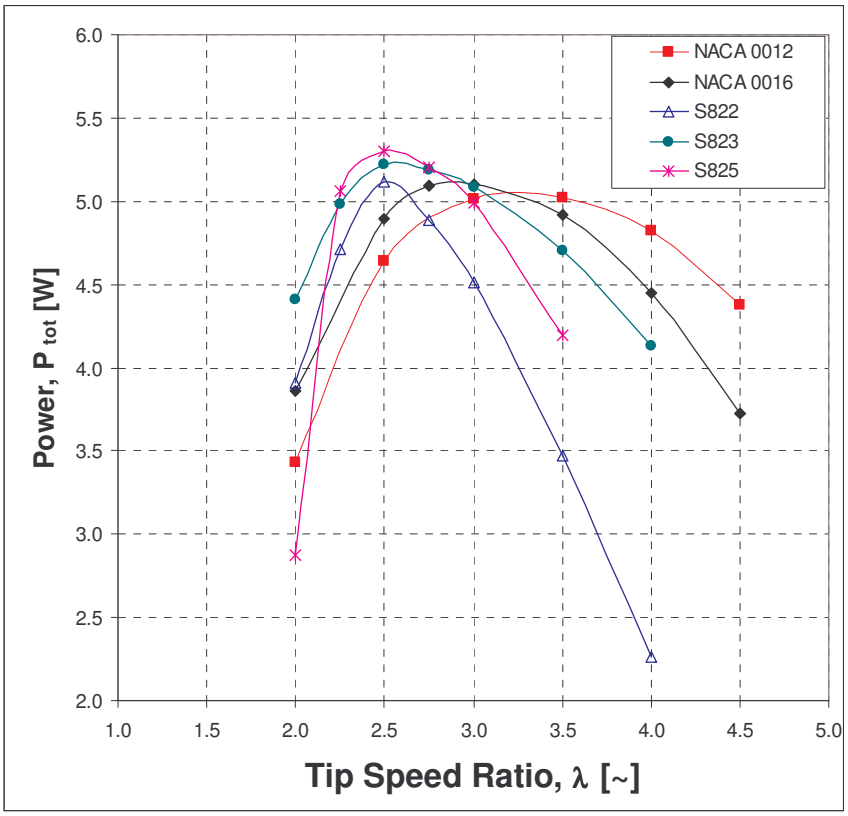

Figure 3.11 Aerodynamic Performance of 5 Hi-Q Rotor Designs with Highest Maximum Attainable Power (c_{eff} = 0.257 ft, b_{eff} = 0.349 ft and $\theta_{AS1} \neq \theta_{AS2}$)

The 5 rotors are analyzed computationally. Results of the CFD analysis of Design 50, summarized in Table 3.4, are presented.

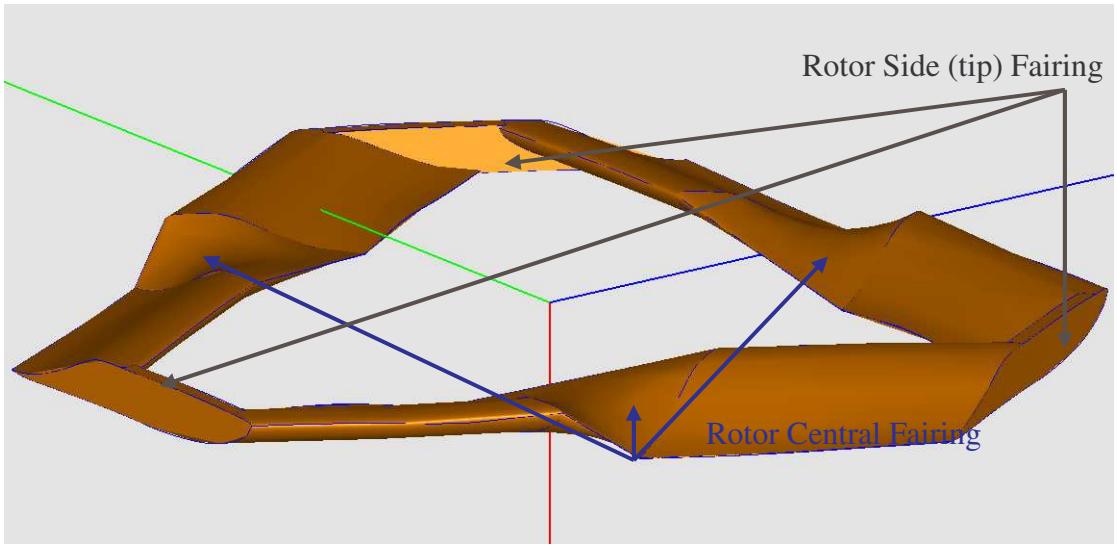

Figure 3.12 The non-Airfoil Sections on Hi-Q Rotor Planform

The primary objectives of analyzing the rotors computationally are:

1. To determine out the effect of the rotor central fairing (shown in Figure 3.12) on the overall aerodynamic performance of the rotor.

2. To find out the effect of the rotor side (tip) fairing (shown in Figure 3.12) on the overall aerodynamic performance of the rotor.

3. To determine the effect of the rotor blade interference on the overall aerodynamic performance of the rotor.

CFD analyses are deemed necessary as the above mentioned effects cannot be modeled by the developed analytical code.

3.5 Effect of Rotor Central Fairing

The rotor surface pressure distribution of rotor design # 50, at a rotor tip speed ratio of 2.5, is presented in Figure 9a and Figure 9 b.

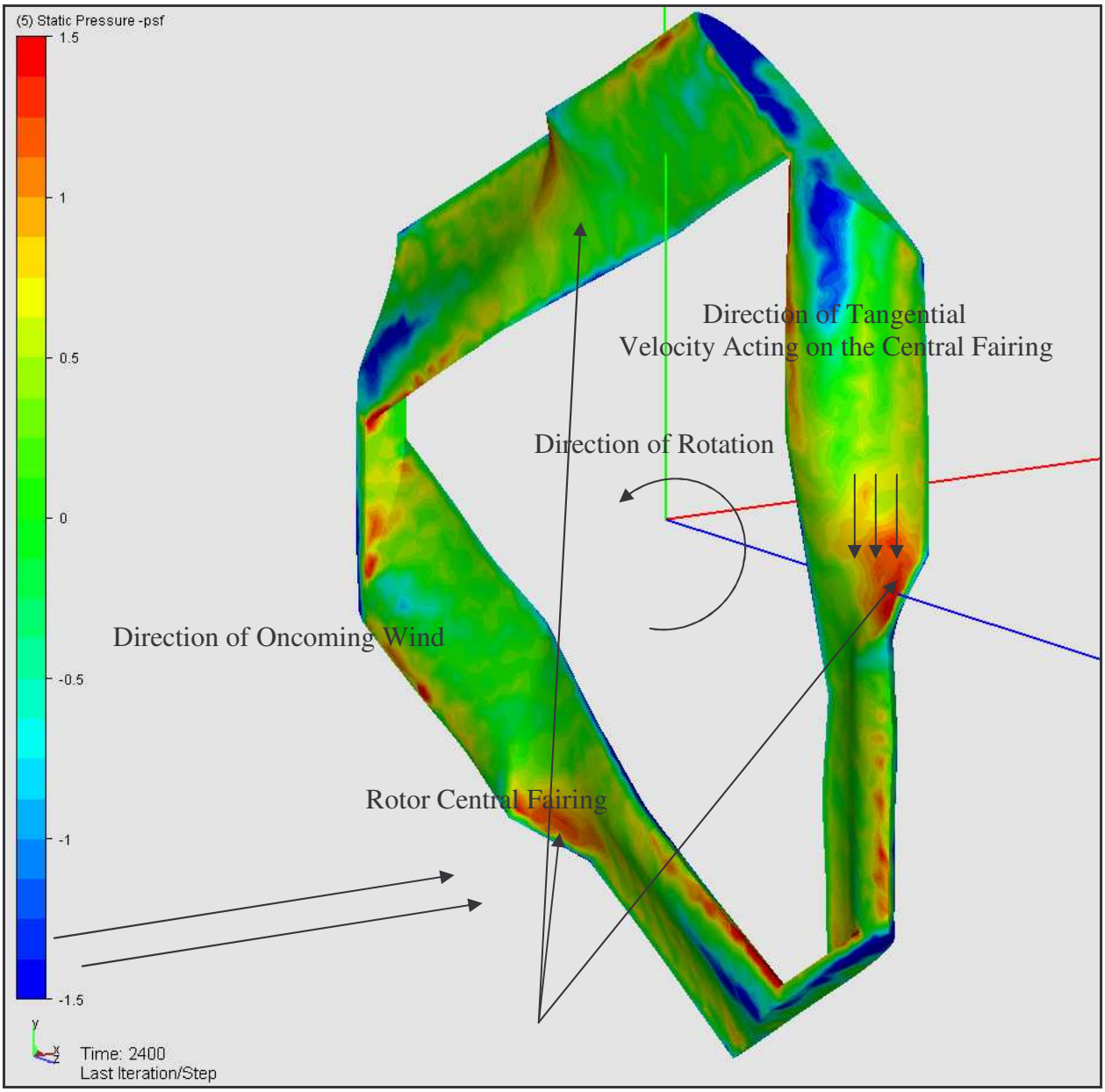

Figure 3.13 Rotor Surface Pressure Distribution of Design 50 (Viewed from front of Rotor)

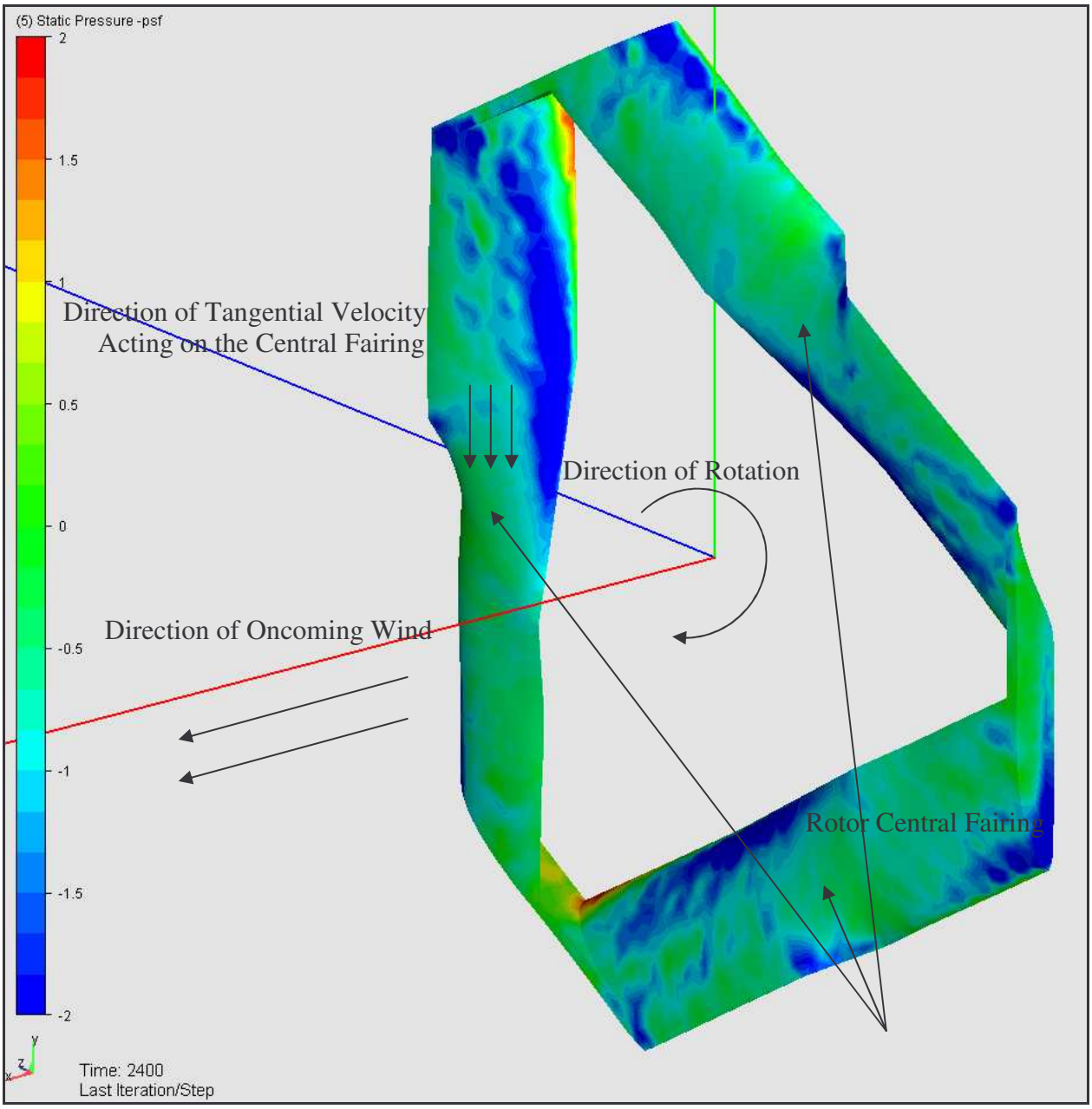

Figure 3.14 Rotor Surface Pressure Distribution of Design 50 (Viewed from back of Rotor)

As observed in Figure 3.13, the front surface of the rotor central fairing is "covered" with high positive pressure (red color). With respect to the direction of the tangential velocity acting on the rotor central fairing, the high positive pressure (at windward side) physically translates to high drag. In other words, the rotor central fairing is producing a (negative) torque which acts against the direction of rotation.

Observing Figure 3.14, it is found that the back surface of the rotor central fairing is "covered" with slightly negative pressure (-0.5 Psf < P < 0). With respect to the direction of the tangential velocity, the negative pressure (at leeward side) also translates to drag, thus producing a (negative) torque which acts against the direction of rotation

Due to the unique geometric configuration of the Hi-Q rotor, the rotor central fairing can be viewed as a small section of wing which connects the Airfoil Section 1 and the Airfoil Section 2. Subsequently, the "twist" on the rotor central fairing is controlled by the pitch distribution of the two airfoil sections. Taking a particular rotor design as an example, if the pitch at the inboard station of both airfoil sections (Refer to Figure 3.1) equals zero, then the "twist" becomes zero, and the drag on the rotor central fairing is minimum.

The ratio of rotor central fairing torque to rotor airfoil section torque of Design 50 is summarized in Table 3.5. From Table 3.5, it is found that the resistive (negative) torque induced by the rotor central fairing is around 4 – 7%, compared to the positive torque generated by the airfoil sections.

Table 3.5 Ratio of Rotor Central Fairing Torque to Rotor Airfoil Section Torque of Design 50

Tip Speed Ratio λ [~]	RPM	$\tau_{\text{Central Fairing}} / \tau_{(AS1 + AS2)}$ [%]
2.00	580	- 4.0
2.25	653	- 5.5
2.50	725	- 6.5

3.6 Effect of Rotor Side (Tip) Fairing

The purpose of the rotor side fairing is to act as a barrier in preventing the high positive (gage) pressure on the front side (pressure side) of the airfoil sections from "escaping" to the low negative (gage) pressure on the back side (suction side) of the airfoil sections. This is known as the tip loss phenomenon. While the rotor tip fairing improves the airfoil section outboard lift coefficient, thus the aerodynamic performance, its presence on the other hand generates drag and thus produces negative torque. Based on the results of the CFD analyses on Design 50, which are summarized in Table 5, it is found that a significant amount of negative torque is generated due to the presence of the rotor tip fairing, which is about 13 – 24%, compared to the positive

torque generated by the airfoil sections. In addition, it is also found that the resistive torque increases with the increase in rotor tip speed ratio.

Table 3.6 Ratio of Rotor Side Fairing Torque to Rotor Airfoil Section Torque of Design 50

Tip Speed Ratio λ [~]	RPM	$\tau_{\text{Side Fairing}} / \tau_{(AS1 + AS2)}$ [%]
2.00	580	- 13.4
2.25	653	- 14.8
2.50	725	- 24.0

Based on the calculated (negative) torque of the rotor side fairings, summarized in Table 3.6, it is concluded that there is much room for improvement in the rotor overall aerodynamic performance if the rotor side fairing is properly designed.

3.7 Effect of Rotor Blade Interference

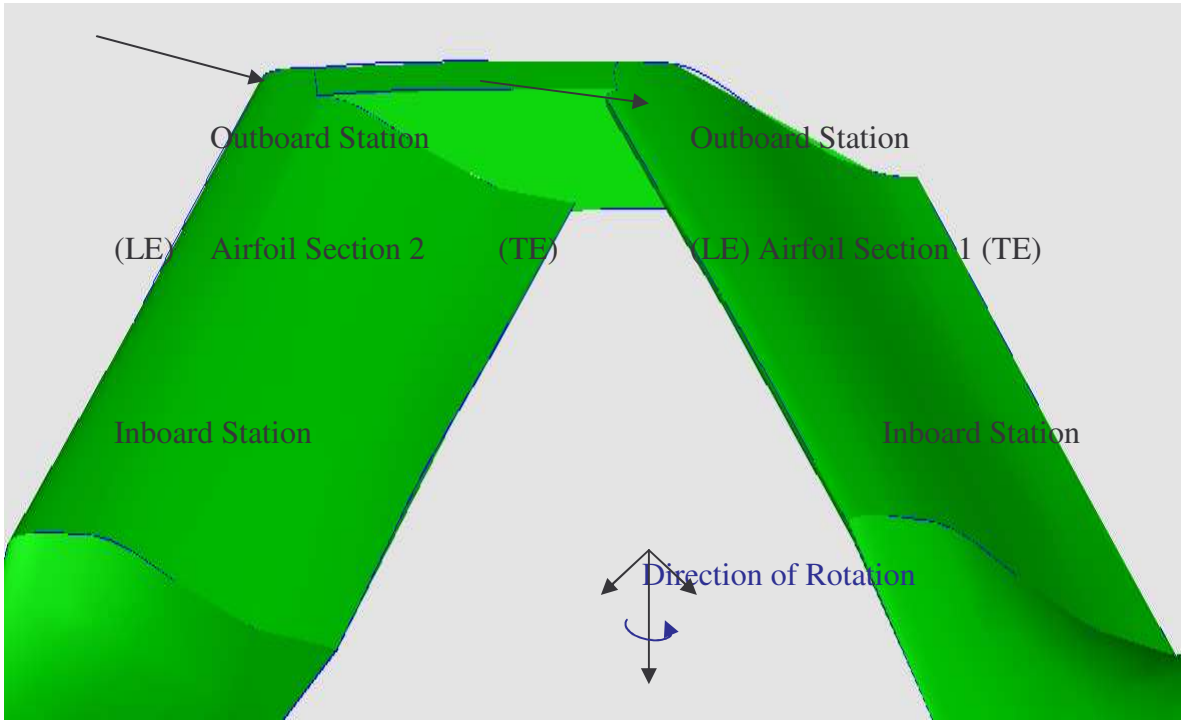

Figure 3.15 The Hi-Q Rotor Geometric Characteristic on Rotor Blade Interference Effect (Viewed from the front of the Rotor)

The developed analytical code does not take into the account of the rotor blade interference effect. Due to the unique geometric characteristics of the Hi-Q rotor, in reality, shown in Figure 3.15, the rotor blade interference effect does exist. The airflow angles "seen" by the outboard stations of Airfoil Section 1, to certain degree, is affected by the downwash from the outboard stations of Airfoil Section 2, due to the close proximity. This is graphically illustrated in Figure 3.16.

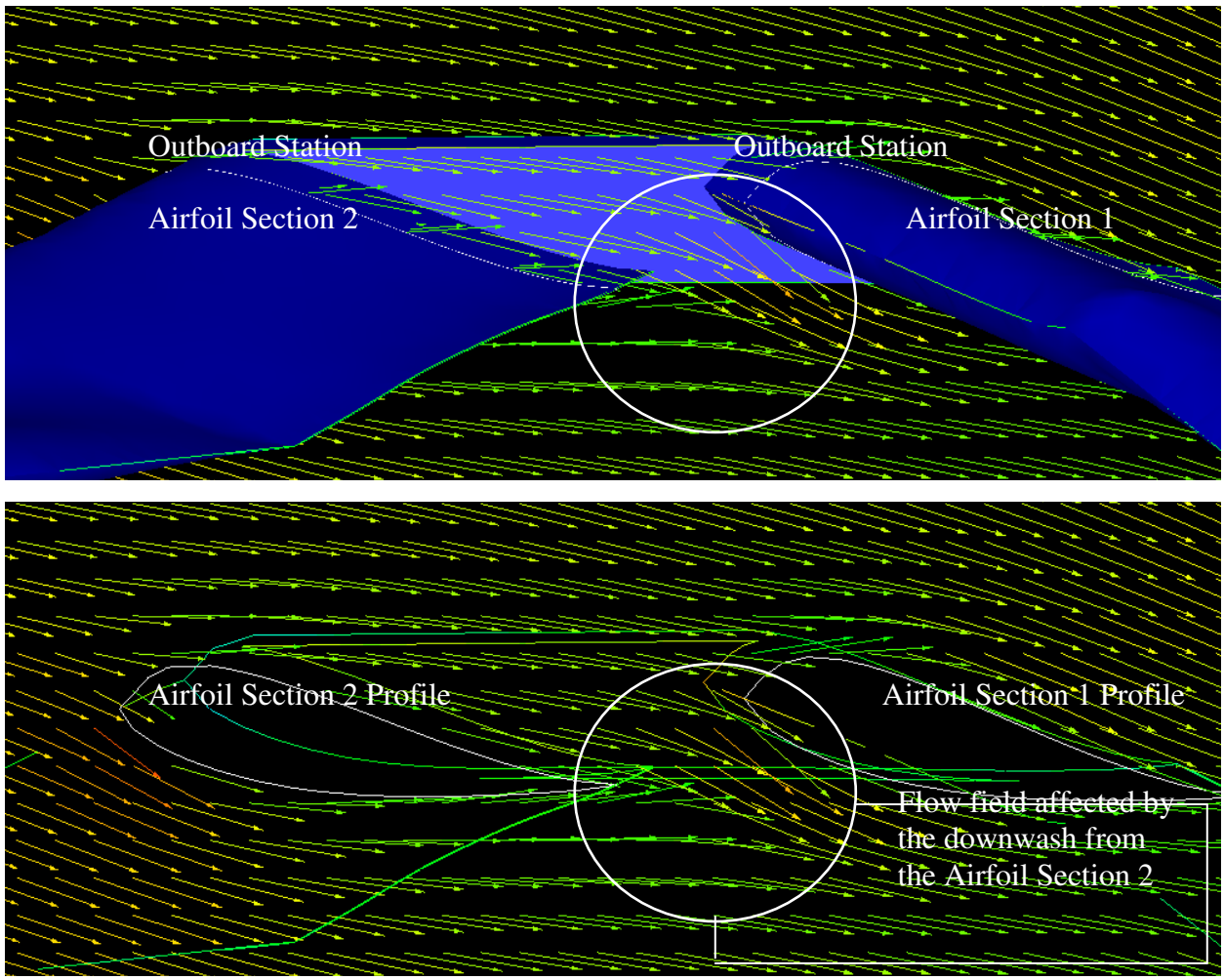

Figure 3.16 The Velocity Vector Plot of Design 50 at the outboard station of Airfoil Section 1 and Airfoil Section 2

As shown in Figure 3.16, the flow field seen by Airfoil Section 1, which is inside the white circle, is somewhat "influenced" by the presence of Airfoil Section 2. The consequence is such that the true local inflow angle, as well as the true local angle of attack at the outboard stations of Airfoil Section 1, is different from those predicted analytically. As a result, the tip speed ratio at

which the rotor is predicted (analytically) to achieve its maximum attainable power, in reality, might not yield a maximum attainable power.

Table 3.7 summarizes the predicted rotor tip speed ratio at which the rotor maximum attainable power is obtained, between the analytical and the computational models. From Table 3.7, it is found that the computationally predicted rotor tip speed ratio, at which the rotor achieves its maximum attainable power, is slightly lower than that predicted by the analytical code.

Table 3.7 Comparison of Rotor Tip Speed Ratio at which the Maximum Attainable Power is achieved, between Analytical and Computational Model

Tip Speed Ratio λ [~]	(Analytical) P_{rotor} / max. P_{rotor} [%]	(CFD) P_{rotor} / max. P_{rotor} [%]
2.00	54.2	90.3
2.25	95.5	100.0
2.50	100.0	60.6
2.75	98.1	N.A.
3.00	94.1	N.A.

Note: N.A. stands for Data Not Available

3.8 Conclusions

- An analytical code is developed to help with designing the Hi-Q rotors.

- 5 different airfoils, 2 different airfoil section chords, 3 different airfoil section planform area and 2 different airfoil section pitch distribution, are selected, resulting in a matrix with 60 designs.

- From the 60 rotor designs, Rotor 50, which is the rotor with the S825 airfoil, an effective chord, c_{eff}, of 0.257 ft, an effective span, b_{eff}, of 0.349 ft and $\theta_{AS1} \neq \theta_{AS2}$, achieves the highest maximum attainable power.

- Analyzing the designed rotor computationally reveals the following effects which cannot be identified by the analytical methods: effect of rotor central fairing, side (tip) fairing and the rotor blade interference on the aerodynamic performance of the rotor.

- The resistive (negative) torque due to the presence of the rotor central and side fairings is not negligible, compared to the positive aerodynamic torque generated by the airfoil sections.

- The effect of the rotor blade interference is such that the local inflow angle, as well as the local angle of attack at the outboard stations of the Airfoil Section 1 is influenced, resulting in a change in the rotor tip speed ratio at which the rotor is predicted (analytically) to achieve its maximum attainable power.

3.9 Conclusions

The geometry of the two airfoils sections of the present Hi-Q rotor configuration can be gradually expanded (radially) inboard towards the center of the Hi-Q rotor hub, similar to those shown in the following figures. With the new configurations, the effective span of the airfoil sections can be further expanded, thus a possible increase in the power performance generation.

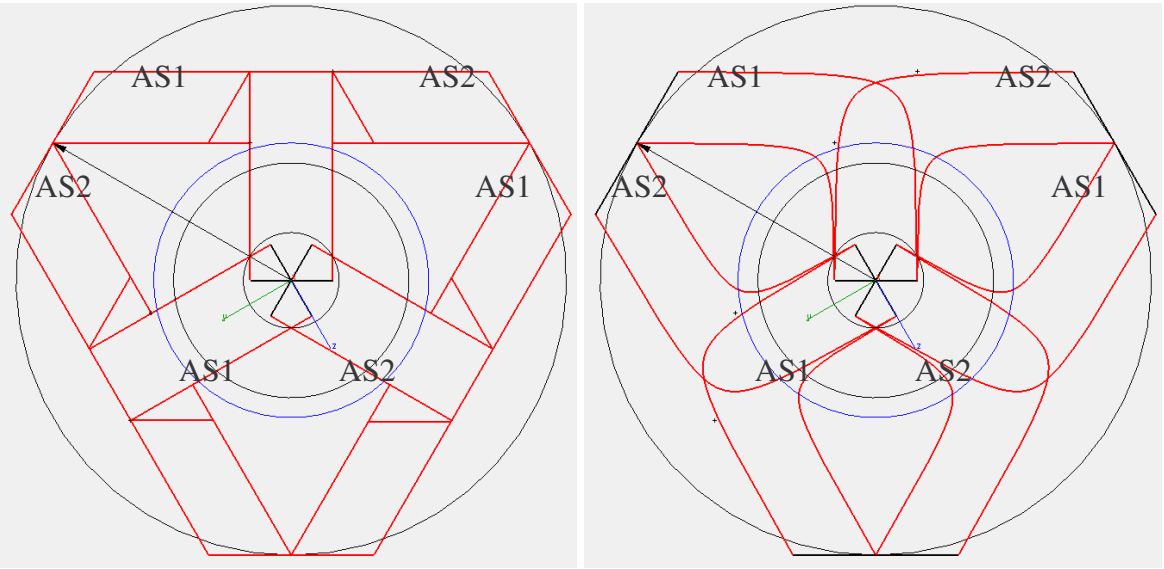

(a) The Present Configuration (b) Possible Future Configurations

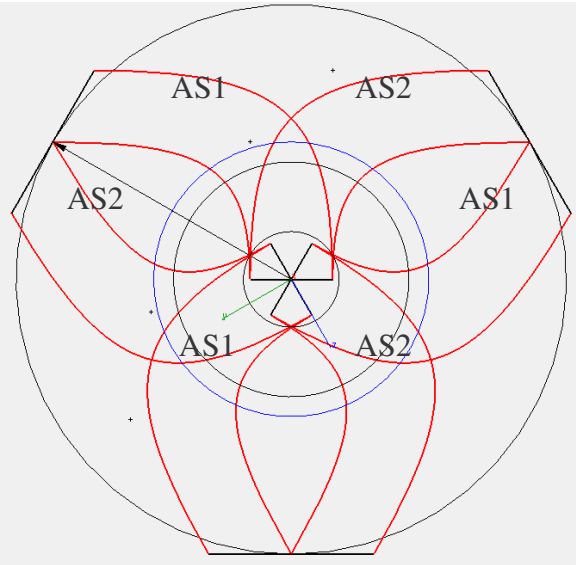

(c) Possible Future Configurations

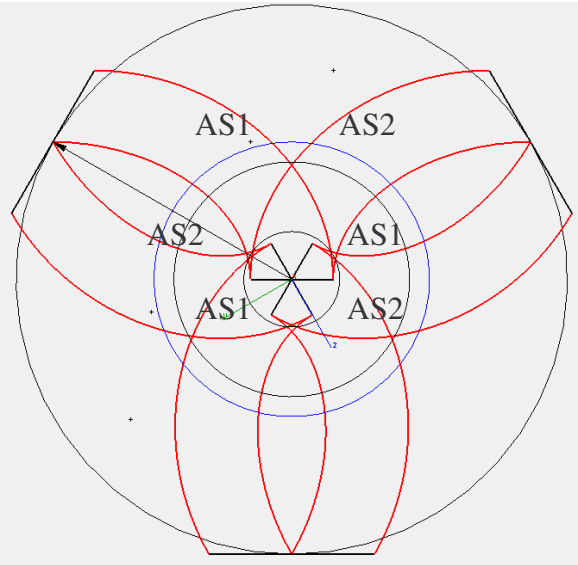

(d) Possible Future Configurations

4. Phase I Aerodynamic Performance of Hi-Q Rotors Tested at KU Wind Tunnel

A total of 7 wind turbine rotors, all having a diameter of 16 inches, are tested at the University of Kansas wind tunnel in August and September of 2007. Results of the aerodynamic performance of the tested rotors are presented in this memo.

The primary objectives of the wind tunnel testing are:

- To compare the aerodynamic performance among the tested rotors, which are designed based on the developed analytical code that uses the blade-element-momentum (BEM) technique.

- The results are then compared to two horizontal axis wind turbine (HAWT) rotors, one of which is designed by Dr. Kyle Wetzel and the other is the Bergey XL.1 HAWT.

A summary of the geometric characteristics of the seven tested wind turbine rotors is listed in Table 1. The geometric parameters are listed in Figure 4.1 through Figure 4.3.

One of the rotors has been tested with different end plates to investigate the effect of end plate size on performance

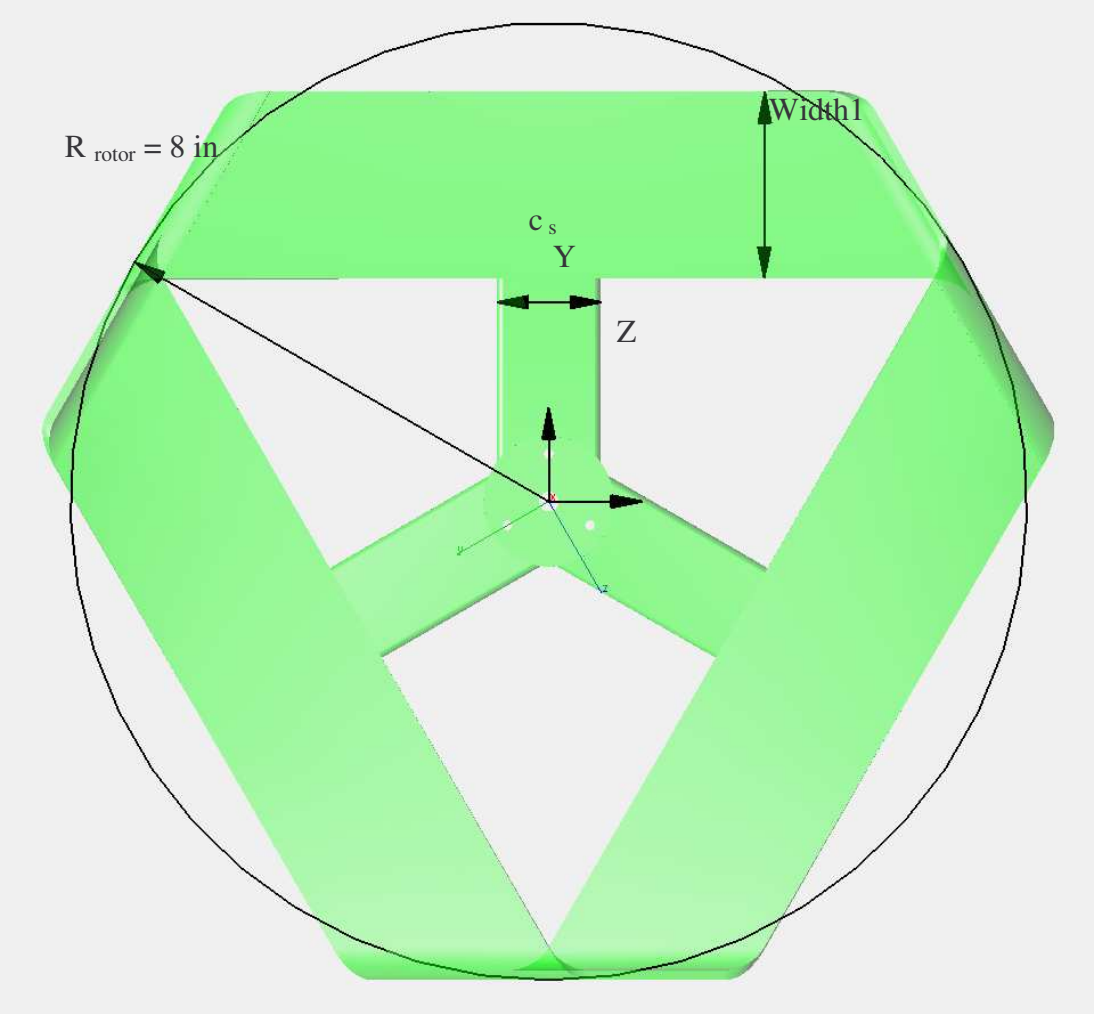

Figure 4.1 The Hi-Q Rotor Planform of Triangular Configuration (R_{rotor} = 8 inches)

Figure 4.2 Hi-Q Rotor #61 3-Bladed Configuration (R_{rotor} = 8 inches)

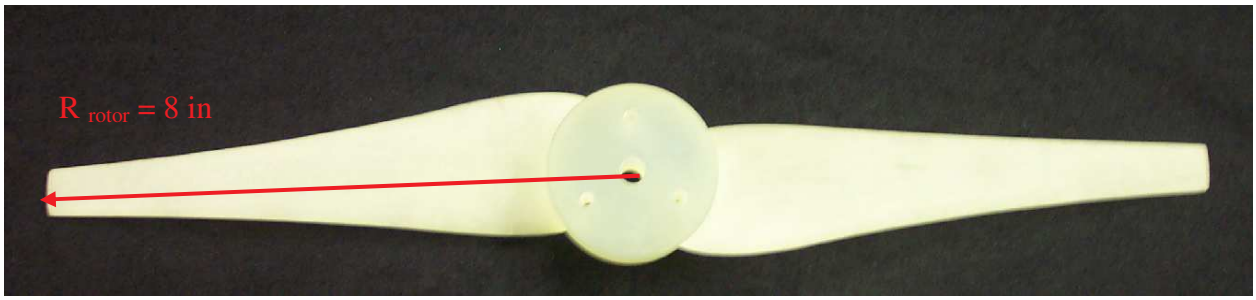

Figure 4.3 Kyle Wetzel Rotor 2-Bladed HAWT Configuration (R_{rotor} = 8 inches)

Table 4.1 Geometric Characteristics of Tested Rotors

Rotor Design # (based on Reference 1)	Airfoil	Width1 [ft]	c_s [ft]	Configuration
2	NACA 0012	0.222	0.10	"Triangular Hi-Q Configuration" Shown in Figure 1
26	S822	0.222	0.10	
38	S823	0.222	0.10	
56	S825	0.333	0.10	
50	S825	0.222	0.10	
61	S825	N.A.	N.A.	"3 Bladed Hi-Q Configuration" Shown in Figure 2
KW (Kyle Wetzel)	Wetzel	N.A.	N.A.	"2 Bladed HAWT Configuration" Shown in Figure 3

4.1 Effect of End Plate on Hi-Q Rotor Performance

Rotor Design #56 uses three endplates of different sizes to investigate the effect of size of the endplates on the aerodynamic performance of the Hi-Q rotors. The schematics of the three endplates are illustrated in Figure 4.4 through Figure 4.6. Pictures of the three different endplates, when mounted on Rotor Design #56, are shown in Figure 4.7 through Figure 4.10.

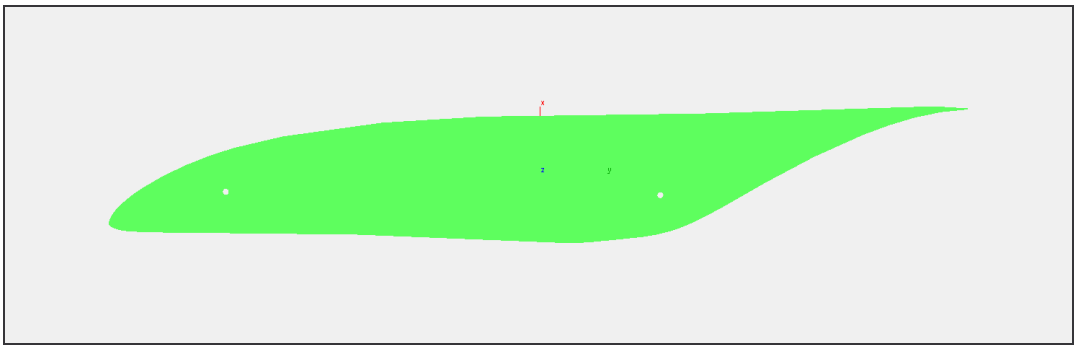

Figure 4.4 Side View of Endplate 1 (Default Size)

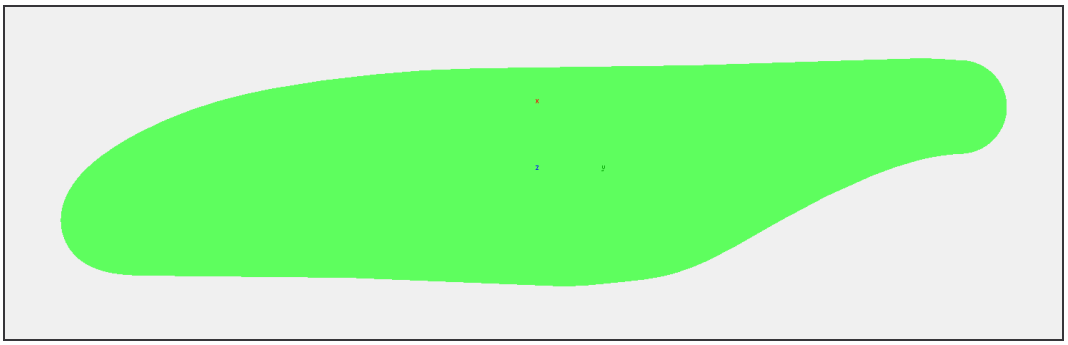

Figure 4.5 Side View of Endplate 2

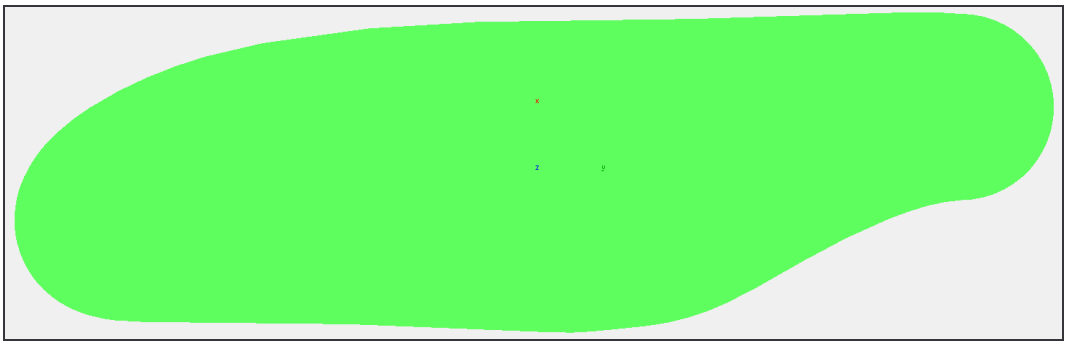

Figure 4.6 Side View of Endplate 3

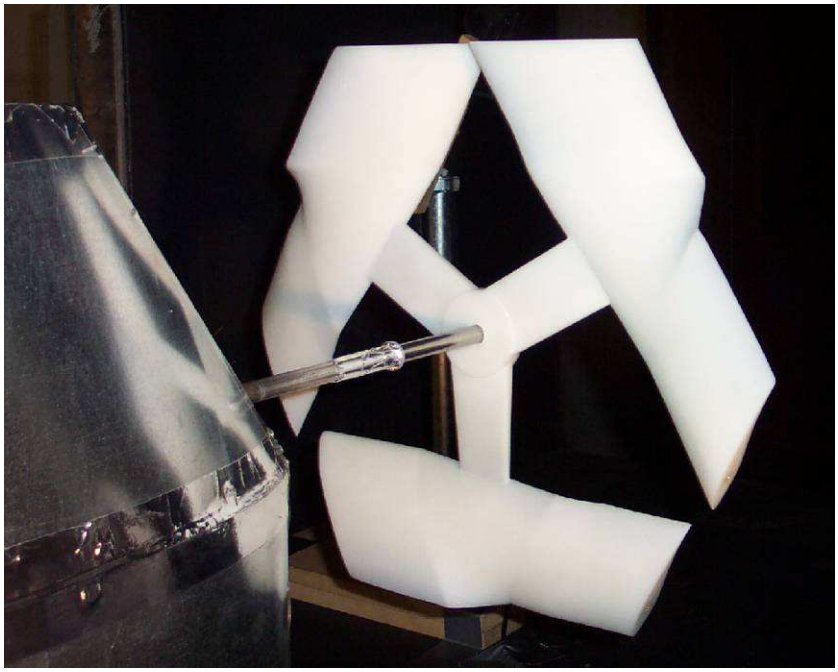

Figure 4.7 Rotor Design # 56 without Endplate

Figure 4.8 Rotor Design # 56 with Endplate 1 (Default Size)

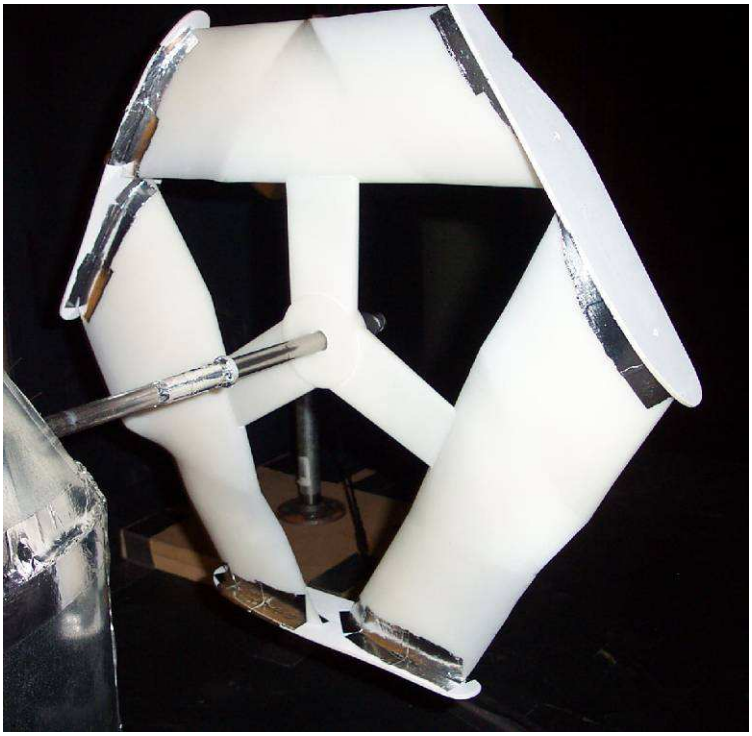

Figure 4.9 Rotor Design # 56 with Endplate 2

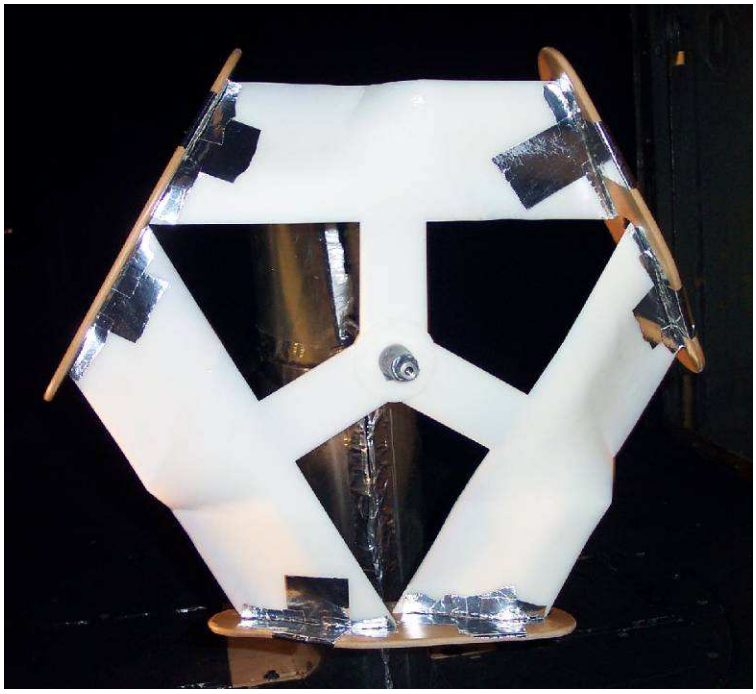

Figure 4.10 Rotor Design # 56 with Endplate 3

Results of the study of end plate effect are summarized in Table 4.2.

Table 4.2 Effect of Endplate on the Aerodynamic Performance of Rotor Design #56

Rotor Design #56	**max. Aerodynamic Power, $P_{aerodynamic}$ [W]**	
	U = 18 [kts]	**U = 26 [kts]**
no Endplate	21.9	47.9
Endplate 1 (Default Size)	19.1	41.4
Endplate 2	17.6	34.4
Endplate 3	17.3	27.6

The net measured power is as follows:

$$P_{net} = VI$$

where: V is voltage readout [Volt]

I is current readout [Amp]

The voltage and current data are measured while the rotor is spinning. The net power, P_{net}, is the product of the measured voltage and the measured current. P_{net} does not account for the electrical and mechanical losses associated with the generator and bearings and therefore P_{net} does not reflect the aerodynamic power of the Hi-Q rotors. The aerodynamic power of the rotor is represented by $P_{aerodynamic}$. The following equation describes the relationship between the P_{net} and $P_{aerodynamic}$.

$$P_{aerodynamic} = \Delta P_{loss} + P_{net}$$

where: ΔP_{loss} is power loss of the generator [W]

The rotor rotational speed, expressed in terms of the shaft RPM, corresponding to the maximum $P_{aerodynamic}$, is summarized in Table 4.3.

Table 4.3 Rotor Design #56 Rotational Speed (at maximum Aerodynamic Power)

Rotor Design #56	**RPM @ max $P_{aerodynamic}$**	
	U = 18 [kts]	**U = 26 [kts]**
no Endplate	642	997
Endplate 1 (Default Size)	592	944
Endplate 2	394	613
Endplate 3	398	491

From Table 4.2 it is found that an increase in the size of the endplate reduces the aerodynamic performance of the rotors. From an aerodynamic point of view, the presence of the end plate is to relieve the rotor blade tip loss effect, thus resulting in an increase in rotor power output. However, from the results of the present wind tunnel experiments, it is observed that the extra drag generated by the presence of the endplate, deteriorates the rotor performance. The endplate is needed so that the Mobius Strip Theory is not violated. Therefore, to minimize the power penalty, the endplate must be kept as small as possible.

4.2 Comparison of Aerodynamic Performance among different Hi-Q rotors

The aerodynamic performance of five Hi-Q rotors are analyzed and compared. Pictures of the five Hi-Q rotors are shown in Figure 4.11 through Figure 4.15.

Figure 4.11 Rotor Design #2

Figure 4.12 Rotor Design #26

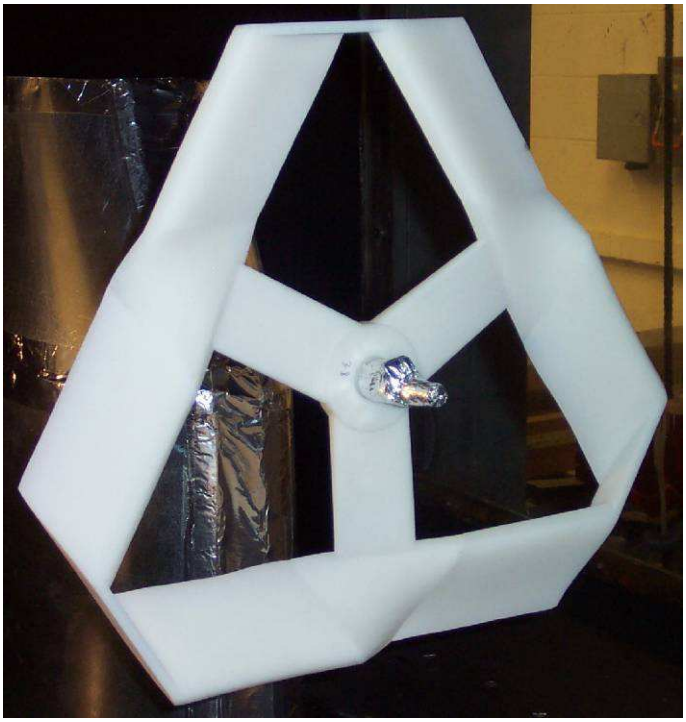

Figure 4.13 Rotor Design #38

Figure 4.14 Rotor Design #50

Figure 4.15 Rotor Design #61

The profiles of the 5 selected airfoils are illustrated in Figure 4.16 through Figure 4.19.

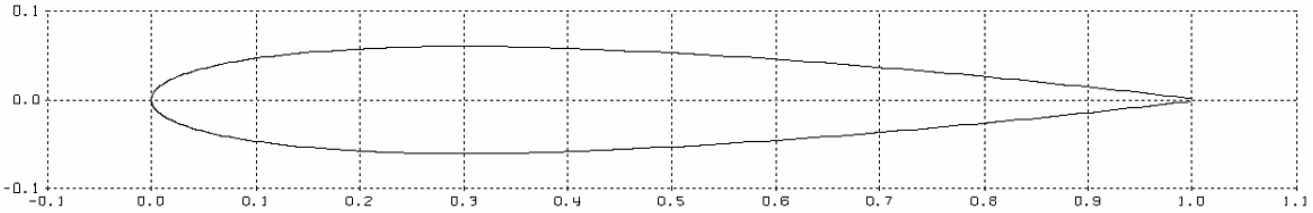

Figure 4.16 NACA 0012 Airfoil Profile on Rotor Design #2

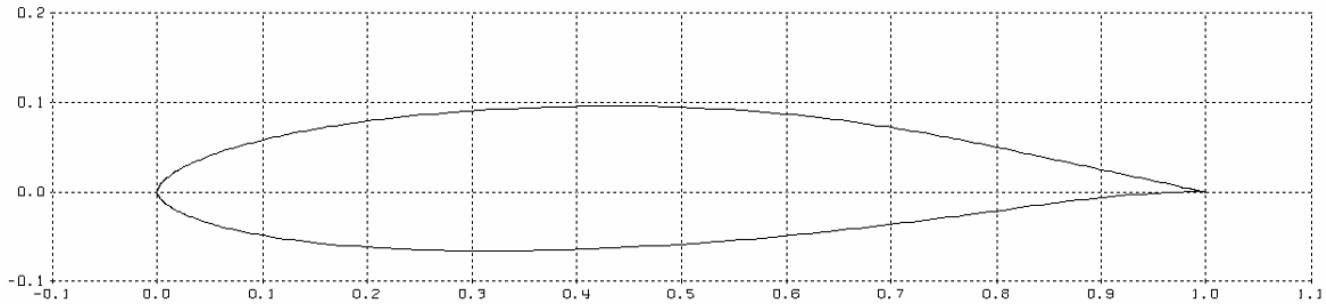

Figure 4.17 S822 Airfoil Profile on Rotor Design #26

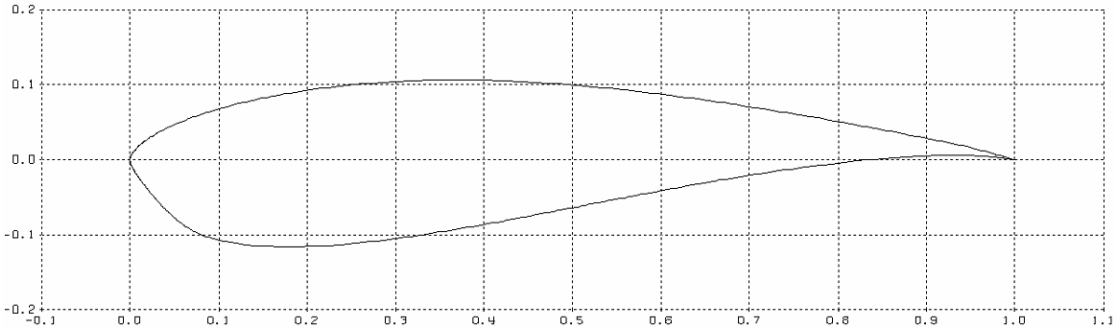

Figure 4.18 S823 Airfoil Profile on Rotor Design #38

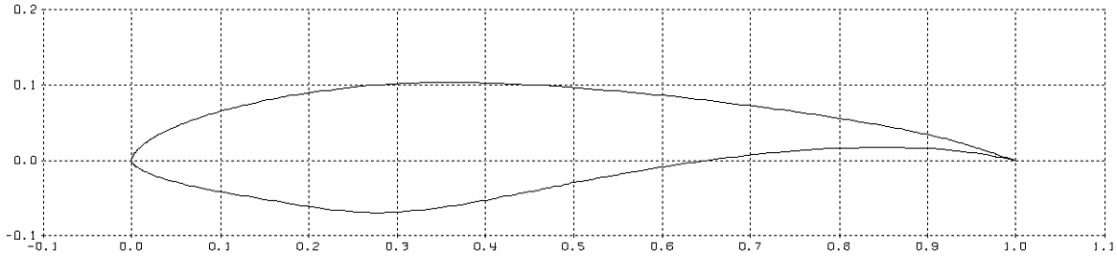

Figure 4.19 S825 Airfoil Profile on Rotor Designs #50 and #61

Results of the generated net and aerodynamic powers, as a function of rotational speed at various wind speeds, of Rotor Design #2, 26, 38, 50 and 61 are illustrated in Figure 4.20 through Figure 4.24.

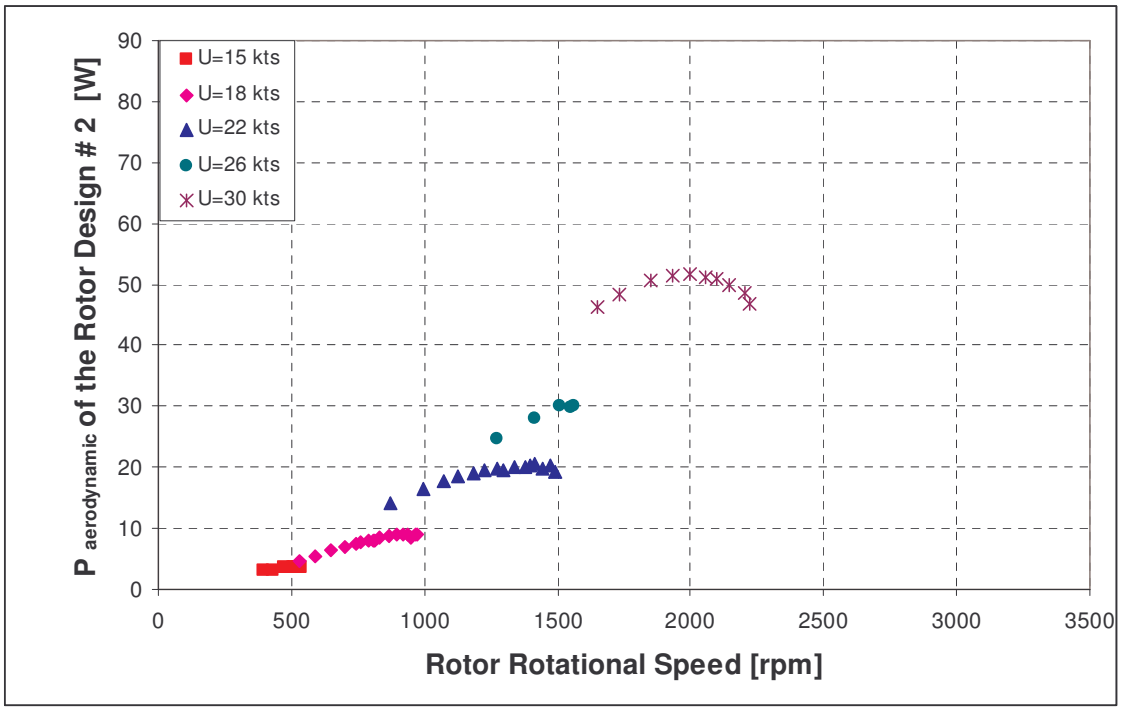

Figure 4.20 Aerodynamic Power of Rotor Design #2

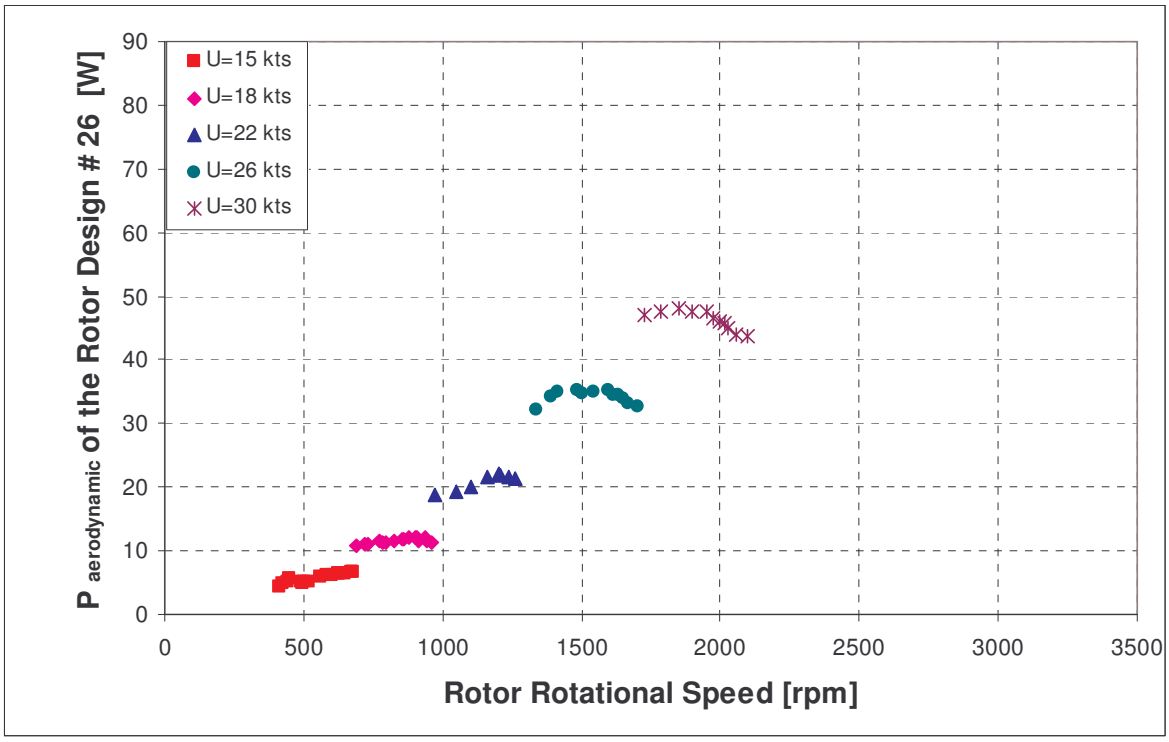

Figure 4.21 Aerodynamic Power of Rotor Design #26

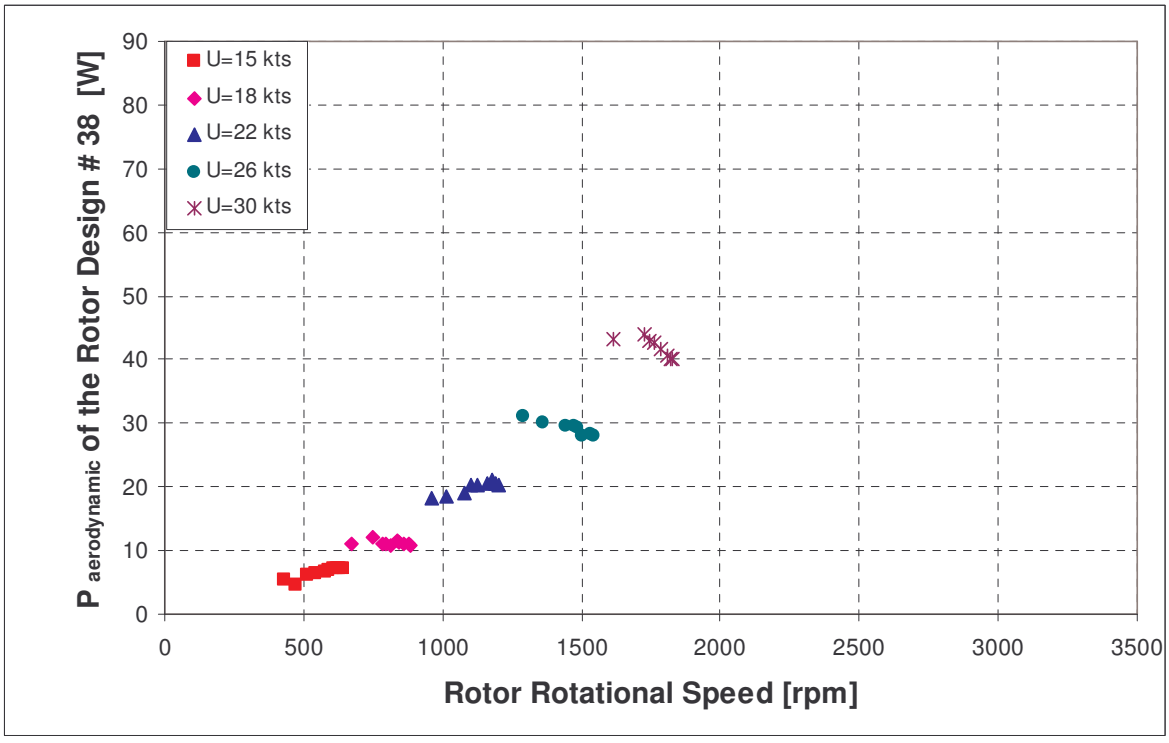

Figure 4.22 Aerodynamic Power of Rotor Design #38

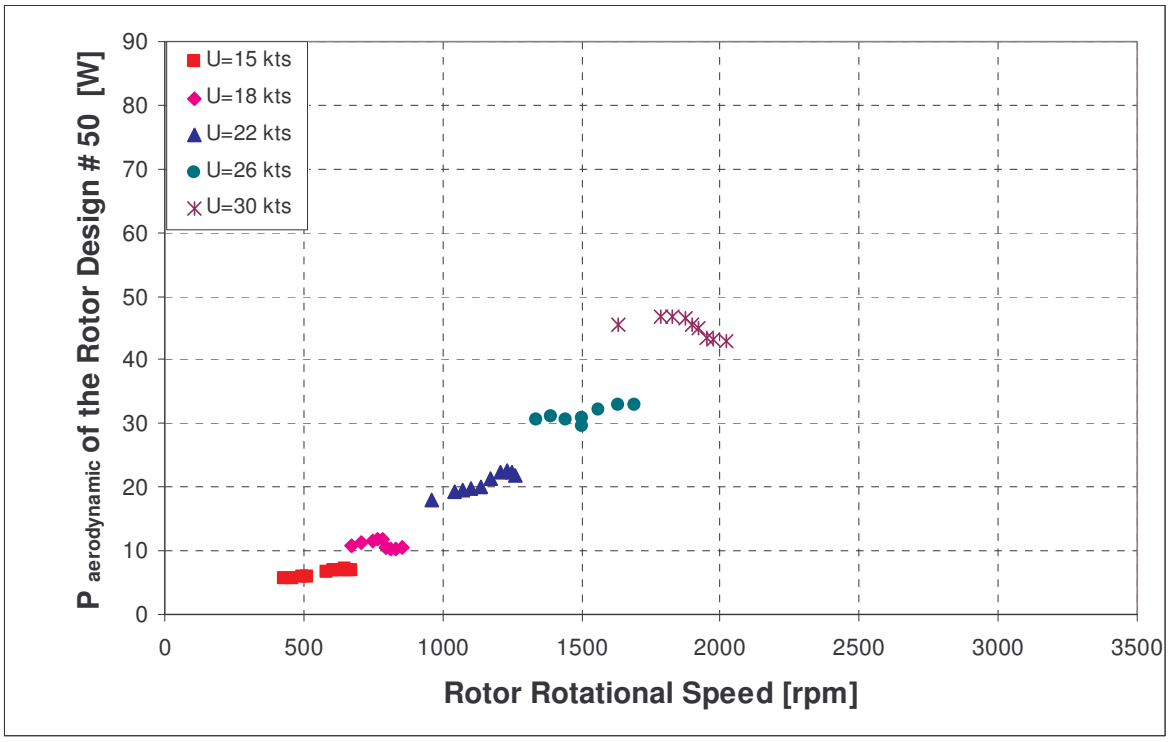

Figure 4.23 Aerodynamic Power of Rotor Design #50

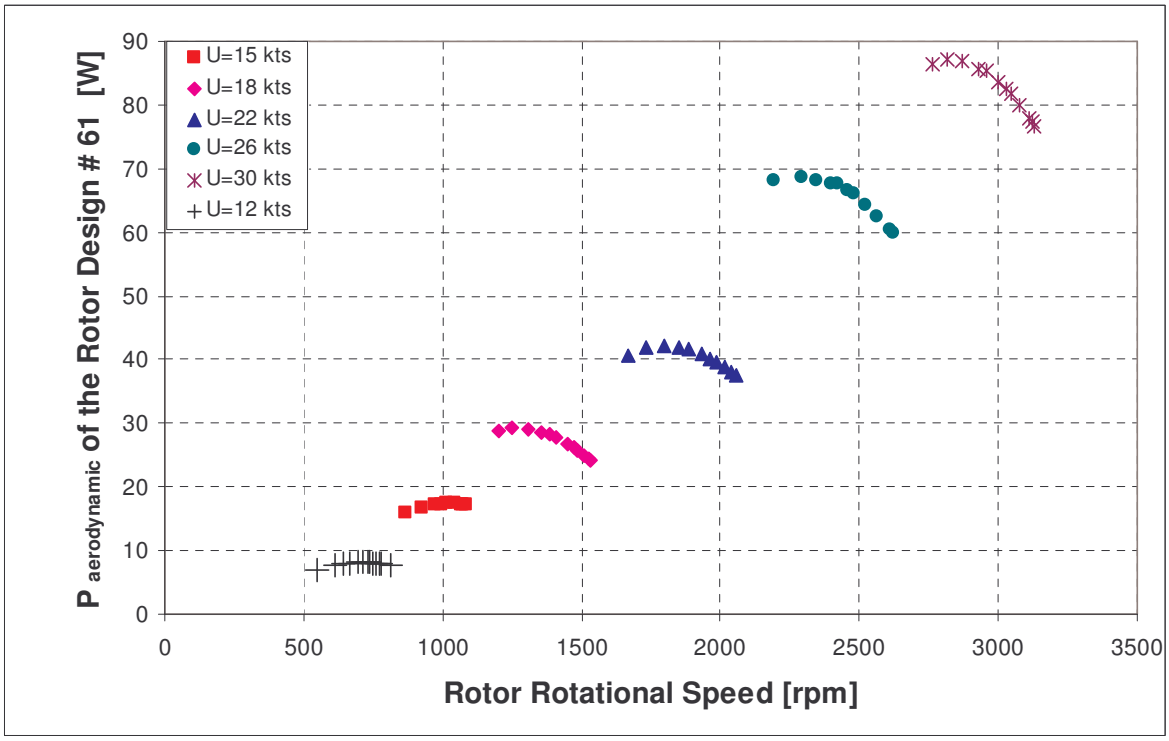

Figure 4.24 Aerodynamic Power of Rotor Design #61

From Figure 4.20 through Figure 4.24 it is found that the generated $P_{aerodynamic}$ of Rotor Design #61, at a given wind speed, on average is a factor of two higher compared to the other four Hi-Q rotors Design #2, 26, 38 and 50.

The maximum attainable $P_{aerodynamic}$ of the 5 tested Hi-Q rotors is summarized in Table 4.4 through Table 4.6 and is graphically illustrated in Figure 4.25.

Table 4.4 The Maximum Attainable $P_{aerodynamic}$ of Five Tested Rotors

Rotor Design Number	Maximum Attainable $P_{aerodynamic}$ [W]				
	U = 15 kts	U = 18 kts	U = 22 kts	U = 26 kts	U = 30 kts
2	3.7	9.1	20.5	30.0	51.8
26	6.6	12.1	22.0	35.2	48.0
38	7.3	12.2	21.2	31.2	43.9
50	7.1	11.8	22.6	33.0	46.8
61	17.4	29.2	42.1	68.5	87.1

Table 4.5 Rotational Speed Corresponding to Maximum Attainable $P_{aerodynamic}$

Rotor Design Number	RPM @ Maximum Attainable $P_{aerodynamic}$				
	U = 15 kts	U = 18 kts	U = 22 kts	U = 26 kts	U = 30 kts
2	469	935	1415	1508	2000
26	676	938	1200	1596	1852
38	617	750	1181	1293	1724
50	647	781	1230	1630	1786
61	1014	1250	1796	2290	2817

Table 4.6 Rotor Tip Speed Ratio Corresponding to Maximum Attainable $P_{aerodynamic}$

Rotor Design Number	Tip Speed Ratio, λ, @ Maximum Attainable $P_{aerodynamic}$				
	U = 15 kts	U = 18 kts	U = 22 kts	U = 26 kts	U = 30 kts
2	1.29	2.15	2.66	2.40	2.76
26	1.86	2.15	2.26	2.54	2.55
38	1.70	1.72	2.22	2.06	2.38
50	1.78	1.80	2.31	2.59	2.46
61	2.79	2.87	3.38	3.64	3.88

The rotor tip speed ratio is defined as:

$$\lambda = \frac{R_{rotor}\omega}{U} \qquad (3)$$

where: ω is the rotor rotational speed [rad/s]

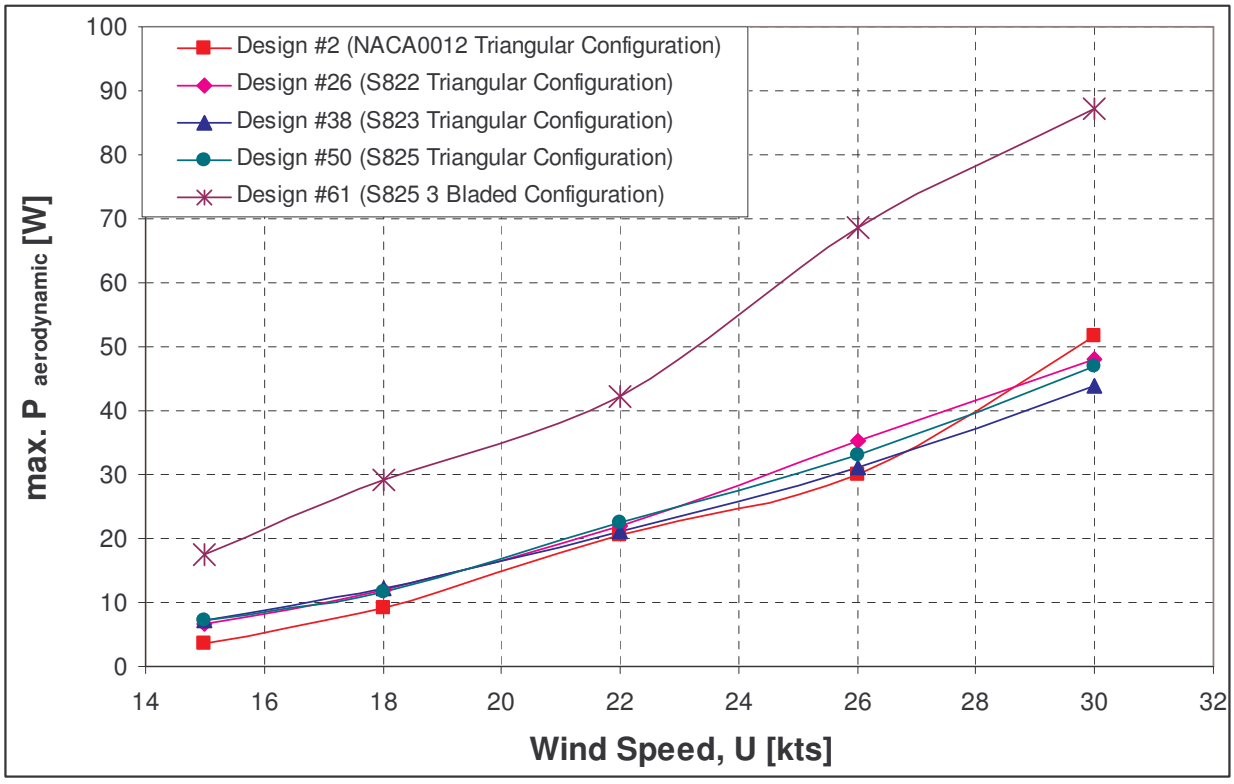

Figure 4.25 The Maximum Attainable $P_{aerodynamic}$ of Five Tested Rotors

From Table 4.4 through Table 4.6 and Figure 4.25, it is obvious that the aerodynamic performance of Rotor Design #61 exceeds the other four Hi-Q rotors. One of the reasons of its (relatively) higher aerodynamic performance is due to its higher rotor rotational speed at any given wind speed. At a wind speed of 22 kts, the rotational speed of the other four Hi-Q rotors ranges from 900–1,500 rpm, while the rotational speed of Rotor Design #61 ranges from 1,650–2,050 rpm. On average this is about 50% higher.

The definition of the rotor aerodynamic power is as follows:

$P_{aerodynamic} = \tau_{aerodynamic}\omega$

Equation 4 implies the importance of having a high rotor rotational speed, when it comes to maximizing power generation. The notion is supported by the results shown in Table 4.5. At various wind speeds, Rotor Design #61 has the highest rotor rotational speed corresponding to the maximum $P_{aerodynamic}$.

4.3 Aerodynamic Performance of Wetzel HAWT Rotor

In this section, the results of the wind tunnel testing on the Wetzel HAWT rotor, designated as Rotor KW, are presented. Figure 4.26 shows the Rotor KW.

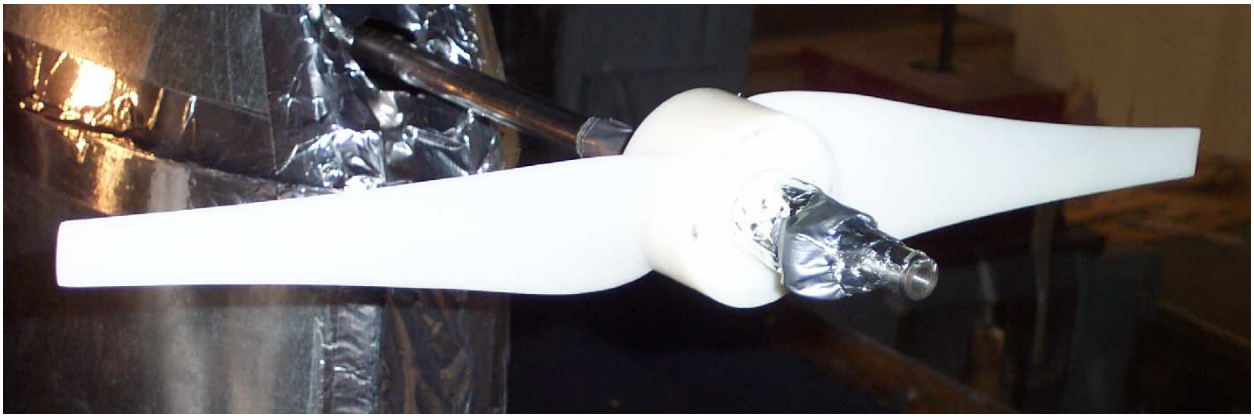

Figure 4.26 Rotor KW

Figure 4.20 through Figure 4.24 show that the minimum sustainable wind speed of the 5 Hi-Q rotors ranges from 12–15 kts. However, a wind speed of 49 kts is required to start turning Rotor KW and the minimum sustainable wind speed of Rotor KW is around 45 kts.

A total of 3 different wind speeds are covered: 45, 50 and 55 kts. Results of the wind tunnel testing of Rotor KW are illustrated in Figure 4.27.

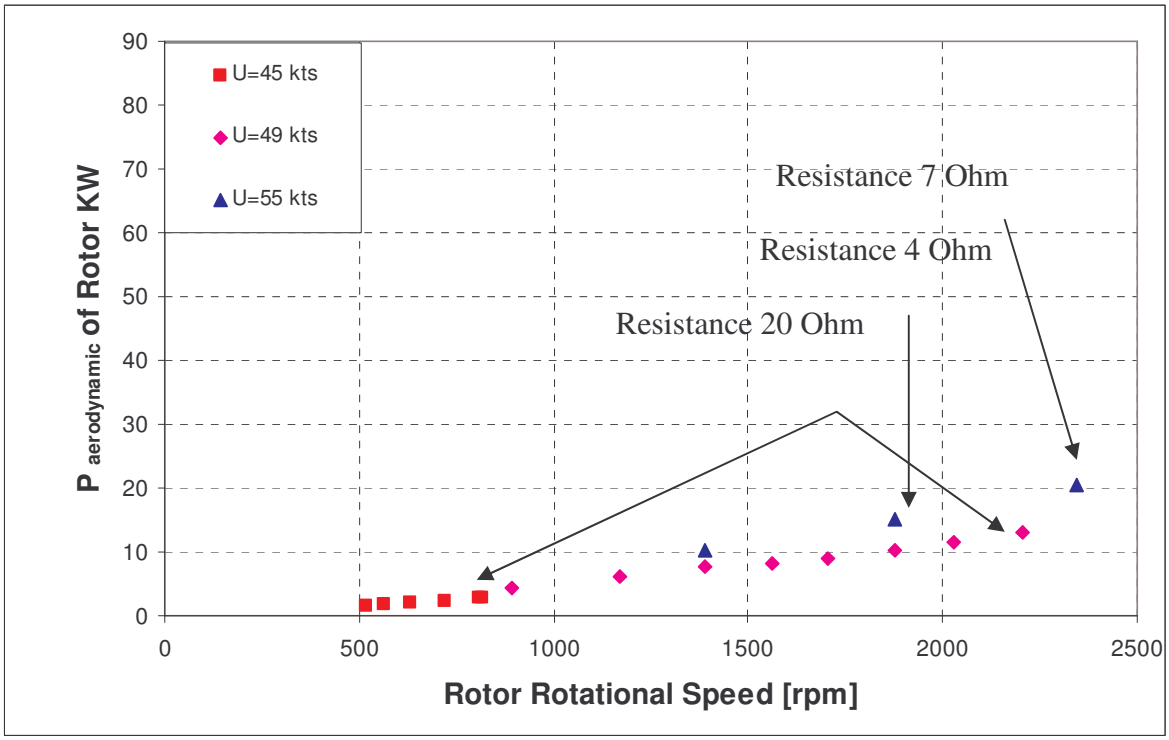

Figure 4.27 Aerodynamic Power of Rotor KW

Figure 4.27 shows that, at wind speeds of 45 kts and 49 kts, the available data points are not enough in identifying the maximum attainable $P_{aerodynamic}$. Reason is as follows:

The primary device controlling the rotor rotational speed is a resistor bank. The resistor bank is designed to cover a resistance range of 1.4–20 Ohm at a given wind speed, a higher resistance setting results in a higher rotor rotational speed. Prior to the beginning of the testing of Rotor KW, based on the wind tunnel results of the 5 tested Hi-Q rotors, it is found that the above resistance range is adequate in identifying the maximum attainable $P_{aerodynamic}$, at wind speed ranges from 15–30 kts.

At a wind speed of 55 kts three data points are taken and the last data point corresponds to a resistance setting of 7 Ohm. The decision to not increase the resistance setting any higher is due to safety considerations. The rotor rotational speed builds up very rapidly. It was thought that the rotor is not structurally sound enough to exceed 2,500 rpm.

The maximum attainable $P_{aerodynamic}$ of Rotor KW, is expected to be at a wind speed higher than 55 kts, outside the scope of the Hi-Q rotor tests. As a result, the aerodynamic performance of

Rotor Design #61, which has the best aerodynamic performance among the 5 tested Hi-Q rotors, instead, is compared to the published aerodynamic performance of Bergey's XL.1 HAWT rotor.

4.4 Performance Comparison between Rotor Design #61 and Bergey XL.1 HAWT rotor

The technical specification of Bergey XL.1 rotor is shown in Figure 4.28 and Figure 4.29.

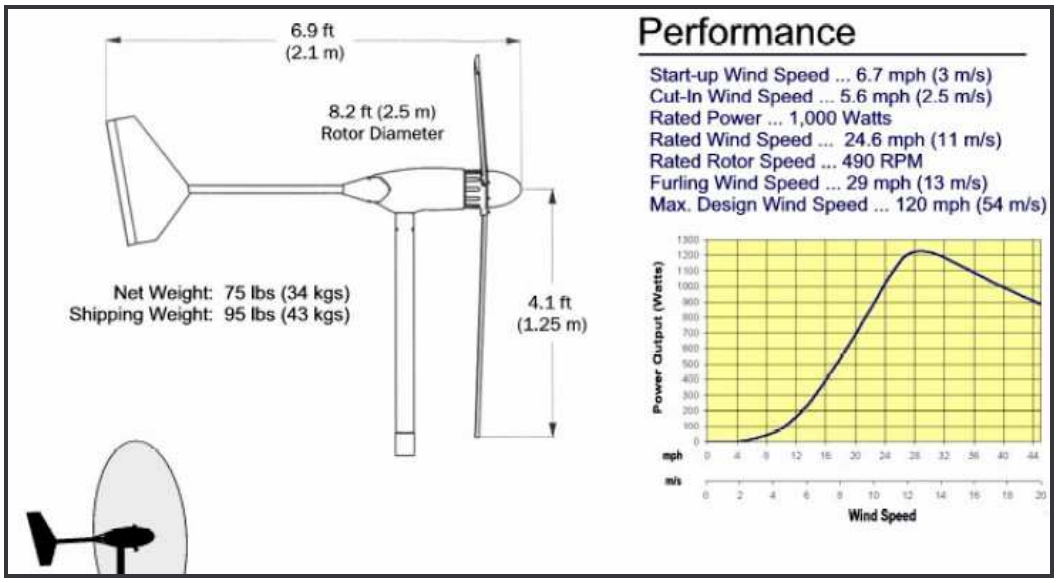

Figure 4.28 Published Technical Specification of Bergey XL.1 HAWT (Reference 2)

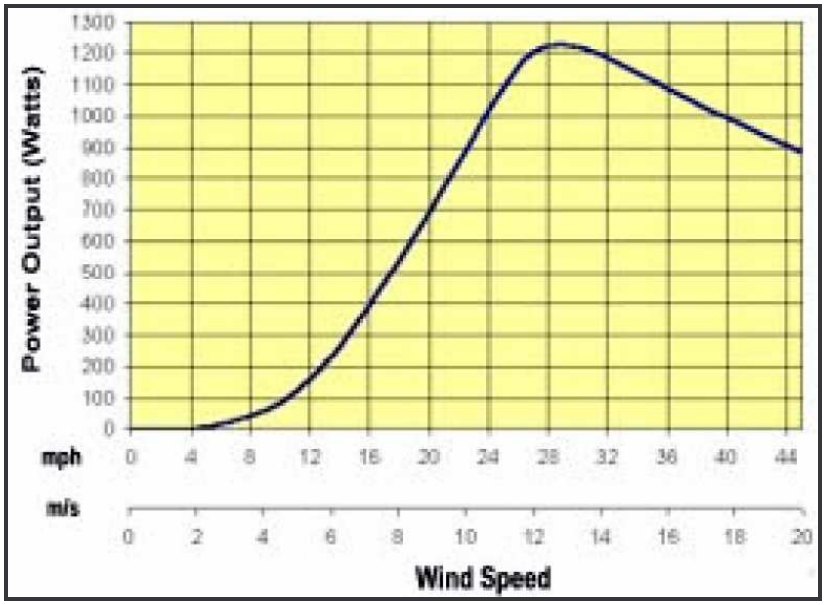

Figure 4.29 Published Technical Specification of Bergey XL.1 HAWT (Reference 2)

The power output performance of Bergey XL.1, shown in Figure 4.29, is digitized and its corresponding power coefficient, as function of wind speed is summarized in Table 4.7.

To compare the rotor performance of Bergey XL.1 HAWT to Rotor Design #61, which do not share a common rotor diameter, the dimensional power output term, expressed in Watts, needs to be converted into a non-dimensional power coefficient, denoted as $C_{p.}$

The rotor power coefficient, C_p, is defined as:

$$C_p = \frac{P}{\frac{1}{2}\rho\pi R_{rotor}{}^2 U^3}$$

Table 4.7 Performance of Bergey XL.1

U [m/s]	U [kts]	P [W]	RPM [rpm]	λ	0.5 ρ AU^3 [W]	C_p
2.24	4.35	8			34	0.236
2.68	5.20	19			57	0.323
3.55	6.90	43			134	0.320
4.23	8.22	71			227	0.311
4.94	9.60	126			361	0.349
5.63	10.95	196			536	0.366
6.18	12.01	259			707	0.366
6.72	13.07	342			911	0.375
7.73	15.03	498			1385	0.360
8.74	16.99	670			2000	0.335
9.50	18.47	804			2569	0.313
10.18	19.79	929			3160	0.294
10.81	21.02	1043			3785	0.276
11.21	21.79	1104	490 [A]	5.72	4220	0.262
11.62	22.60	1168			4703	0.248
12.11	23.53	1212			5313	0.228
12.56	24.42	1229			5936	0.207
12.78	24.85	1233			6252	0.197
13.29	25.83	1222			7029	0.174
13.84	26.91	1206			7942	0.152
14.49	28.17	1172			9112	0.129

A: Only the rated RPM of 490 is published by Bergey Wind Power

Table 4.7 (Contd.) Performance of Bergey XL.1

U [m/s]	U [kts]	P [W]	RPM [rpm]	λ	0.5 ρ AU^3 [W]	C_p
15.39	29.92	1126			10924	0.103
16.47	32.02	1065			13385	0.080
17.25	33.52	1021			15359	0.066
18.25	35.48	974			18202	0.053
19.05	37.03	930			20703	0.045
19.94	38.75	890			23726	0.038

From Table 4.7 it can be determined that at a rated wind speed of 11.21 m/s (or 21.79 kts), the rated power coefficient of Bergey XL.1 is 0.262. A rated rotor rotational speed of 490 rpm translates to a rated rotor tip speed ratio of 5.72. The power output performance of Bergey XL.1 HAWT refers to the actual power output, after all the losses are accounted for. The aerodynamic power of Rotor Design #61 refers to the "pure" aerodynamic power output of just the rotor. According to Reference 3, an overall mechanical and electrical efficiency of 90% on the generator can be assumed. Based on this above assumption, the rated aerodynamic power coefficient of Bergey XL.1 rotor can be calculated as 0.262/0.9 = 0.291.

Based on the results summarized in Table 4.4 through Table 4.6, the power coefficient vs. rotor tip speed ratio, of the 5 tested Hi-Q rotors, at various wind speeds, is plotted in Figure 4.30 through Figure 4.34.

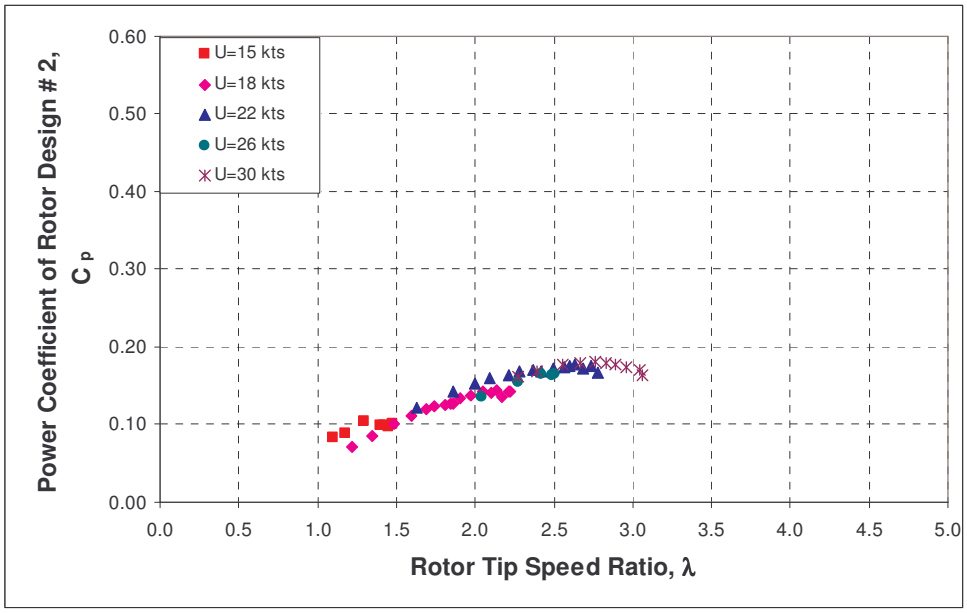

Figure 4.30 Power Coefficient of Rotor Design #2

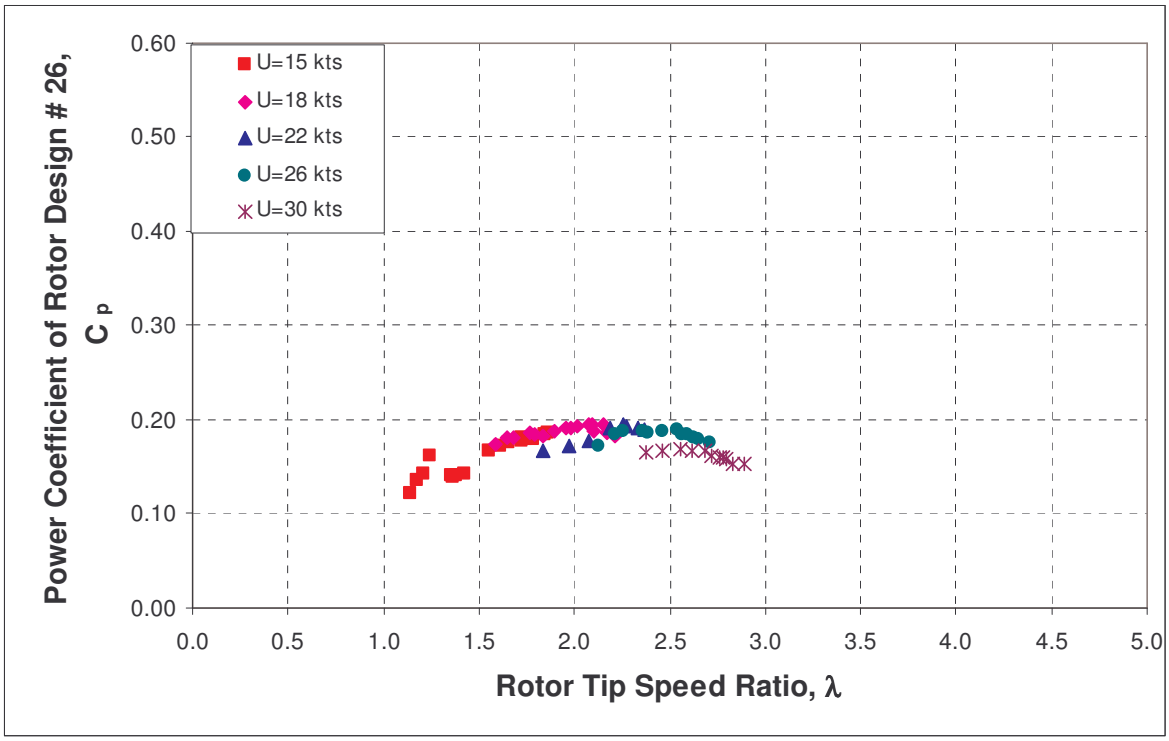

Figure 4.31 Power Coefficient of Rotor Design #26

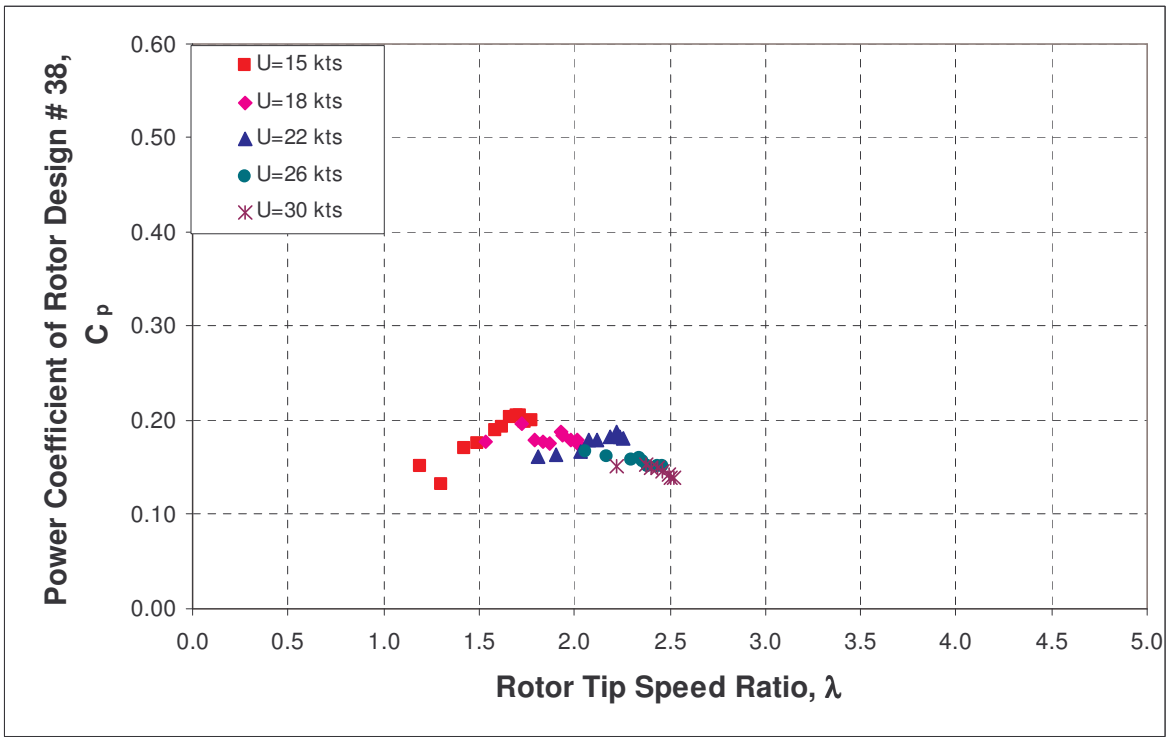

Figure 4.32 Power Coefficient of Rotor Design #38

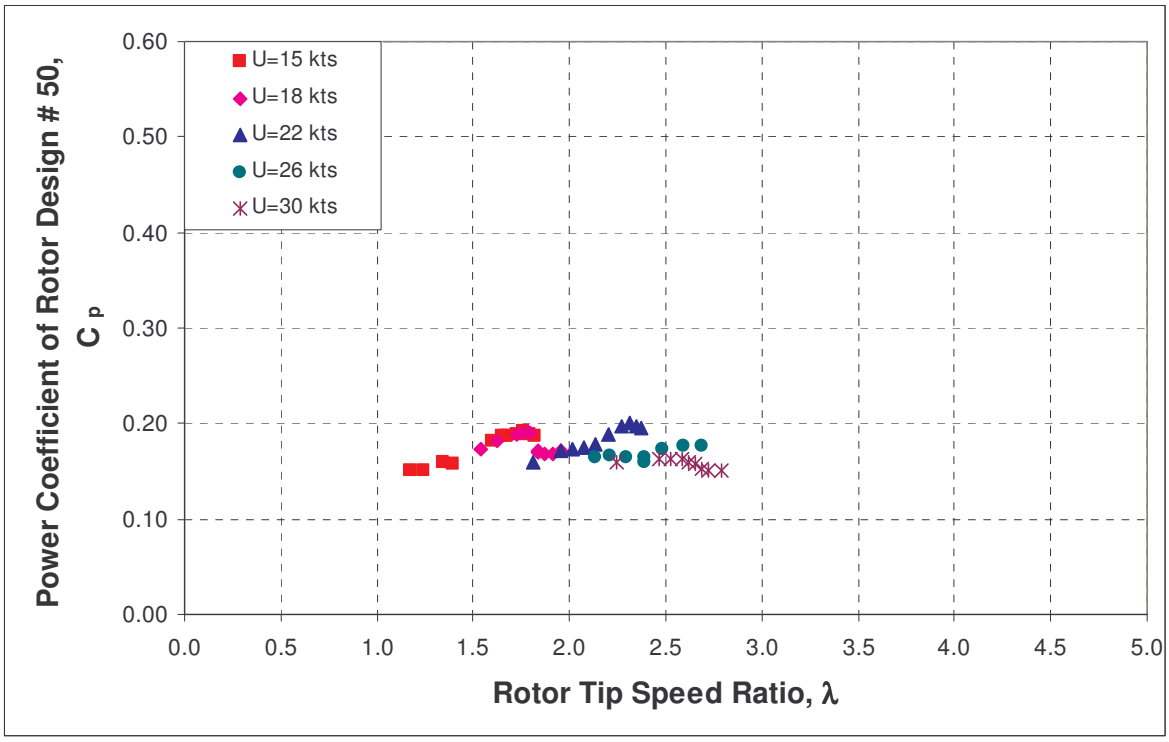

Figure 4.33 Power Coefficient of Rotor Design #50

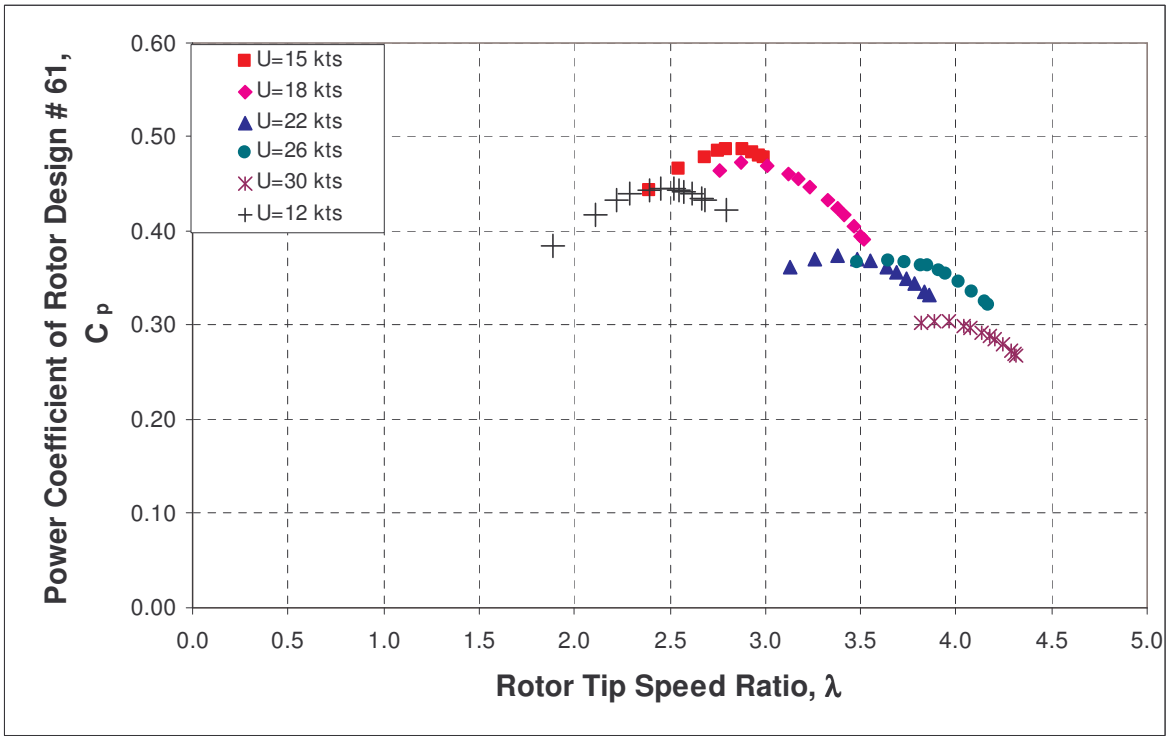

Figure 4.34 Power Coefficient of Rotor Design #61

From Table 4.4 through Table 4.6, the maximum power coefficient of the 5 tested Hi-Q rotors, at various wind speeds, is calculated. Results are summarized in Table 4.8.

Table 4.8 Maximum Attainable Power Coefficient of 5 tested Hi-Q Rotors

Rotor Design Number	Maximum Attainable C_P				
	U = 15 kts	U = 18 kts	U = 22 kts	U = 26 kts	U = 30 kts
2	0.104	0.147	0.182	0.161	0.181
26	0.185	0.195	0.195	0.189	0.168
38	0.205	0.197	0.188	0.168	0.153
50	0.199	0.191	0.200	0.177	0.164
61	0.487	0.473	0.373	0.368	0.305

The aerodynamic performance of Bergey XL.1 rotor, taken into account an overall mechanical and electrical loss of 10%, as a function of wind speed, is plotted in Figure 4.35.

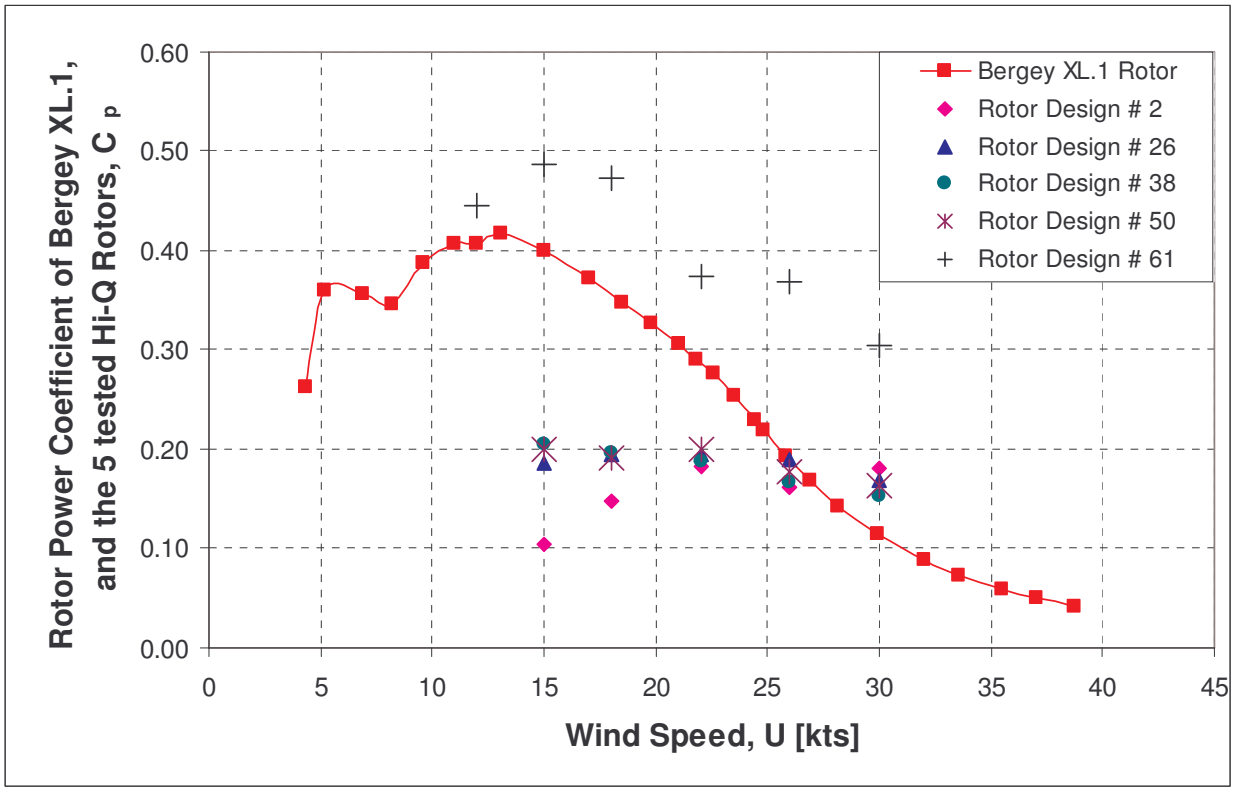

Figure 4.35 Rotor Power Coefficient of Bergey XL. and 1 HAWT 5 Hi-Q Rotors

From Figure 4.35, it is observed that over the range of tested wind speeds (12 kts – 30 kts), the rotor power coefficient of Rotor Design # 61 is higher than Bergey XL.1 HAWT.

4.5 Startup Wind Speed of 5 tested Hi-Q Rotors

Based on Figure 4.28, the startup wind speed of Bergey XL.1 HAWT equals 5.8 kts. Rotor Design #61 has a start up wind speed of 13 kts and a minimum sustainable wind speed of 12 kts. The other four Hi-Q rotors have a relatively higher start up speed of 16 kts and their minimum sustainable wind speeds are 15 kts. The startup speed is dependent on the generator and bearing system used.

4.6 Conclusions

- A total of 7 rotors are tested in the KU wind tunnel.

- The endplate is needed so that the Mobius Strip Theory is not violated. It is found that an increase in the size of the endplate reduces the aerodynamic performance of the rotors. To minimize the power penalty, the endplate must be kept as small as possible.

- The aerodynamic performance of Rotor Design #61 exceeds the other four Hi-Q rotors: Designs #2, 26, 38 and 50, by an average factor of two.

- Rotor KW is found to have a high start up wind speed of 49 kts. Its minimum sustainable wind speed equals 45 kts.

- The rotor aerodynamic performance of the 5 tested Hi-Q rotors is compared with the Bergey XL.1 HAWT. Results show that over the range of tested wind speeds (12–30 kts), the rotor power coefficient of Rotor Design #61 is higher than the Bergey XL.1 HAWT.

5. Wind Tunnel Model and Setup

5.1 Model Details

Three models are considered for the wind tunnel tests: Design 61 from Phase I, Conventional HAWT Bergey XL.1 and the conventional HAWT used in Phase I. All the three models are designed in modular fashion so as to test various configurations with varying number of blades. All the models have a diameter of 16 inches. Figure 5.1 through Figure 5.3 show the models described.

Figure 5.1 Modular Design 61 from Phase I

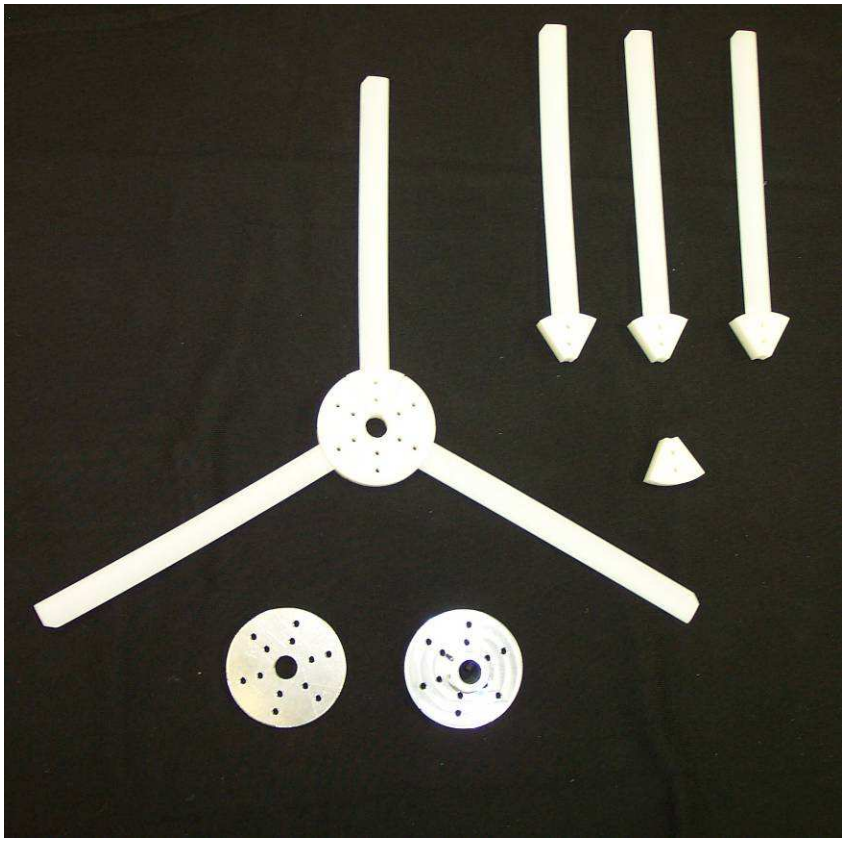

Figure 5.2 Modular Conventional HAWT Bergey XL.1(Scaled)

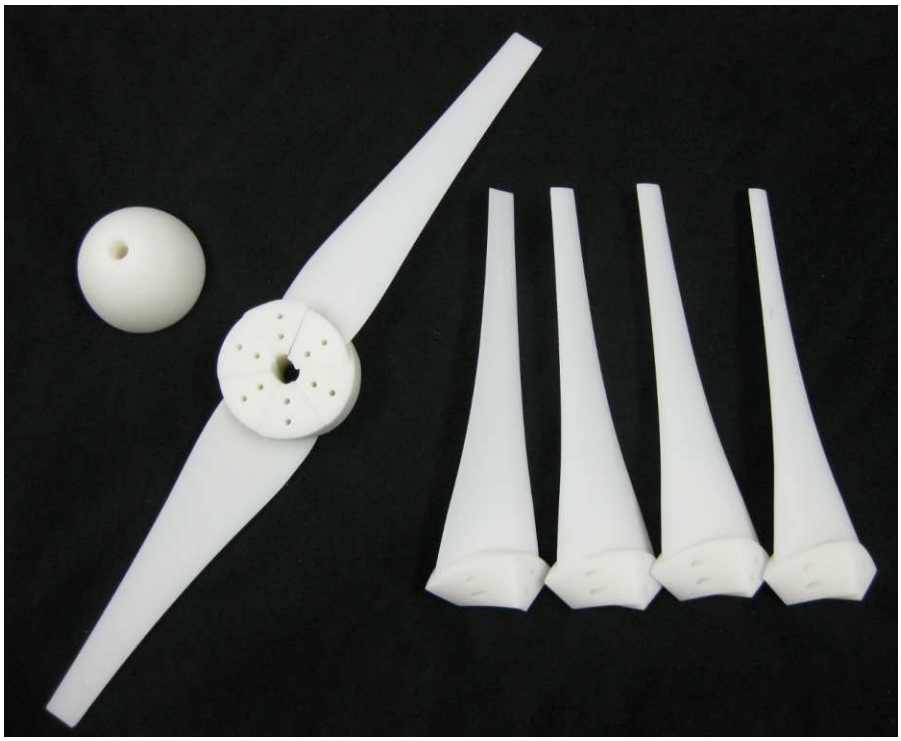

Figure 5.3 Modular Conventional HAWT used in Phase I

5.2 Model Details

All the models are made using stereo lithography techniques (Reference 2). The models are made from a material called Accura 55 which has similar mechanical properties to ABS plastic. Typical properties of Accura 55 are as shown in Table 5.1 (Reference 2). The subscripts t and f stand for tension and flexure respectively, E is the modulus and σ is the stress.

Table 5.1 Accura 55 Properties

E_t [ksi]	460 - 490
σ_t [psi]	9,200 - 9,850
E_f [ksi]	390 - 470
σ_f [psi]	12,830 - 15,920

Design 61 is modularized to study the effects of the blades and the blade tips. It is proposed to run tests with and without the blade tips to see the difference in performance.

The full scale conventional HAWT Bergey XL.1 with one of the blades attached to the hub is as shown in Figure 5.4.

Figure 5.4 Full Scale Conventional HAWT Bergey XL.1

Figure 5.5 shows the generator of the Bergey XL.1 which is built into the hub.

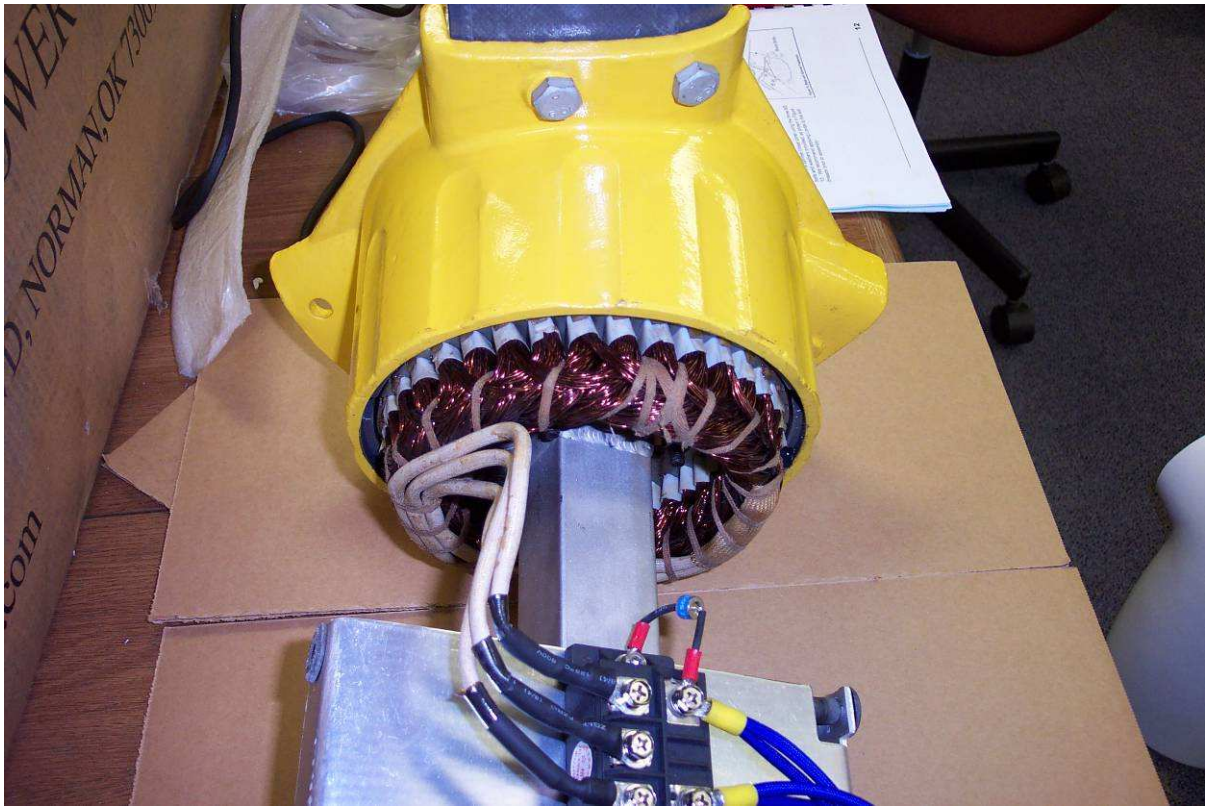

Figure 5.5 Conventional HAWT Bergey XL.1 Generator

A 3D CAD model of the full scale Bergey XL.1 is created using Reference 5. Figure 5.6 shows the parametric 3D CAD model.

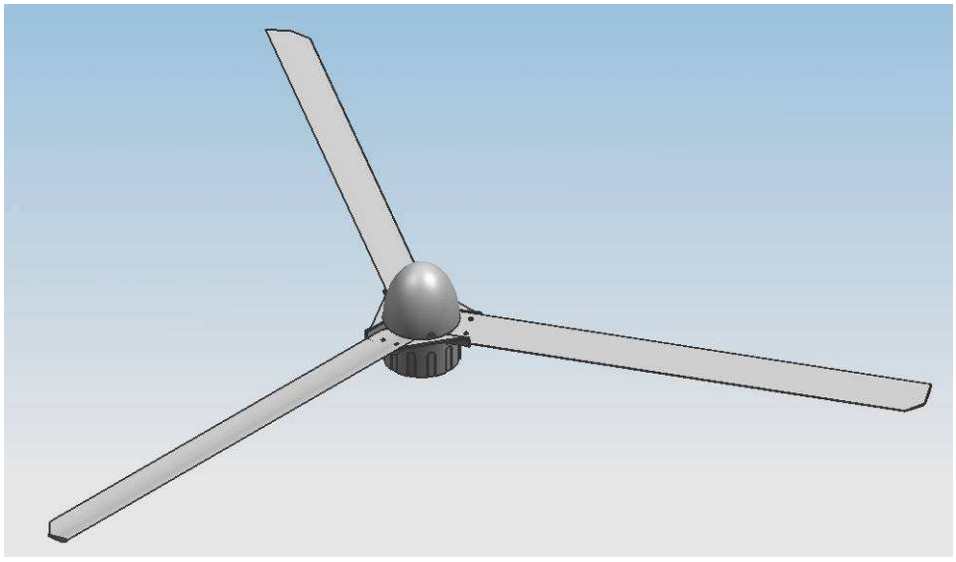

Figure 5.6 Parametric 3D CAD Model of the Bergey XL.1

Figure 5.7 shows one of the blades the Bergey XL.1.

Figure 5.7 Bergey XL.1 Blade

The conventional HAWT Bergey XL.1 is scaled down to the 16 inch diameter model. This caused the blades to lose a significant amount of stiffness. The blades are therefore coated with an alloy of Nickel to give them more stiffness.

5.3 Generator Calibration

The generator on the Bergey XL.1 has to be calibrated. The test stand to be used or this purpose is as shown in Figure 5.8. The test stand consisting of a torque sensor, RPM sensor, bearings, and flex couplers is mounted on an aluminum frame. The generator is connected to a resistor box. The resistance can be varied in the resistor box simulating load conditions. Figure 5.9 shows the resistor box used for the calibration. The voltage and current from the generator are measured and the torque and RPM are measured from the torque and RPM sensors respectively.

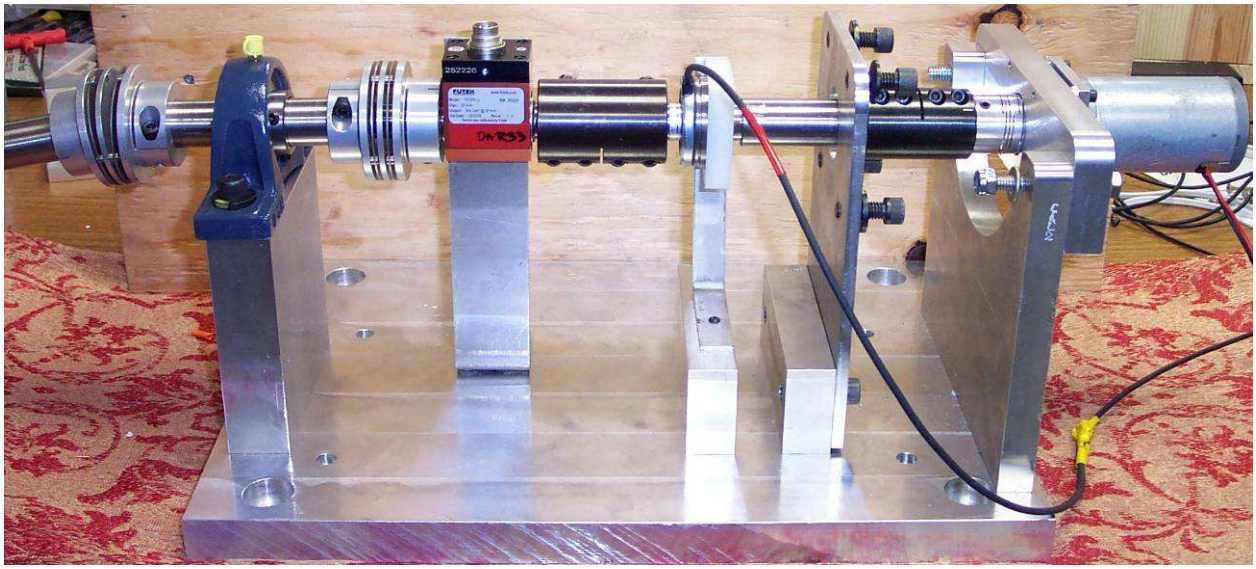

Figure 5.8 Generator Calibration Stand

Figure 5.9 Resistor Box

5.4 Wind Tunnel Testing

The models are to be tested in the open loop wind tunnel at the University of Kansas. The wind tunnel is as shown in Figure 5.10. The test stand is proposed to be set up upstream of the test section. A truss fixture is designed to be able to mount the models and the test stand in this section of the wind tunnel.

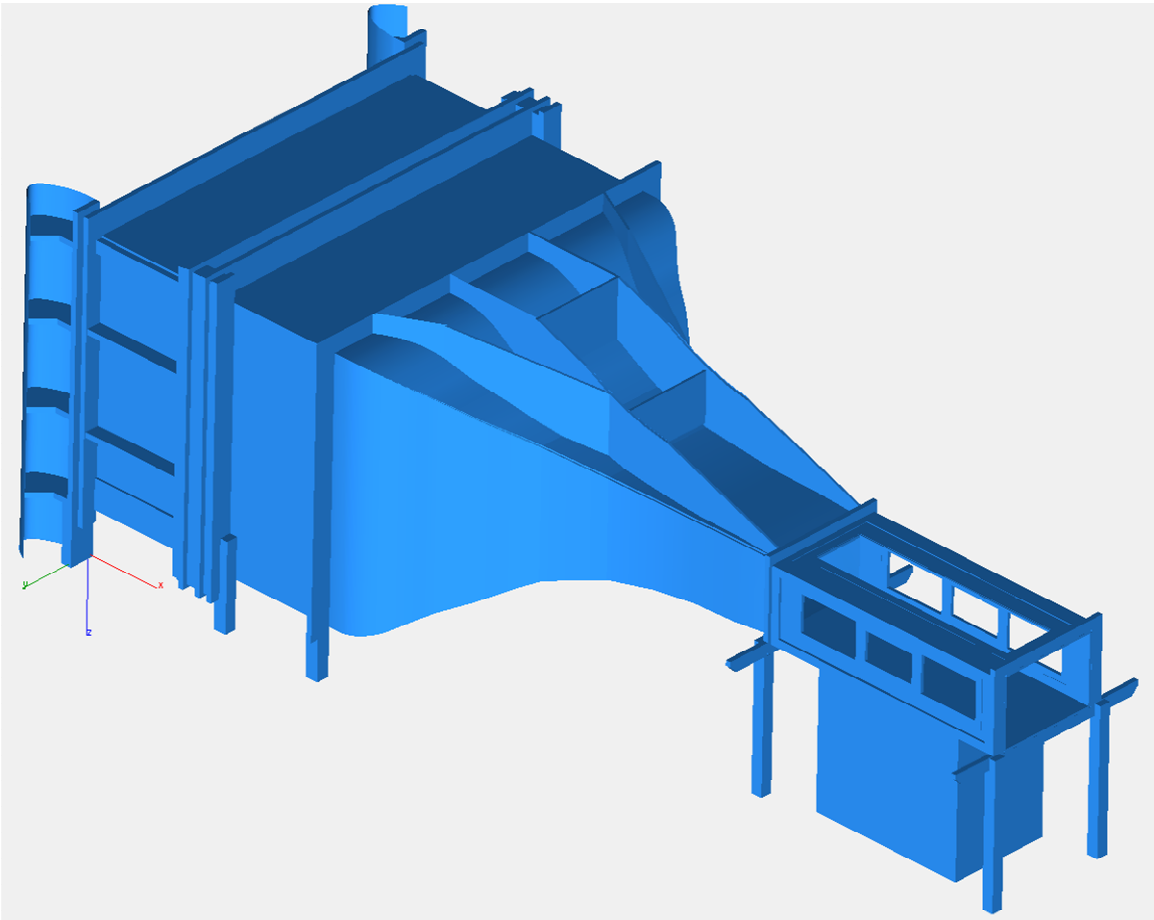

Figure 5.10 KU Small Wind Tunnel

6. Results of Hi-Q Phase II Wind Tunnel Testing

6.1 Wind Tunnel Models

A total of 22 wind turbine rotor model configurations, all having a diameter of 16 inches, are tested at the University of Kansas open loop wind tunnel in August and September of 2008. Results of the aerodynamic performance of the tested rotor configurations are presented in this memo.

The primary objective of the wind tunnel testing is to compare the aerodynamic performance among the tested rotors configurations, which include Hi-Q Design # 61, Hi-Q Design # 62, two horizontal axis wind turbine (HAWT) rotors, one of which is designed by Dr. Kyle Wetzel and the other is the Bergey XL.1 HAWT.

A summary of the geometric characteristics of the 22 tested wind turbine rotor model configurations is listed in Table 6.1. Figure 6.1 through Figure 6.4 show the wind turbine rotors described.

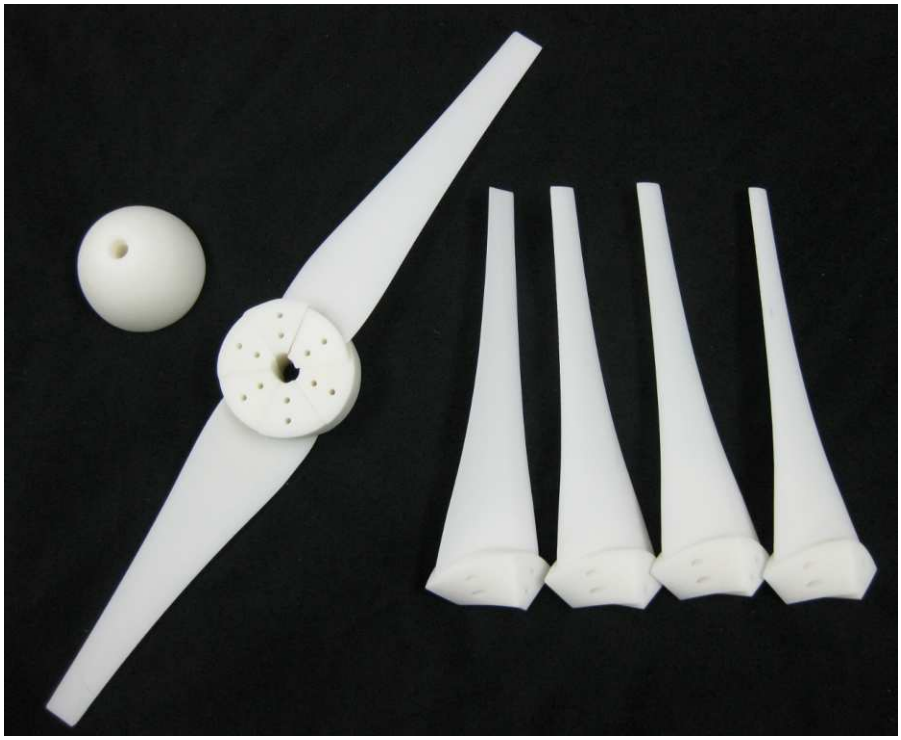

Figure 6.1 Modular Conventional HAWT: Wetzel Rotor

Figure 6.2 Modular Hi-Q Design # 61

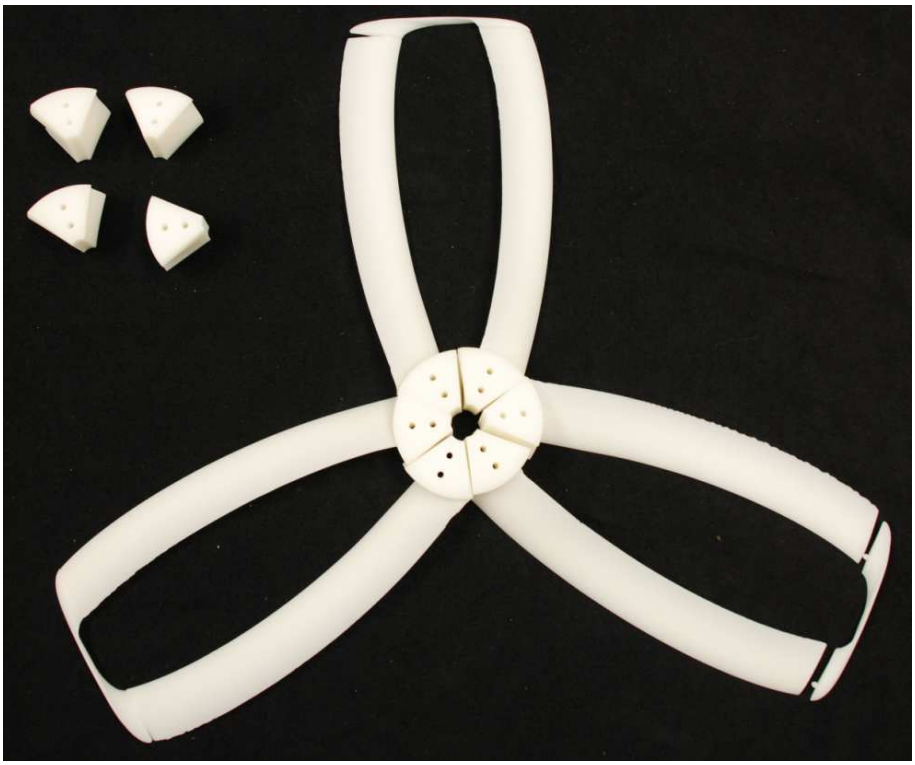

Figure 6.3 Modular Hi-Q Design # 62

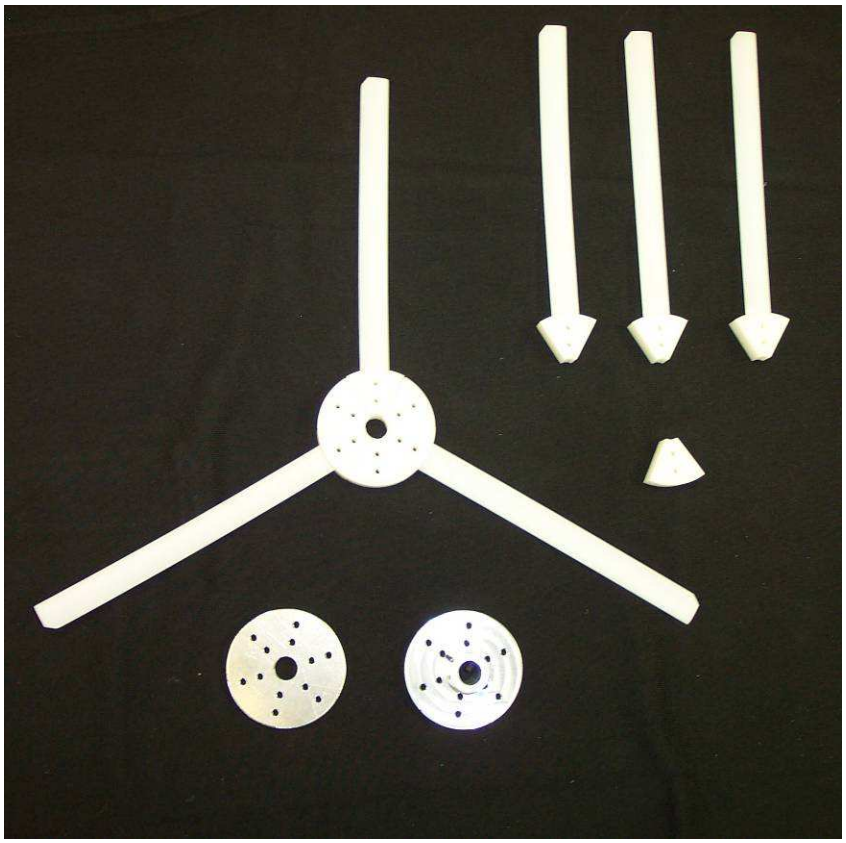

Figure 6.4 Modular Conventional HAWT: Bergey XL.1

Table 6.1 Geometric Characteristics of Tested Rotor Model Configuration

Model Configuration #	Rotor	Number of Blades	End Plates
1	Wetzel	2	N.A.
2	Wetzel	3	N.A.
3	Wetzel	6	N.A.
4	Hi-Q # 61 (Fwd)	2	OFF
5	Hi-Q # 61 (Fwd)	3	OFF
6	Hi-Q # 61 (Aft)	2	OFF
7	Hi-Q # 61 (Aft)	3	OFF
8	Hi-Q # 61 (Paired)	2	OFF
9	Hi-Q # 61 (Paired)	3	OFF
10	Hi-Q # 61 (Paired)	2	ON
11	Hi-Q # 61 (Paired)	3	ON
12	Hi-Q # 62 (Fwd)	2	OFF
13	Hi-Q # 62 (Fwd)	3	OFF
14	Hi-Q # 62 (Aft)	2	OFF
15	Hi-Q # 62 (Aft)	3	OFF
16	Hi-Q # 62 (Paired)	2	OFF
17	Hi-Q # 62 (Paired)	3	OFF
18	Hi-Q # 62 (Paired)	2	ON
19	Hi-Q # 62 (Paired)	3	ON
20	Bergey	2	N.A.
21	Bergey	3	N.A.
22	Bergey	6	N.A.

6.2 Wind Tunnel Testing Results

Case 1: Hi-Q Design # 61, 2-Bladed Pair, Endplates vs. No Endplates

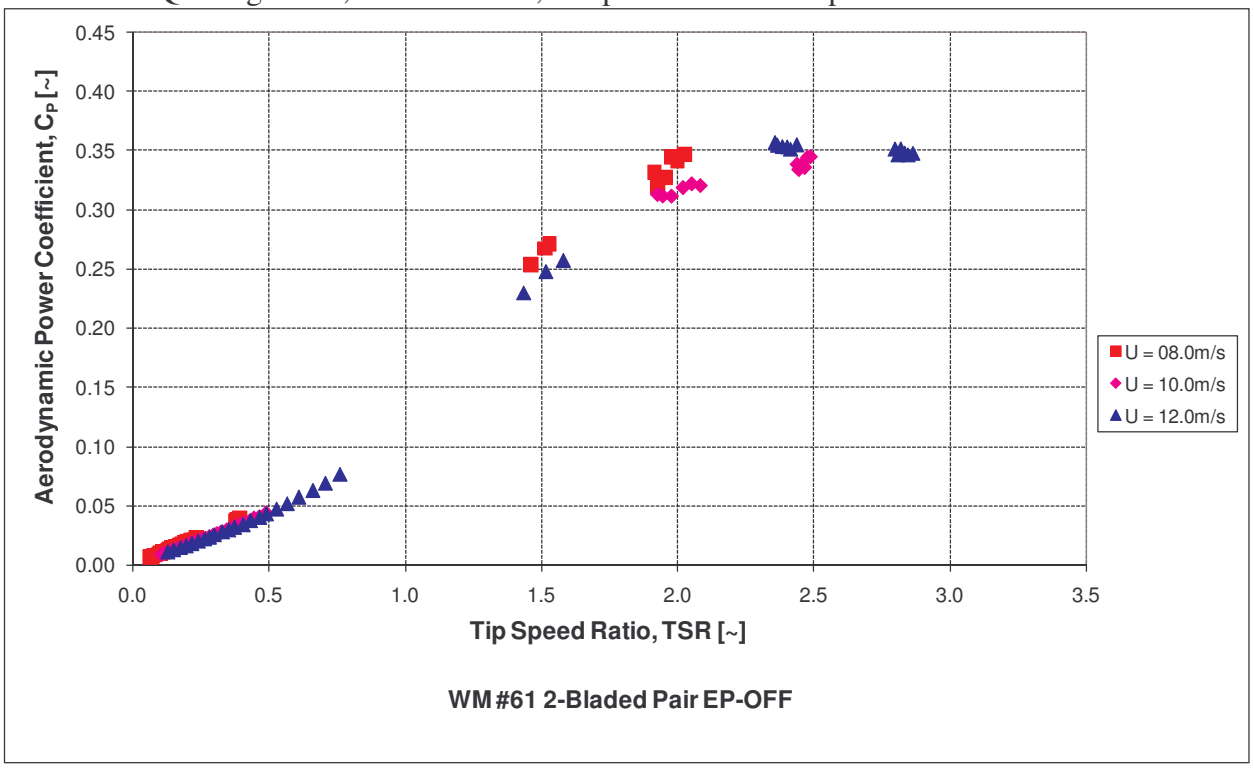

Figure 6.5 C_p of Hi-Q Design # 61 (2-Bladed Pair) with No Endplates

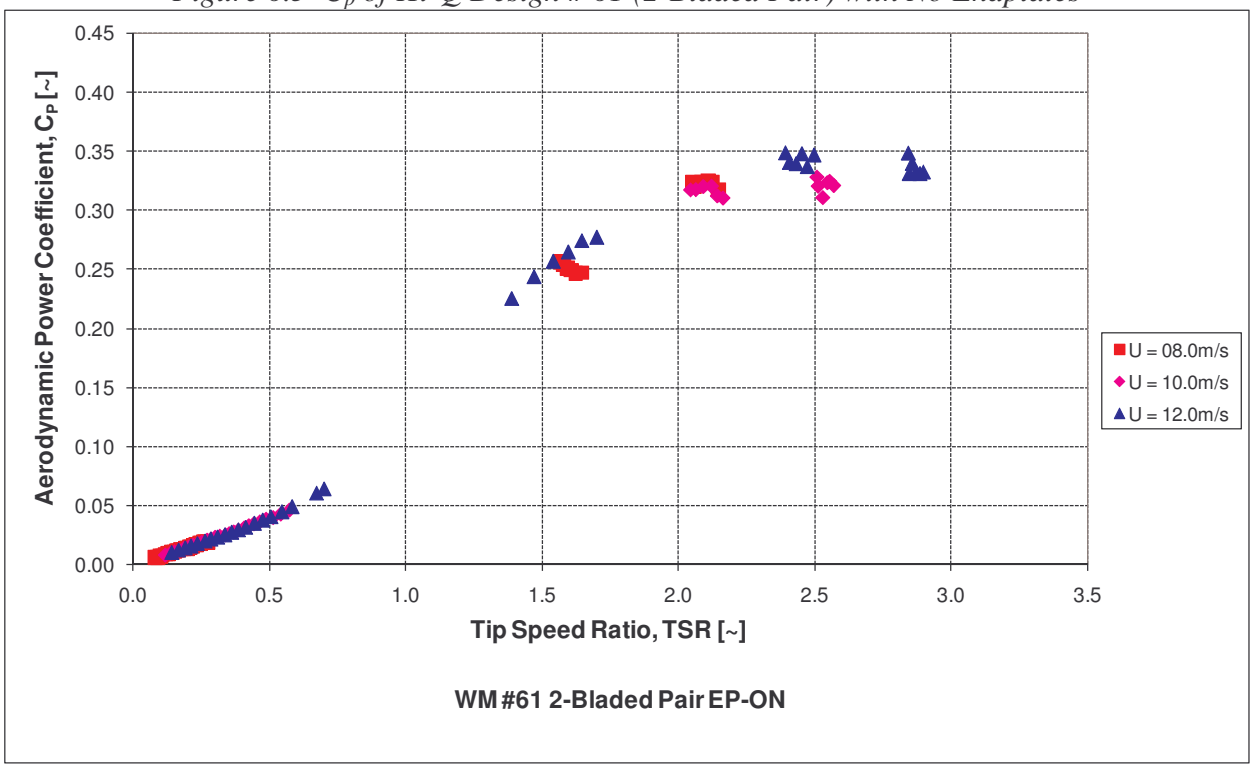

Figure 6.6 C_p of Hi-Q Design # 61 (2-Bladed Pair) with Endplates

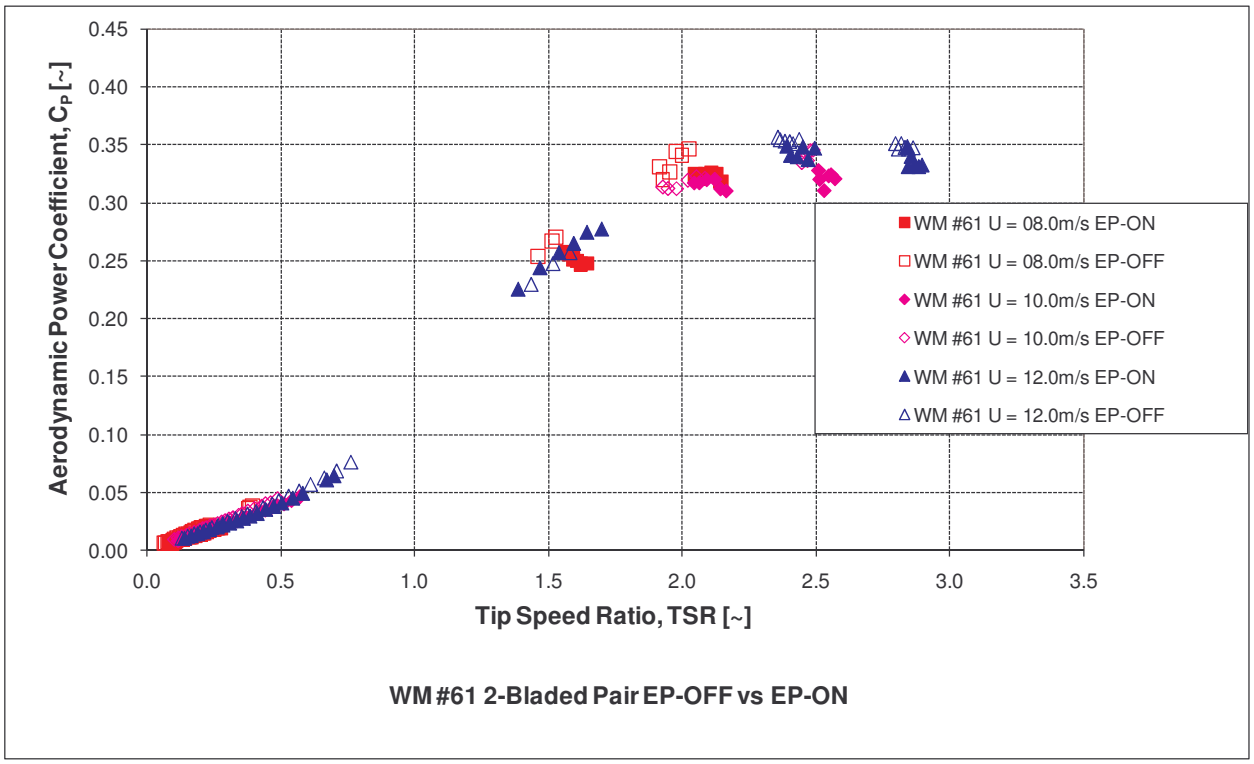

Figure 6.7 C_p of Hi-Q Design # 61 of 2-Bladed Pair (Endplates vs. no Endplates)

Case 2: Hi-Q Design # 61, 3-Bladed Pair, Endplates vs. No Endplates

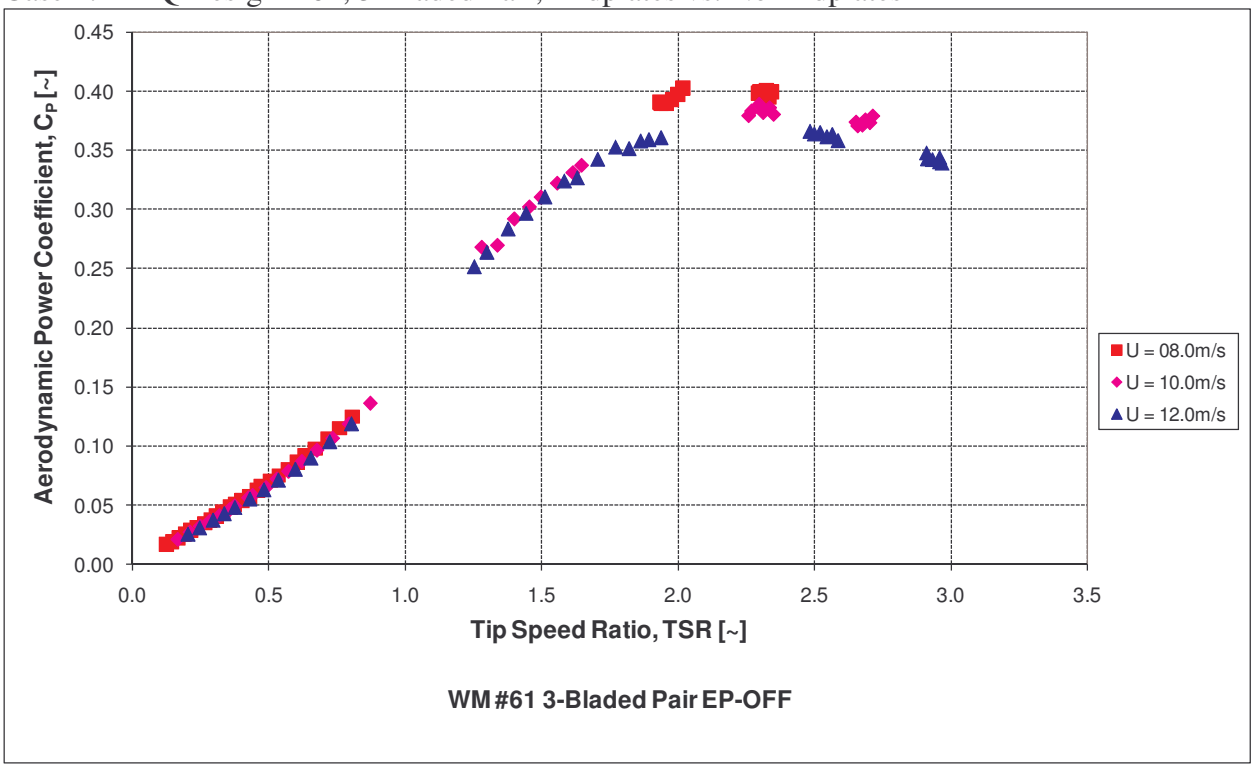

Figure 6.8 C_p of Hi-Q Design # 61 (3-Bladed Pair) with No Endplates

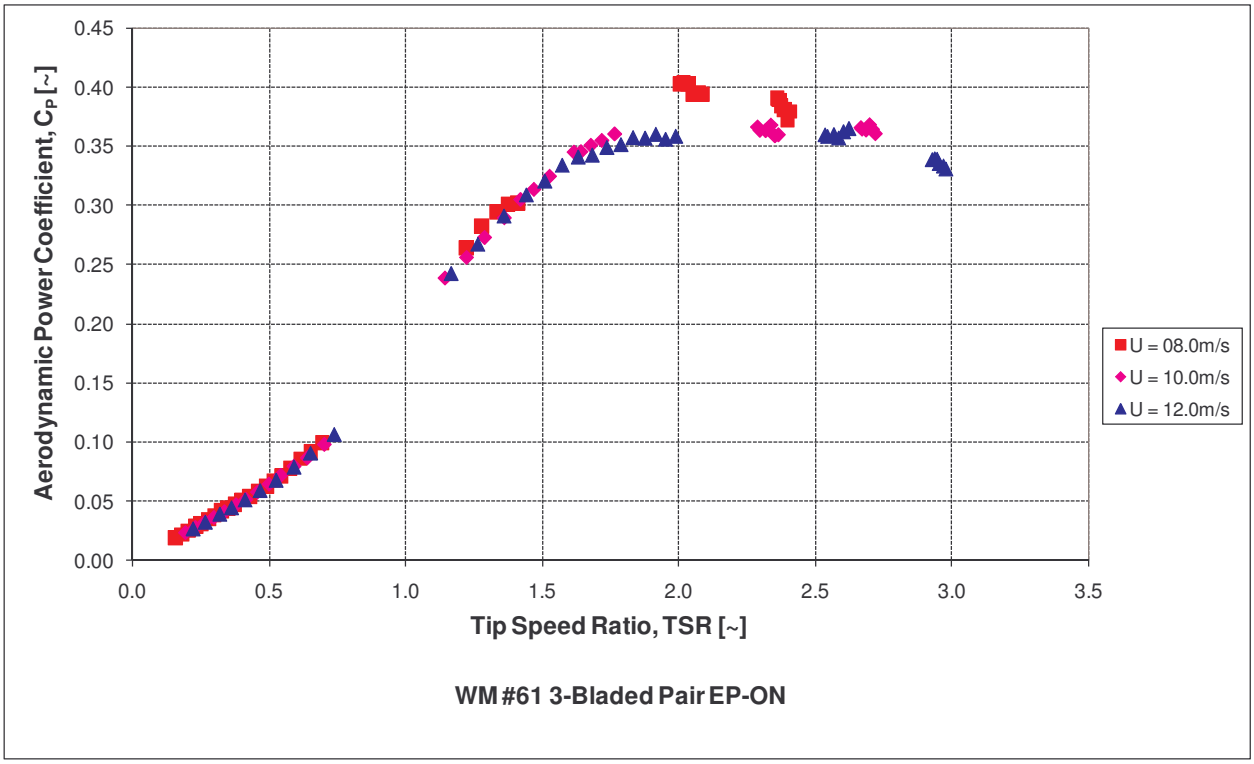

Figure 6.9 C_p of Hi-Q Design # 61 (3-Bladed Pair) with Endplates

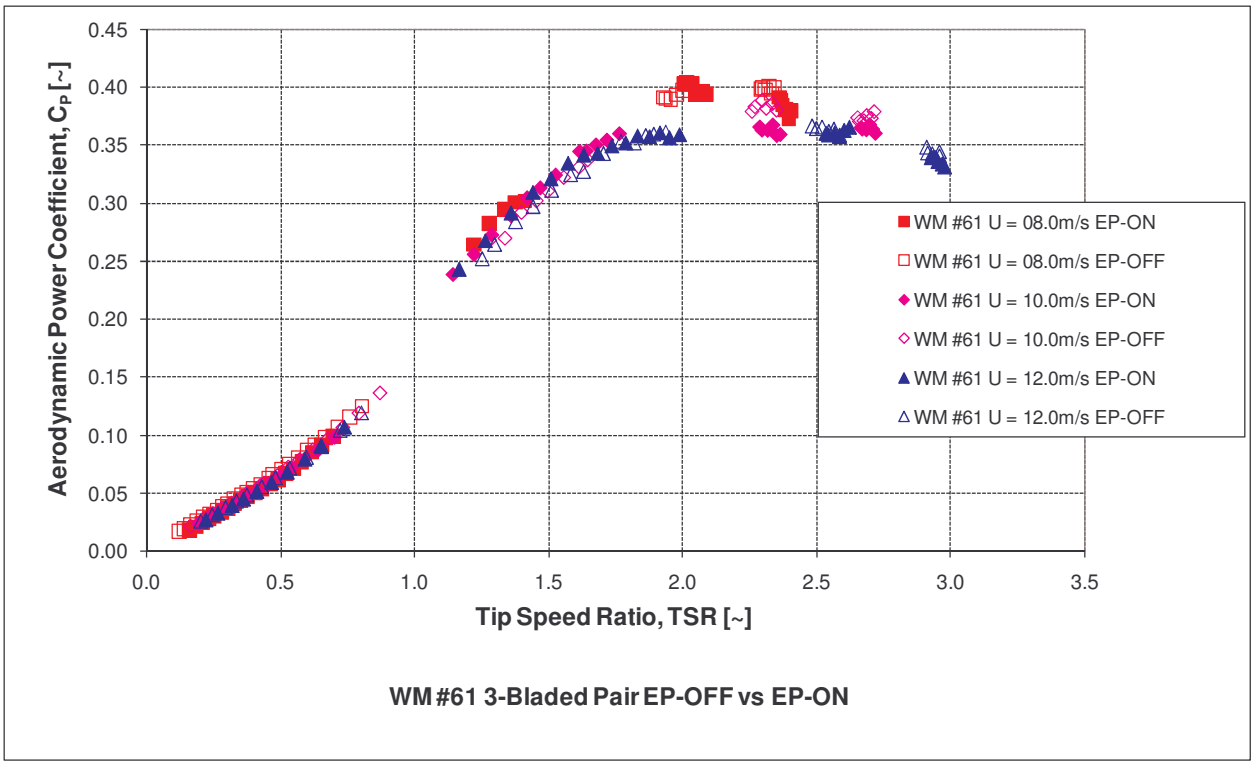

Figure 6.10 C_p of Hi-Q Design # 61 3-Bladed Pair (Endplates vs. no Endplates)

Case 3: Hi-Q Design # 61, with Endplates (2-Bladed Pair vs. 3-Bladed Pair)

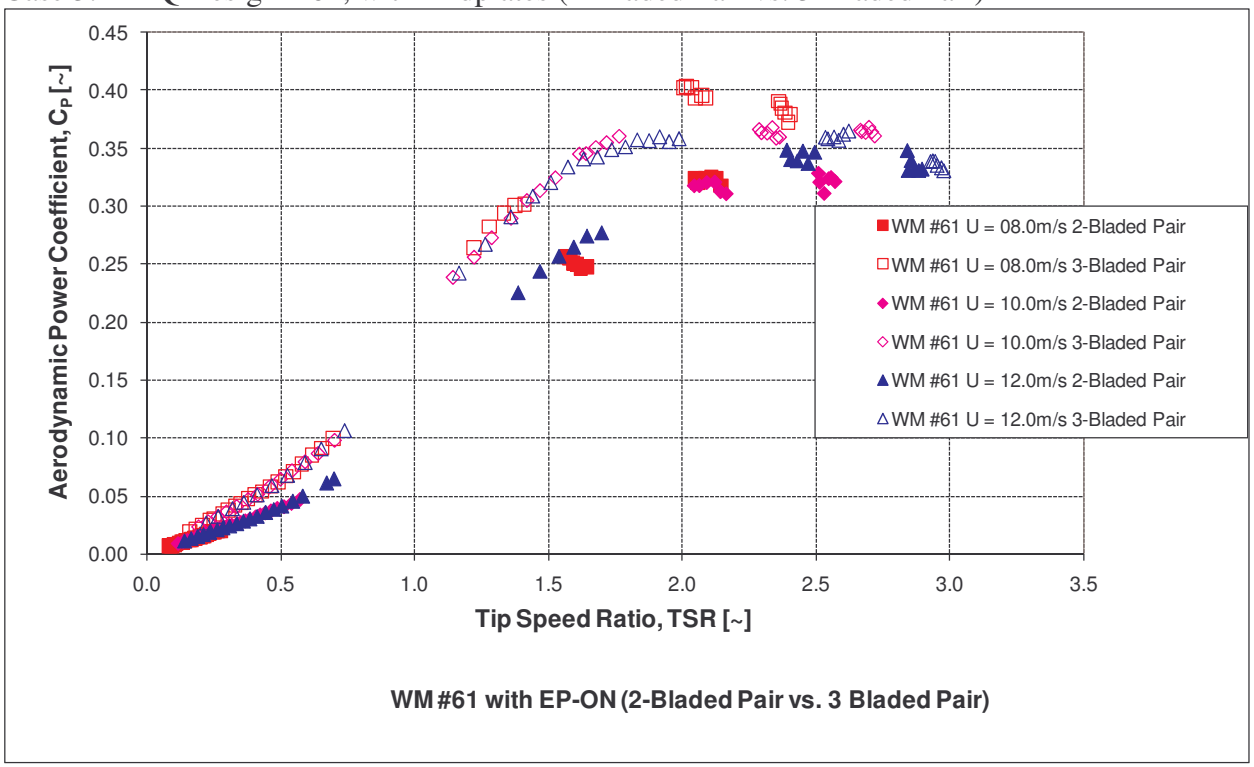

Figure 6.11 C_p of Hi-Q Design # 61 with Endplates (2 Bladed Pair vs. 3 Bladed Pair)

Case 4: Hi-Q Design # 61 vs. Hi-Q Design # 62, No Endplates (2-Bladed Pair vs. 3-Bladed Pair)

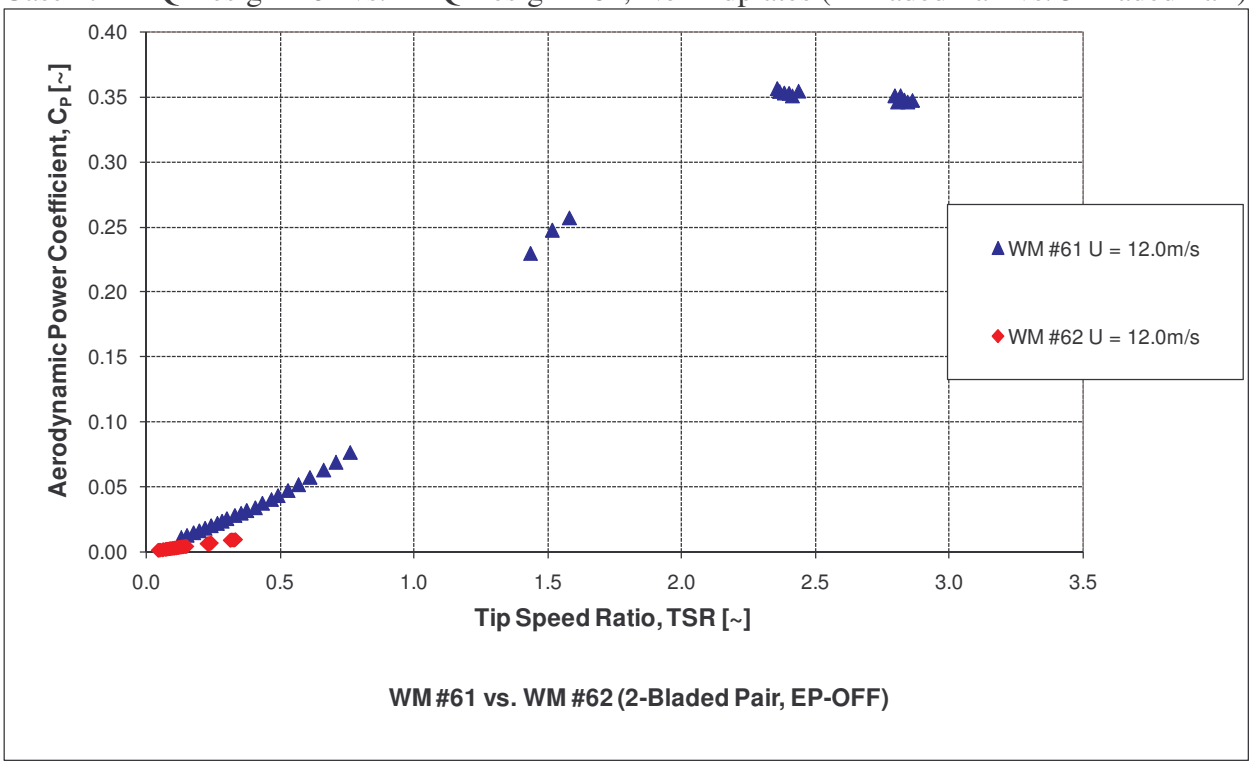

Figure 6.12 C_p of Hi-Q Design # 61 vs. Hi-Q Design # 62, with No Endplates (2 Bladed Pair)

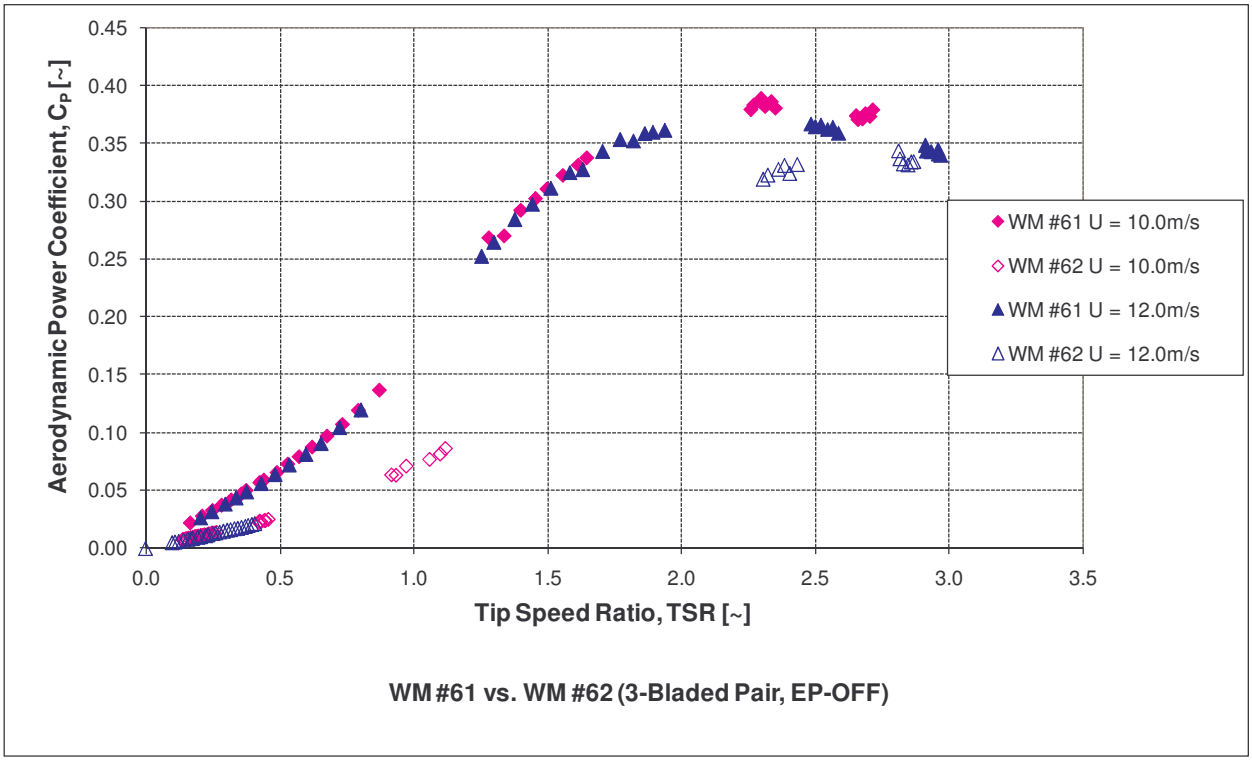

Figure 6.13 C_p of Hi-Q Design # 61 vs. Hi-Q Design # 62, with no Endplates (3 Bladed Pair)

Case 5: Hi-Q Design # 61, no Endplates (3-Bladed Fwd vs. 3-Bladed Aft and 3-Bladed Pair)

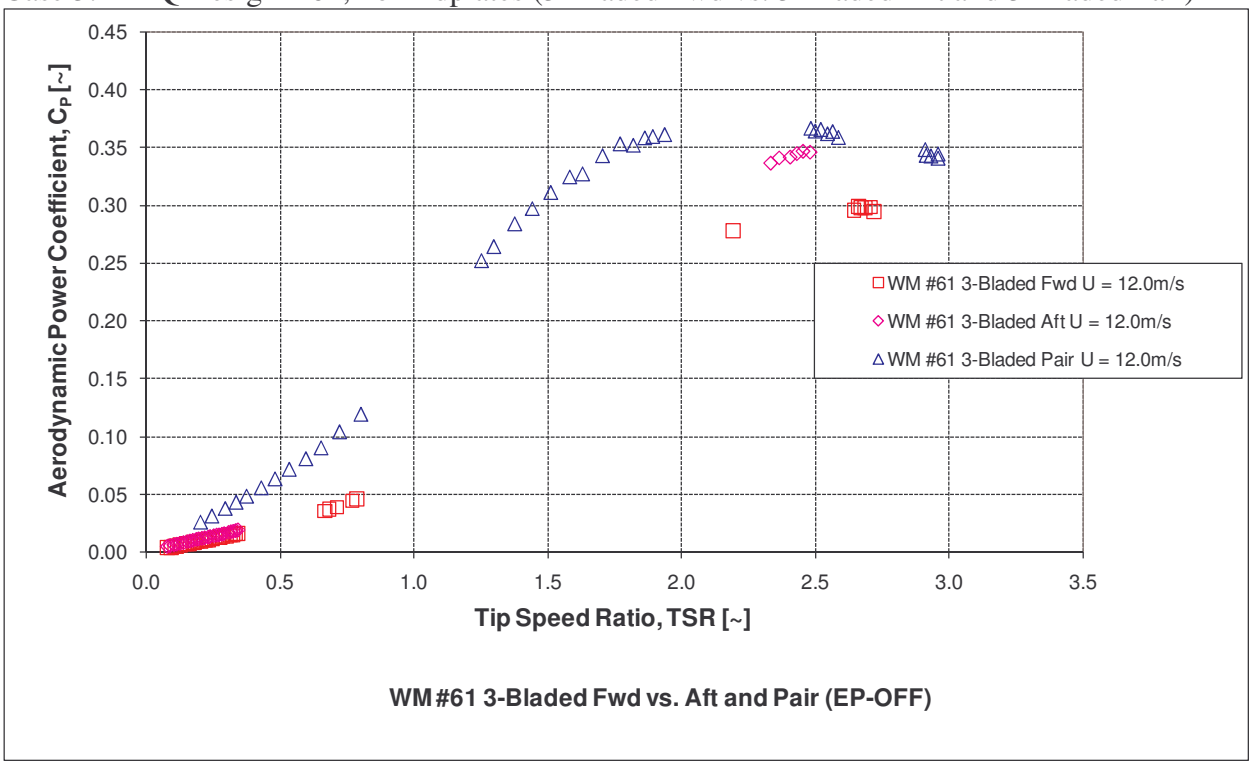

Figure 6.14 C_p of Hi-Q Design # 61 with no Endplates (3 Bladed Fwd vs. 3 Bladed Aft and 3 Bladed Pair)

Case 6: Wind Mill Minimum Sustainable Wind Speed (Free-Spinning)

Table 6.2 Wind Mill Rotational Speed (No Generator Load) as Function of Wind Speed

Wind Speed [m/s]	**Wind Mill Rotational Speed (No Generator Load) [rpm]**						
	Hi-Q 61 2-Bladed with Endplates	**Hi-Q 61 3-Bladed with Endplates**	**HAWT KW 2-Bladed**	**HAWT KW 3-Bladed**	**HAWT KW 6-Bladed**	**HAWT Bergey 3-Bladed**	**HAWT Bergey 6-Bladed**
2.0		245					
2.5		351					
3.0	460	479					
3.5	592	608			615		
4.0	629	738	932	955	766		456
4.5	888	861	1138	1162	928		550
5.0	1016	995	1400	1345	1099		1086
5.5	1154	1128	1550	1482	1252		1239
6.0	1294	1265	1832	1500	1409	1138	1454
6.5	1391	1344	2100	1938	1461	1438	1468
7.0	1602	1539	2262	2104	1668	1550	1465
7.5	1721	1632	2390	2222	1790	1578	
8.0	1838	1745	2942	2715	1940		
8.5		1862			2051		
9.0		2050			2208		
9.5		2170			2432		
10.0		2300					

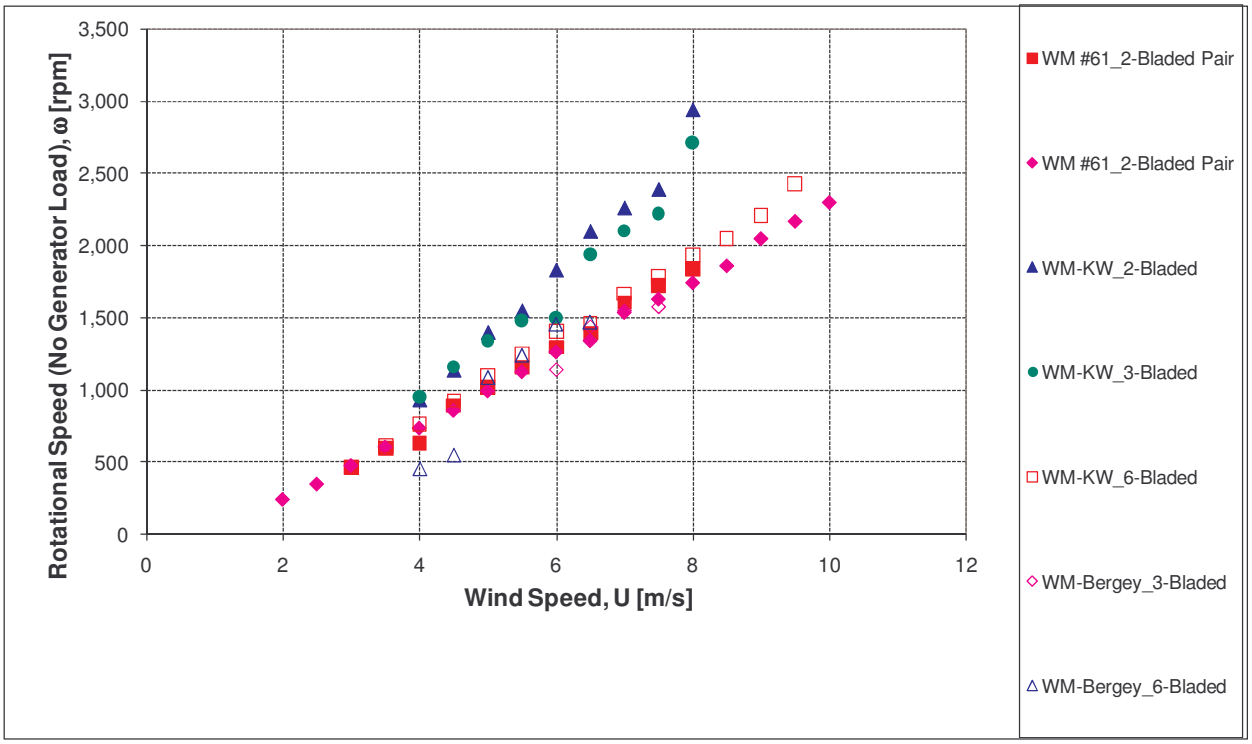

Figure 6.15 Wind Mill Rotational Speed (No Generator Load) of Different Wind Mills.

The first point of each data set corresponds to the minimum sustainable (no load) rotor rotational speed. Hi-Q rotor has a lower start-up speed, compared to other HAWT rotors tested.

6.3 Conclusions from Wind Tunnel Testing

1 Design # 61 (with or with no endplates) performs better than Design # 62.
2 Cut in speed of Design # 61 is much lower than a conventional tested HAWT, no matter the number of blades on the HAWT.
3 Connected endplates on Design # 61 have a slight performance gain over no tips for the 3-bladed Design # 61.
4 Connected endplates on Design # 61 will help with the structural rigidity of the wind mill and will lower structure weight.
5 Torque at low wind speeds for Design # 61 is higher than the tested conventional HAWT and will cause the windmill to generate power at lower wind speeds.
6 In the current test setup we were not able to start the conventional HAWT, no matter how many blades, indicating that startup torque is much lower than Design # 61.
7 Design # 61 will start generating energy at a lower wind speed than a conventional tested HAWT.

6.4 Recommendations from Wind Tunnel Testing

1. Test two more types of endplates on Design # 61 to see if more performance improvement is possible.
2. Lower resistance and initial torque of the generator used, by replacing it with another device to construct power curves of the Bergey 3-bladed and Wetzel (2 and 3 bladed) to compare with Design #61,
3. Continue full scale manufacturing of Design # 61 mounted on a Bergey XL.1 generator and test against a 3-bladed Bergey XL.1 side-by-side to compare overall energy output over a time period.

7. Aerodynamic Power Coefficient Comparison

7.1 Model Comparison

Additional wind tunnel testing is performed to identify the aerodynamic power coefficient, as function of wind mill tip speed ratio, of the following three wind mills:

1. 3 Bladed Hi-Q Design # 61 with a modified endplate (shown in Figure 7.1)
2. 3 Bladed Bergey wind mill rotor (shown in Figure 7.2)
3. 3 Bladed Kyle Wetzel wind mill rotor (shown in Figure 7.3)

The geometric characteristics of the three wind mills are summarized in Table 7.1.

Table 7.1 Geometric Characteristics of Tested Rotor Model Configuration

Wind Mill Rotor	Number of Blades	End Plates	$R_{wind\text{-}mill}$ [in]	Blockage Ratio [%]
Hi-Q Design # 61	3 Pair	YES	8.0	10.0
Bergey	3	N.A.	14.8	34.2
KW Rotor	3	N.A.	8.0	10.0

where blockage ratio is defined as the ratio of rotor reference area to wind tunnel test section area:

$$BR = \frac{\pi \left(R_{wind-mill} \right)^2}{H_{test-section} D_{test-section}}$$

$$H_{test-section} = 38.2 \text{ in}$$

$$W_{test-section} = 54.5 \text{ in}$$

Figure 7.1 3 Bladed Hi-Q Design # 61 Rotor with Modified End Plates

Figure 7.2 3-Bladed Bergey Rotor

Figure 7.3 3-Bladed Kyle Wetzel Rotor

Results are illustrated in Figure 7.4.

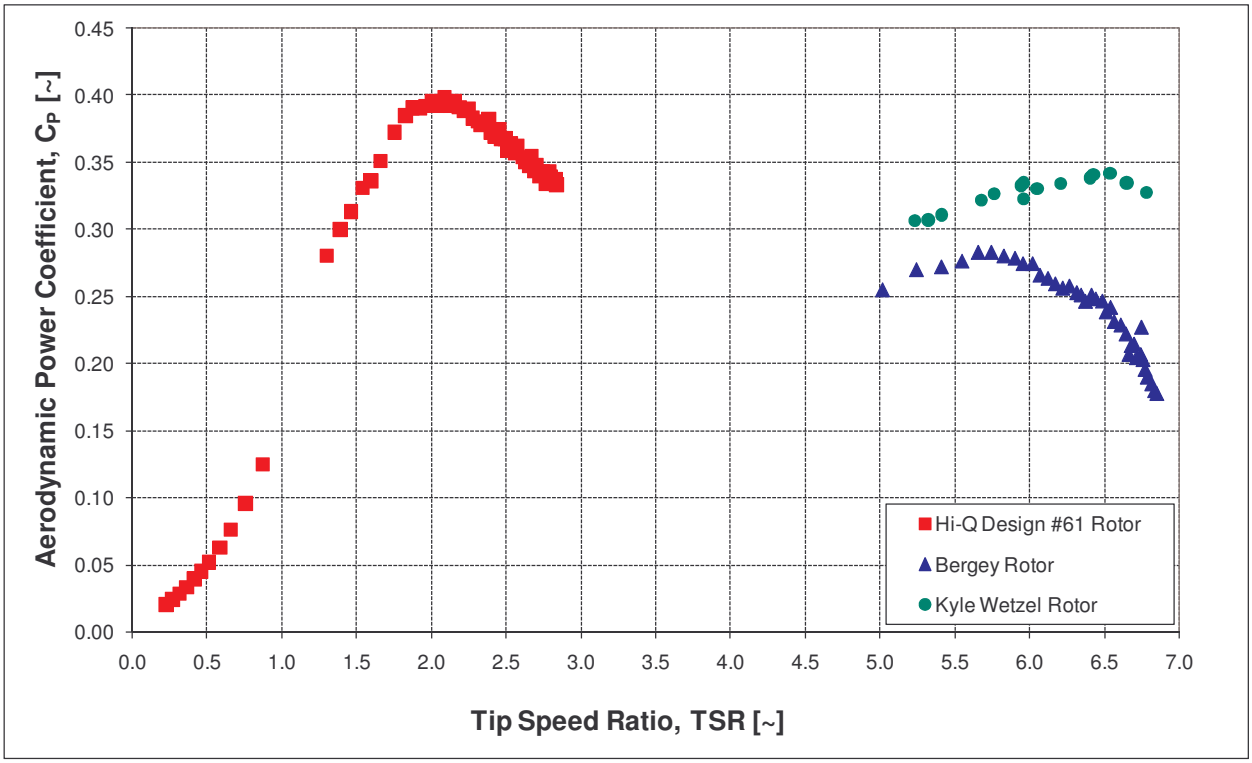

Figure 7.4 C_p of the Three Tested Rotors

Observing Figure 7.4, it is found that the maximum aerodynamic power coefficient of Hi-Q Design # 61 Rotor of 0.40, is the highest among the three tested rotors. The $C_{p\ max}$ of Kyle Wetzel rotor is about 0.06 less than the Hi-Q Design # 61 Rotor. The maximum aerodynamic power coefficient of Bergey rotor of 0.28, in reality should be further reduced to account for the effect of high wind tunnel blockage ratio.

In conclusion, among the three tested rotors, the Hi-Q Design # 61 rotor has the highest aerodynamic performance. Operating at a lower tip speed ratio will decrease the noise levels for the same wind speed.

8. Aerodynamic Loads for Structural Analysis of the Hi-Q Design # 61

8.1 Analysis

One type of analysis is considered, i.e. the linear static analysis. In linear static analysis, the design loads are static aerodynamic loads (RPM = 0) at a wind speed of 52.5 m/s. This wind speed implies the wind mill is designed to satisfy the Wind Turbine Class III extreme wind speed requirement, set forth by the International Electrotechnical Commission (IEC) (Reference 6).

8.2 Aerodynamic Loads

To obtain the aerodynamic loads, a single static rotor blade (RPM = 0) is analyzed using computational methods (CFD), at a wind speed of 11.0 m/s. The software used for the computational analysis is CFdesign (Reference 7). Prior to the CFD analysis, the single rotor blade is divided into 60 smaller surfaces, as shown in Figure 8.1. The main reason of creating multiple surfaces on the rotor blade, especially in the blade leading edge region, is to enable a more accurate capture of aerodynamic loads, due to the presence of a high pressure gradient.

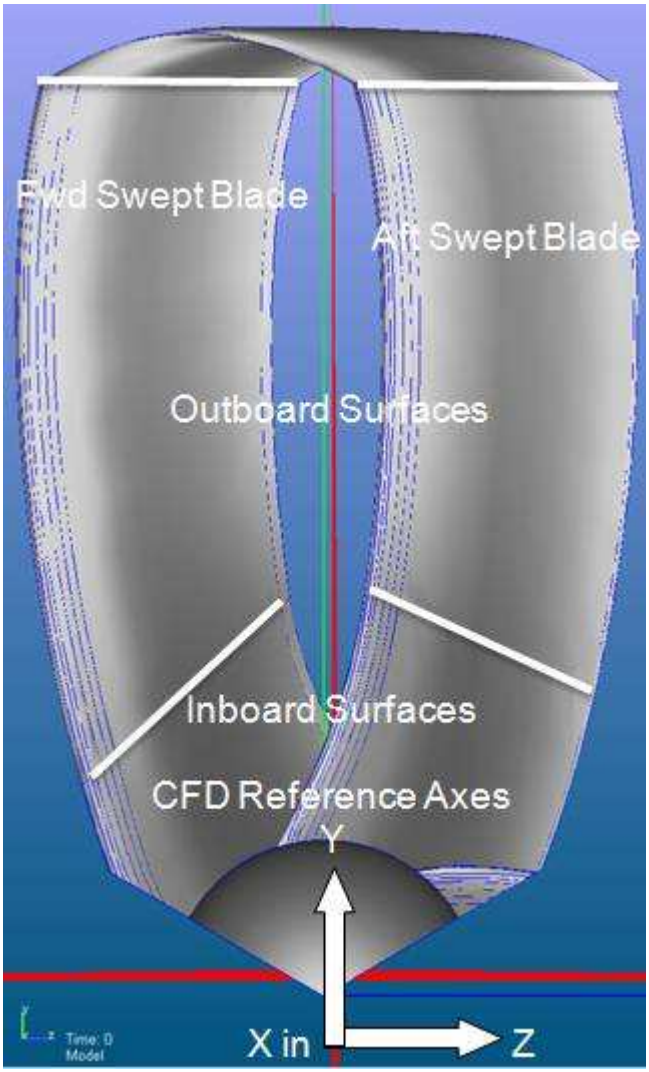

Figure 8.1 Coordinate Systems of A Single Rotor Blade

At the completion of the CFD analysis, the aerodynamic forces (F_x, F_y and F_z) acting on each of the surfaces are calculated. Results are then extracted from CFdesign, tabulated in a spreadsheet and adjusted to reflect the true loads at the design wind speed of 52.5 m/s, using the following methods:

$$F_{x\,(52.5\ m/s)} = F_{x\,(11.0\ m/s)}\left[\frac{52.5}{11.0}\right]^2$$

$$F_{y\,(52.5\ m/s)} = F_{y\,(11.0\ m/s)}\left[\frac{52.5}{11.0}\right]^2$$

$$F_{z\,(52.5\ m/s)} = F_{z\,(11.0\ m/s)}\left[\frac{52.5}{11.0}\right]^2$$

A summary of the resultant loads is listed in Table 8.1 and Table 8.2.

Table 8.1 Static Aerodynamic Loads (Inboard Surfaces) at 52.5 m/s

Surface Designation*	F_x [lb]	F_y [lb]	F_z [lb]
FSB01	0.025	0.020	0.066
FSB02	-6.989	-2.619	-9.237
FSB03	-0.235	-0.194	-0.665
FSB04	-0.193	-0.182	-0.637
FSB05	-0.135	-0.164	-0.610
FSB06	-0.036	-0.072	-0.294
FSB07	-0.003	-0.061	-0.287
FSB08	0.062	-0.014	-0.164
FSB09	-0.073	-0.020	0.003
FSB10	-0.318	-0.121	-0.109
FSB11	-0.287	-0.005	-0.162
FSB12	-0.239	-0.102	-0.166
FSB13	-5.010	-1.484	-7.853
FSB14	-0.132	0.002	-0.388
ASB01	-0.032	0.028	-0.151
ASB02	-13.196	4.239	-19.223
ASB03	-0.475	0.086	-1.077
ASB04	-0.459	0.075	-1.134
ASB05	-0.416	0.052	-1.219
ASB06	-0.168	0.007	-0.675
ASB07	-0.094	-0.025	-0.742
ASB08	0.076	-0.041	-0.304
ASB09	-0.685	0.207	0.050
ASB10	-1.181	0.338	-0.315
ASB11	-1.055	0.297	-0.434
ASB12	-1.671	0.471	-0.899
ASB13	-1.243	0.354	-0.823
ASB14	-0.965	0.277	-0.726
ASB15	-9.372	3.281	-14.825
ASB16	0.002	-0.002	0.015

* Refer to Figure 8.2 and Figure 8.3 on the definition of surface designation

Table 8.2 Static Aerodynamic Loads (Outboard Surfaces) at 52.5 m/s

Surface Designation*	F_x [lb]	F_y [lb]	F_z [lb]
FSB01	-0.149	0.094	-1.675
FSB02	-27.200	-1.281	-66.523
FSB03	-0.314	-0.269	-3.078
FSB04	-0.224	-0.274	-2.951
FSB05	-1.144	-0.261	-2.682
FSB06	0.064	-0.116	-1.133
FSB07	0.100	-0.081	-0.703
FSB08	-0.253	0.008	0.385
FSB09	-1.663	-0.224	-0.214
FSB10	-2.666	-0.542	-1.622
FSB11	-1.862	-0.427	-1.709
FSB12	-1.538	-0.358	-1.741
FSB13	-13.425	-1.680	-37.372
FSB14	0.020	0.091	-1.240
ASB01	-0.005	0.010	-0.189
ASB02	-21.429	0.656	-54.347
ASB03	-0.328	-0.118	-2.454
ASB04	-0.267	-0.131	-2.484
ASB05	-0.118	-0.142	-2.522
ASB06	0.051	-0.075	-1.302
ASB07	0.218	-0.074	-1.342
ASB08	0.262	-0.008	-0.411
ASB09	-1.207	-0.002	-0.213
ASB10	-1.877	-0.073	-1.077
ASB11	-1.511	-0.074	-1.160
ASB12	-2.142	-0.112	-2.016
ASB13	-1.492	-0.079	-1.675
ASB14	-1.159	-0.059	-1.480
ASB15	-9.055	0.534	-35.256
ASB16	0.034	0.022	-0.532

* Refer to Figure 8.2 and Figure 8.3 on the definition of surface designation

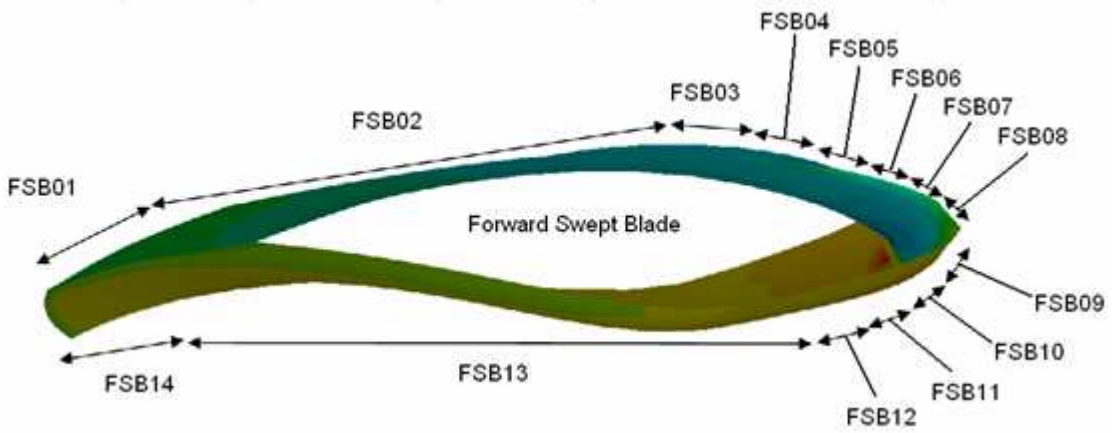

Figure 8.2 Surface Designation on the Forward Swept Blade

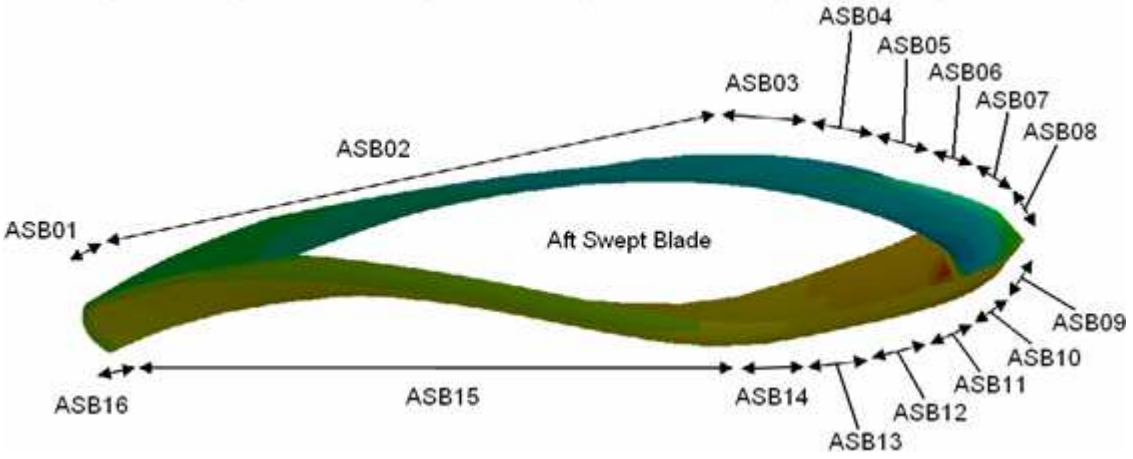

Figure 8.3 Surface Designation on the Aft Swept Blade

9. Finite Element Structural Analysis of the Hi-Q Design # 61

The finite element analysis (FEA) carried out using NEi Nastran (Reference 8):

Figure 9.1 shows the finite element model analyzed in Nastran (Reference 8).

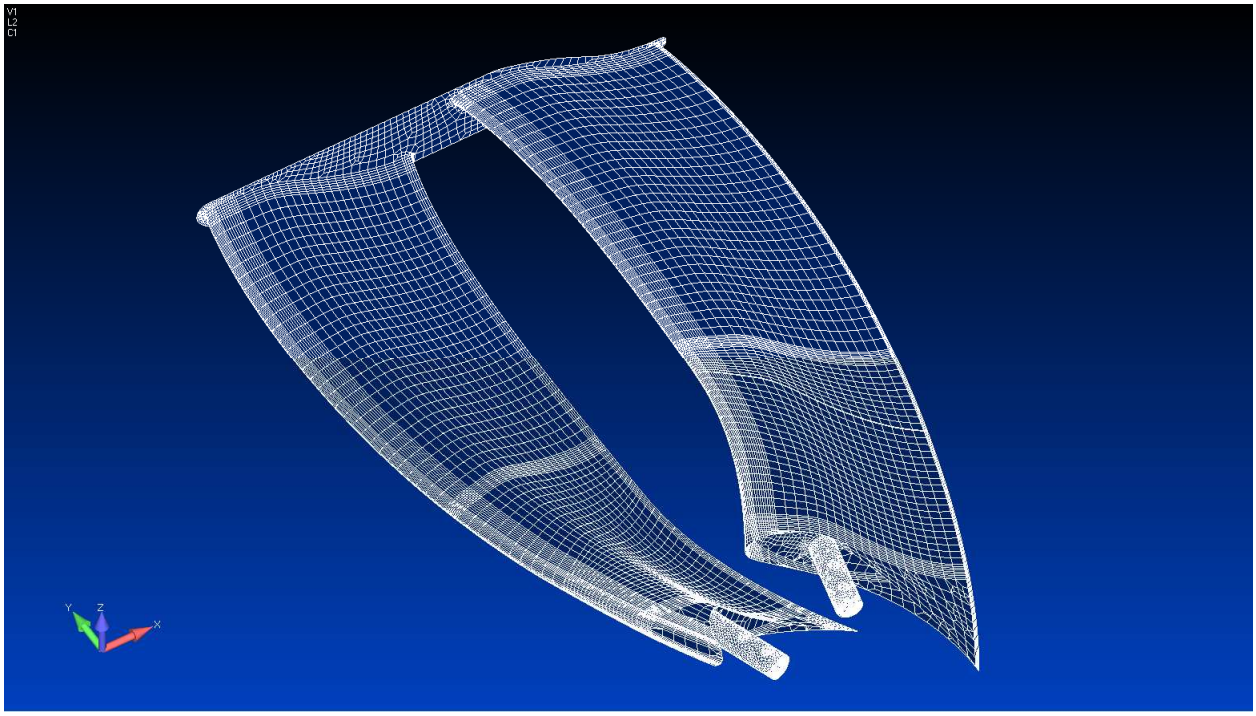

Figure 9.1 Finite Element Model

9.1 Materials

The wind mill blade skins and the endplate are made of Cytec 977-3 carbon prepreg cloth. The circular spars are made of AISI 4130 steel. The ribs are made of 2024 Aluminum. The mechanical properties are as shown in Figure 9.2 through Figure 9.5. Due to the unavailability of the mechanical properties of Cytec 977-3, LTM 25ST 2x2 Twill Quasi-isotropic material properties are used (Reference 9) which is similar.

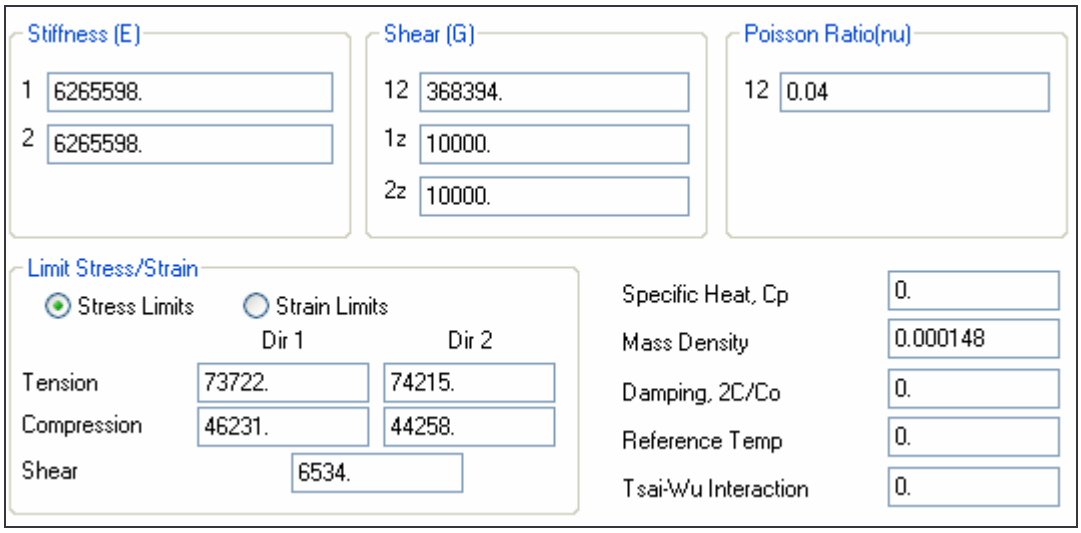

Figure 9.2 LTM 25ST 2x2 Twill: Quasi-isotropic (Reference 10)

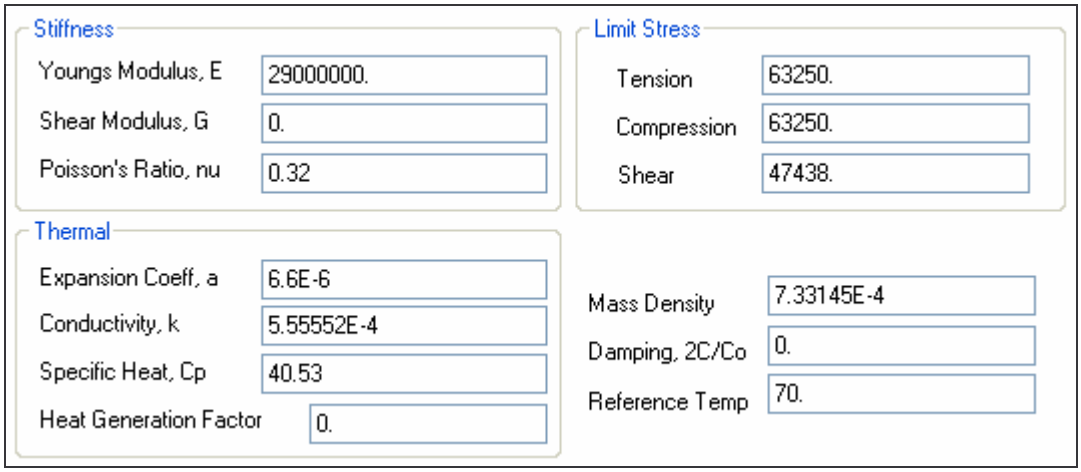

Figure 9.3 AISI 4130 Steel (Reference 11)

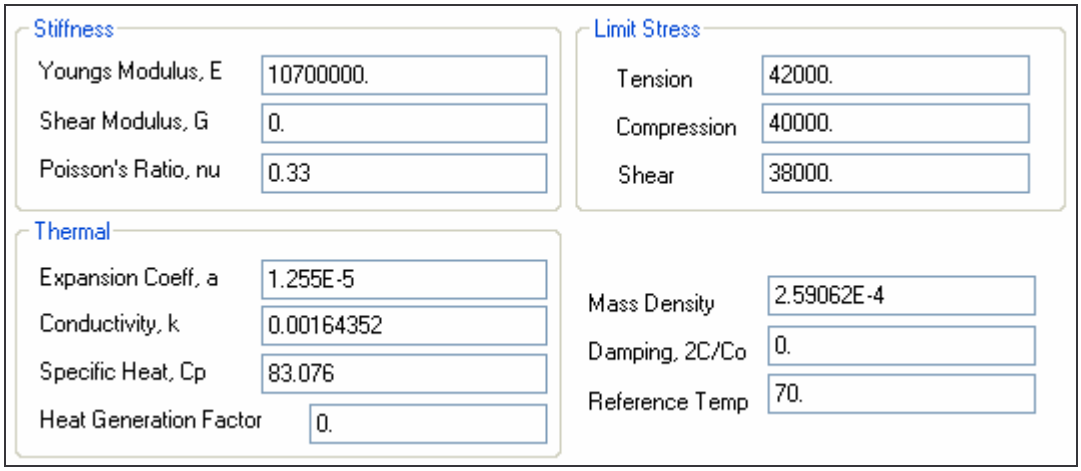

Figure 9.4 2024 T351 Aluminum (Reference 11)

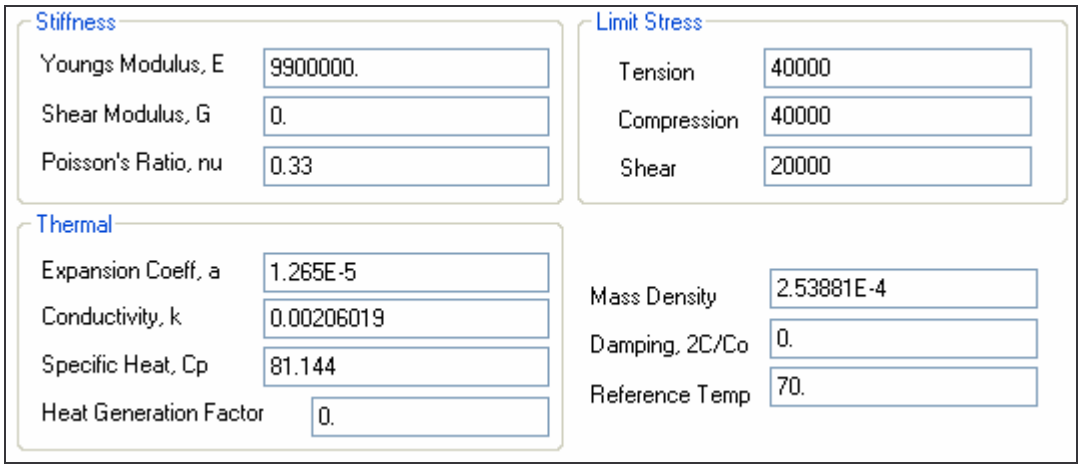

Figure 9.5 6061 T651 Aluminum (Reference 11)

9.2 Model Description

The layup schedule used on the skins and leading edges are as shown in Figure 9.6.

--- Top of Layup --- Total Thickness = 0.042

Ply ID	Global Ply	Material	Thickness	Angle
4		2..LTM 25ST 2x2 Twill (...	0.016	0.
3		2..LTM 25ST 2x2 Twill (...	0.005	45.
2		2..LTM 25ST 2x2 Twill (...	0.005	45.
1		2..LTM 25ST 2x2 Twill (...	0.016	0.

--- Bottom of Layup ---

Figure 9.6 Blade Skins, Leading Edge

The layup schedule used on the skins in the region of the ribs are as shown in Figure 9.7.

Total Thickness = 0.138

Ply ID	Global Ply	Material	Thickness	Angle
10		2..LTM 25ST 2x2 Twill (...	0.016	0.
9		2..LTM 25ST 2x2 Twill (...	0.016	0.
8		2..LTM 25ST 2x2 Twill (...	0.016	0.
7		2..LTM 25ST 2x2 Twill (...	0.005	45.
6		2..LTM 25ST 2x2 Twill (...	0.016	0.
5		2..LTM 25ST 2x2 Twill (...	0.016	0.
4		2..LTM 25ST 2x2 Twill (...	0.005	45.
3		2..LTM 25ST 2x2 Twill (...	0.016	0.
2		2..LTM 25ST 2x2 Twill (...	0.016	0.
1		2..LTM 25ST 2x2 Twill (...	0.016	0.

--- Bottom of Layup ---

Figure 9.7 Blade Skins in the region of the Ribs

The layup schedule used on the trailing edges are as shown in Figure 9.8.

--- Top of Layup --- Total Thickness = 0.032

Ply ID	Global Ply	Material	Thickness	Angle
2		2..LTM 25ST 2x2 Twill (...	0.016	0.
1		2..LTM 25ST 2x2 Twill (...	0.016	0.

--- Bottom of Layup ---

Figure 9.8 Blade Trailing Edge

The layup schedule used on the end cap are as shown in Figure 9.9.

--- Top of Layup --- Total Thickness = 0.096

Ply ID	Global Ply	Material	Thickness	Angle
6		2..LTM 25ST 2x2 Twill (...	0.016	0.
5		2..LTM 25ST 2x2 Twill (...	0.016	45.
4		2..LTM 25ST 2x2 Twill (...	0.016	0.
3		2..LTM 25ST 2x2 Twill (...	0.016	0.
2		2..LTM 25ST 2x2 Twill (...	0.016	45.
1		2..LTM 25ST 2x2 Twill (...	0.016	0.

--- Bottom of Layup ---

Figure 9.9 End Cap

The ply orientations on the different components are as shown in Figure 9.10 and Figure 9.11.

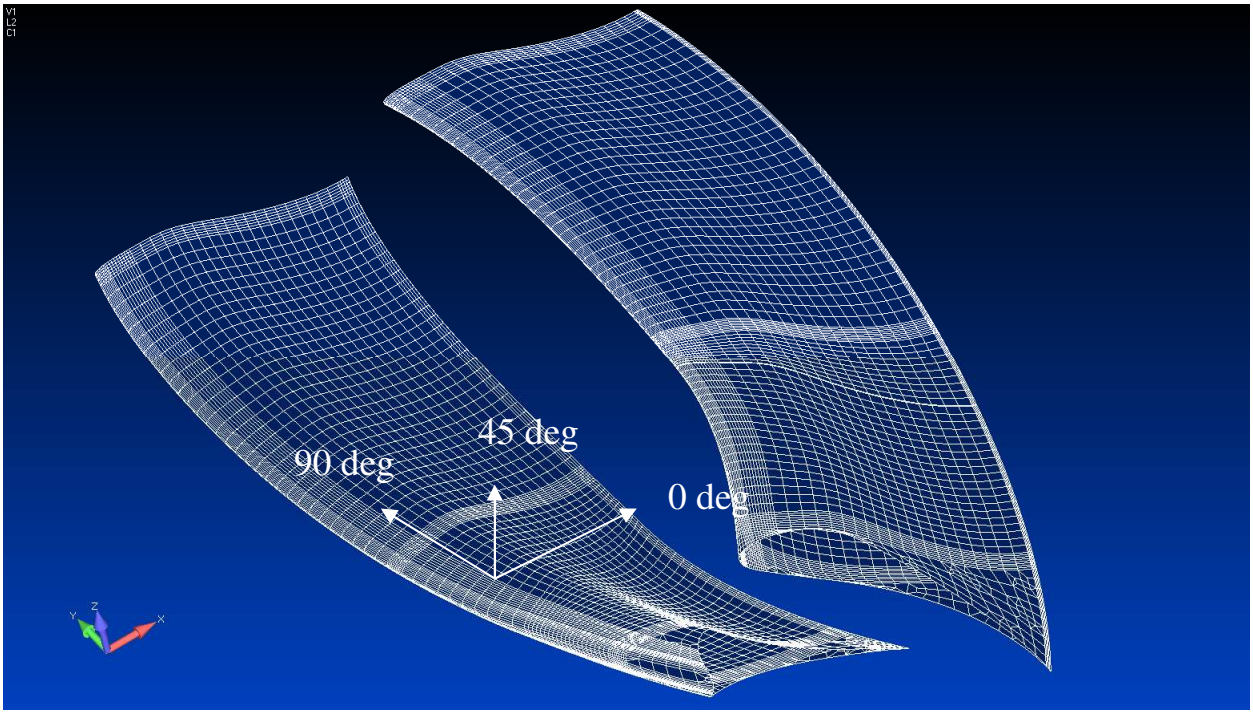

Figure 9.10 Ply Orientation Reference on Blade Skins, Leading and Trailing Edges

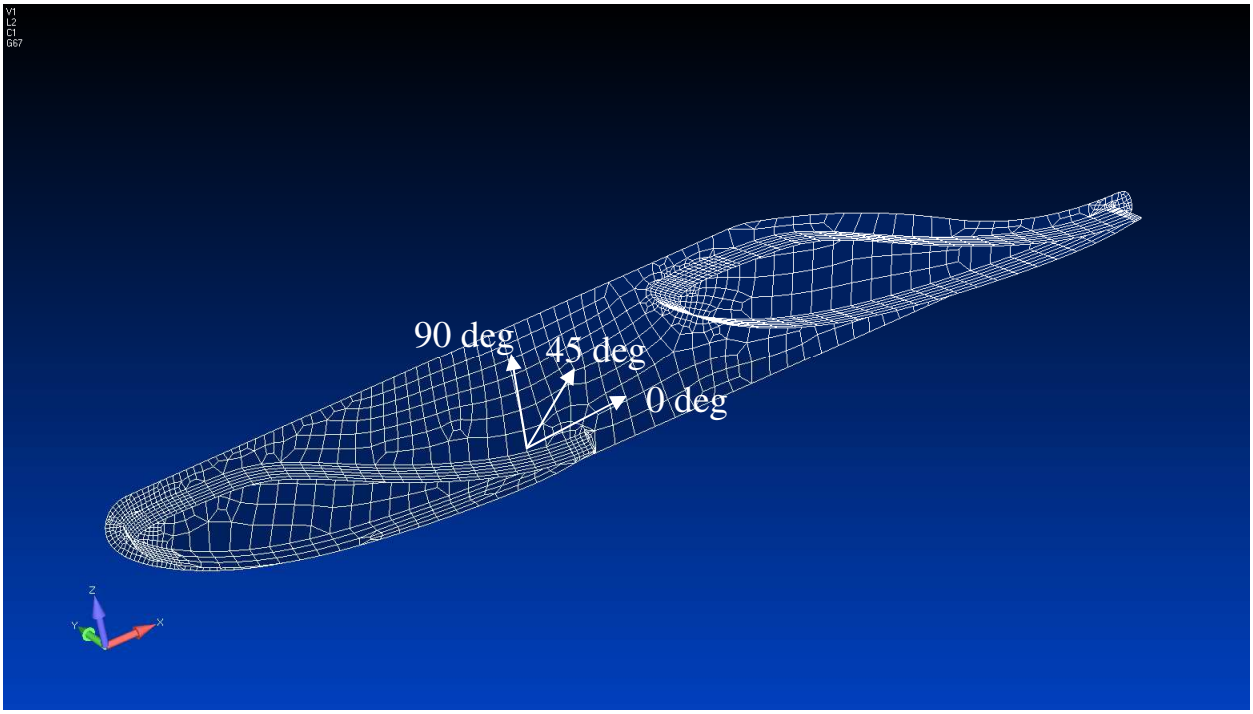

Figure 9.11 Ply Orientation Reference on End Cap

The ribs are made of 2024 Aluminum. The shear web is 0.125 inch thick and the flange is 0.25 inch thick. Figure 9.12 shows the rib geometry.

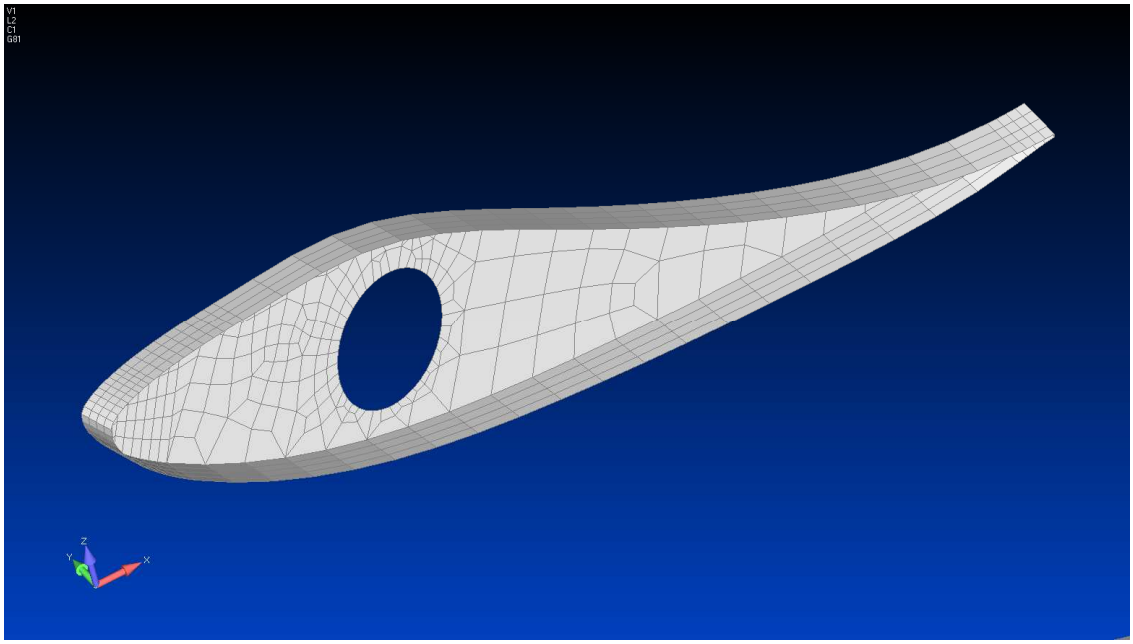

Figure 9.12 Rib Geometry

The spars are made of 4130 steel and are circular in cross section. The outer diameter is 1.5 inches and the thickness is 0.095 inches. The spar has inserts made out of 6061 T651 Aluminum on the inboard side up to the first inboard rib to increase the effectiveness by having a closed cross section as against a tubular cross section. The spar on the prototype is 0.125 inch. This increased thickness should relieve the stresses better. Figure 9.13 shows the spar geometry.

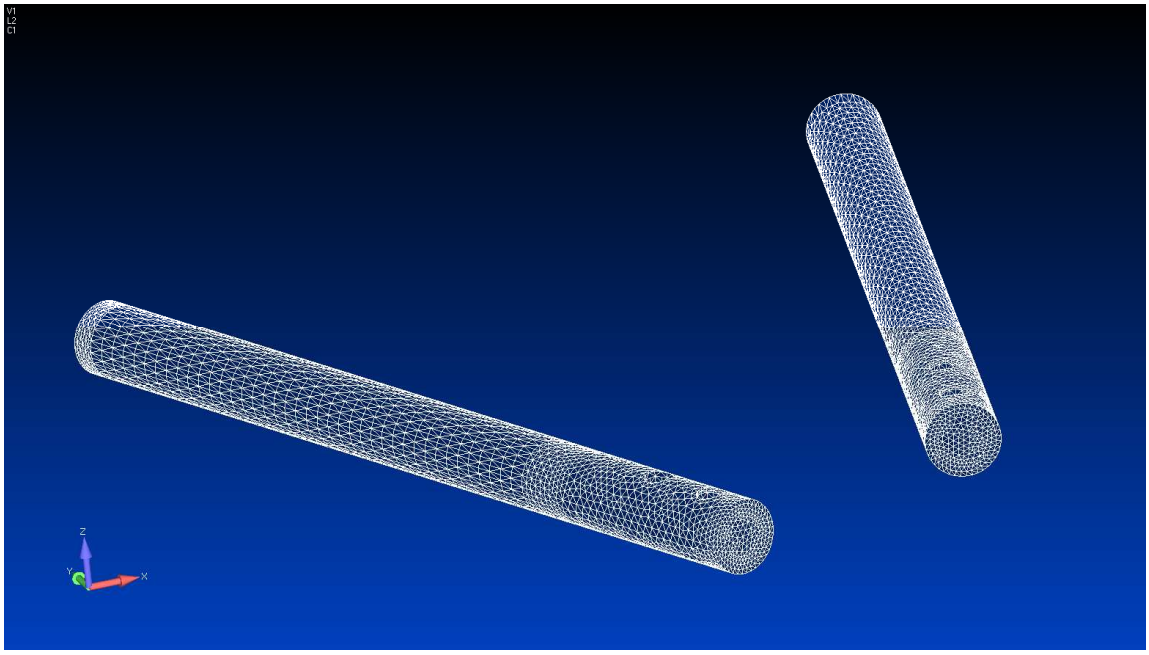

Figure 9.13 Spar Geometry

9.3 Linear Static Analysis

A wind speed of 52.5 m/s is established from Reference 6 for static load case. A rotational speed of 500 rpm along with a wind load at 17 m/s is used for the dynamic load case. Linear quasi-static analysis is carried out with the wind mill orientated perpendicular to the wind direction.

A factor of safety of 1.35 is used for the loads (Reference 6). Maximum Strain theory is used to predict ply failure. Composite ply failure is indicated by the maximum failure index. If this index is greater than one, then there is a ply failure. The analysis results presented here are the results of several trade studies. The analysis is carried out assuming unbraided conditions. Also it is beneficial to keep a symmetric laminate so there are no warping issues during cure.

9.4 Stresses

Figure 9.14 and Figure 9.15 show the composite maximum failure index in the blade skins for static and dynamic load cases.

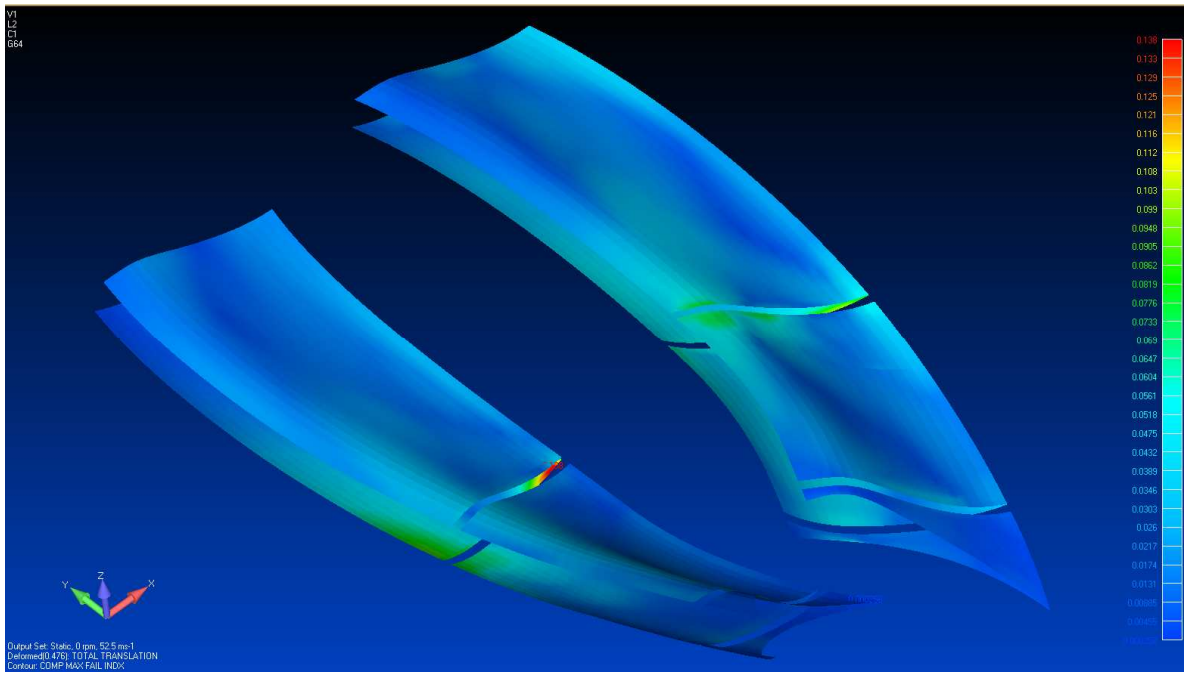

Figure 9.14 Static Load, Blade Skins, Composite Max. Failure Index (0.138)

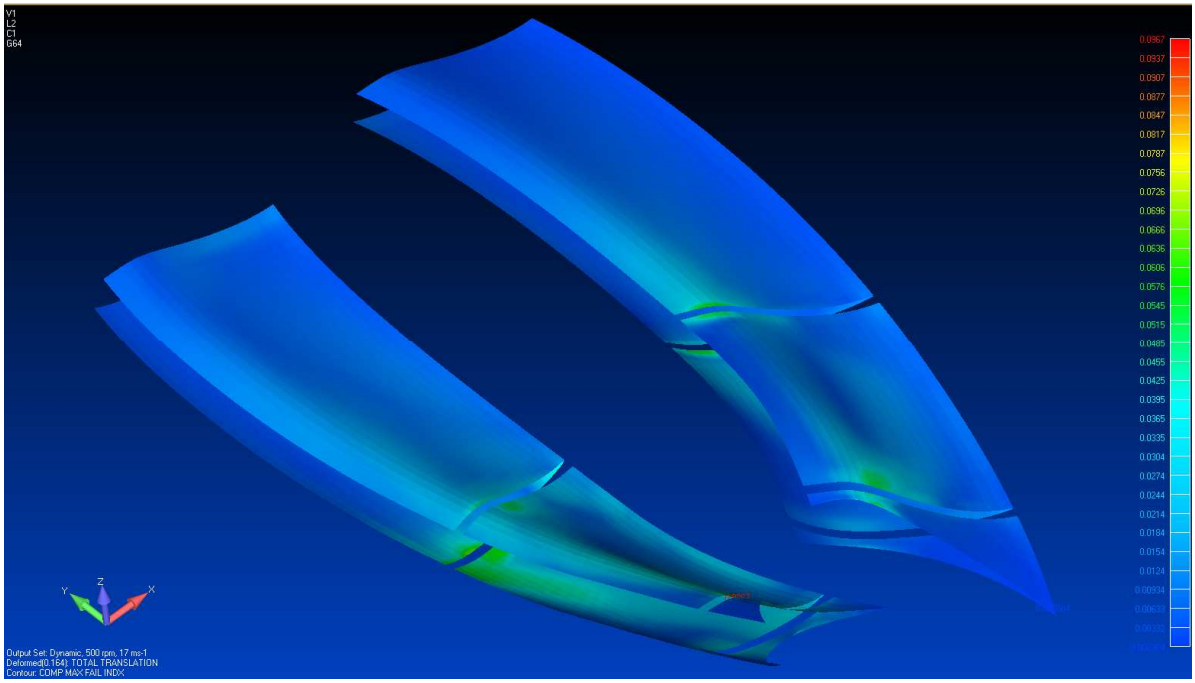

Figure 9.15 Dynamic Load, Blade Skins, Composite Max. Failure Index (0.097)

Figure 9.16 and Figure 9.17 show the composite maximum failure index in the blade skins in the region of the ribs.

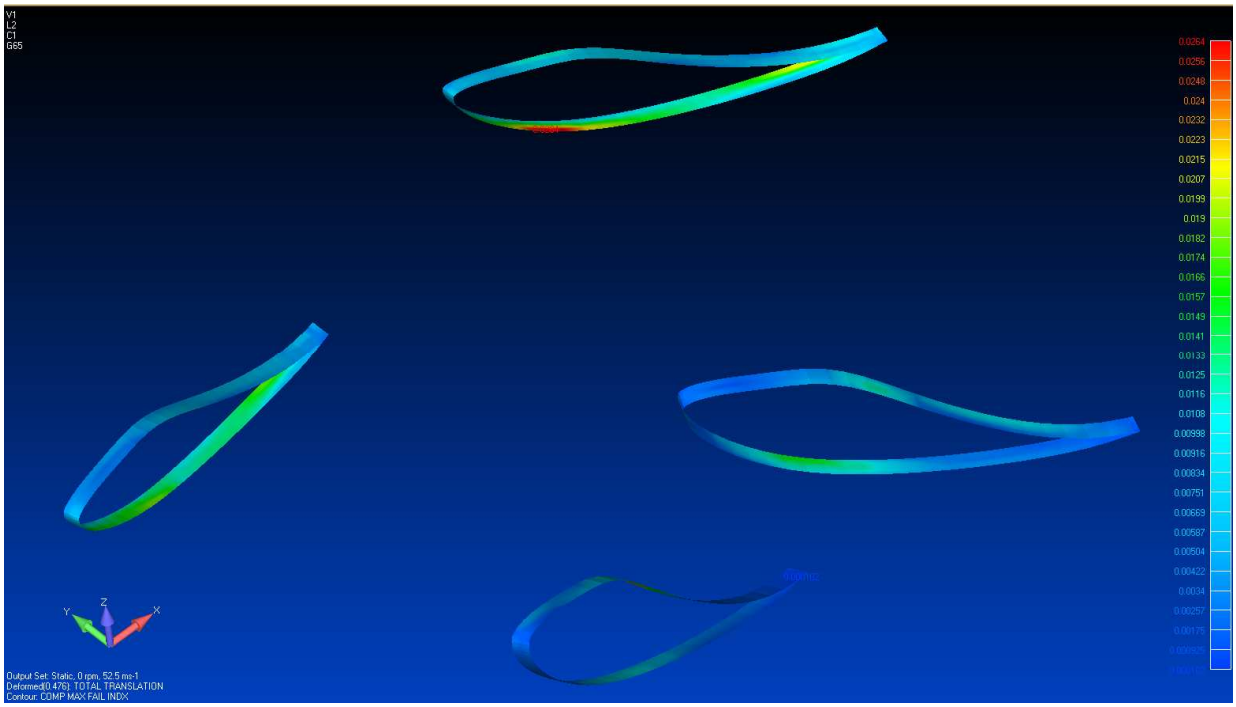

Figure 9.16 Static Load, Blade-Rib Skins, Composite Max. Failure Index (0.026)

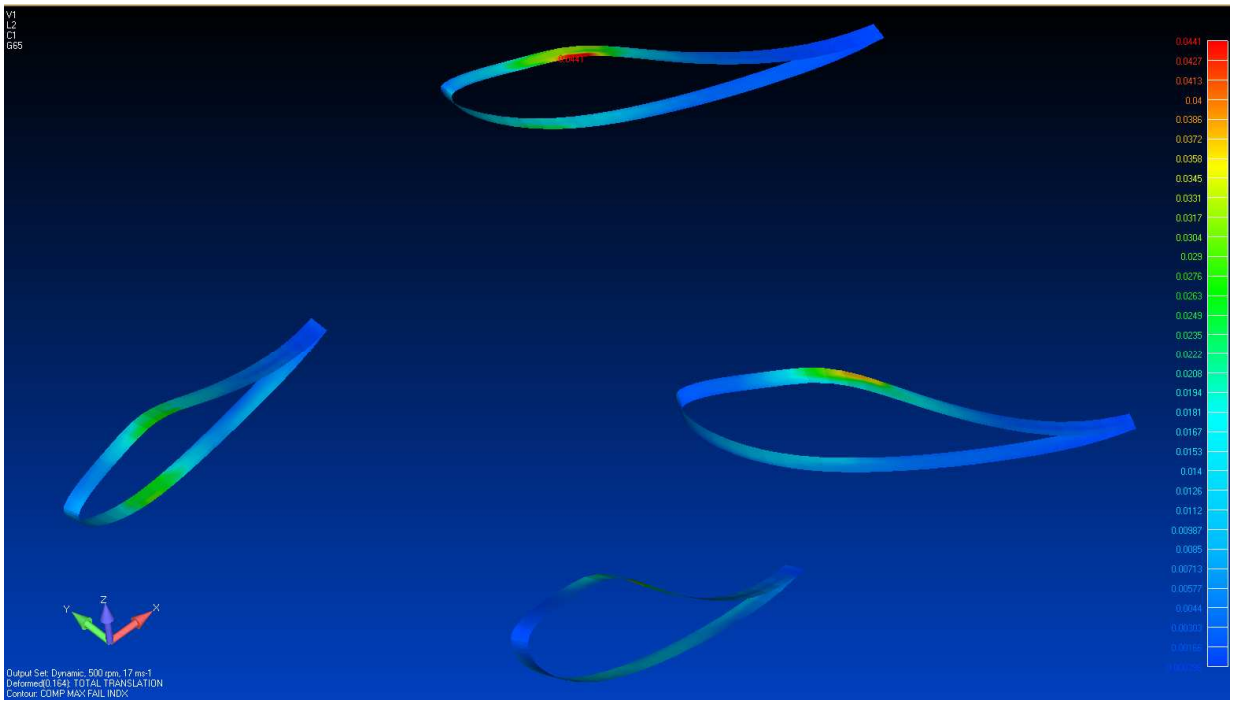

Figure 9.17 Dynamic Load, Blade-Rib Skins, Composite Max. Failure Index (0.044)

Figure 9.18 and Figure 9.19 show the composite maximum failure index in the blade trailing edges.

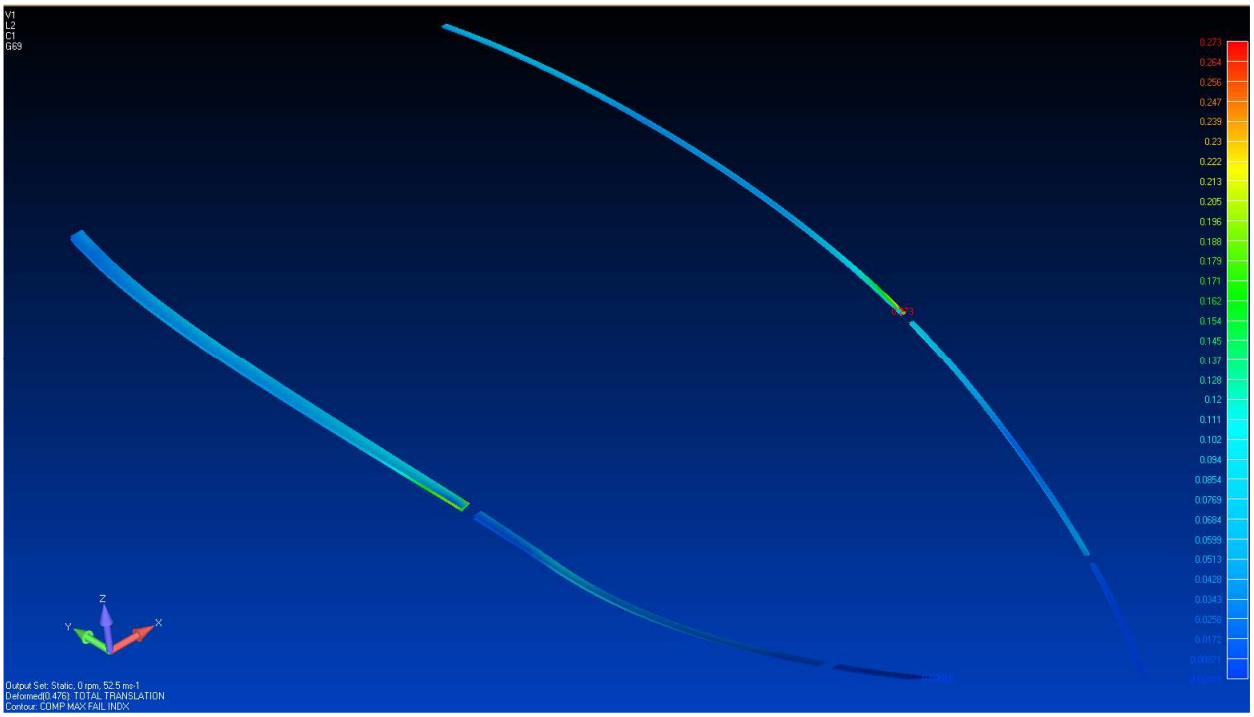

Figure 9.18 Static Load, Blade Trailing Edge Skin, Composite Max. Failure Index (0.273)

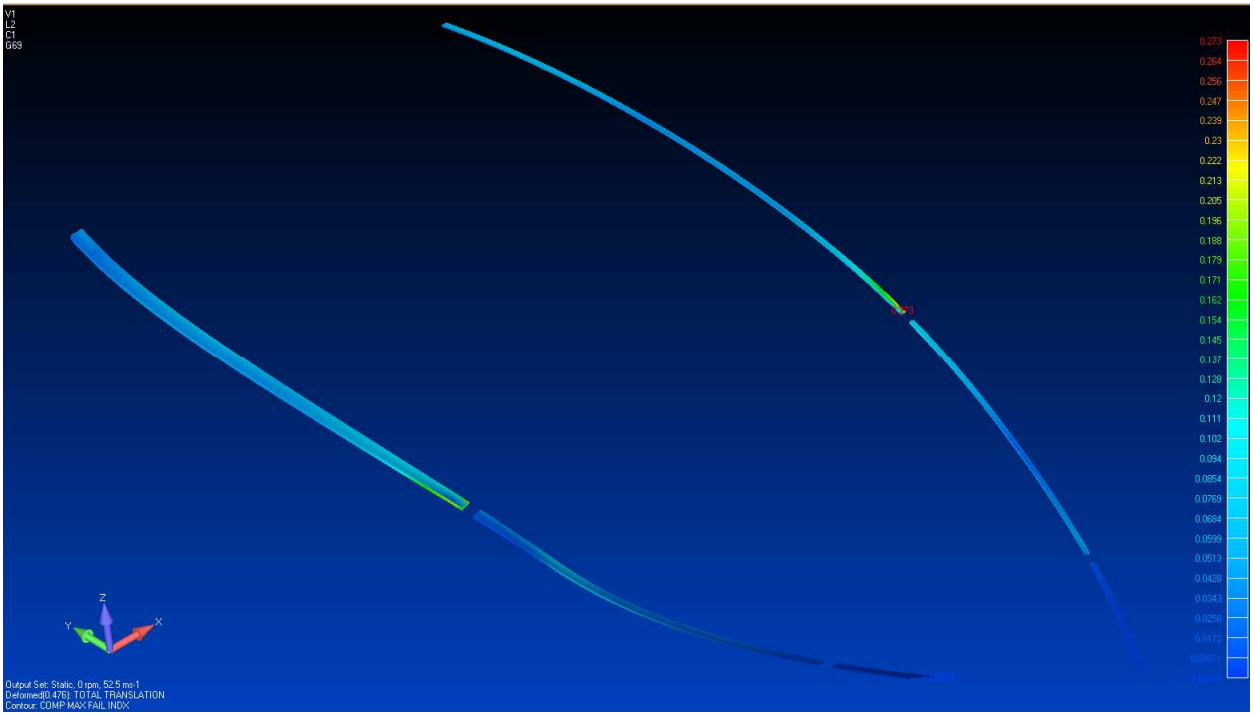

Figure 9.19 Dynamic Load, Blade Trailing Edge Skin, Composite Max. Failure Index (0.118)

Figure 9.20 and Figure 9.21 show the composite maximum failure index in the blade leading edges.

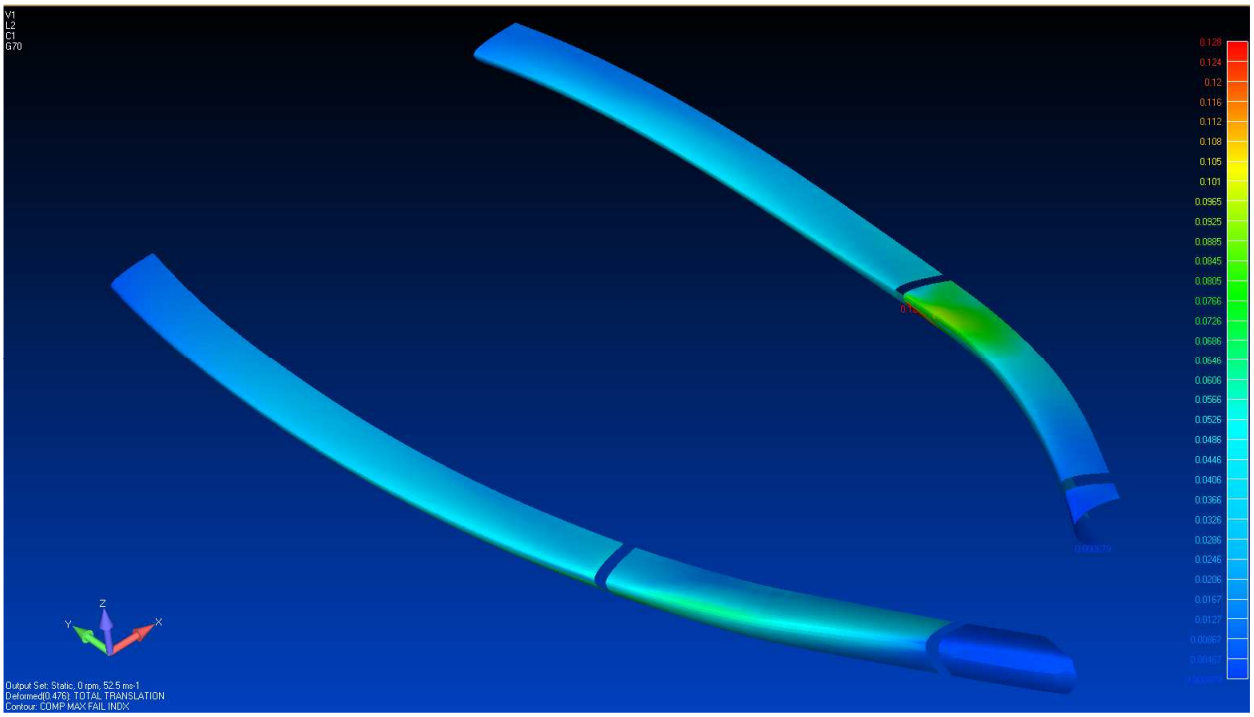

Figure 9.20 Static Load, Blade Leading Edge Skin, Composite Max. Failure Index (0.128)

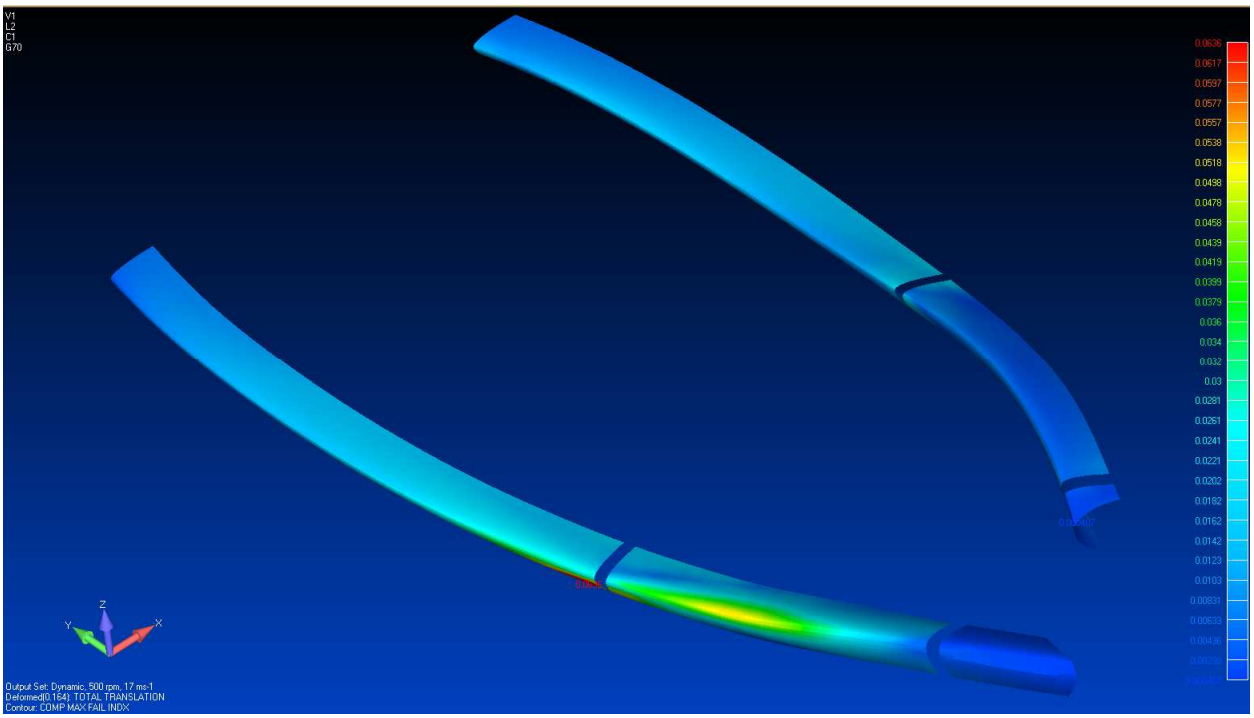

Figure 9.21 Dynamic Load, Blade Leading Edge Skin, Composite Max. Failure Index (0.064)

Figure 9.22 and Figure 9.23 show the composite maximum failure index in the blade trailing edges.

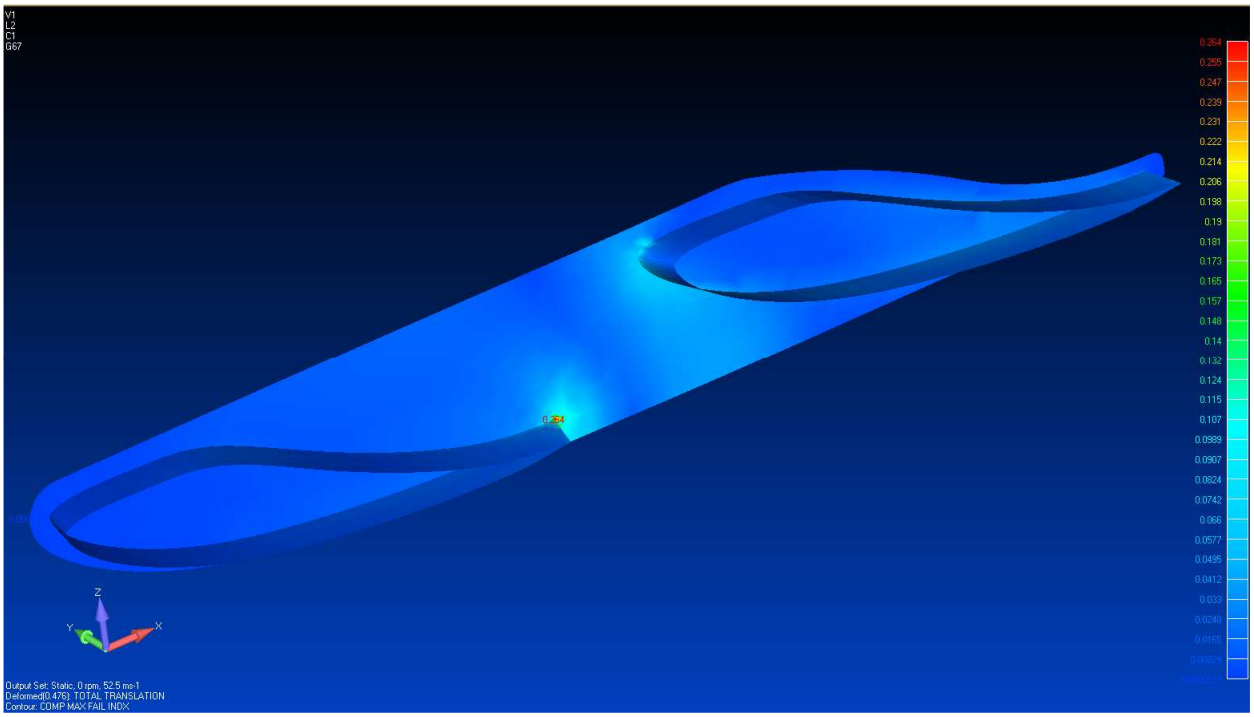

Figure 9.22 Static Load, End Cap, Composite Max. Failure Index (0.264)

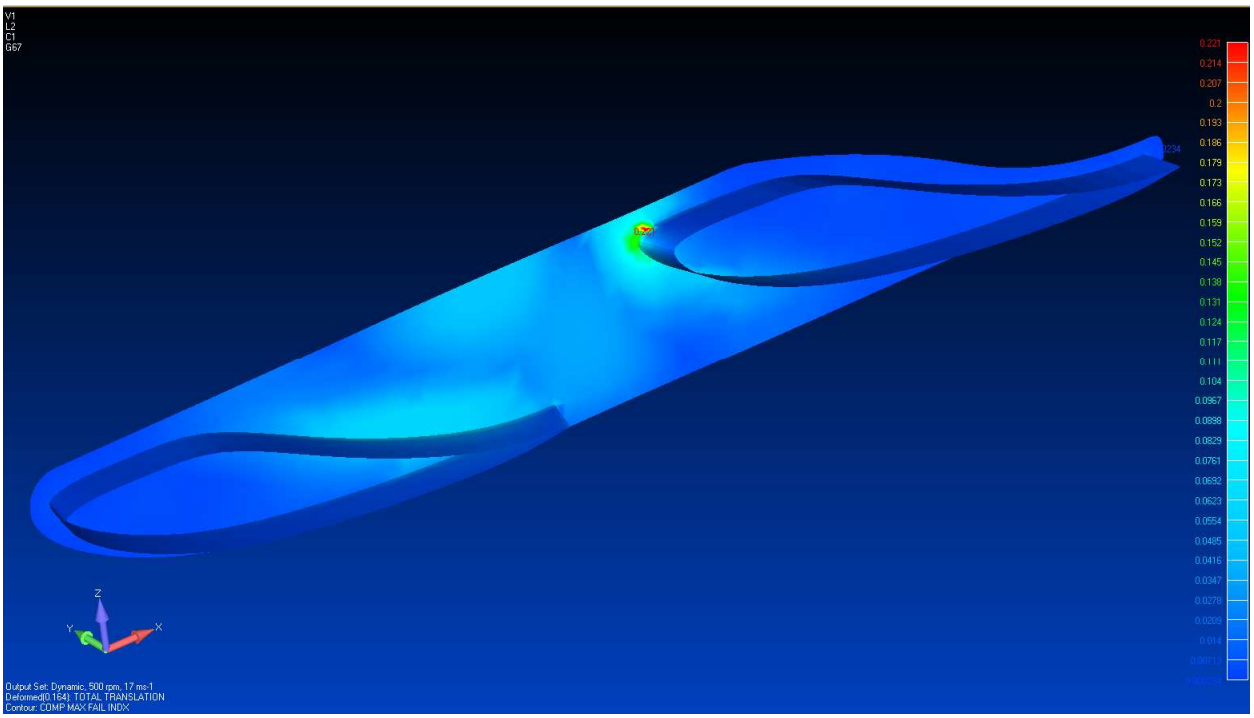

Figure 9.23 Dynamic Load, End Cap, Composite Max. Failure Index (0.221)

Figure 9.24 and Figure 9.25 show the maximum and minimum principal stresses and Figure 9.26 shows the maximum shear stress in the blade skins for the critical load case.

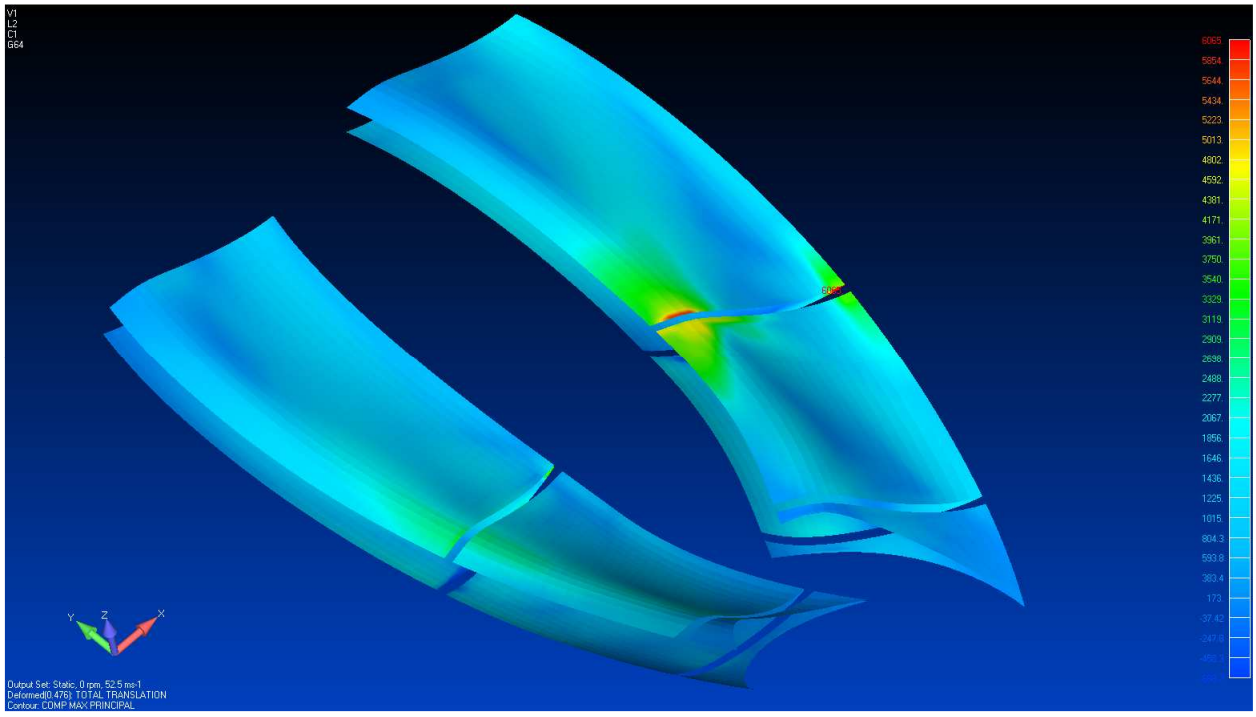

Figure 9.24 Static Load, Blade Skins, Max. Principal Stress ($\sigma_{1_{max}}$ =6,065 psi)

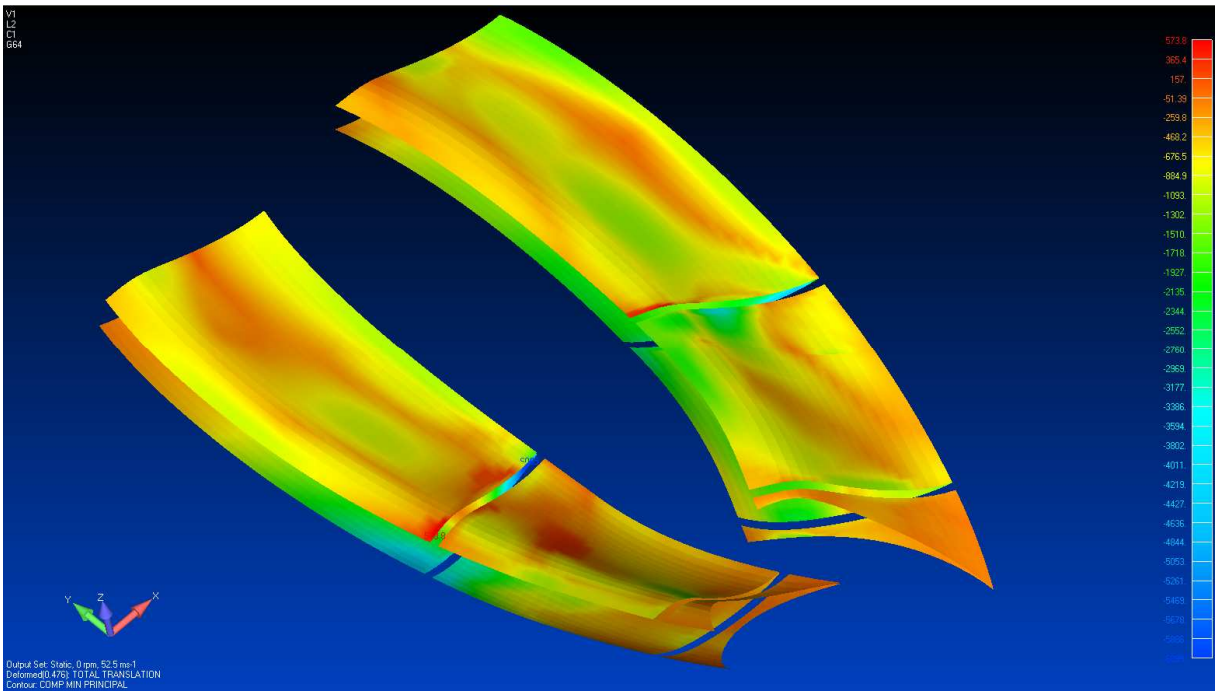

Figure 9.25 Static Load, Blade Skins, Min. Principal Stress ($\sigma_{1_{min}}$ =-6,095 psi)

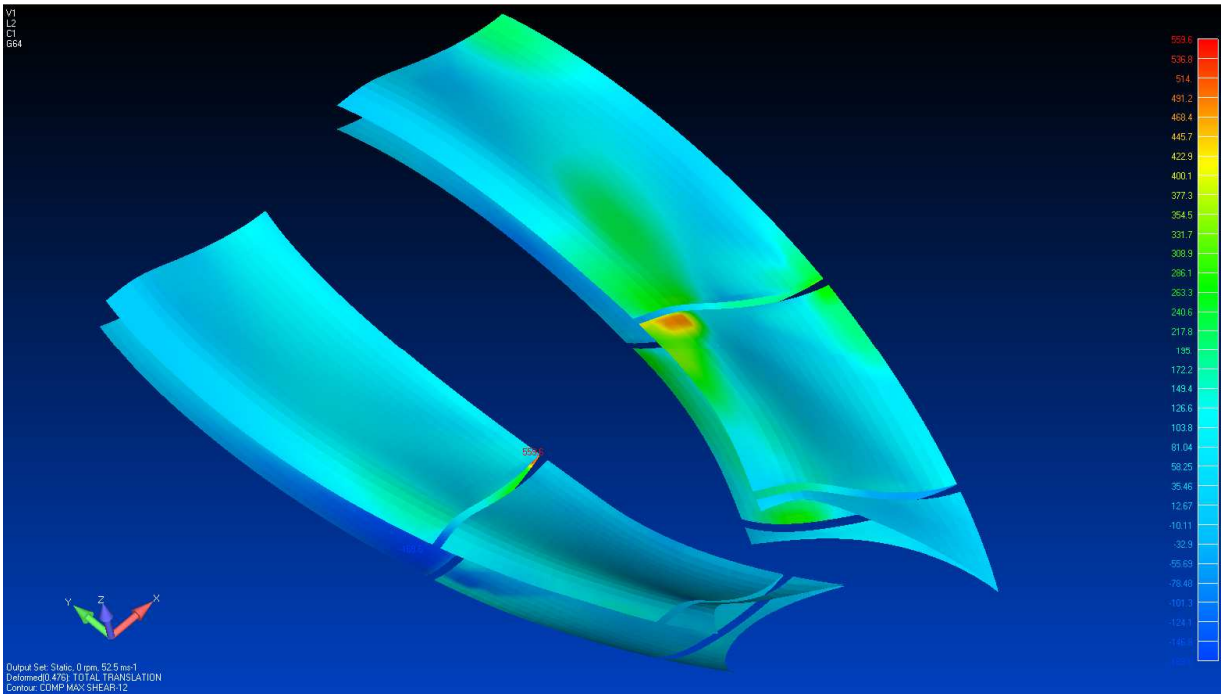

Figure 9.26 Static Load, Blade Skins, Max. Shear Stress (τ_{12} =560 psi)

Figure 9.27 and Figure 9.28 show the maximum and minimum principal stresses and Figure 9.29 shows the maximum shear stress in the blade skins in the region of the ribs for the critical load case.

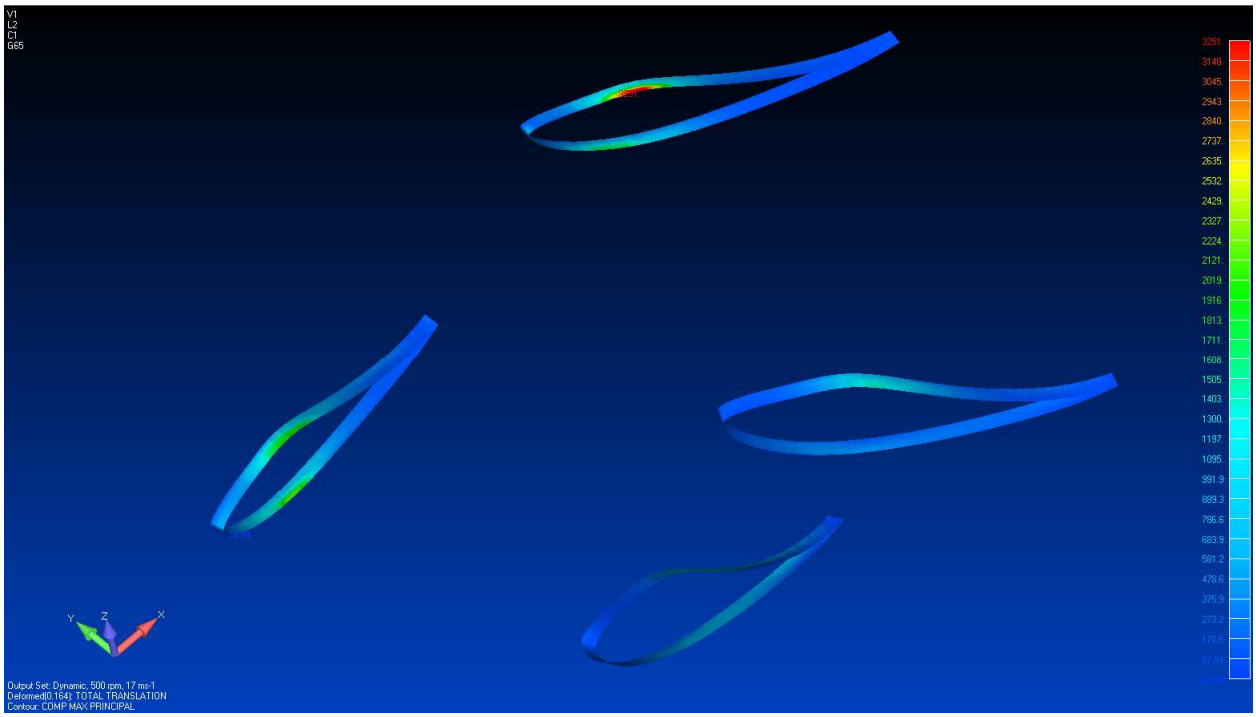

Figure 9.27 Dynamic Load, Blade-Rib Skins, Max. Principal Stress ($\sigma_{1_{max}}$ =3,251 psi)

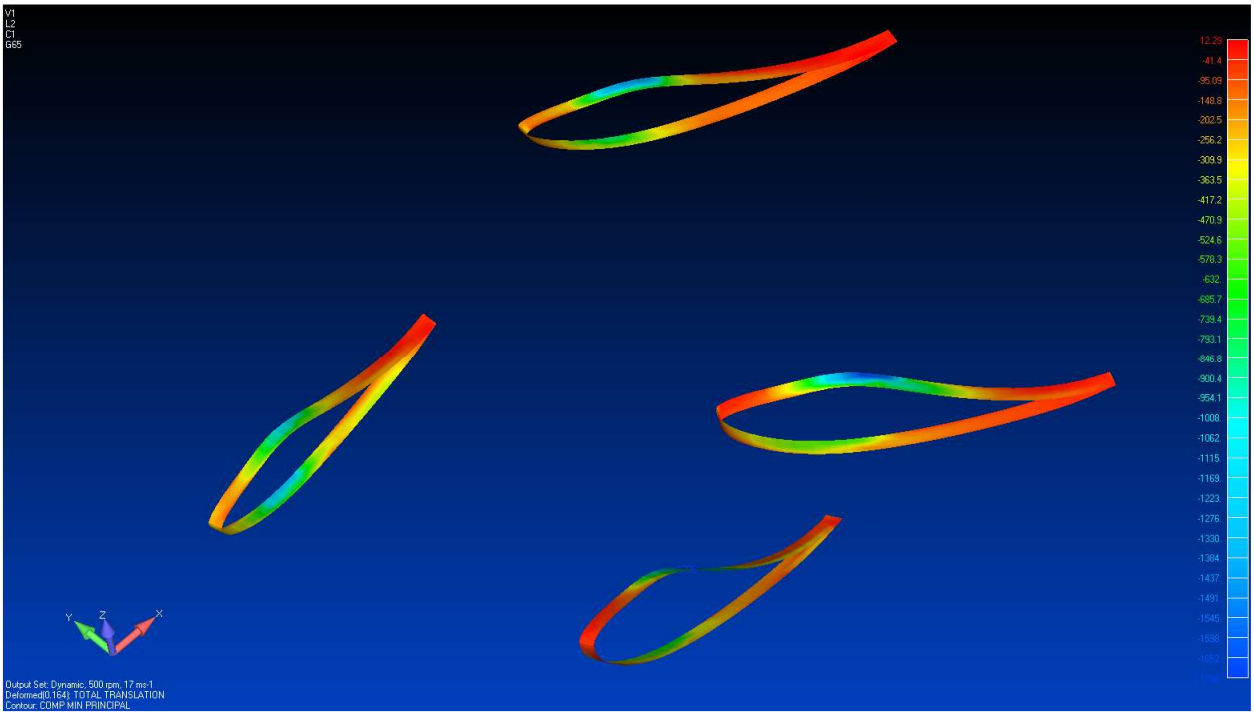

Figure 9.28 Dynamic Load, Blade-Rib Skins, Min. Principal Stress ($\sigma_{1_{min}}$ =-1,706 psi)

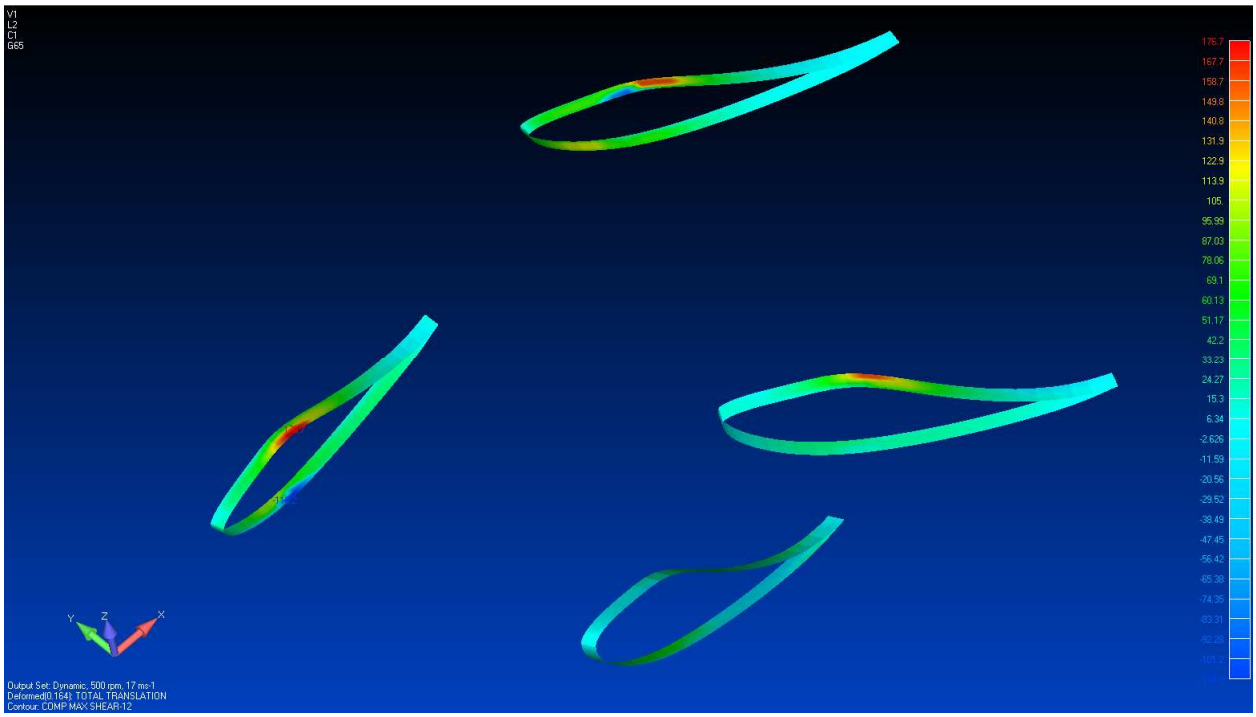

Figure 9.29 Dynamic Load, Blade-Rib Skins, Max. Shear Stress (τ_{12} =177 psi)

Figure 9.30 and Figure 9.31 show the maximum and minimum principal stresses and Figure 9.32 shows the maximum shear stress in the blade trailing edge for the critical load case.

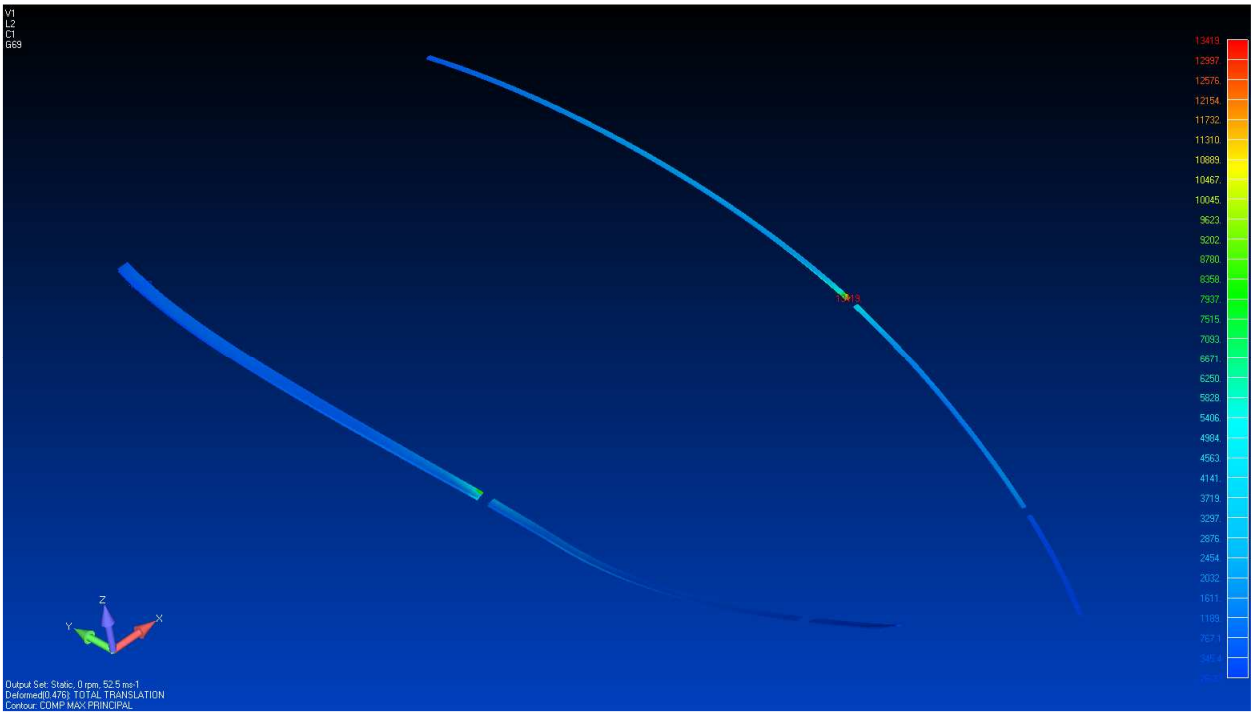

Figure 9.30 Static Load, Blade Trailing Edge Skin, Max. Principal Stress ($\sigma_{1_{max}}$ =13,419 psi)

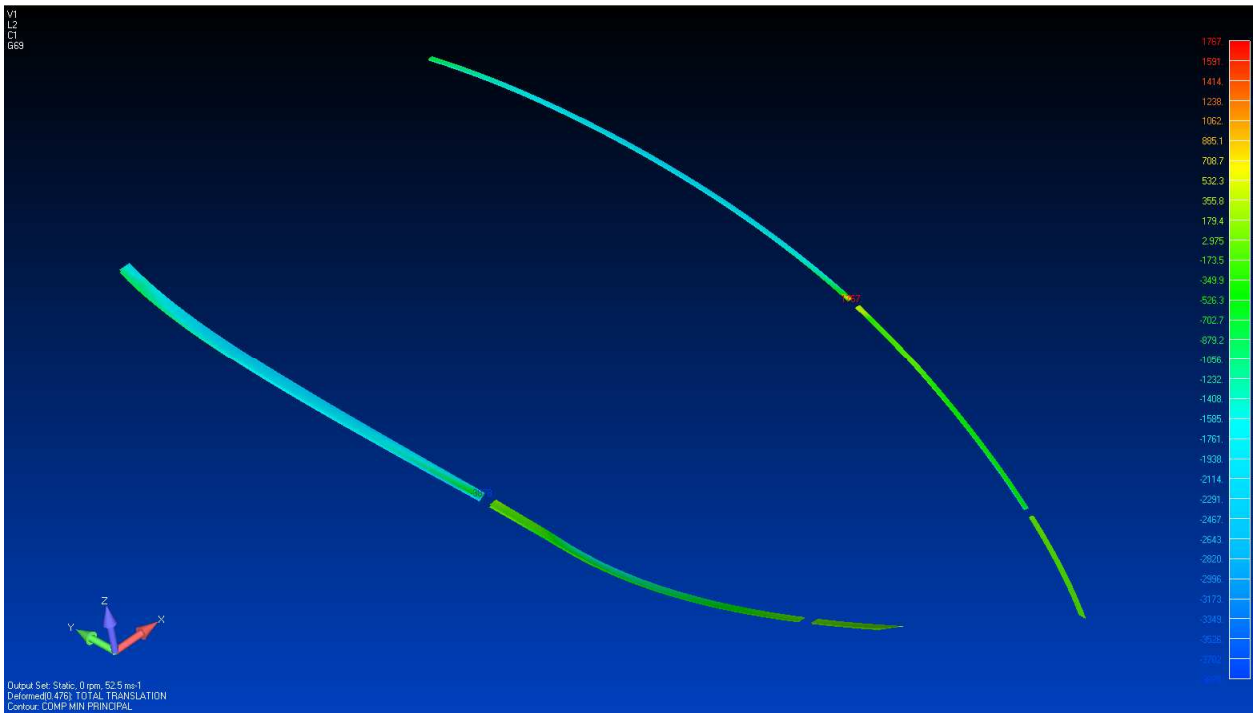

Figure 9.31 Static Load, Blade Trailing Edge Skin, Min. Principal Stress ($\sigma_{1_{min}}$ =-3,878 psi)

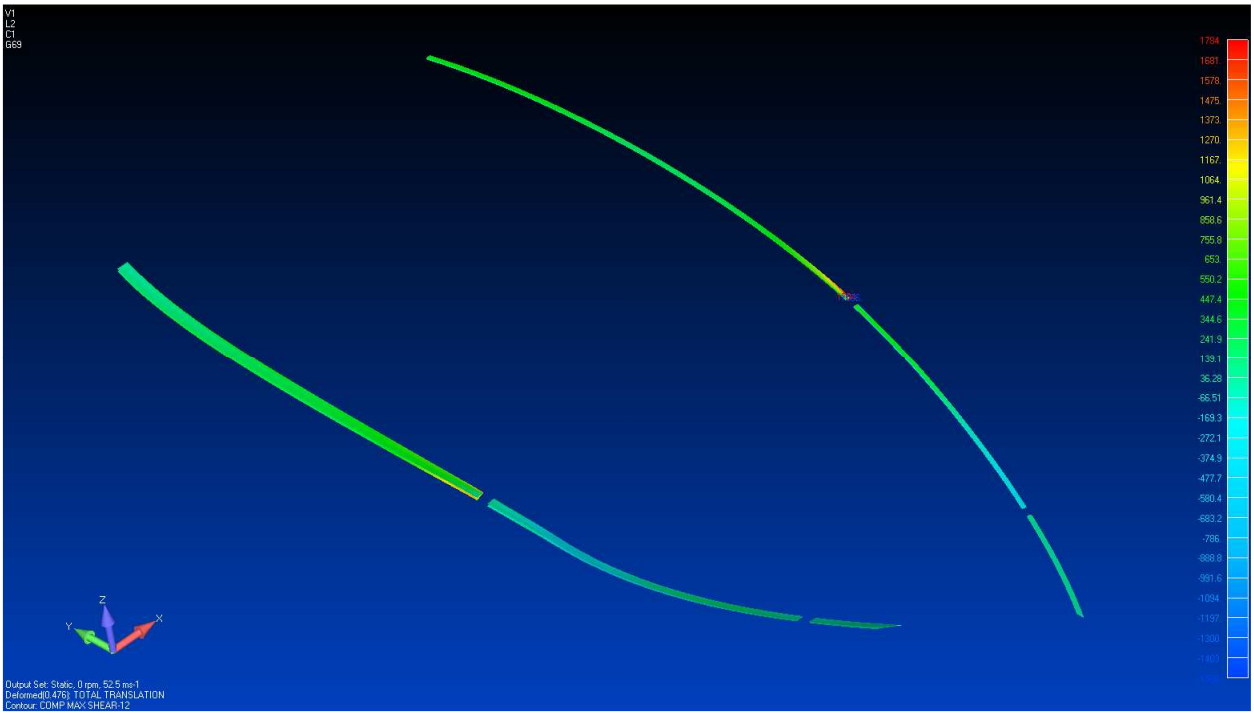

Figure 9.32 Static Load, Blade Trailing Edge Skin, Max. Shear Stress (τ_{12} =1,784 psi)

Figure 9.33 and Figure 9.34 show the maximum and minimum principal stresses and Figure 9.35 shows the maximum shear stress in the blade leading edge for the critical load case.

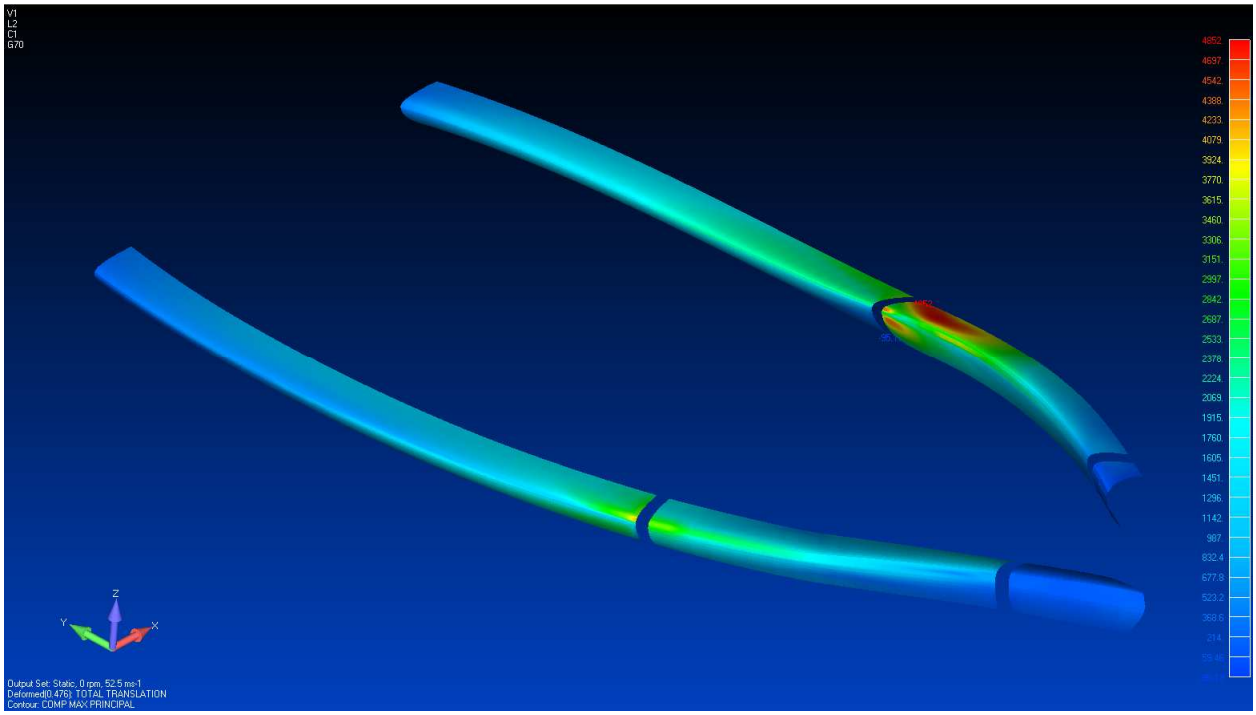

Figure 9.33 Static Load, Blade Leading Edge Skin, Max. Principal Stress ($\sigma_{1_{max}}$ =4,852 psi)

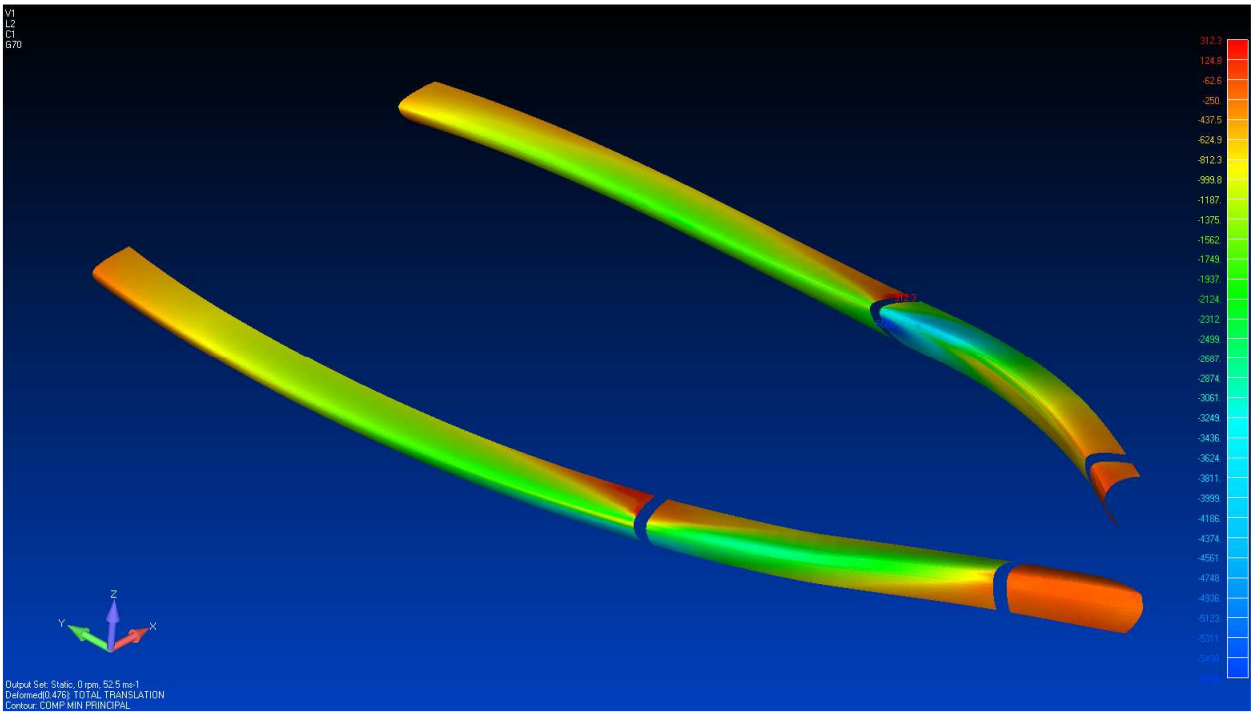

Figure 9.34 Static Load, Blade Leading Edge Skin, Min. Principal Stress ($\sigma_{1_{min}}$ =-5,686 psi)

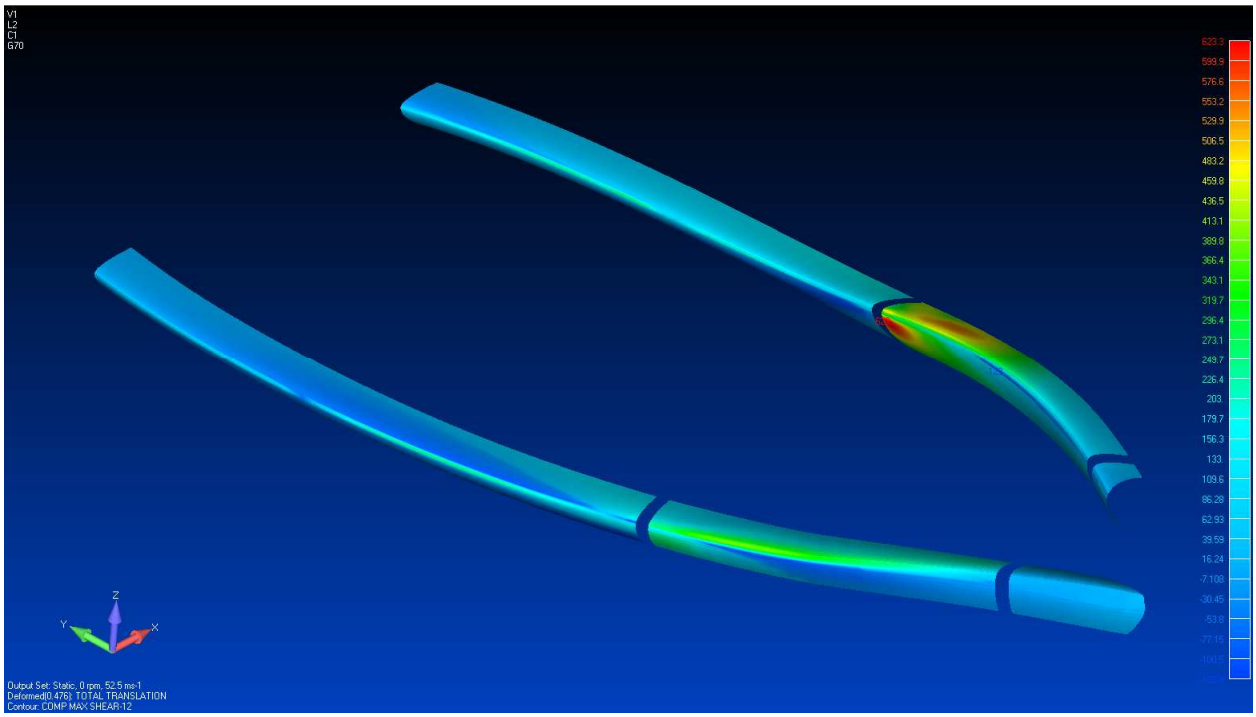

Figure 9.35 Static Load, Blade Leading Edge Skin, Max. Shear Stress (τ_{12} =623 psi)

Figure 9.36 and Figure 9.37 show the maximum and minimum principal stresses and Figure 9.38 shows the maximum shear stress in the blade end cap for the critical load case.

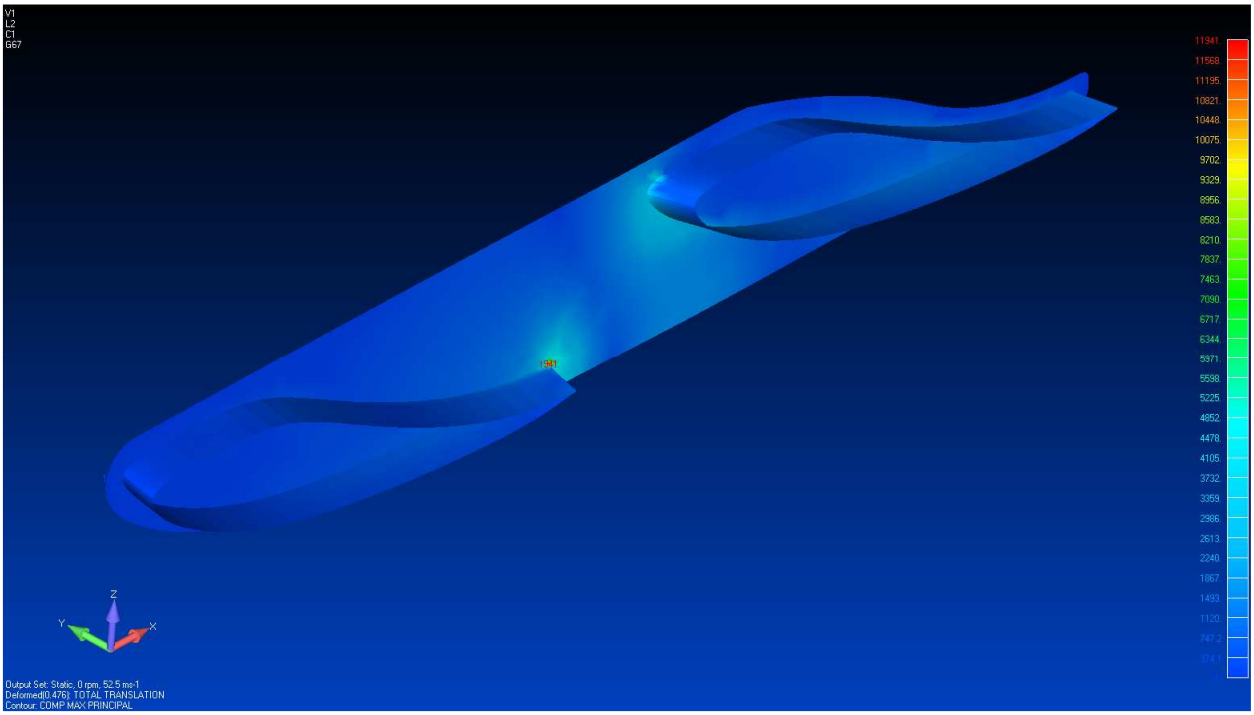

Figure 9.36 Static Load, End Cap, Max. Principal Stress ($\sigma_{1_{max}}$ =11,941 psi)

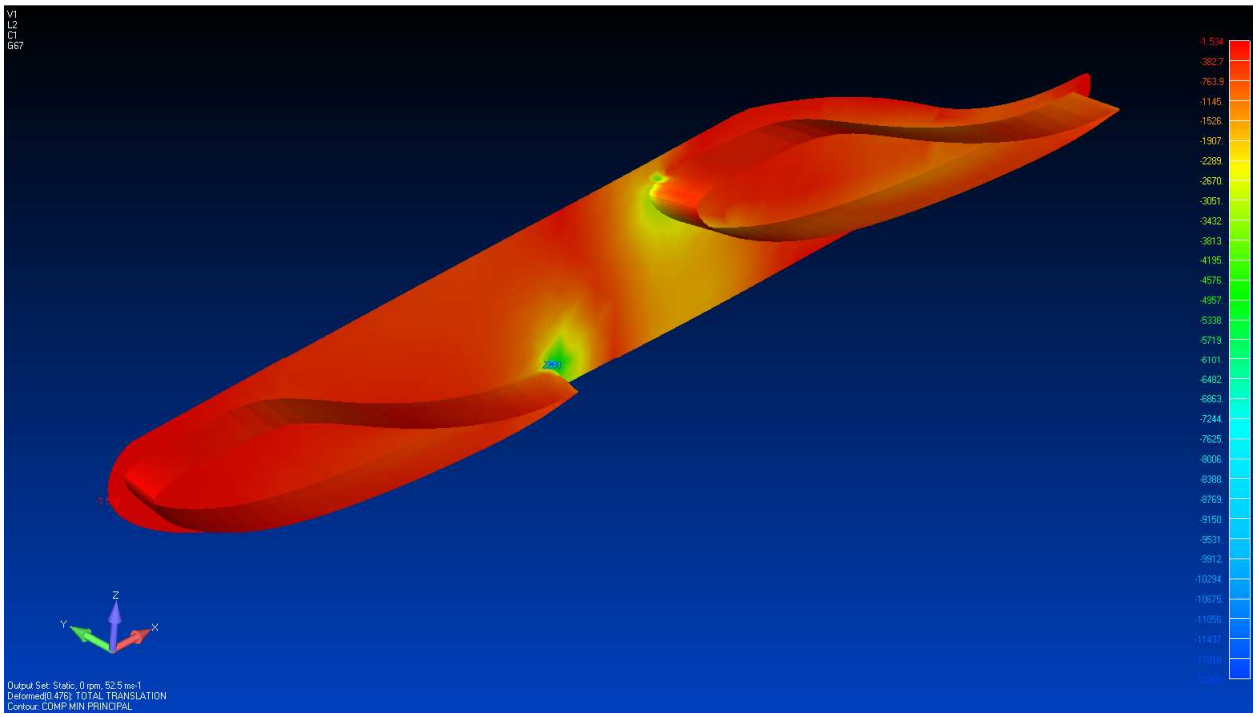

Figure 9.37 Static Load, End Cap, Min. Principal Stress ($\sigma_{1_{min}}$ =-12,200 psi)

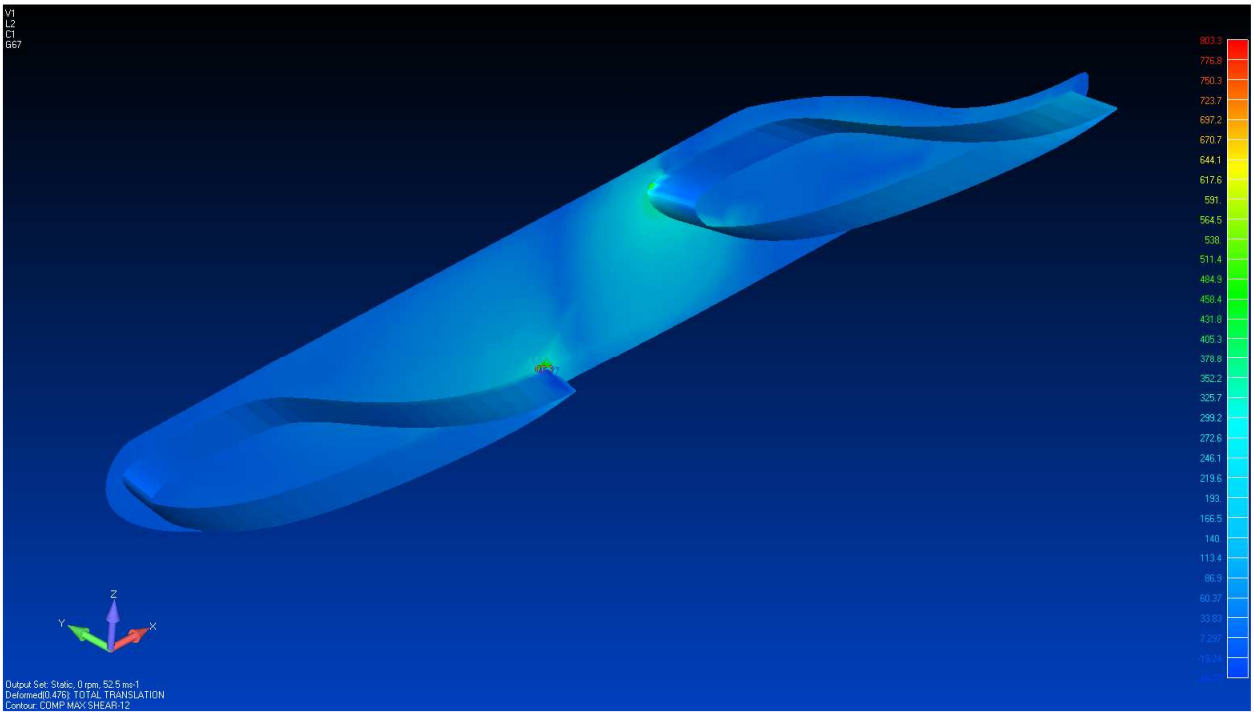

Figure 9.38 Static Load, End Cap, Max. Shear Stress (τ_{12} =803 psi)

Figure 9.39 and Figure 9.40 show the maximum and minimum principal stresses and Figure 9.41 shows the maximum shear stress in the ribs for the critical load case.

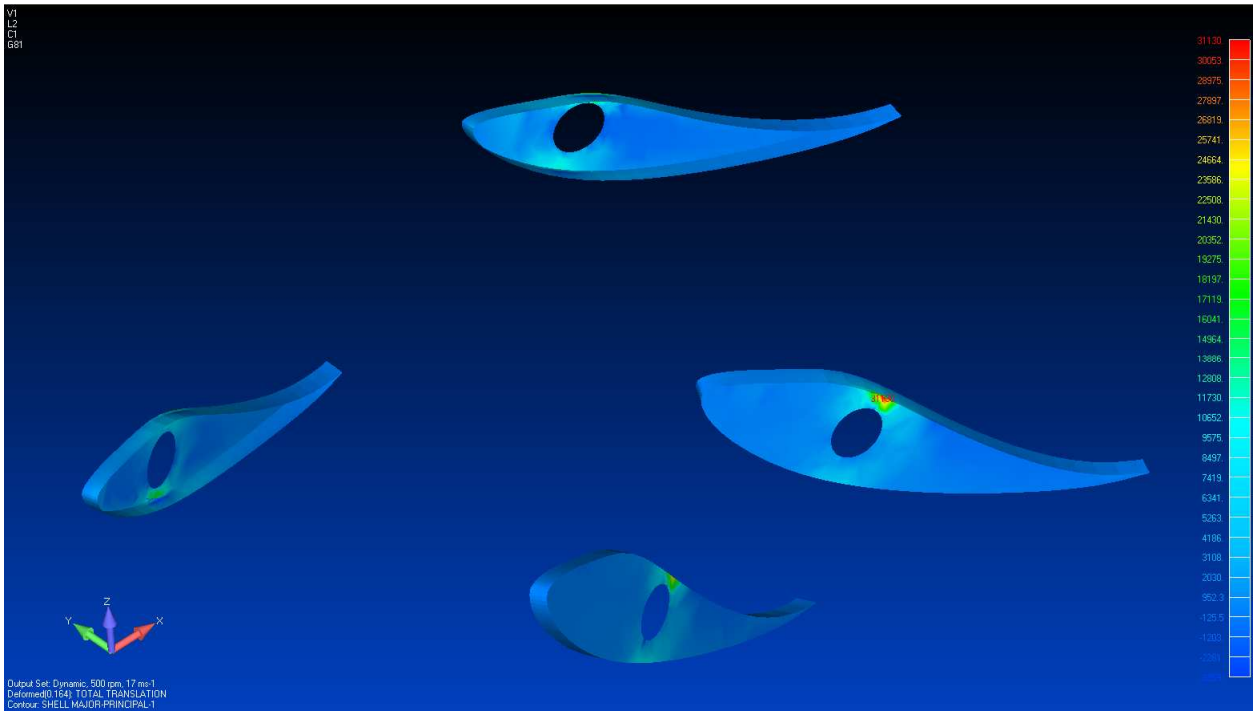

Figure 9.39 Dynamic Load, Ribs, Max. Principal Stress ($\sigma_{1_{max}}$ =31,130 psi)

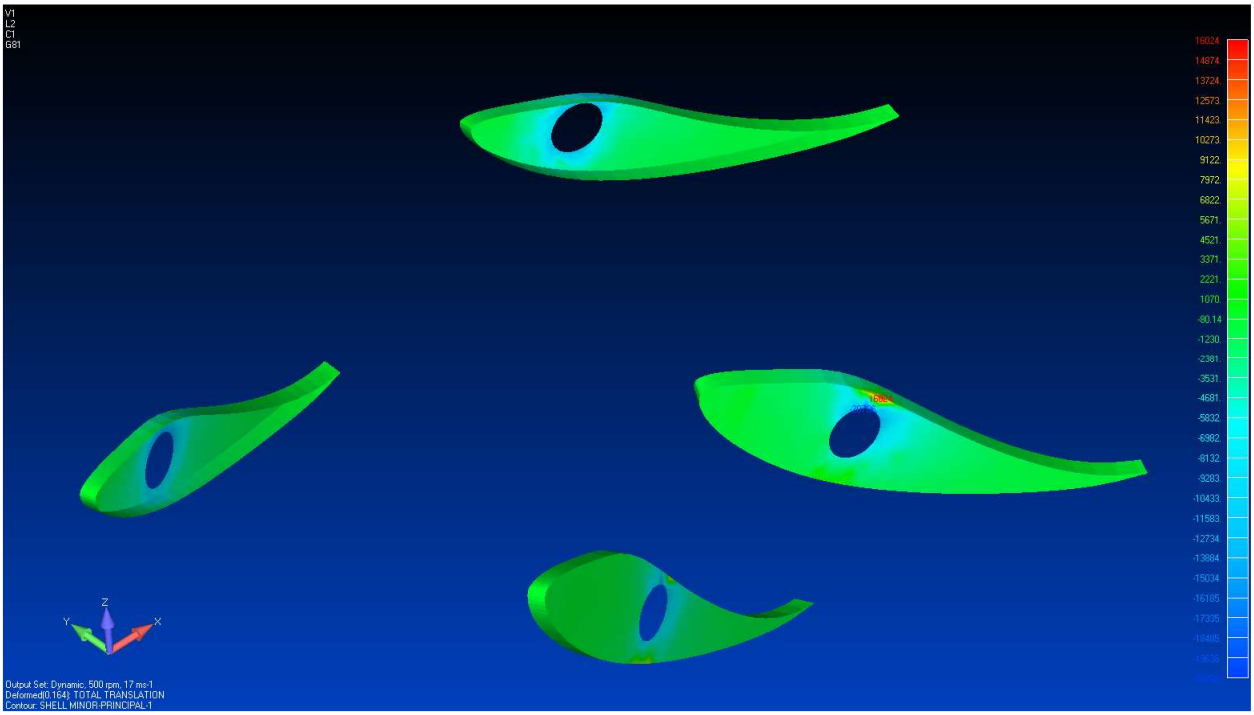

Figure 9.40 Dynamic Load, Ribs, Min. Principal Stress ($\sigma_{1_{min}}$ =-20,786 psi)

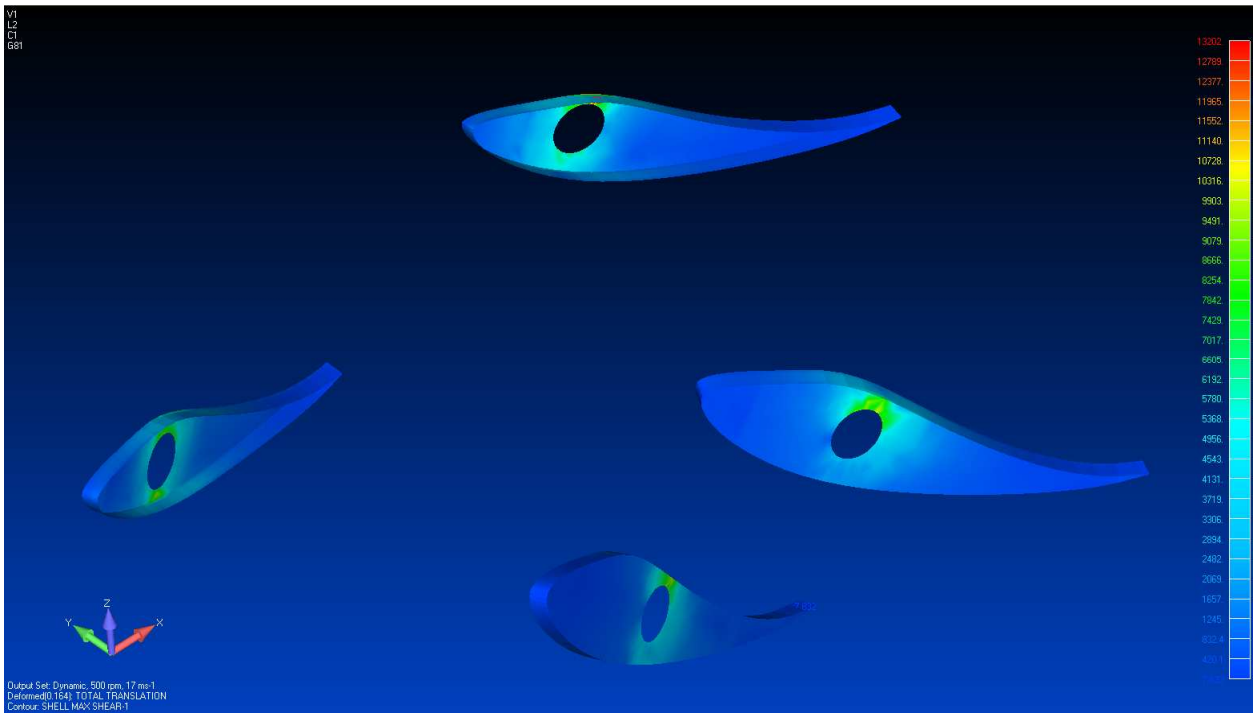

Figure 9.41 Dynamic Load, Ribs, Max. Shear Stress ($\tau_{\max}$ =13,202 psi)

Figure 9.42 and Figure 9.43 show the maximum and minimum principal stresses and Figure 9.44 shows the maximum shear stress in the circular spars for the critical load case.

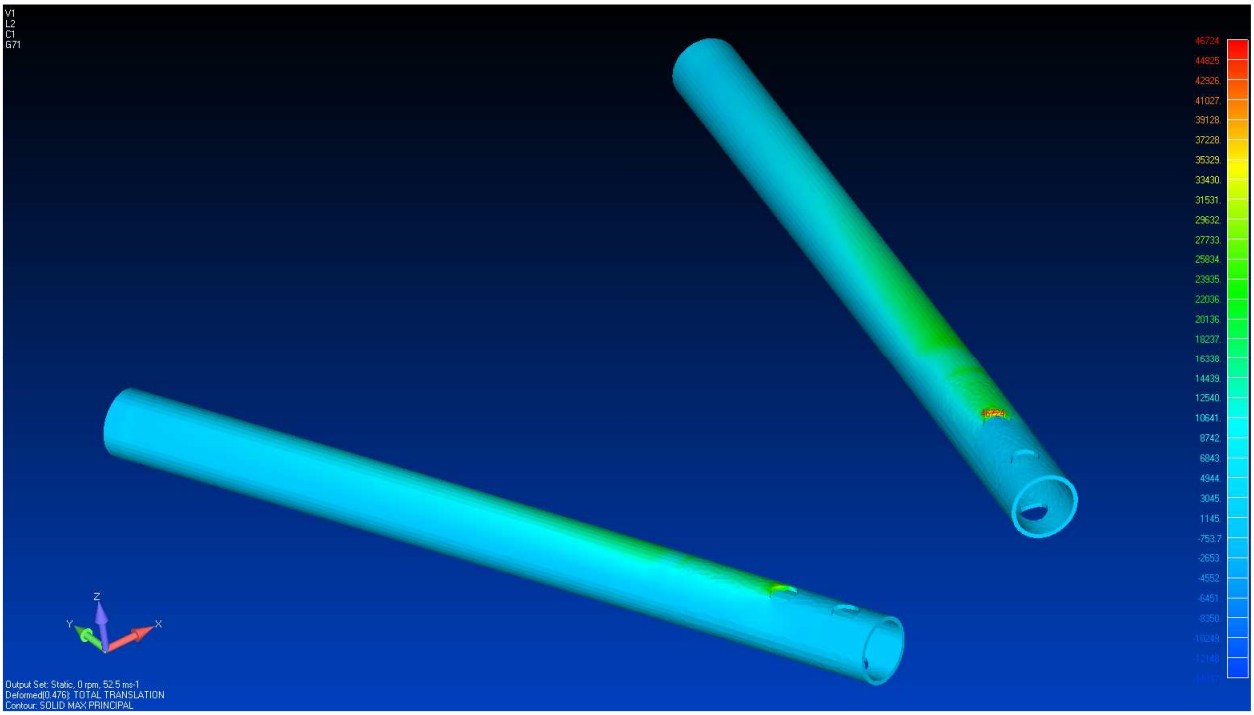

Figure 9.42 Static Load, Spars, Max. Principal Stress ($\sigma_{1_{max}}$ =46,724 psi)

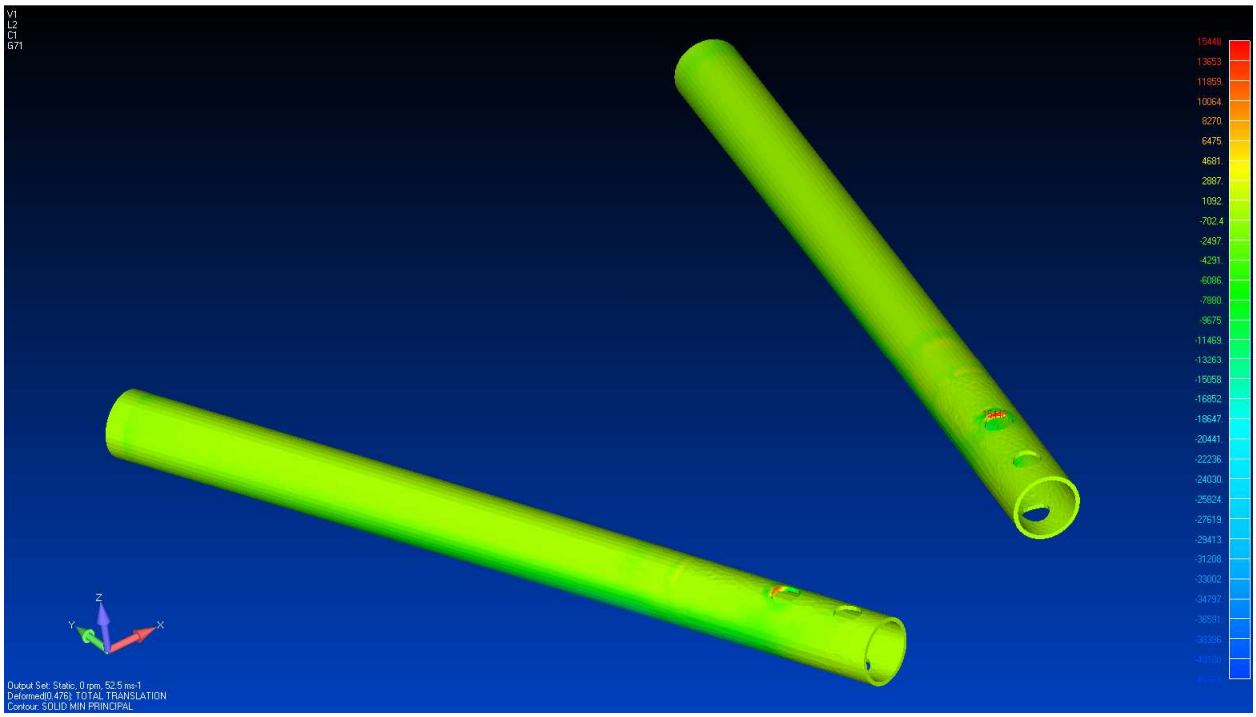

Figure 9.43 Static Load, Spars, Min. Principal Stress ($\sigma_{1_{min}}$ =-41,974 psi)

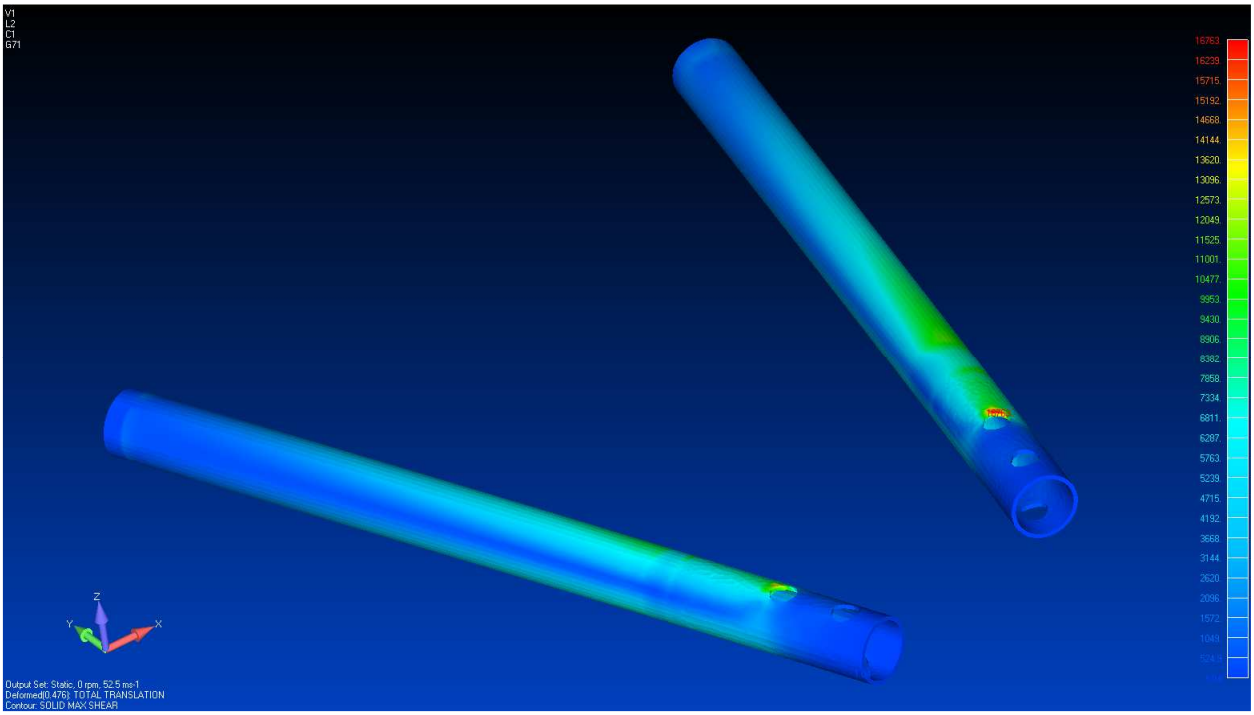

Figure 9.44 Static Load, Spars, Max. Shear Stress ($\tau_{\max}$ =16,763 psi)

Figure 9.45 and Figure 9.46 show the maximum and minimum principal stresses and Figure 9.47 shows the maximum shear stress in the circular spars inserts for the critical load case.

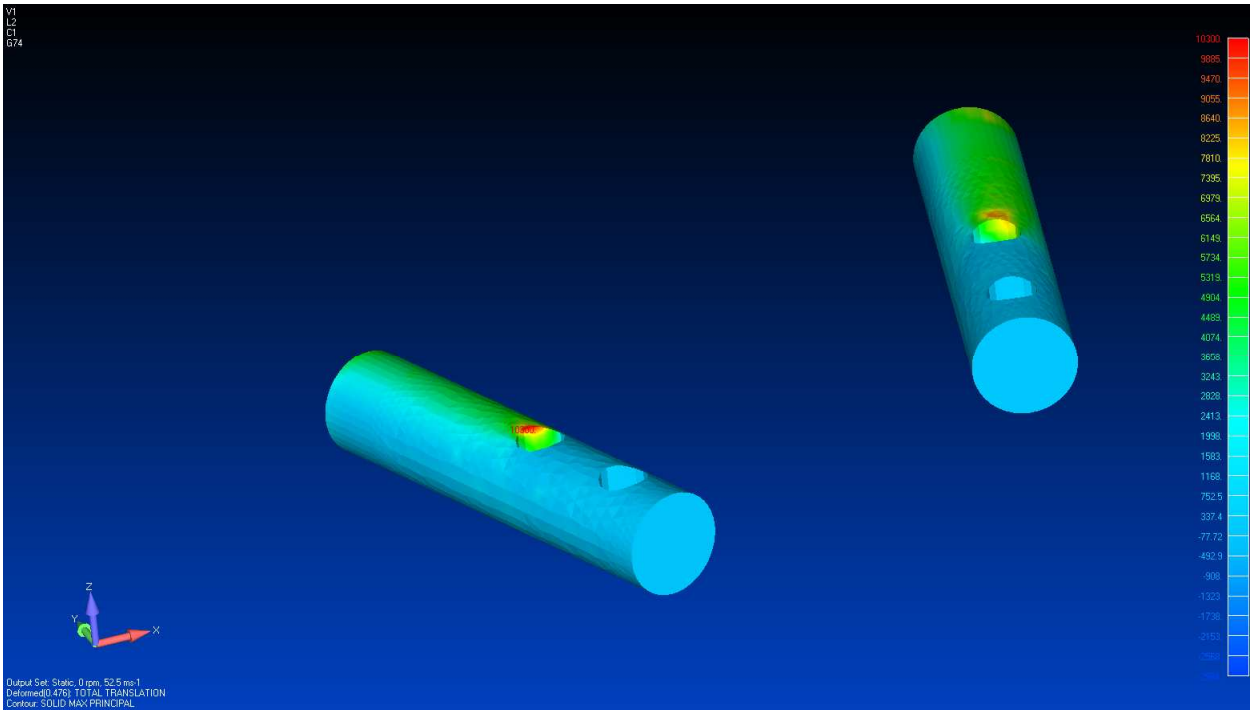

Figure 9.45 Static Load, Spar Inserts, Max. Principal Stress ($\sigma_{1_{max}}$ =10,300 psi)

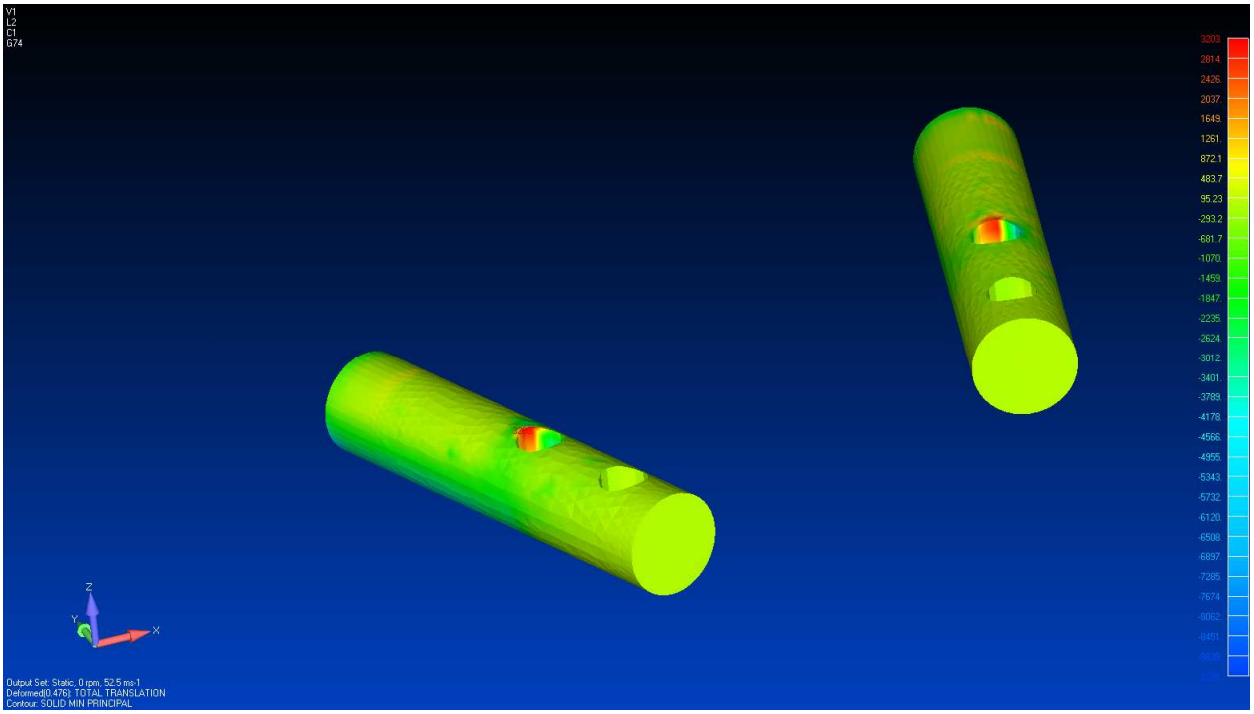

Figure 9.46 Static Load, Spar Inserts, Min. Principal Stress ($\sigma_{1_{min}}$ =-9,228 psi)

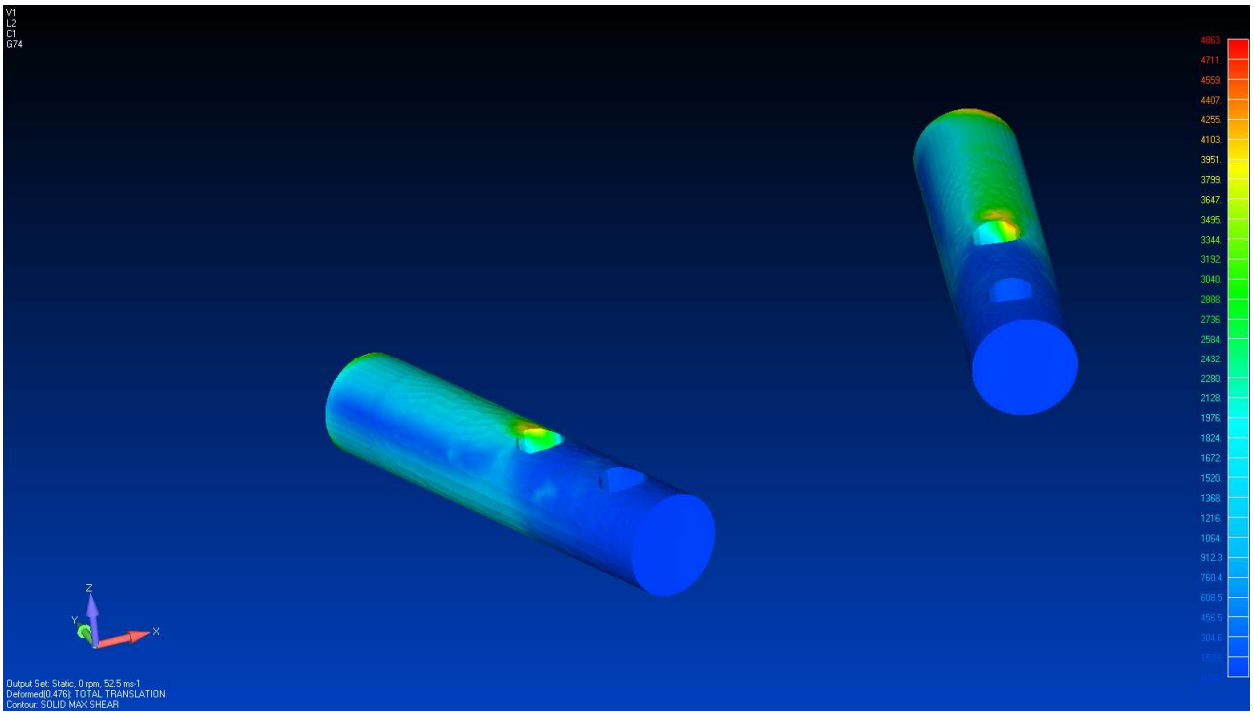

Figure 9.47 Static Load, Spar Inserts, Max. Shear Stress ($\tau_{\max}$ =4,863 psi)

The maximum and minimum principal stresses developed in the various components are as tabulated in Table 9.1.

Table 9.1 Summary of Stresses

Component	Major Principal Stress [psi]	Minor Principal Stress [psi]	Max Shear Stress [psi]
Blade Skins	6,065	-6,095	560
Blade Skins in the Region of Ribs	3,251	-1,706	177
Blade Trailing Edge Skin	13,419	-3,878	1,784
Blade Leading Edge Skin	4,852	5,686	623
End Cap	11,941	-12,200	803
Ribs	31,130	-20,786	13,202
Spars	46,724	-41,974	16,763
Spar Inserts	10,300	-9,228	4,863

Based on the yield stress and the actual stress, the safety factors in the various components are calculated as shown in Table 9.2.

Table 9.2 Summary of Safety Factors

Component	Major Principal Stress [psi]	Minor Principal Stress [psi]	Max Shear Stress [psi]
Blade Skins	12.16	7.26	11.67
Blade Skins in the Region of Ribs	22.68	25.94	36.92
Blade Trailing Edge Skin	5.49	11.41	3.66
Blade Leading Edge Skin	15.19	7.78	10.49
End Cap	6.17	3.63	8.14
Ribs	1.51	2.26	1.78
Spars	1.35	1.51	1.89
Spar Inserts	3.88	4.33	4.11

9.5 Fastener Sizing Analysis

Reaction loads from the finite element model are extracted to size the fasteners that connect the spars to the hub.

9.6 Conclusions from Finite Element Structural Analysis

The lowest factor of safety is 1.35 and is considered adequate for the current analysis. Fillets are not modeled in the present analysis. The presence of washers, fillets and rounded corners will reduce the stress concentrations. Fatigue analysis has not been carried out. A detailed fatigue analysis is warranted if this prototype design is to be used as a production model and will be operated over a longer period.

10. Sizing of the Vertical Tail Fin for the Hi-Q Design # 61 Wind Mill

10.1 Forces and Moments Acting on the Bergey XL.1 Wind Turbine

The forces and moments acting on the Bergey XL.1 wind turbine (illustrated in Figure 10.1 through Figure 10.4), with respect to the tower hinge and tail hinge, are examined.

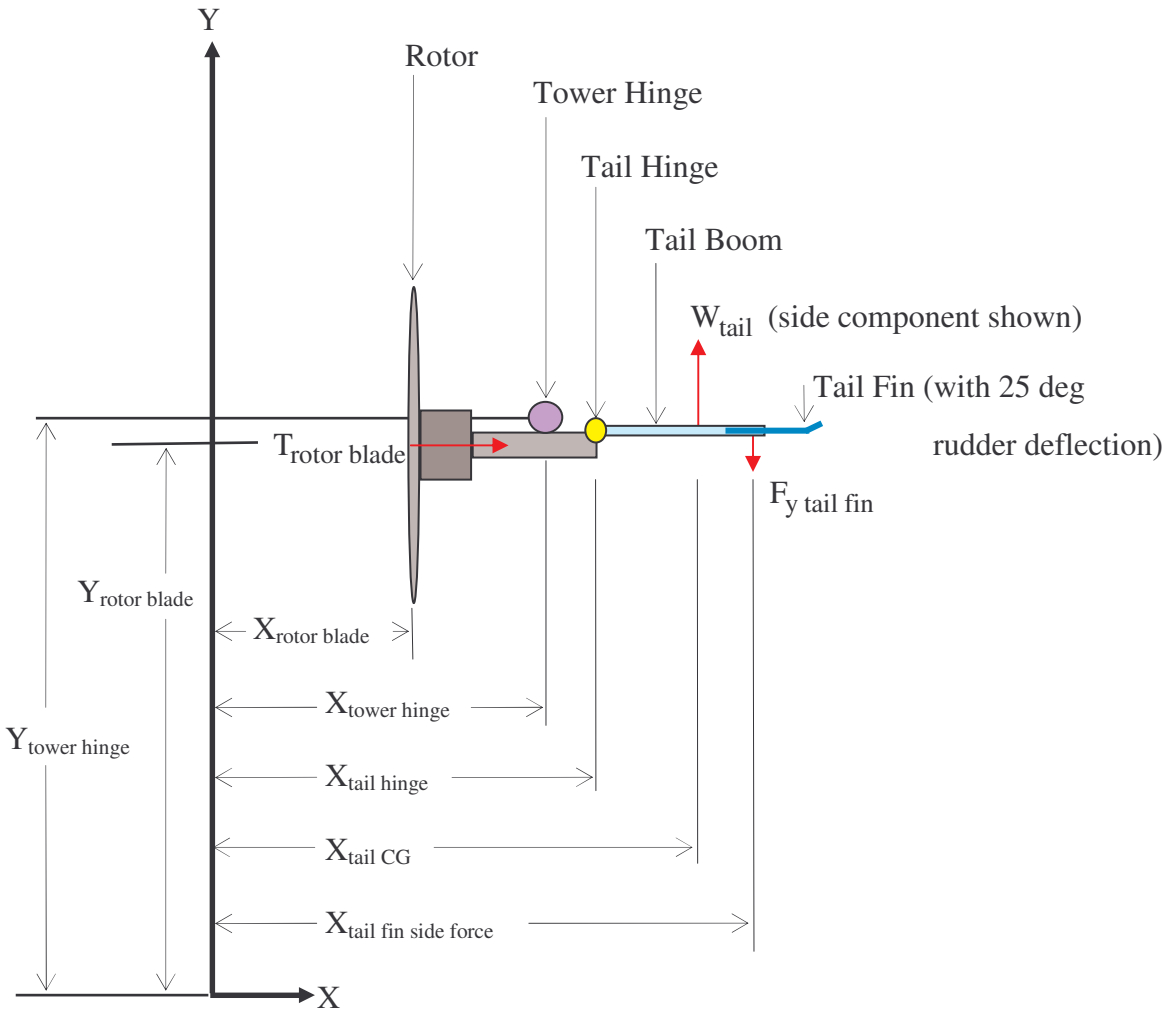

Figure 10.1 Forces and Moments Acting on the Bergey XL.1 (Top View)

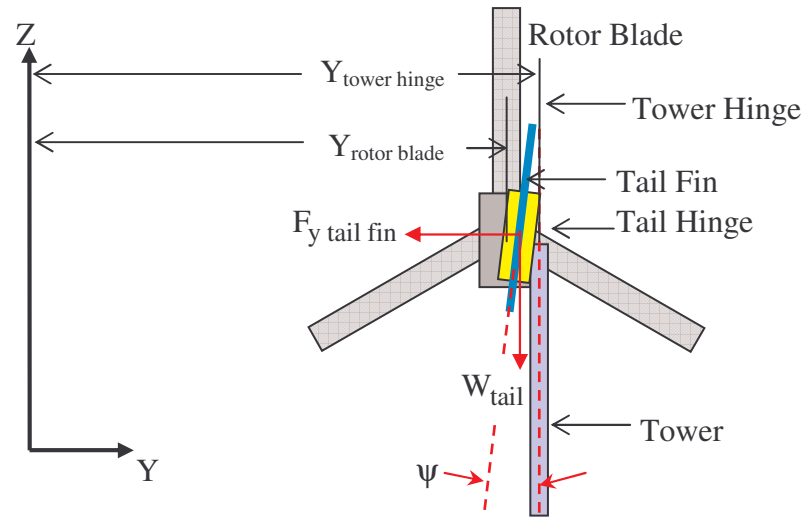

Figure 10.2 Forces and Moments Acting on the Bergey XL.1 (Back View)

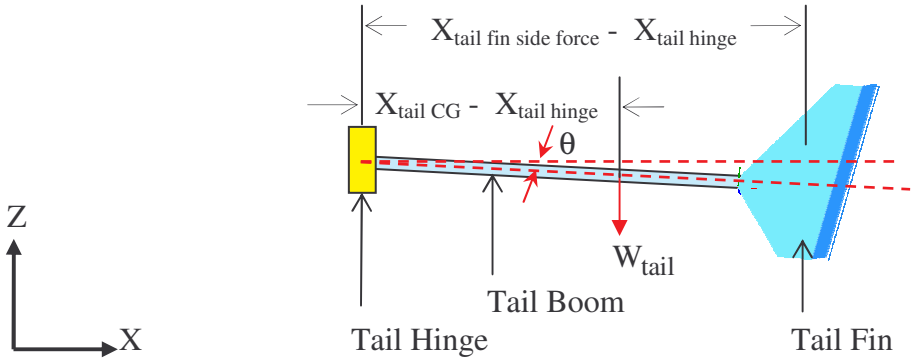

Figure 10.3 Bergey XL.1 Tail Section (Side View)

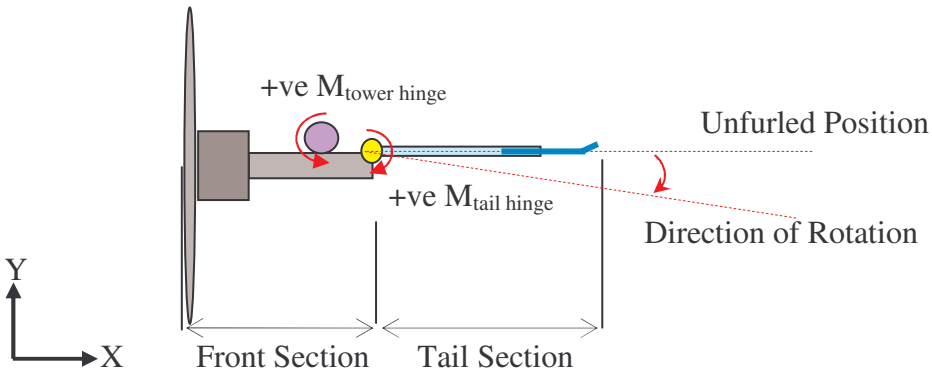

Figure 10.4 Moments about the Tower Hinge and the Tail Hinge (Top View)

As illustrated in Figure 10.3, the forces acting on the tail section of the Bergey XL.1 include:

1. The side force of the tail fin, $F_{y\ tail\ fin}$.
2. The weight of the tail fin and the tail boom combined (or $W_{tail} = W_{tail\ fin} + W_{tail\ boom}$)

The sum of the (directional) moments acting about the tail hinge, based on Figure 10.3, is as follows:

$$M_{tail\ hinge} = F_{y\ tail\ fin} \cos\psi \left(X_{tail\ fin\ side\ force} - X_{tail\ hinge} \right) - W_{tail} \sin\psi \left(X_{tail\ CG} - X_{tail\ hinge} \right) - M_{tail\ hinge\ friction}$$

where:

$$F_{y\ tail\ fin} = \frac{1}{2} \rho \left(V_{wind} \right)^2 S_{tail\ fin} C_{y\ tail\ fin}$$

$C_{y\ tail\ fin}$ = The non-dimensional side force coefficient of the tail fin, calculated by AAA (Reference 12).

$M_{tail\ hinge\ friction}$ = The static friction on the tail hinge.

From the above equation, it is found that, of the three terms on the right hand side of the equation, the first term, $F_{y\ tail\ fin} \cos\psi \left(X_{tail\ fin\ side\ force} - X_{tail\ hinge} \right)$, increases with an increase in wind speed. The second and the third terms are constants.

Based on the AAA calculation (Reference 12), the side force coefficient of the tail fin, $C_{y\ tail\ fin}$, taking the 25 deg rudder deflection into consideration (as illustrated in Figure 10.1), equals 0.5096. According to Bergey XL.1 Owners Manual (Reference 13), the tail section begins furling when wind speed exceeds 12.5 m/s. This implies:

1. At wind speed < 12.5 m/s, the sum of the moments acting about the tail hinge (shown in Equation for $M_{tail\ hinge}$) is negative.
2. At wind speed = 12.5 m/s, the sum of the moments acting about the tail hinge (shown in Equation for $M_{tail\ hinge}$) is zero.
3. At wind speed > 12.5 m/s, the sum of the moments acting about the tail hinge (shown in Equation for $M_{tail\ hinge}$) is positive.

Note: Positive tail hinge moment is clockwise, based on Figure 10.4.

Using the Equation for $M_{\text{tail hinge}}$, the magnitude of the tail hinge friction, $M_{\text{tail hinge friction}}$, is calculated.

$$M_{\text{tail hinge}} = \frac{1}{2}\rho\left(V_{\text{wind}}\right)^2 S_{\text{tail fin}} C_{\text{y tail fin}} \cos\psi \left(X_{\text{tail fin side force}} - X_{\text{tail hinge}}\right)$$
$$- W_{\text{tail}} \sin\psi \left(X_{\text{tail CG}} - X_{\text{tail hinge}}\right) - M_{\text{tail hinge friction}}$$
$$\Rightarrow 0 = \frac{1}{2}\left(1.225\frac{\text{kg}}{\text{m}^3}\right)\left(12.5\frac{\text{m}}{\text{s}^2}\right)^2 \left(0.1685\text{m}^2\right)(0.5096)\cos(7.7\text{deg})(1.002\text{m})$$
$$-(60.507\text{N})\sin(7.7\text{deg})(0.692\text{m}) - M_{\text{tail hinge friction}}$$
$$\Rightarrow M_{\text{tail hinge friction}} = 2.55 \text{ N-m}$$

The calculated tail hinge friction of 2.55 N-m is a constant and does not vary with a change in wind speed.

As illustrated in Figure 10.3 and Figure 10.4, the forces acting on the front section of the Bergey XL.1 include:

1. The thrust force of the rotor blades, $T_{\text{rotor blade}}$.
2. The side force of the tail fin, $F_{\text{y tail fin}}$ (which acts at the tail hinge).

The sum of the (directional) moments acting about the tower hinge, based on Figure 10.4, is expressed as follows:

$$M_{\text{tower hinge}} = T_{\text{rotor blade}}\left(Y_{\text{tower hinge}} - Y_{\text{rotor blade}}\right) - F_{\text{y tail fin}} \cos\psi \left(X_{\text{tail hinge}} - X_{\text{tower hinge}}\right)$$

where:

$$T_{\text{rotor blade}} = \sigma_{rotor}\frac{1}{2}\rho\left(V_{\text{wind}}\right)^2 S_{\text{rotor}}$$
$$\sigma_{rotor} = \frac{S_{\text{blade}}}{S_{\text{rotor}}} = \frac{0.372\text{m}^2}{\frac{\pi}{4}(2.438\text{m})^2} = 0.080 \text{ (Bergey 3-Bladed Rotor)}$$
$$S_{\text{rotor}} = \frac{\pi}{4}D^2_{\text{rotor}} = \frac{\pi}{4}(2.438\text{m})^2 = 4.67 \text{ m}^2$$

Note: Positive tower hinge moment is counter-clockwise, based on Figure 10.4.

Observing Equation for $M_{\text{tower hinge}}$, it is found that the rotor blade thrust force is always trying to push the rotor away from the oncoming wind. The moment induced by the rotor blade thrust, $T_{\text{rotor blade}}\left(Y_{\text{tower hinge}} - Y_{\text{rotor blade}}\right)$, needs to be balanced by the moment induced by the vertical tail fin side force, $F_{\text{y tail fin}} \cos\psi\left(X_{\text{tail hinge}} - X_{\text{tower hinge}}\right)$. There are three different conditions where the front section of the wind mill operates in:

1. When the sum of the moments acting about the tower hinge is negative, the wind mill tries to yaw to the right side (clockwise, as shown in Figure 10.4). The tail boom is not allowed to rotate clockwise past the unfurled position. Therefore the tail fin acts as a vertical tail of an airplane, provides directional stability to the wind mill and consequently yaws the rotor "back" to the oncoming wind. This implies the wind mill is directionally stable.

2. When the sum of the moments acting about the tower hinge is zero, the wind mill always points straight toward the oncoming wind, at wind speeds up to the tail boom furling wind speed. This implies the wind mill is directionally stable.

3. When the sum of the moments acting about the tower hinge is positive, the wind mill tries to yaw to the left side (counter-clockwise, as shown in Figure 10.4), and therefore increases the side force produced by the vertical tail fin. When the sum of the moments acting about the tail hinge (based on Equation for $M_{\text{tail hinge}}$) becomes positive, the tail section begins furling and that results in the wind mill yawing "away" from the oncoming wind. This implies the wind mill is directionally unstable.

It is desirable that the new vertical tail fin is sized so that it generates enough vertical tail fin side force such that the wind mill operates in the 2nd condition. In addition, the new vertical tail fin is located so that the tail section does not furl at wind speed < 12.5 m/s.

10.2 Sizing of the Vertical Tail Fin for the Hi-Q Design #61 Rotor Blades

Unlike the 3-bladed Bergey XL.1 rotor blades, the 3-bladed Hi-Q Design #61 rotor blade has a much higher rotor solidity ratio. Based on CFD analysis conducted on the Hi-Q Design #61 rotor blade, the non-dimensional rotor thrust coefficient, $C_{T\ rotor\ Hi\text{-}Q}$, as function of rotor tip speed ratio, λ, is identified. It is shown in Figure 10.5.

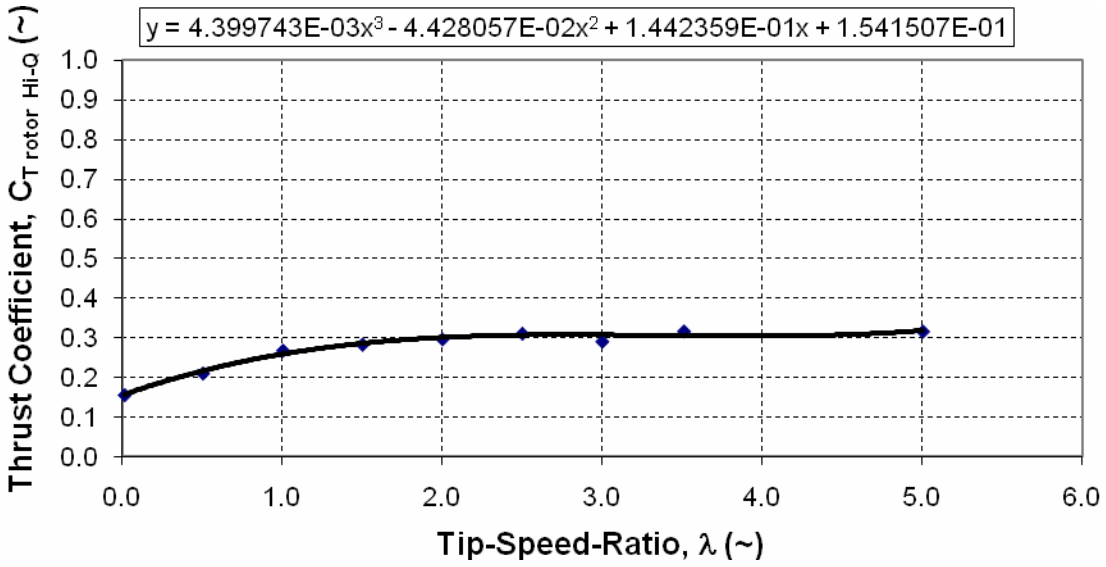

Figure 10.5 Change in Hi-Q Design #61 Rotor Thrust Coefficient as function of Tip Speed Ratio

The thrust coefficient of the Hi-Q Design #61 rotor is as follows:

$$C_{T\ rotor\ Hi\text{-}Q} = f(\lambda) = 4.399743\times10^{-3}\lambda^3 - 4.428057\times10^{-2}\lambda^2 + 1.442359\times10^{-1}\lambda + 1.541507\times10^{-1}$$

The thrust force of the Hi-Q Design #61 rotor is expressed as follows:

$$T_{rotor\ blade\ Hi\text{-}Q} = C_{T\ rotor\ Hi\text{-}Q}\frac{1}{2}\rho\left(V_{wind}\right)^2 S_{rotor}$$

It is observed in Figure 10.5 that the thrust coefficient of the Hi-Q Design #61 rotor levels off at 0.307.

Comparing the magnitude of the rotor thrust force between the Bergey XL.1 rotor blades and the Hi-Q Design #61 rotor blades, at a given wind speed, the Bergey XL.1 rotor thrust force is 27% of the Hi-Q Design #61 rotor thrust force. Repeating the calculation documented in Section 10.1, it is found that there is a need to resize the present vertical tail fin of 0.169 m^2, when the Hi-Q Design #61 rotor blades are mounted, to make sure that:

1. The furling of the tail boom does not occur at wind speed below 12.5 m/s.
2. The wind mill has adequate directional stability at wind speed up to 12.5 m/s.

Using equations described and AAA (Reference 12), the sizing of the new vertical tail fin, based on the above two criteria, are performed.

The sizing process produces a total of 9 different vertical tail fin designs. A summary of the geometrical and aerodynamic characteristics of the 9 designs are listed in Table 10.1.

Table 10.1 Geometric and Aerodynamic Characteristics of the 9 Vertical Tail Fins

Tail Fin #	$b_{tail\ fin}$ [in]	$c_{tail\ fin}$ [in]	$S_{tail\ fin}$ [ft^2]	$c_{tail\ rudder}$ [in]	$\delta r_{tail\ rudder}$ [deg]	$C_{y\ tail\ fin}$ [~]	$X_{LE\ tail\ fin} - X_{tail\ hinge}$ [in]
1	72	30	15.00	7.50	10.6	0.3099	6.10
2	72	24	12.00	6.00	11.9	0.3886	4.65
3	72	18	9.00	4.50	14.6	0.5172	4.21
4	72	15	7.50	3.75	18.0	0.6232	4.13
5	72	12	6.00	3.00	26.0	0.7770	4.29
6	60	30	12.50	7.50	15.0	0.3728	4.09
7	60	24	10.00	6.00	17.4	0.4659	3.54
8	60	18	7.50	4.50	24.6	0.6214	3.58
9	60	15	6.25	3.75	32.7	0.7456	3.74

Of the 9 tail fin designs, Tail Fin #8 is selected. The new vertical tail fin is shown in Figure 10.6.

Note: $S_{tail\ fin} = 7.5\ ft^2 = 0.6968\ m^2$.

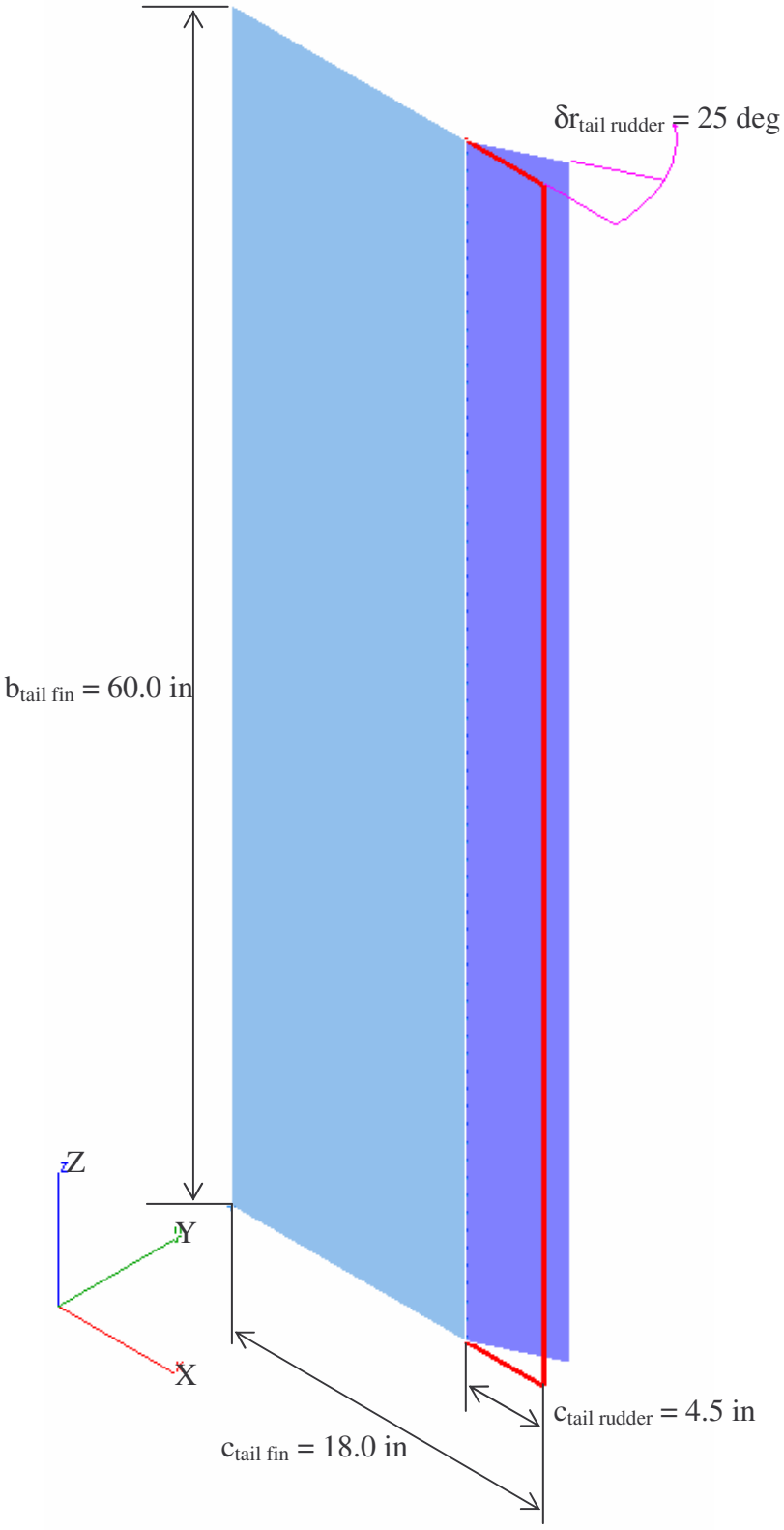

Figure 10.6 Isometric View of the New Vertical Tail Fin (Tail Fin #8)

11. Hi-Q #61 Assembly and Installation Instructions

11.1 Assembly and Installation Instructions

The first step is to install the main generator/hub assembly on the tower in order to have a base to work from. Using the six M10 x 35mm bolt, attach the tube adapter to whatever structure is being used. Install the bolts using the red Loctite provided. One thing to note is that the wiring needs to be addressed at this stage. Some components may need to be installed before or just after this step depending on the equipment being used. When the two power cables are attached, make sure to use the nylon zip ties to relieve any strain the slip ring assembly might see due to the weight of the wires running down the tower.

Next install the generator shroud and tail boom bumpers using the M5 hardware provided. Use blue Loctite on these bolts.

Tail Assembly: If the tower is in a position such that the tail boom can be installed next then do it; otherwise install it last. First install the tail fin to the boom if it is not already done. Use the M5 hardware provided with a locking washer and a fender washer. Use red Loctite on these screws. It is important that these screws not be over tightened or the balsa core will deform. Just tighten until a slight deformation is visible in the aluminum skin. There is a wood spacer and an aluminum bearing plate which need to be installed with the tail fin. The wood spacer between the tail boom and fin, and the bearing plate on top of the tail fin. Once this is done, attach the boom to the generator using the 12mm tail pivot pin. This should slide in easily by hand. Once installed, retain the pin using the washer and cotter pin provided. See Figure 11.1 for details. Once lower cotter pin is installed fold it over the pivot pin similar to the top cotter pin.

Figure 11.1 Tail Pivot Pin Installation

The next step is installing the blades. Begin by placing one bolt in each of the outer mounting holes for all of the blades. There needs to be a washer on the head of all the bolts except the inner bolt of the forward swept blade. Refer to Figure 11.2 for details.

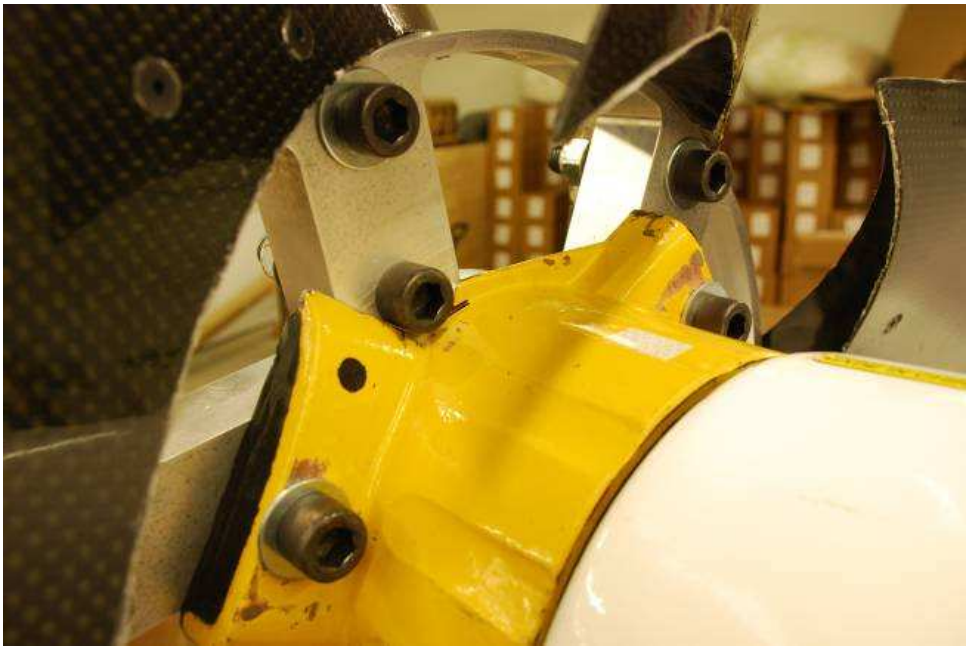

Figure 11.2 Blade Bolt Installation

Install the blade using the first bolt to position it correctly. Each blade is marked at the root with a number to be matched with the corresponding number on the hub. Once one bolt is in and there are enough threads showing to install the saddle, washer, and nut; do this to retain the blade while installing the second bolt. You will need to use a hammer to position the blade/insert the bolts. Once both bolts are installed and secure in a blade, move on to the next one. Assemble the odd number blades first, followed by the even numbers to maintain some balance. There are three different length bolts used in this step and when installed correctly, there should be roughly the same number of threads showing past the nut when tightened down. Figure 11.3 demonstrates what the finished installation should look like.

Figure 11.3 Blade Installation

When installing the blades, it is important that the correct hardware stacking sequence be used. The correct sequence begins with the aluminum pipe saddle on top of the blade support tube, followed by a washer, and then the nyloc lock nut. Tighten these down using the 15/16" socket on the air gun and the ½" allen socket. If there is no air available, just use another ratcheting wrench and tighten as hard as you can. Figure 11.4 shows the correct stack properly installed.

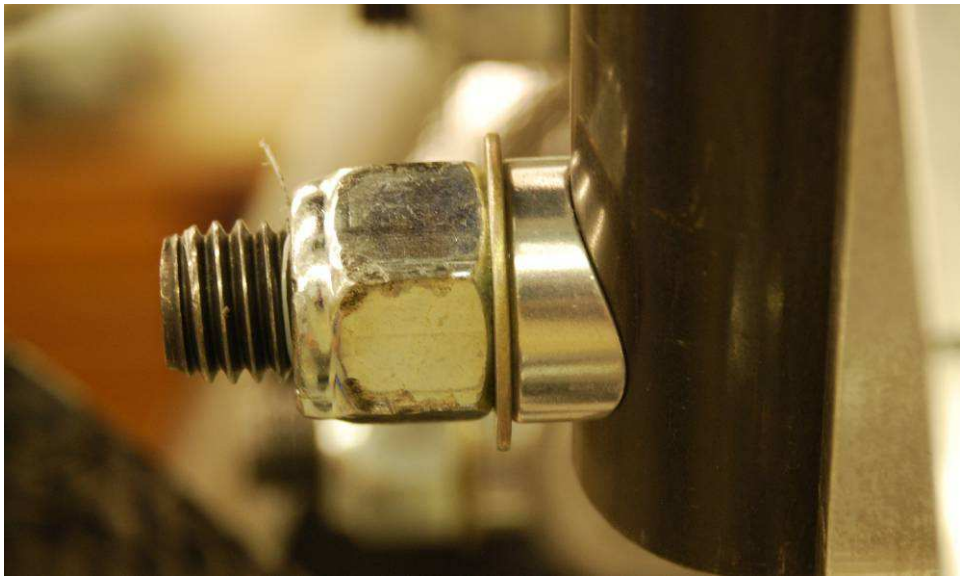

Figure 11.4 Blade Hardware Stacking

Once all the blades are installed, mount the spinner using the number on the brackets and hub to locate. You may need to rotate the spinner as you're mounting it to get it past the roots of the blades. Use ¼" self tapping screws with lock washers and washers. Use red Loctite on these. Do not over tighten or the aluminum threads will strip. Figure 11.5 shows this in detail.

Figure 11.5 Spinner Installation

The last thing to install are the endplates. Locate these using the numbers on the blades. Use the ¾" flat head Allen screws. The nut plates on the endplates are locking so no Loctite is needed here. Start all screws in one endplate before tightening any of them fully so it is easier to align all of the holes. If a hole is not aligned enough to insert a screw, use a small screwdriver in the adjacent hole to position the blade long enough to thread in a screw. Use setting 10 on the Craftsman drill to install the screws to the proper torque.

12. Hi-Q #61 Installation at West Texas A&M University

12.1 Introduction

The purpose of this chapter is to discuss the installation of the Hi-Q Design 61 wind mill blades and Bergey XL.1 at West Texas A&M University in Canyon, TX. Figure 12.1 shows the complete Hi-Q #61 blade assembly.

Figure 12.1 Design #61 Assembly

Figure 12.2 shows the Bergey XL.1 assembly.

Figure 12.2 Bergey XL.1 Assembly

The Bergey XL.1 was shipped to West TX A&M from Lawrence, KS. This windmill was assembled by West TX A&M personnel on a Bergey supplied tilt-up tower. The Hi-Q #61 assembly was transported by car to Canyon, TX and installed by DARcorporation personnel with help from West TX A&M personnel.

12.2 Installation

The Bergey XL.1 was erected on June 8, 2009 and was fully operational at the end of the day.

The following instrumentation was used for both the Bergey XL.1 and the Hi-Q #61:

Unit	Manufacturer	Description	Accuracy
Logger	Onset Computer	HOBO U30-NRC 15 channel	
Anemometer	Onset Computer	#40 standard sensor S-WSA-M003	within 0.1 m/s (0.2 mph) for the range 5 m/s to 25 m/s (11 mph to 55 mph)
Power Transducer	CR Magnetics	30 amp CR5400 series	1.0% of reading
Barometric Pressure	Onset Computer	S-BPB-CM50	±3 mbar at full range
voltage	Onset Computer	S-VIA-CM14	±1.221 millivolts

Figure 9.3 shows the instrumentation with the Bergey battery charge controllers in one box.

Figure 12.3 Instrumentation

The Hi-Q #61 assembly was installed on a Rohn SSV tilt-up tower at 63 ft. Both towers are 140 ft apart. Design #61was mounted on the tower on June 8 and erected on June 9 when it becaome fully operational. The autofurling system was tested and adjusted for proper functioning on June 9, 2009. The operation of both wind mills was monitored by DAR personnel until June 11. During those days wind speeds of up to 62 mph were recorded. The windmills were lowered on June 11 and checked for any damage or loose hardware. No damage was found.

Further operation of both wind mills was conducted by West TX A&M University personnel until July 22, 2009. On regular intervals both towers were lowered to inspect for damage and to check the electronics.

13. West Texas A&M University Testing IEC Data Interpretation

13.1 Introduction

The purpose of this document is to display the results of the testing done on the Hi-Q prototype turbine design #61 and the Bergey XL.1 turbine at the West Texas A&M University wind turbine testing facility. In order to provide comparative, concise data, the IEC wind turbine power performance measurement international standard (Reference 14) was used to normalize the data. The goal of this study is to compare performance data from both turbines by filtering any erroneous data and signal noise.

13.2 Normalization Process

Following the process detailed in the IEC standard, the first step in calculating the power curve is to take the pressure, temperature, and relative humidity measurements from testing and calculate the air density on site.

The following is from Section 6.4 of Reference 14. Air density shall be derived using air pressure and air temperature data collected during testing. Relative humidity should also be factored into the density calculations using the following equation.

$$\rho = \frac{1}{T}\left(\frac{B}{R_0} - \phi P_w\left(\frac{1}{R_0} - \frac{1}{R_w}\right)\right)$$

Where:

B is the barometric pressure (Pa)

T is the absolute temperature (K)

ϕ is the relative humidity (0-1)

R_0 is the gas constant of dry air (287.05 J/kg-K)

R_w is the gas constant of water vapor (461.5 J/kg-K)

P_w is the vapor pressure (Pa)

$$P_w = 0.0000205 e^{(0.0631846 \times T)}$$

Once the air density is calculated it is used in conjunction with the ISO standard atmosphere to normalize the power output.

The following is from Section 8.1 of Reference 14. The data is normalized to two reference air densities. The first is the ISO standard atmosphere (1.225kg/m^3). The second is the average of the measured air density at the test site during the periods of valid data.

For a wind turbine which is stall regulated data normalization shall be applied to the measured power output using the following equation.

$$P_n = P_{10\,\min} \times \frac{\rho_0}{\rho_{10\,\min}}$$

Where:

P_n is the normalized power output (watt)

$P_{10\,\min}$ is the measured power average over 10 min (watt)

ρ_0 is the reference air density (1.225 kg/m^3)

$\rho_{10\,\min}$ is the calculated air density using (1) averaged over 10 min (kg/m^3)

The normalized power data and measured wind speed data is then averaged over 10 minute periods to further refine the data.

The following is from Section 8.2 of Reference 14. To determine the measured power curve, use the method of bins for the normalized data sets. Using 0.5 m/s bins, calculate the mean values of the normalized wind speed and power output for each bin using the following equations.

$$V_i = \frac{1}{N_i} \sum_{j=1}^{N_i} V_{n,i,j}$$

$$P_i = \frac{1}{N_i} \sum_{j=1}^{N_i} P_{n,i,j}$$

Where:

V_i is the normalized and averaged wind speed in bin i

$V_{n,i,j}$ is the normalized wind speed of data set j in bin i

P_i is the normalized and averaged power output in bin i

$P_{n,i,j}$ is the normalized power output of data set j in bin i

N_i is the number of 10 minute data sets in bin i

Another useful interpretation of the data is the power coefficient, which uses the averaged normalized data to relate the power curve to the air density and rotor swept area.

The following is from Section 8.4 of Reference 14. The power coefficient C_p should be added to the test results and presented. The following equation is used to determine this coefficient.

$$C_{p,i} = \frac{P_i}{\frac{1}{2}\rho_0 A V_i^3}$$

Where:

$C_{p,i}$ is the power coefficient in bin i

V_i is the normalized and averaged wind speed in bin i

P_i is the normalized and averaged power output in bin i

A is the swept area of the wind turbine rotor (m^2)

ρ_0 is the reference air density (1.225 kg/m^3)

13.3 Data Presentation

Once the data is averaged and normalized, the power curves are plotted with reference to 0.5m/s bins in order to visualize the turbine's characteristics. Figure 13.1 (Reference 15) displays the power curve for the Bergey XL.1 turbine. Of particular interest is how the power output is greatest at the rated wind speed of 11m/s, but substantially less at 6-7 m/s, which is where a large portion of the data was taken. Figure 13.2 shows the power coefficient versus bin wind speed plot.

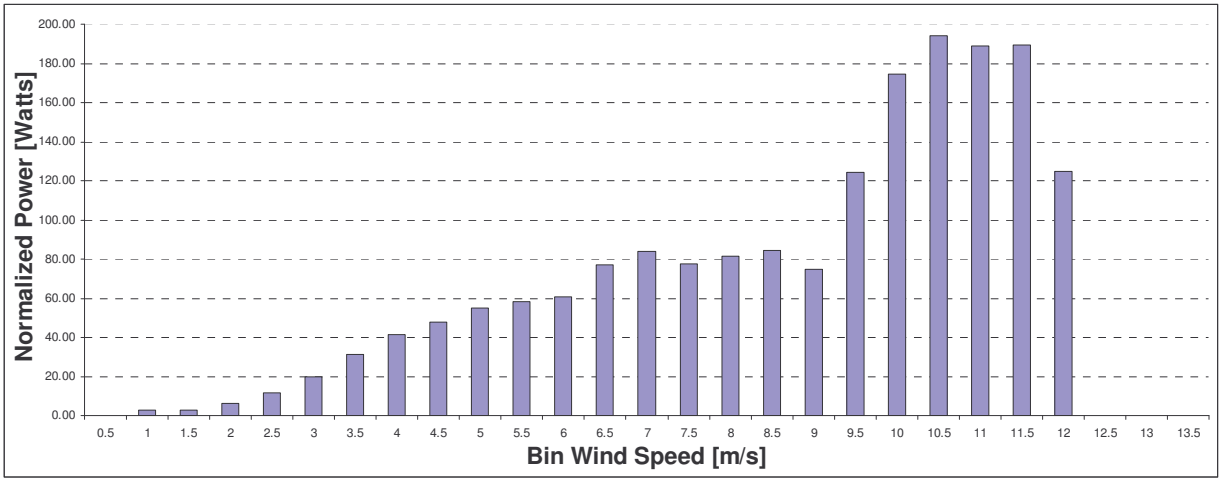

Figure 13.1 Bergey XL.1 Test Data - Normalized Average Power vs. Bin Wind Speed

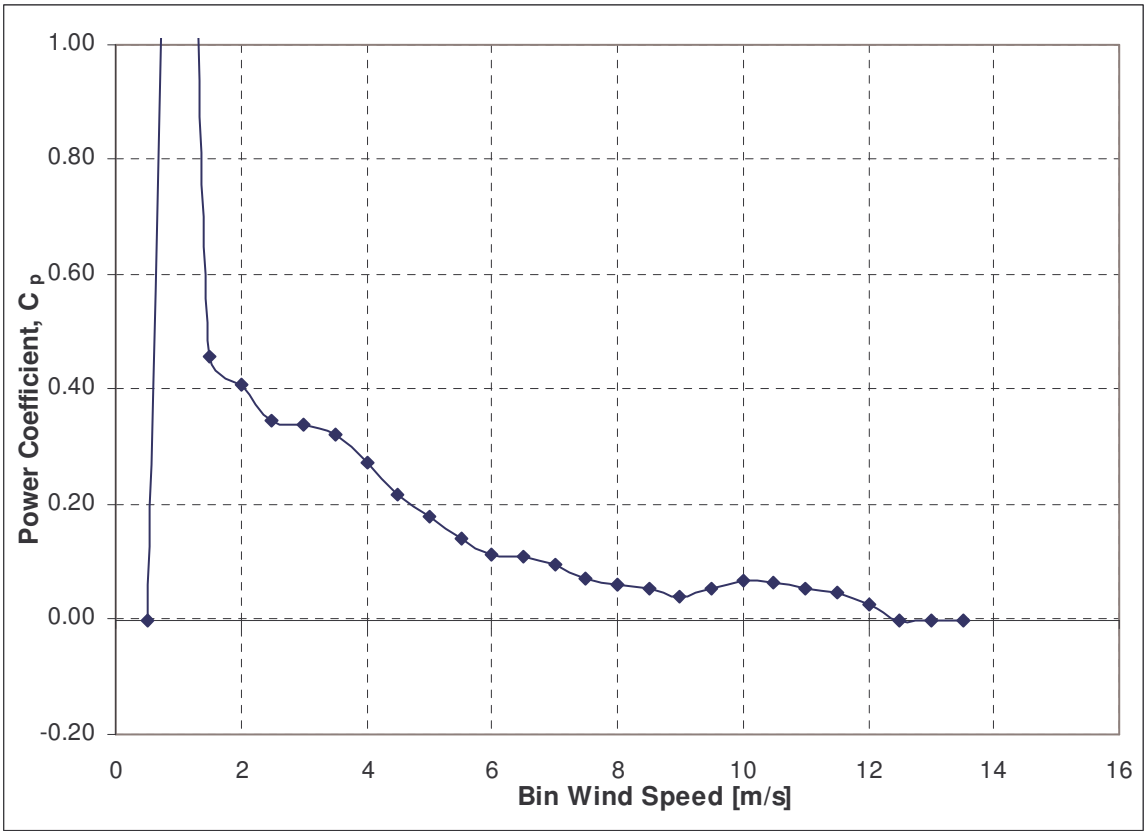

Figure 13.2 Bergey XL.1 Power Coefficient

Figure 13.3 (Reference 16) displays the power curve for the Hi-Q prototype turbine. Even though the maximum output of this turbine is less, it is almost 15% more productive at 6-7 m/s. Figure 13.4 shows the power coefficient versus bin wind speed plot.

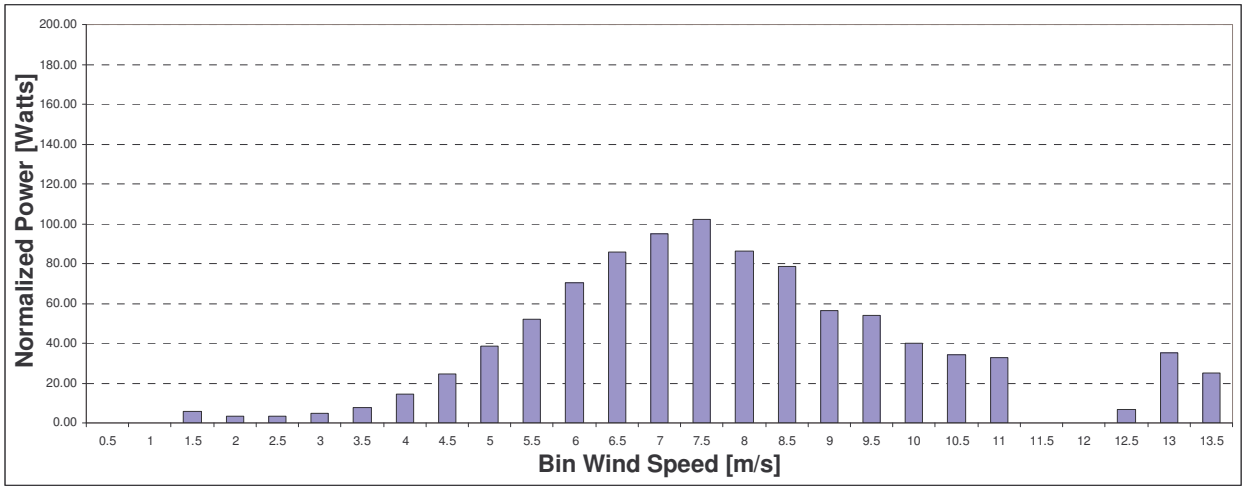

Figure 13.3 Hi-Q #61 Test Data - Normalized Average Power vs. Bin Wind Speed

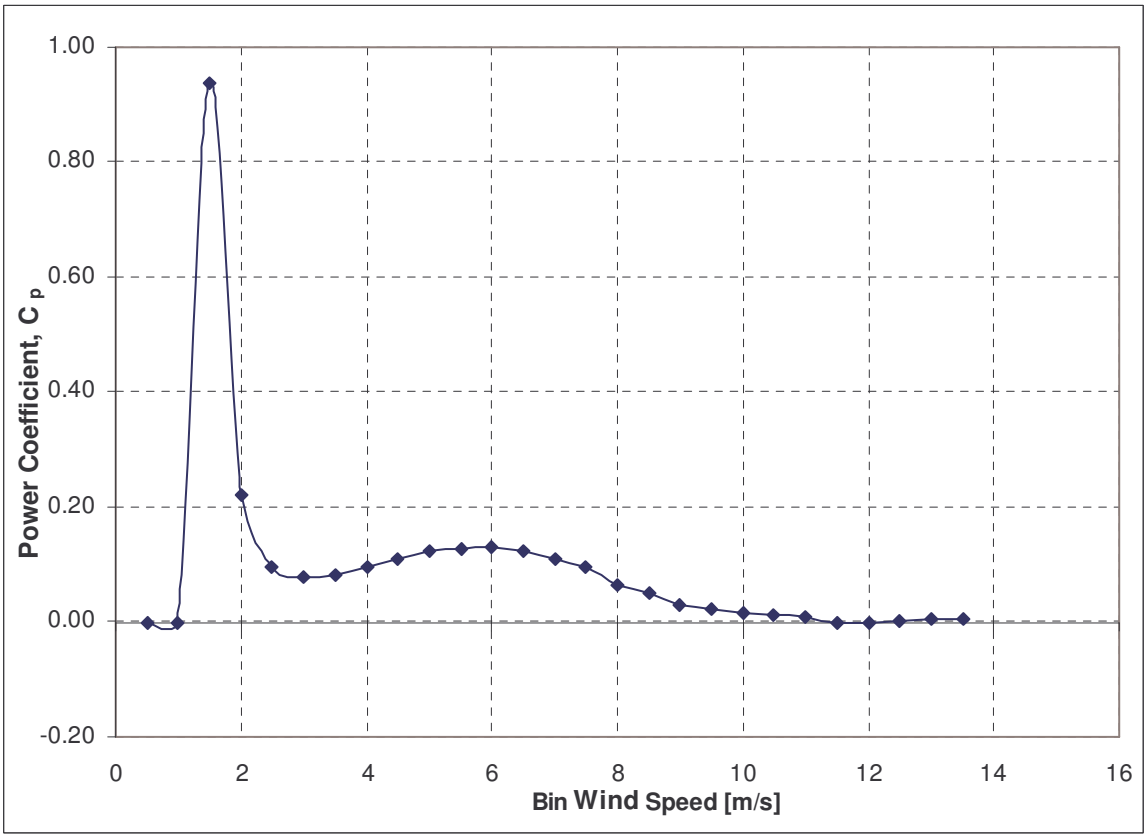

Figure 13.4 Hi-Q #61Power Coefficient

13.4 Comparison

Looking at the data collected for the two turbines, it is observed that the Bergey XL.1 is more productive at 9 m/s and up. This makes it a better choice in only Class 6 and 7 wind speed locations (Reference 17). The Hi-Q #61 wind turbine is more productive from 6 m/s to 8 m/s, making it ideal in Class 3, 4, and 5 wind speed locations. Figure 13.5 shows this information. The sudden decrease in power output of Hi-Q #61 wind turbine at wind speeds of 8 m/s and above is attributed to the furling of the tail boom. If the furling system is improved, i.e. delaying the furling of the tail boom at a higher wind speed, then it is very possible to see an increase in the normalized average power of Hi-Q #61 wind turbine, at wind speeds above 8 m/s.

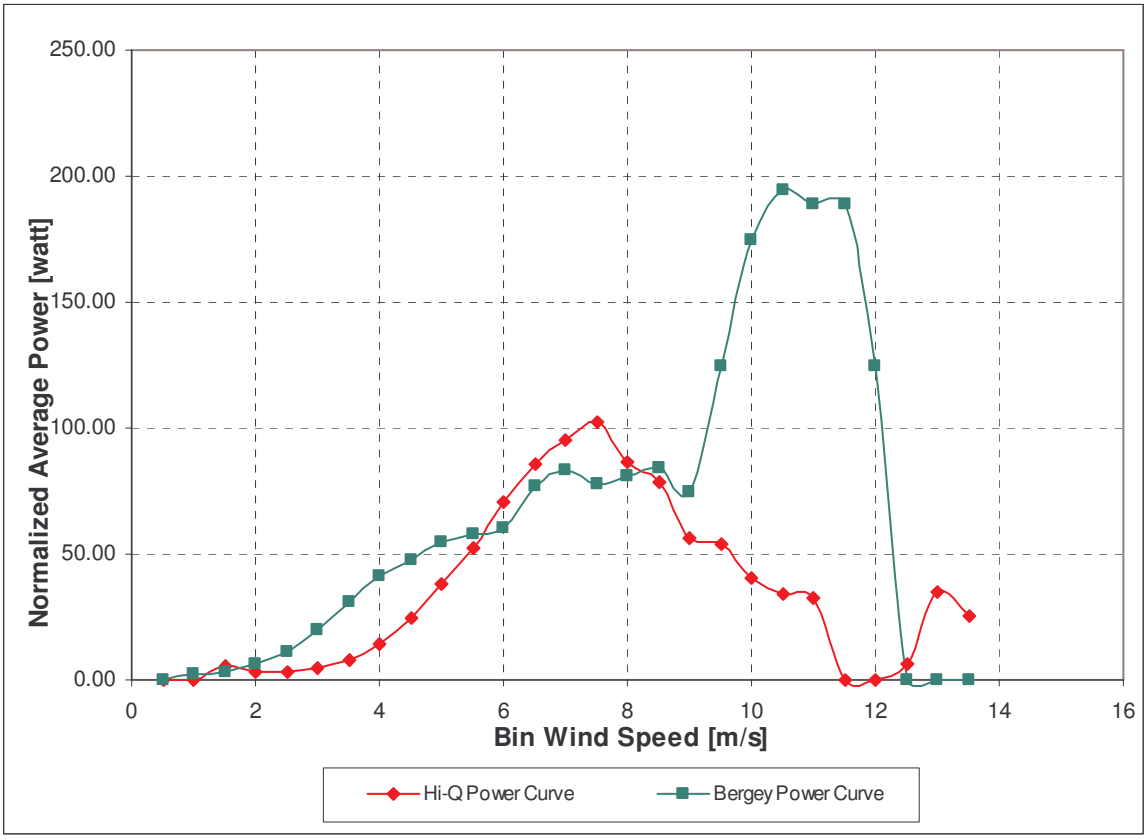

Figure 13.5 Power Curve Comparison

14. Conclusions and Recommendations

14.1 Conclusions

Based on the data collected, the results of our first full-scale prototype wind turbine proved that higher energy can be captured at lower wind speeds with the new Hi-Q Rotor. The Hi-Q Wind Turbine is more productive than the Bergey from 6 m/s to 8 m/s, making it ideal in Class 3, 4, and 5 wind sites.

Early wind tunnel testing showed that the cut-in-speed of the Hi-Q rotor is much lower than a conventional tested HAWT (Horizontal Axis Wind Turbine) enabling the Hi-Q Wind Turbine to begin collecting energy before a conventional HAWT has started spinning. Also, torque at low wind speeds for the Hi-Q Wind Turbine is higher than the tested conventional HAWT and enabled the wind turbine to generate power at lower wind speeds.

Looking at the data collected for the two turbines, it is observed that the Bergey XL.1 is more productive at 9 m/s and up, making it a better choice for Class 6 and 7 wind sites. HOWEVER, the sudden decrease in power output of the new Hi-Q Rotor at wind speeds of 8 m/s and above is attributed to the furling of the tail boom. By improving the furling system, customizing it for low wind speed, it is likely that there will be an increase in the normalized average power of the Hi-Q Wind Turbine at wind speeds above 8 m/s. Even though the maximum output of the Hi-Q Rotor is less than the Bergey, the Hi-Q Rotor is almost 15% more productive at 6-7 m/s. Even with a poorly functioning generator, significant improvements over the standard Bergey XL.1 were observed at these low wind speeds,

The final results in this first full scale prototype confirm our contention that the Hi-Q Rotor design is ideal for harvesting wind in low wind sites, Class 2, 3, 4, and 5, and has application in the critical and heretofore untapped areas that are closer to cities, "load centers," and may even be used directly in urban areas. The additional advantage of the Hi-Q Rotor's non-conventional blade tips, which eliminates most air turbulence, is noise reduction which makes it doubly ideal for populated urban areas.

14.2 Recommendations

Hi-Q Products recommends one final stage of development to take the Hi-Q Rotor through Technology Readiness Levels 8-9. During this stage of development, the rotor will be redesigned to further increase efficiency, match the rotor to a more suitable generator, and lower the cost of manufacturing by redesigning the structure to allow for production in larger quantities at lower cost.

In addition to optimizing the rotor design, it is necessary to further optimize the performance before taking it to market and commercialization by finding a better generator, one more suitable for lower wind speeds and rpms should be used in all future testing. Also, the autofurling system for the Hi-Q Rotor needs adjustment and the Bergey XL.1 settings should not be used. It is recommended to further experiment with the proper hinge locations and fin sizes to obtain the optimal settings for the autofurling system. DARcorporation, Hi-Q Products' design and research team, recommends further optimizing the blade shapes in conjunction with cheaper manufacturing processes to make construction of the blades more cost effective.

The redesigned rotor will be tested first in the wind tunnel to increase efficiency. It is expected that more slender blades with a different endplate/endcap can be designed to improve rotor efficiency. Slender blades will lower the cost of materials too. Several generators will be spec'd out, preferably in the 3-5KW range which is a more suitable power range for powering houses. The generators will be calibrated and the generator with peak performance in the 200-300 rpm range will be chosen. The blade design will be adjusted in such a way that it will operate at this optimum rpm range. Matching the aerodynamic design of the blades to the generator peak efficiency will result in an optimal operating wind mill.

The design will be perfected using the DAR developed Blade Element Method (BEM) software and CFD tools. Several scale models of the designs will be tested in the wind tunnel to select to best design. Once the best design is chosen, full scale design will proceed. Loads will be determined using CFD analysis. The rotor will be designed in carbon fiber composites. Where possible the aluminum parts and steel shafts of the full size rotor will be replaced with composites. The generator attachment and rotor hub will be designed from scratch. A new

autofurling system will be specifically designed for this rotor instead of reusing an existing design. The design will be manufactured by DARcorporation and installed at West Texas A&M University for a period of three months. During testing the power curves will be established for the full scale rotor and generator combination. This phase of development will include the commercial market validation of the technology and prepares the foundation for production preparation.

The potential impact of this fully developed technology will be the expansion and proliferation of energy renewal into the heretofore untapped Class 2, 3, 4, and 5 Wind Sites, or the large underutilized sites where the wind speed is broken by physical features such as mountains, buildings, and trees. Market estimates by 2011, if low wind speed technology can be developed are well above: 13 million homes, 675,000 commercial buildings, 250,000 public facilities. Estimated commercial exploitation of the Hi-Q Rotor show potential increase in U.S. energy gained through the clean, renewable wind energy found in low and very low wind speed sites. This new energy source would greatly impact greenhouse emissions as well as the public sector's growing energy demands.

15. References

1. Wetzel, Kyle K., Estimated Performance Envelope for a Small Wind Turbine, Document Number 27.03.001.A, 2005/01/03.
2. http://www.bergey.com/Products/XL1.Spec.pdf , last accessed 09/30/2007.
3. Manwell, J.; McGowan, J., Rogers, A. Wind Energy Explained: Theory, Design and Application, John Wiley & Sons Ltd. 2002.
4. www.harvest-tech.com, Last accessed 07/15/2008
5. Unigraphics NX 5.0, UGS Corp, 2007.
6. International Electrotechnical Commission, IEC 61400-1, Edition 3.0, 2005-08.
7. Blue Ridge Numerics, Inc., www.cfdesign.com (Last accessed on Oct 7th 2009).
8. NEi Nastran for Windows, Version 9.1.3, Noran Engineering, 2007.
9. E-mail from Balaji Kaushik, Dated 04/06/2009, Titled "Re: Nastran".
10. E-mail from John Nixon, Dated 04/03/2008, Titled "Re: LTM24ST".
11. E. Oberg, F. Jones, H. Horton, H. Ryffel, Machinery's Handbook, 28th Edition, Industrial Press, 2008.
12. Advanced Aircraft Analysis, version 3.2. DARcorporation, 2009.
13. BWC XL.1 24 VFC Battery Charging System Owners Manual, http://www.bergey.com/Products/XL1.24.OM.V2.2.pdf (last accessed on 2009/05/12).
14. International Electrotechnical Commission, IEC 61400-12-1, Edition 1.0, 2005.
15. Roberts, N., IEC Data Bergey.xls.
16. Roberts, N., IEC Data Hi-Q.xls.
17. http://www.windpoweringamerica.gov/pdfs/wind_maps/us_windmap.pdf, last accessed: 09/18/09.

Appendix A. Final Task Schedule

Task Number	Task Description	Task Completion Date				Percent Complete
		Original Planned	Revised Planned	Actual	Percent Complete	
1.	Review, investigate and define prototype parameters.	03/31/07	n/a	03/31/07	03/31/07	100%
1.1	Determine the range of thickness-to-chord ratio and camber that might be optimal.	05/31/07	n/a	05/31/07		100%
1.2	Determine the likely range of Reynolds numbers to be experienced.	05/31/07	n/a	05/31/07		100%
1.3	Determine 2 or 3 appropriate airfoils or families of airfoils to be investigated.	05/31/07	n/a	05/31/07		100%
1.4	Assess trailing edge thickness constraints and adjust the airfoil designs and performance appropriately.	03/31/07	n/a	03/31/07	03/31/07	100%
1.5	Define 3 or 4 alternative rotor shapes that will offer improvement in performance.	05/31/07	n/a	05/31/07		100%

1.6	Define range of rotor coning angles. Discretize this design space into 5 values.	05/31/07	n/a	05/31/07		100%
1.7	Define analysis matrix.	05/31/07	n/a	05/31/07		100%
1.8	Develop a code that will analyze performance of the Hi-Q Rotor.	05/31/07	n/a	05/31/07		100%
1.9	Using code from Task 1.8 analyze 60 designs from Task 1.7 to find the optimal distributions of chord and twist.	05/31/07	n/a	05/31/07		100%
1.10	Determine 3 or 4 of best from 60 designs and use CFD to analyze variations on tip designs for each.	06/15/07	n/a	06/30/07	5 designs analyzed in CFD to date	100%
1.11	From results of Task 1.10 select optimum designs to be fabricated in Task 2.	06/15/07	n/a	06/30/07		100%
2.	Based on selected geometry of Task 1, 5 small 16-inch models are designed. Test two models and compare data with CFD results to calibrate CFD data.	09/30/07		09/30/07		100%
3.	Run the 16” models in batches of two models per test with one final configuration test in University of Kansas small wind tunnel.	09/30/07		09/30/07		100%

4.	Analyze all data obtained in wind tunnel testing.	09/30/07		09/30/07		100%
4a.	Report and document Phase One final results of tests with recommendations.	09/30/07		09/30/07		100%
5.	Wind Tunnel Testing	6/30/08	10/17/08	1/8/09		100%
6.	Full Scale Design	8/16/08	10/31/08	1/8/09		100%
7.	Rotor Hub Modification	9/16/08	11/28/08	11/28/08		100%
8.	Full Scale Rotor Manufacturing	10/16/08	2/28/09	2/28/09		100%
9.	Calibration of Generator	9/16/08	11/01/08	2/10/09		100%
10.	Full Scale Testing	1/16/09	8/10/09	7/28/09		100%
11.	Data Reduction	1/16/09	8/24/09	9/29/09		100%
12.	Reports	2/16/09	8/24/09	10/27/09		100%

Appendix B. Final Spending Schedule

Task	Approved Budget	Project Expenditures	
		Current	Cumulative to Date
Task 1 Analytical Analysis	$201,992		$220,627.00
Task 2 Model Design	$23,074		$44,763.00
Task 3 Models, Wind Tunnel & Test Support	$45,929		$54,146.43
Task 4 Data Analysis	$34,883		$18,103.82
Task 4a Reporting (Phase One)	$38,027		$43,027.75
Task 5 Wind Tunnel testing	$55,820		$161,093.50
Task 6 Full Scale Design	$30,200		$60,813.65
Task 7 Rotor Hub Modification	$18,530		$13,875.00
Task 8 Full Scale Rotor Manufacturing	$66,770		$127,484.75
Task 9 Calibration of Generator	$790		$2,062.00
Task 10 Full Scale Testing	$46,545		$49,746.10
Task 11 Data Reduction	$4,790	$4,857	$11,868.00
Task 12 Reporting	$19,800	13,494	$22,104.00
Total	$587,150	$18,351	$829,715.00
DOE Share	$250,000	$1,170.00	$250,000.00
Cost Share	$337,150	$17,181.00	$579,715.00

Appendix C. Final Cost Share Contributions

Funding Source	Approved Cost Share		This Quarter		Cumulative to Date	
	Cash	In-Kind	Cash	In-Kind	Cash	In-Kind
DARcorporation	$1,000	$69,450		$2,695.00	$32,482.78	$225,767.60
Hi-Q Products, Inc.	$29,985	$236,715	$8,320.00	$6,166.00	$76,737.62	$244,727.00
Total	$30,985	$306,165	$8,320.00	$8,861.00	$109,220.40	$470,494.60
Cumulative Cost Share Contributions					$579,715.00	